Additive engineering and interface engineering for high-quality perovskite films toward efficient and stable perovskite solar cells

by

Qiaoyun Chen

A thesis

presented to the University of Waterloo

in fulfillment of the

thesis requirement for the degree of

Doctor of Philosophy

in

Mechanical and Mechatronics Engineering (Nanotechnology)

Waterloo, Ontario, Canada, 2025

© Qiaoyun Chen 2025

Examining Committee Membership

The following served on the Examining Committee for this thesis. The decision of the Examining Committee is by majority vote.

External Examiner:	Dr. Fengling Zhang Professor Department of Physics, Chemistry and Biology (IFM) Linköping University
Supervisors:	Dr. Kevin P. Musselman Associate Professor Department of Mechanical and Mechatronics Engineering University of Waterloo
	Dr. Bo Song Professor College of Chemistry, Chemical Engineering and Materials Science Soochow University
Internal Members:	Dr. Peng Peng Assistant Professor Department of Mechanical and Mechatronics Engineering University of Waterloo
	Dr. Xiaoyu Wu Assistant Professor Department of Mechanical and Mechatronics Engineering University of Waterloo
Internal-external Member:	Dr. Vivek Maheshwari Associate Professor Department of Chemistry University of Waterloo

Author's Declaration

This thesis consists of material all of which I authored or co-authored: see Statement of Contributions included in the thesis. This is a true copy of the thesis, including any required final revisions, as accepted by my examiners.

I understand that my thesis may be made electronically available to the public.

Statement of Contributions

A version of Chapter 4 has been published as Chen Q., Asgarimoghaddam H., Ji W., Wu W., Cao J., Wang R., Yu W., Nie X., Zhou Y., Song B., Musselman K. P. CuS nanosheets as additives in the hole transport layers for stable *p-i-n* perovskite solar cells. *Nano Energy* **2025**, *135*, 110652. I was responsible for the design of the experiment, synthesis of CuS nanosheets, fabrication of films and devices, characterization of the films and devices such as X-ray diffraction (XRD), UV−vis spectra, atomic force microscopy (AFM), Fourier transform infrared (FTIR), photoluminescence (PL) spectra, time-resolved PL (TRPL) spectra, space-charge-limited current (SCLC) test, current density–voltage (*J–V*) curves, external quantum efficiency (EQE) curves, and electrochemical impedance spectroscopy (EIS), collection and analysis of the data, and manuscript drafting and revision. Asgarimoghaddam H. and Yu W. assisted in the fabrication of devices. Wu W. and Nie X. carried out the scanning electron microscopy (SEM) of perovskite films. Wang R. assisted in the measurement of X-ray photoelectron spectroscopy (XPS) and ultraviolet photoelectron spectroscopy (UPS). Cao J. assisted in the Kelvin probe force microscopy (KPFM) measurement. Ji W., Zhou Y., Song B. and Musselman K. P. provided supervision of this work and support in the manuscript revision.

A version of Chapter 5 is in preparation for publication as Chen Q., Nie X., Zeng Y., Wang R. , Ji W., Zhou Y., Song B., Musselman K. P. CuS-nanoparticle-induced-porous PbI_2 for high-performance *p-i-n* perovskite solar cells. I was responsible for the design of the experiment, synthesis of CuS nanoparticles, fabrication of films and devices, the measurement of dynamic light scattering (DLS), characterization of the films and devices such as XRD, UV−vis spectra, PL spectra, TRPL spectra, SCLC test, *J–V* curves, EQE curves, transient photovoltage (TPV) spectra, transient current (TPC) spectra and EIS, collection and analysis of the data, and manuscript drafting and revision. Nie X. carried out the SEM of nanoparticles and perovskite films. Zeng Y. carried out the transmission electron microscopy (TEM) of nanoparticles. Wang R. assisted in the measurement of XPS. Ji W., Zhou Y., Song B. and Musselman K. P. provided supervision of this work and support in the manuscript revision.

A version of Chapter 6 has been submitted as Chen Q., Nie X., Ji W., Su R., Yang X., Wu W., Wang R., Zhang Z., Musselman K. P., Zhou Y. and Song B. Soybean lecithin as a passivator and compatibilizer in *p-i-n* perovskite solar cells. *ACS Appl. Mater. Interfaces* **2025**, *17*(31), 44481–44489. I was responsible for the design of the experiment, fabrication of films and devices, characterization of the films and devices such as XRD, UV−vis spectra, PL spectra, TRPL spectra, *J–V* curves, EQE curves, collection and analysis of the data and manuscript drafting and revision. Nie X. carried out

the SEM of perovskite films and assisted in the measurement of XPS, UPS, nuclear magnetic resonance (^{1}H-NMR) and the manuscript revision. Su R. and Yang X. carried out the confocal laser scanning fluorescence microscopy (CLSM) and assisted in the device fabrication and the measurement of TPC and TPV. Wu W. assisted in the SEM measurement. Wang R. assisted in the measurement of contact angles. Zhang Z. and Musselman K. P. provided support in the manuscript revision. Ji W., Zhou Y.and Song B provided supervision of this work and support in the manuscript revision.

A version of Chapter 7 has been in preparation for publication as Chen Q., Fu J., Ji W., Zhang, J., Zhang Z., Wu W., Nie X., Musselman K. P., Zhou Y. and Song B. Synergistic effect of guanidinium iodide and cesium iodide for enhanced perovskite crystal quality and device performance in hybrid perovskite solar cells. I was responsible for the design of the experiment, fabrication of films and devices, characterization of the films and devices such as XRD, UV−vis spectra, PL spectra, TRPL spectra, *J–V* curves, EQE curves, collection and analysis of the data and manuscript drafting and revision. Fu J. assisted in the device fabrication, the measurement of FTIR, KPFM and CLSM and the manuscript revision. Zhang, J. assisted in the device fabrication, SCLC test, the measurement of contact angles, TPV and TPC and the manuscript revision. Wu W. and Nie X. carried out the SEM of perovskite films. Zhang Z. assisted in the measurement of the CLSM and the manuscript revision. Musselman K. P. provided support in the manuscript revision. Ji W., Zhou Y.and Song B provided supervision of this work and support in the manuscript revision.

Chapter 1, 2, 3 and 8 are originally written by Qiaoyun Chen and have never been published before.

My publications during my PhD are listed below:

1. **Chen Q.**, Asgarimoghaddam H., Ji W., Wu W., Cao J., Wang R., Yu W., Nie X., Zhou Y., Song B., Musselman K. P., CuS Nanosheets as Additives in the Hole Transport Layers for Stable *p-i-n* Perovskite Solar Cells. *Nano Energy* **2025,** *135*, 110652.

2. **Chen Q.**, Yang X., Zhang J., Fu J., Jiang Z., Song B., Xu P., Zhou Y., Defect Passivation by a Betaine-Based Zwitterionic Molecule for High-Performance *p-i-n* Methylammonium-Based Perovskite Solar Cells. *Sol. Energy Mater. Sol. Cells* **2024,** *264*, 112615.

3. **Chen Q.**, Nie X., Ji W., Su R., Yang X., Wu W., Wang R., Zhang Z., Musselman K. P., Zhou Y. and Song B., Soybean Lecithin as a Passivator and Compatibilizer in *p-i-n* Perovskite Solar Cells. *ACS Appl. Mater. Interfaces* **2025**, *17* (31), 44481–44489.

4. Shao N., **Chen Q.**, Tao R., Yu W., Nie X., Ji W., Su Y., Zhou Y., Song B., Pb Defect Passivation and FA Immobilization: Towards Efficient and Stable Perovskite Solar Cells. *J. Mater. Chem. A* **2025,** *13* (22), 16870–16878.

5. Yu W., Cheng X., **Chen Q.**, Zhang Z., Zhou J., Wang R., Nie X., Zhang J., Ji W., Zhou Y., and B Song B., Halogenated and Dopant-free Hole Transport Materials for *n-i-p* Perovskite Solar Cells. *ACS Appl. Mater. Interfaces* **2025** *17* (27), 39270–39280.

6. Tao R., Wu T., Ji W., **Chen Q.**, Zhang Z., Rui D., Dong B., Zhou Y., Song B., Interface Modification and Crystallization Control of Efficient and Stable Perovskite Solar Cells Using Dicyandiamide. *J. Mater. Chem. A* **2025,** *13* (18), 13542–13550.

7. Cao J., **Chen Q.**, Wu W., Fu J., Zhang Z., Chen L., Wang R., Yu W., Wang L., Nie X., Zhang J., Zhou Y., Song B., Li Y., Chlorinated-$Ti_3C_2T_F$ as a Dual-Functional Buried Interface on SnO2 Electron-Transporting Layers for 25.09% High-Performance *n-i-p* Perovskite Solar Cells. *Energy Environ. Sci.* **2024,** *17* (10), 3454–3469.

8. Wang R., Yang X., **Chen Q.**, Su R., Wu W., Cao J., Yu W., Zhou Y., Song B., Li Y., Enhancing the Humidity Stability of Perovskite Films through Interfacial Modification with Differentiated Hydrophilic Organics. *ACS Appl. Mater. Interfaces* **2024,** *16* (35), 45799–45808.

9. Asgarimoghaddam H., **Chen Q.** Y., Ye F., Shahin A., Marchione O. A. C., Song B., Musselman K. P., Spatial Atomic Layer Deposition of Nitrogen-Doped Alumina Thin Films for High-Performance Perovskite Solar Cell Encapsulation. *Nano Energy* **2024,** *127*, 109782.

10. Asgarimoghaddam H., **Chen Q.** Y., Ye F., Shahin A., Song B., Musselman K. P., Zinc Aluminum Oxide Encapsulation Layers for Perovskite Solar Cells Deposited Using Spatial Atomic Layer Deposition. *Small Methods* **2024,** *8* (3), 2300995.

11. Rui D., Fu J., **Chen Q.**, Cao J., Wu W., Chen L., Zhang J., Zhang Z., Zhou Y., Song B., Surface Engineering Based on Ionic Liquids for Efficient and Stable $CsPbI_3$ Perovskite Solar Cells. *J. Mater. Chem. A* **2024,** *12* (13), 7847–7855.

12. Wu W., **Chen Q.**, Cao J., Fu J., Zhang Z., Chen L., Rui D., Zhang J., Zhou Y., Song B., Chirality-Induced Crystallization and Defect Passivation of Perovskites: Toward High-Performance Solar Cells. *ACS Appl. Mater. Interfaces* **2024,** *16* (13), 16340–16350.

13. Asgarimoghaddam H., **Chen Q.**, Ye F., Shahin A., Song B., Musselman K. P., Effect of Different Oxygen Precursors on Alumina Deposited Using a Spatial Atomic Layer Deposition System for Thin-Film Encapsulation of Perovskite Solar Cells. *Nanotechnology* **2023,** *35* (9), 095401.

14. Khamgaonkar S., **Chen Q.**, Musselman K., Maheshwari V., Stable Perovskite Photocathodes for Efficient Hydrogen Evolution in Acidic and Basic Conditions. *J. Mater. Chem. A* **2023,** *11* (37), 20079–20088.

15. Wu T., Ji W., Zhang L., **Chen Q.**, Fu J., Zhang J., Zhang Z., Zhou Y., Dong B., Song B., High-Quality Perovskite Films Prepared by Nucleus Epitaxial Growth for Efficient and Stable Perovskite Solar Cells. *J. Mater. Chem. A* **2023,** *11* (7), 3599–3607.

16. Yang X., Ji W., **Chen Q.**, Su R., Zhang L., Wang A., Zhang T., Zhou Y., Song B., Highly Stable Perovskite Solar Cells by Reducing Residual Water-Induced Decomposition of Perovskite. *Chin. J. Chem.* **2023,** *41* (13), 1594–1602.

17. Zhang Z., Fu J., **Chen Q.**, Zhang J., Huang Z., Cao J., Ji W., Zhang L., Wang A., Zhou Y., Dong B., Song B., Dopant-Free Polymer Hole Transport Materials for Highly Stable and Efficient $CsPbI_3$ Perovskite Solar Cells. *Small* **2023,** *19* (11), e2206952.

18. Wang Y., **Chen Q.**, Fu J., Liu Z., Sun Z., Zhang S., Zhu Y., Jia X., Zhang J., Yuan N., Zhou Y., Song B., Li Y., Annealing- and Doping-Free Hole Transport Material for *p-i-n* Perovskite Solar Cells With Efficiency Achieving Over 21%. *Chem. Eng. J.* **2022,** *433*, 133265.

19. Huang Z., Fu J., Ji W., Zhang L., **Chen Q.**, Zhang Z., Zhou Y., Song B., Additive-Assisted Defect Passivation of Perovskite With Metformin Hydrochloride: Toward High-Performance p-i-n Perovskite Solar Cells. *J. Phys.: Energy* **2022,** *4* (4), 044010.

20. Su R., Yang X., Ji W., Zhang T., Zhang L., Wang A., Jiang Z., **Chen Q.**, Zhou Y., Song B., Additive-Associated Antisolvent Engineering of Perovskite Films for Highly Stable and Efficient *p–i–n* Perovskite Solar Cells. *J. Mater. Chem. C* **2022,** *10* (48), 18303–18311.

21. Jiang Z., Fu J., Zhang J., **Chen Q.**, Zhang Z., Ji W., Wang A., Zhang T., Zhou Y., Song B., Reducing Trap Densities of Perovskite Films by the Addition of Hypoxanthine for High-Performance and Stable Perovskite Solar Cells. *Chem. Eng. J.* **2022,** *436*, 135269.

22. Ye F., Ayub A., Chang D., Chernikov R., **Chen Q.**, Karimi R., Wettig S., Sanderson J., Musselman K. P., Molybdenum Blues with Tunable Light Absorption Synthesized by Femtosecond Laser

Irradiation of Molybdenum Trioxide in Water/Ethanol Mixtures. *Adv. Opt. Mater.* **2022,** *10* (23), 2201304.

Abstract

Perovskite solar cells (Pero-SCs) have emerged as one of the research hotspots due to the rapidly increasing power conversion efficiency (PCE) from 3.8% to 27.3%, a simple and environmentally friendly preparation process and great commercialization potential. Despite significant progress, Pero-SCs still face considerable challenges in achieving commercialization, particularly in further enhancing their efficiency and long-term stability. Perovskite layers play critical roles in determining device performance, governing exciton absorption, charge transport and recombination dynamics, and overall device stability. However, during the fabrication of perovskite layers, it is challenging to completely suppress the formation of defects and non-radiative recombination centers, which significantly impact charge carrier dynamics. Moreover, the inherent soft-lattice nature of perovskite materials renders them highly sensitive to environmental factors, accelerating degradation and ultimately compromising device performance and long-term stability. To obtain stable high-quality perovskites, additive engineering has emerged as a highly effective strategy. Furthermore, the growth substrates underlying the perovskite layers play a critical role in governing perovskite crystallization kinetics and film morphology, such that interface engineering is also receiving significant attention. Among various modification materials, inorganic compounds are widely adopted due to their superior stability and semiconducting properties, zwitterionic molecules offer additional advantages owing to their multifunctional groups, and perovskite A-site cation halides can facilitate structural modulation of the perovskite lattice. Consequently, these three categories of additives have been investigated for performance enhancement in Pero-SCs. In this thesis, inorganic copper sulfide (CuS) nanomaterials, the zwitterionic molecule soybean lecithin (SL), guanidium iodide (GAI) and cesium iodide (CsI) are selected as additives for the hole transport layer or perovskite layers to improve the PCE and stability. The research is presented as four studies：

1) Although poly[bis(4-phenyl) (2,4,6-trimethylphenyl) amine] (PTAA) is a widely used hole transport layer (HTL) in Pero-SCs, its poor conductivity and the mismatched energy levels between PTAA and formamidinium-based perovskites increase interfacial carrier recombination and charge-transport resistance. To solve these problems, inorganic CuS nanosheets were synthesized and applied as additives in PTAA for the first time. After the addition of CuS, the conductivity of the HTL improves, and the energy levels are better aligned. In addition, perovskite growth is controlled through the interaction between CuS and PbI_2, thus improving the quality of the perovskite films, which reduces

nonradiative recombination. The addition of CuS into PTAA improved the PCE from 21.99 % to 22.92 %. Moreover, both the thermal and humidity stability improved.

2) Although excess PbI_2 can passivate perovskite boundaries and improve the PCE, under continuous illumination, the decomposition of PbI_2 will introduce non-radiative recombination centers and destroy the device stability. To mitigate the side effects of PbI_2, CuS nanoparticles were synthesized and incorporated into the PbI_2 solution. The interaction between PbI_2 and the CuS nanoparticles inhibited the PbI_2 crystallization and decreased the PbI_2 particle size. With the addition of CuS nanoparticles, more porous PbI_2 films were obtained and the reaction between PbI_2 and ammonium salts was facilitated due to smoother diffusion of formamidinium iodide (FAI). In addition, CuS nanoparticles can replace PbI_2 to prevent defects. As a result, the PCE of Pero-SCs increased from 23.21% to 24.31% with improved N_2, humidity and light stability.

3) The low affinity caused by the mismatched surface energies of the perovskite precursor solution and the underlayer is the main reason for the poor coverage of perovskite films, which is also responsible for the pinholes in the perovskite films. To solve this problem, amphiphilic SL, which has two long aliphatic chains, is applied as an additive in the perovskite precursor solution. The amphiphilic nature of SL improves the coverage of perovskite films on hydrophobic PTAA, which is conducive to the fabrication of large-scale devices. In addition, the C=O, P=O, and quaternary ammonium groups in the zwitterion segment can passivate charged defects, thus decreasing the defect density of perovskite films. Notably, the PCE of the corresponding Pero-SCs with an active area of 0.1 cm^2 increased from 20.11% to 22.93%. Furthermore, the SL-modified devices with an active area of 1.1 cm^2 demonstrated a PCE of 18.32%. The SL-modified Pero-SCs also showed better humidity stability than the pristine Pero-SCs.

4) GAI and CsI have been demonstrated as effective functional additives to FAI and PbI_2, respectively, significantly enhancing the PCE and stability of perovskite solar cells. It has been observed that the introduction of GAI into the PbI_2 lattice forms a long-range hydrogen-bonding network within the $[PbI_6]^{4-}$ octahedra. However, the large GA^+ induces lattice distortion. To address this, this study innovatively introduces Cs^+ ions, which have smaller atomic radii, to synergistically regulate crystal growth kinetics and successfully achieve lattice stress balance. Experimental results show that the synergistic effect of GAI and CsI significantly reduces the defect-state density in the perovskite thin film (from 3.0×10^{16} to 2.3×10^{16} cm^{-3}). A *n-i-p* structured device based on this approach

achieves an efficiency of 24.29% (compared to 22.66% for the control group) and exhibits excellent operational stability under 80 ± 5% relative humidity at room temperature — retaining 86% of its initial efficiency after 1000 hours of storage. This study provides a new technological pathway for improving perovskite crystal quality and device performance through cation-size-engineering strategies.

In summary, in order to solve various problems existing in perovskite films, SL, CuS nanomaterials, GAI and CsI with different properties and functions were utilized in additive engineering and interface engineering. These strategies passivated the defects in perovskite, regulate the growth of perovskite, adjust the content of PbI_2, thereby reducing non-radiative recombination, promoting charge transfer, and improving device efficiency and stability.

Acknowledgements

Time flies, and my four-year doctoral journey has come to an end in the blink of an eye. Looking back, I am deeply grateful for the unwavering support and guidance I have received throughout this period.

First and foremost, I would like to express my sincerest gratitude to my supervisors, Dr. Kevin P. Musselman and Dr. Bo Song. To Dr. Musselman, it has been a tremendous honor to be part of your research group. When I first arrived in Canada, your patient guidance and thoughtful solutions to my questions helped alleviate my initial nervousness and anxiety. In research, you have consistently encouraged my ideas, providing invaluable suggestions and granting me the chance to explore and grow. Your trust and understanding during unforeseen challenges have been a great source of strength. Your professionalism, kindness toward students, and diligent management of the lab have made my doctoral experience both memorable and rewarding. To Professor Song, I am deeply thankful for your mentorship and trust over the past decade. Your insightful perspectives have broadened my research horizons. Under your guidance, I have gained profound insights into both academic research and interpersonal relationships. Over the years, I have come to appreciate the essence of the "ROH" concept, which has inspired me to continually strive for excellence. I am truly grateful to both of you for fostering an exceptional research environment—one that emphasizes not only hard work but also collaboration, trust, and open-mindedness. Furthermore, I am deeply grateful to Dr. Yi Zhou for her guidance and support throughout my research. Her encouragement to participate in academic conferences significantly broadened my scholarly perspectives.

Then I would like to express my sincere appreciation to all the group members. I am deeply grateful to Dr. Hatameh Asgarimoghaddam and Dr. Fan Ye for guiding me in familiarizing myself with the laboratory environment and instrument operations. My heartfelt appreciation goes to Xiaoting Nie, Rui Wang, Dr. Zelong Zhang, Lei Chen, Wenting Wu, Ji Cao, Xue Liu, Yueji Li, Wei Yu, Yuanyuan Zeng, Lijie Wang and Ming Yin for their assistance with my projects. Furthermore, I am indebted to other group members in both Dr. Kevin Musselman's group and Dr. Bo Song's group for their trust, encouragement, and stimulating discussions, from which I have learned immensely. Thank you all for your help in both research and daily life and for making my life more enjoyable with your warmth and camaraderie.

I am deeply grateful to both the University of Waterloo and Soochow University for their invaluable support in this joint training program. This unique opportunity has allowed me to benefit from diverse educational approaches and immerse myself in different cultural environments. In addition, I would like to appreciate the other financial support including WIN NanoFellowship, International Experience Awards and the awards for published papers. My sincere thanks go to an outstanding research platform and fostering a productive academic atmosphere provided by University of Waterloo and Soochow University.

To my beloved family, words cannot fully express my gratitude. You have been my unwavering pillar of support - offering thoughtful advice when I faced important decisions, yet always respecting my choices and encouraging me to pursue my path. Your unconditional love and support have given me the strength and confidence to move forward steadfastly in life.

Finally, I would like to thank myself. Through moments of uncertainty and challenges, I have learned to maintain optimism and continue striving forward. I am truly grateful for the opportunity to continuously enhance my skills and grow both professionally and personally throughout this journey.

Table of Contents

Examining Committee Membership ii

Author’s Declaration iii

Statement of Contributions iv

Abstract ix

Acknowledgements xii

List of Figures xviii

List of Tables xxvii

List of Abbreviations xxix

List of Symbols xxxi

Chapter 1 Introduction 1

1.1 Perovskite solar cells 1

1.2 Perovskite layers 2

1.3 Thesis objective 3

1.4 Chapter Synopses 5

Chapter 2 Literature Review 7

2.1 Factors influencing the perovskite quality 7

2.1.1 Numerous defects 7

2.1.2 Excess PbI_2 8

2.1.3 Mismatched surface energy 9

2.1.4 Thermodynamically unstable perovskite framework 10

2.1.5 External factors affecting the stability of perovskite films 11

2.2 Additive engineering for high-quality perovskite 13

2.2.1 Inorganic nanomaterials 13

2.2.2 Zwitterionic molecules 17
2.2.3 A-site cation halides 24
2.3 Buried interface engineering for high-quality perovskite 31
2.3.1 Interactions at the perovskite-substrate interface 32
2.3.2 Modulation of surface energy 34
2.3.3 Epitaxial growth 36
Chapter 3 Methodology 39
3.1 Photovoltaic performance parameters 39
3.2 EQE measurement 39
3.3 Stability measurement 40
Chapter 4 CuS Nanosheets as Additives in the Hole Transport Layers for Stable *p-i-n* Perovskite Solar Cells 44
4.1 Introduction 44
4.2 Experimental methods 45
4.2.1 Materials 45
4.2.2 Synthesis of CuS nanosheets 45
4.2.3 Fabrication of devices 45
4.2.4 Characterization 46
4.3 Results and discussion 46
4.3.1 Characterization of the CuS nanosheets 46
4.3.2 Improving the conductivity, energy-level alignment, and charge transport 47
4.3.3 Improving the perovskite quality 50
4.3.4 Device performance 55
4.3.5 Stability of devices 58

4.4 Conclusions 59

Chapter 5 CuS-Nanoparticle-Induced Porous PbI_2 for High-Performance *p-i-n* Perovskite Solar Cells 61

5.1 Introduction 61

5.2 Experiment methods 62

5.2.1 Materials 62

5.2.2 Synthesis of CuS nanoparticles 62

5.2.3 Fabrication of devices 62

5.2.4 Characterization 63

5.3 Results and discussion 63

5.3.1 Making PbI_2 films more porous 63

5.3.2 Improving the quality of perovskite films and hole transport 67

5.3.3 Improving device performance 70

5.3.4 Improved device stability 73

5.4 Conclusions 75

Chapter 6 Soybean Lecithin as a Passivator and Compatibilizer in *p-i-n* Perovskite Solar Cells 76

6.1 Introduction 76

6.2 Experimental Methods 77

6.2.1 Materials 77

6.2.2 Fabrication of devices 77

6.2.3 Characterization 77

6.3 Results and discussion 78

6.3.1 Improving the coverage of perovskite films 78

6.3.2 Improving the quality of perovskite films 79

6.3.3 Improving the device performance 85
6.3.4 Potential of SL in practical applications 88
6.4 Conclusions 90
Chapter 7 Synergistic Effect of Guanidinium Iodide and Cesium Iodide for Enhanced Perovskite Crystal Quality and Device Performance in Hybrid Perovskite Solar Cells 91
7.1 Introduction 91
7.2 Experimental methods 92
7.2.1 Materials 92
7.2.2 Fabrication of devices 92
7.2.3 Characterization 93
7.3 Results and discussion 93
7.3.1 Improved device performance and stability 93
7.3.2 High-quality perovskite films 96
7.3.3 Better charge transport 101
7.4 Conclusions 103
Chapter 8 Conclusions and Outlook 104
8.1 Conclusions 104
8.2 Contributions 105
8.3 Outlook 105
References 107
Appendix A Supporting Information of Chapter 4 129
Appendix B Supporting Information of Chapter 5 134
Appendix C Supporting Information of Chapter 6 138
Appendix D Supporting Information of Chapter 7 144

List of Figures

Figure 1.1 (a) Efficiencies certified by the National Renewable Energy Lab. (b) Schematic diagram of *p-i-n* and *n-i-p* device structures of Pero-SCs. 1

Figure 1.2 Schematic diagram of working principle of Pero-SCs. 2

Figure 1.3 Perovskite structure in Pero-SCs. 3

Figure 2.1 Various type of perovskite defects.[15] Reprinted with permission from *Adv. Energy Mater.* 2024, 14 (6), 2302659. Copyright 2023 Wiley-VCH GmbH. 8

Figure 2.2 Schematic representation of the effect of PbI_2 on the device performance. (a) An organic-rich surface layer impedes the extraction of photoexcited charge carriers. (b) Under continuous illumination, PbI_2 is generated, which facilitates charge extraction. (c) Simultaneously, the photolysis of PbI_2 leaves voids that negate its beneficial effect on charge collection and creates recombination centers.[30] Reprinted with permission from *J. Phys. Chem. Lett.* 2020, 11 (16), 6505–6512. Copyright 2020 American Chemical Society. 9

Figure 2.3 Photograph of perovskite films deposited on a hydrophobic HTL.[39] Reprinted with permission from *Adv. Mater.* 2017, 29 (22), 1606363. Copyright 2017 WILEY-VCH Verlag GmbH & Co. KGaA, Weinheim. 10

Figure 2.4 (a) Possible decomposition pathway of hybrid halide perovskites in the presence of water.[45] Reprinted with permission from *Nano Lett.* 2014, 14(5), 2584-2590. Copyright 2014 American Chemical Society. (b) Absorption spectra and photographs of $CH_3NH_3PbI_3$ films on glass before (black) and after (red) ageing in dry air under illumination.[27] Reprinted with permission from *Energy Environ. Sci.* 2016, 9, 1655–1660. Copyright 2016 The Royal Society of Chemistry. (c) PL spectra and (d) in-situ PL spectra of $Cs_{0.15}MA_{0.07}FA_{0.78}Pb(I_{0.76}Br_{0.24})_3$ under illumination.[48] Reprinted with permission from *Chem. Eng. J.* 2025, 520, 165704. Copyright 2025 Elsevier B.V. 12

Figure 2.5 (a) Proposed nucleation and growth route of perovskite with and without $Ti_3C_2T_x$ additive.[52] Reprinted with permission from *Small* 2018, 14 (47) 1802738. Copyright 2018 WILEY-VCH Verlag GmbH & Co. KGaA, Weinheim. (b) Geometry-optimized structure of the $Ti_3C_2Cl_x$ QDs-$MAPbI_3$ heterojunction based on the DFT calculation.[53] (c) Schematic energy-level diagram of perovskite films without and with $Ti_3C_2Cl_x$.[53] Reprinted with permission from *Chem. Eng. J.* 2022, 432, 134382. Copyright 2021 Elsevier B.V. (d) Schematic of the defect passivation and better charge extraction in

perovskite by the Pb−Se coordination bonds formed between WSe_2 and $MAPbI_3$.[55] Reprinted with permission from *J. Phys. Chem. Lett.* 2021, 12 (29), 6883–6888. Copyright 2021 American Chemical Society. 15

Figure 2.6 (a) Schematic diagram of the $FAPbI_3$-PbS nanosheet epitaxial heterostructure with the interfacial strain.[60] Reprinted with permission from *Adv. Funct. Mater.* 2023, 33 (38), 2304140. Copyright 2023 Wiley-VCH GmbH. (b) The schematic illustration of perovskite crystallization.[62] Reprinted with permission from *J. Mater. Chem. A*, 2022, 10 (7), 3605–3617. Copyright 2022 The Royal Society of Chemistry. 17

Figure 2.7 Chemical structures of (a) DPSI, (b) L-alanine, (c) IMS, (d) SBMA, (e) EIMS, (f) ZIL, (g) FSA, and (h) ASP. 20

Figure 2.8 A schematic representation of the interactions involving D-PFPAA and the perovskite, including the coordination between carbonyl/fluorine and Pb^{2+}, the hydrogen bonding between amine and I^-, and the hydrophobic properties of fluorine. [73] Reprinted with permission from *J. Mater. Chem. A*, 2022,10 (19), 10750–10758. Copyright 2022 The Royal Society of Chemistry. 21

Figure 2.9 Chemical structures of (a) SQ and (b) CAPB. (c) Energy-level diagrams of the Pero-SCs based on SQ molecules.[74] Reprinted with permission from *ACS Appl. Mater. Interfaces* 2019, 11, 10012–10020. Copyright 2019 American Chemical Society. (d) Energy-level diagrams of the Pero-SCs CAPB.[75] Reprinted with permission from *Mater. Today Energy* 2025, 52, 101933. Copyright 2025 Elsevier Ltd. 23

Figure 2.10 (a) Schematic illustration of the zwitterionic surfactant-assisted meniscus coating at room temperature. (b) Schematic illustration of the coordinate interaction between TAH and charged defects at the perovskite surface and GBs and spontaneous formation of a moisture barrier.[76] Reprinted with permission from *Joule*, 2020, 4 (11), 2404–2425. Copyright 2020 Elsevier Inc. 24

Figure 2.11 (a) The calculated Cs/Pb atomic ratio of the film.[80] Reprinted with permission from *Nano Energy* 2016, 27, 87-94. Copyright 2016 Elsevier Ltd. UV-visible absorption of (b) Cs_0M and (c) $Cs_{10}M$ films annealed at 130 ℃ for 3 hours in dry air with the corresponding images.[81] Reprinted with permission from *Energy Environ. Sci.*, 2016, 9 (6), 1989–1997. Copyright 2016 The Royal Society of Chemistry. (d) Results of temperature-dependent conductivity measurement of perovskite films without Cs (w/o) and with Cs (w/Cs).[82] Reprinted with permission from *Chem. Eng. J.* 2022, 431 (4), 133713.

Copyright 2022 The Authors. Thermal stability and film formation dependence on processing conditions. Evolution of total Gibbs energy during the crystallization process (e) without and (f) with the seed crystal.[84] Reprinted with permission from *Nat. Commun.* 2018, 9, 1607. Copyright 2018 The Author(s). 27

Figure 2.12 Optimized simulated structure of the unit cell of $MA_{0.75}GA_{0.25}PbI_3$ including the six H-bond distances with respect to I atoms. [87] Reprinted with permission from *Nat. Energy* 2017, 2, 972–979. Copyright 2017 Macmillan Publishers Limited, part of Springer Nature. 29

Figure 2.13 (a) Grazing-incident XRD patterns of 0.2 GA and 0.6 GA films with different incident angles varying from 0.5° to 7°.[92] Reprinted with permission from *J. Mater. Chem. A,* 2019, 7 (16), 9486-9496. Copyright 2019 The Royal Society of Chemistry. (b) *J–V* curves of the Pero-SCs without and with GAI measured in different scan directions.[94] Reprinted with permission from *Adv. Funct. Mater.* 2019, 29 (1), 1806479. Copyright 2018 WILEY-VCH Verlag GmbH & Co. KGaA, Weinheim. (c) Top-view SEM images of perovskite films without Cs^+ doping, with 5% Cs^+, and with Cs^+ and GA^+.[95] Reprinted with permission from *Adv. Mater.* 2020, 32 (42), 2004630. Copyright 2020 Wiley-VCH GmbH. 31

Figure 2.14 (a) 2D contour maps of UV-Vis spectra of the perovskite film prepared without and with PC buried interface modification during the spinning process.[20] Reprinted with permission from *Energy Environ. Sci.*, 2025, 18 (8), 3659–3667. Copyright 2025 The Royal Society of Chemistry. (b) Proposed evolution of the nucleation and crystallization during the film-forming process with and without interface-modifying materials. [98] Reprinted with permission from *Angew. Chem. Int. Ed.* 2024, 63 (48), e202409330. Copyright 2024 Wiley-VCH GmbH. 34

Figure 2.15 Schematic illustrations of perovskite film formation on organic HTLs with and without PFN as well as corresponding photographs and SEM images.[39] Reprinted with permission from *Adv. Mater.* 2017, 29 (22), 1606363. Copyright 2017 WILEY-VCH Verlag GmbH & Co. KGaA, Weinheim. 36

Figure 2.16 (a) Side view of atomic crystal heterojunction of $MAPbI_3$ and MoS_2.[105] Reprinted with permission from *Adv. Mater.* 2019, 31 (24), 1807689. Copyright 2019 WILEY-VCH Verlag GmbH & Co. KGaA, Weinheim. (b) Side view of crystal structure and lattice constant of perovskite and WS_2.[106] Reprinted with permission from *Adv. Funct. Mater.* 2020, 30 (38), 2002358. Copyright 2020 WILEY-VCH Verlag GmbH & Co. KGaA, Weinheim. (c) Detailed diagram of the mechanism of MXene

bridging SnO_2 and perovskite.[107] Reprinted with permission from *Angew. Chem. Int. Ed.* 2022, 61 (43), e202210970. Copyright 2022 Wiley-VCH GmbH. (d) MXene-induced crystal epitaxial growth diagram of the perovskite.[108] Reprinted with permission from *Energy Environ. Sci.*, 2024, 17 (10), 3454–3469. Copyright 2024 The Royal Society of Chemistry. 38

Figure 3.1 Typical *J-V* curve. 39

Figure 3.2 Typical EQE curve and J_{int}. 40

Figure 4.1 SEM images of the CuS nanosheets (a) before and (b) after grinding. (c) EDX spectrum of CuS nanosheets on a silicon substrate. (d) XRD pattern of the CuS nanosheets.[144] Reprinted with permission from *Nano Energy* 2025, 135, 110652. Copyright 2025 The Author(s). 47

Figure 4.2 (a) Transmission spectra of HTLs. (b) *J-V* curves of devices based on ITO/HTL/Ag. (c) UPS spectra of HTLs. (d) Energy level diagrams of the HTLs and perovskite. [144] Reprinted with permission from *Nano Energy* 2025, 135, 110652. Copyright 2025 The Author(s). 49

Figure 4.3 (a) Steady-state PL and (b) TRPL of perovskite films on PTAA and PTAA-CuS. [144] Reprinted with permission from *Nano Energy* 2025, 135, 110652. Copyright 2025 The Author(s). .. 50

Figure 4.4 Top-view SEM images of perovskite films formed on (a) PTAA and (b) PTAA-CuS. Cross-sectional SEM images of perovskite films formed on (c) PTAA and (d) PTAA-CuS. (e) XRD patterns of perovskite films formed on PTAA and PTAA-CuS. (f) *J-V* curves in the dark of hole-only devices based on perovskite films formed on PTAA and PTAA-CuS for SCLC analysis.[144] Reprinted with permission from *Nano Energy* 2025, 135, 110652. Copyright 2025 The Author(s). 52

Figure 4.5 (a) Pb 4f and (b) I 3d XPS spectra of the PbI_2 samples. (c) Cu 2p and (d) S 2p XPS spectra of the CuS samples. (e) Schematic illustration of the interactions between PbI_2 and CuS.[144] Reprinted with permission from *Nano Energy* 2025, 135, 110652. Copyright 2025 The Author(s). 54

Figure 4.6 (a) *J-V* characteristic curves, (b) EQE spectra, (c) steady-state outputs, and (d) PCE histograms of the control and PTAA-CuS-based devices.[144] Reprinted with permission from *Nano Energy* 2025, 135, 110652. Copyright 2025 The Author(s). 56

Figure 4.7 (a) Plots of V_{OC} versus light intensity, (b) *J–V* curves in the dark, and (c) Nyquist plots measured near the V_{OC} under dark conditions for Pero-SCs without and with CuS. (d) The equivalent circuit for EIS fitting.[144] Reprinted with permission from *Nano Energy* 2025, 135, 110652. Copyright 2025 The Author(s). 58

Figure 4.8 PCE evolution of Pero-SCs analyzed from 5 samples for each group. (a) Stored at 65–70 °C in N_2. (b) Stored in air with an RH of 40–50%. All the samples were stored in the dark.[144] Reprinted with permission from *Nano Energy* 2025, 135, 110652. Copyright 2025 The Author(s). 59

Figure 5.1 (a) Pb 4f and (b) I 3d XPS spectra of PbI_2. (c) Cu 2p and (d) S 2p XPS spectra of CuS nanoparticles. 64

Figure 5.2 (a) XRD patterns of PbI_2 films without and with CuS nanoparticles. Top-view SEM images of PbI_2 films (b) without and (c) with CuS nanoparticles. (d) The schematic illustration of perovskite films based on different PbI_2 films. 66

Figure 5.3 Top-view SEM images of perovskite film (a) without and (c) with CuS. Cross-sectional SEM images of perovskite film (b) without and (d) with CuS. (e) XRD patterns of the perovskite films. (f) *J-V* curves in the dark of hole-only devices based on the different perovskite films for SCLC analysis. 68

Figure 5.4 (a) Steady-state PL and (b) TRPL of different perovskite films on glass. (c) Steady-state PL and (d) TRPL of different perovskite films on ITO/2PACz. 70

Figure 5.5 (a) *J-V* curves, (b) PCE histograms from 160 cells, (c) steady-state outputs, and (d) EQE spectra of the control and Pero-SC with CuS. 71

Figure 5.6 (a) Plots of V_{OC} versus P_{light}, (b) dark *J-V* curves, (c) normalized TPV and (d) normalized TPC curves of the control and Pero-SC with CuS 73

Figure 5.7 PCE evolution of Pero-SCs. (a) Stored in N_2 in the dark (analyzed from 10 samples for each group). (b) Stored in air with an RH of 30-40% in the dark (analyzed from 10 samples for each group). (c) Exposed to continuous illumination (white LED) at 35 ± 5 °C in an N_2-filled glovebox. All the samples were without encapsulation. 74

Figure 6.1 Contact angles of PbI_2 precursor solution (a) without SL and (c) with SL. Photographs of perovskite films (b) without SL and (d) with SL on PTAA.[165] Reprinted with permission from *ACS Appl. Mater. Interfaces* 2025, 17(31), 44481–44489. Copyright 2025 American Chemical Society. . 79

Figure 6.2 (a) FTIR spectra of SL and SL + PbI_2. (b) Top-view and cross-sectional SEM images of the perovskite films without and with SL. (c) Schematic illustration of the interactions between the perovskite and SL.[165] Reprinted with permission from *ACS Appl. Mater. Interfaces* 2025, 17 (31), 44481–44489. Copyright 2025 American Chemical Society. 81

Figure 6.3 (a) UV–vis spectra of perovskite films without and with SL. (b) XRD patterns of perovskite films without and with SL. *J-V* curves measured in the dark for (c) electron-only and (d) hole-only devices based on perovskite films without and with a SL for SCLC analysis. [165] Reprinted with permission from *ACS Appl. Mater. Interfaces* 2025, 17 (31), 44481–44489. Copyright 2025 American Chemical Society. 83

Figure 6.4 (a) Steady-state PL spectra of perovskite films without and with SL on glass substrates. (b) TRPL of perovskite films without and with SL on glass substrates. CLSM images of perovskite films (c) without and (d) with SL on glass substrates under ambient conditions.[165] Reprinted with permission from *ACS Appl. Mater. Interfaces* 2025, 17 (31), 44481–44489. Copyright 2025 American Chemical Society. 84

Figure 6.5 (a) *J–V* curves, (b) statistical PCEs analyzed from 30 individual cells in each group, (c) steady-state outputs, (d) EQE curves of the control and SL-modified devices.[165] Reprinted with permission from *ACS Appl. Mater. Interfaces* 2025, 17 (31), 44481–44489. Copyright 2025 American Chemical Society. 86

Figure 6.6 (a) Dark *J-V* curves, (b) plots of V_{OC} versus light intensity, (c) normalized TPV and (d) normalized TPC curves of the control and SL-modified devices.[165] Reprinted with permission from *ACS Appl. Mater. Interfaces* 2025, 17 (31), 44481–44489. Copyright 2025 American Chemical Society. 88

Figure 6.7 (a) Photo of a device with an effective area of 1.1 cm^2. (b) *J-V* curve of a 1.1 cm^2 Pero-SC doped with SL.[165] Reprinted with permission from *ACS Appl. Mater. Interfaces* 2025, 17 (31), 44481–44489. Copyright 2025 American Chemical Society. 89

Figure 6.8 (a) PCE evolution of unencapsulated Pero-SCs stored in air with RHs ranging from 40%~50%. (b) Photographs of perovskite films over time stored in air with RHs ranging from 40%~50%.[165] Reprinted with permission from *ACS Appl. Mater. Interfaces* 2025, 17 (31), 44481–44489. Copyright 2025 American Chemical Society. 90

Figure 7.1 (a) *J*−*V* curves of the champion Pero-SCs. (b) EQE curves and J_{int} of the Pero-SCs. (c) V_{OC} and (d) PCE distribution analyzed from 30 cells. 94

Figure 7.2 PCE evolution of (a) unencapsulated devices in N_2 (b) encapsulated devices stored in air with an RH of 80–85%. (c) Photographs of different perovskite films over time. All the samples were stored in the dark. 95

Figure 7.3 (a) FTIR spectra of GAI and GAI+PbI_2. (b) Schematic diagram of perovskite film fabrication. 96

Figure 7.4 Top-view SEM images of (a) the pristine perovskite film and (b) GCP film. Cross-sectional SEM images of (c) the pristine perovskite film and (d) GCP film. (e) $J-V$ curves of electron-only devices based on different perovskite films. (f) Absorption coefficient-photon energy plots of different perovskite films. 98

Figure 7.5 (a) Steady-state PL and (b) TRPL of perovskite films without and with GAI and CsI. CLSM images of perovskite films (c) without and (d) with GAI and CsI. All the perovskite films were deposited on glass substrates. 100

Figure 7.6 (a) Height AFM image (b) KPFM potential image and (c) the corresponding section analysis of height and V_{CPD} along the blue lines of the pristine perovskite films. (d) Height AFM image (e) KPFM potential image and (f) the corresponding section analysis of height and V_{CPD} along the blue lines of the perovskite films with GAI and CsI. 101

Figure 7.7 (a) Dark *J-V* curves. (b) Plots of V_{OC} versus P_{light}. (c) Normalized TPV. (d) Mott-Schottky plots of the control and GCP-SC. 102

Figure A1 Size distribution of the CuS nanosheets.[144] Reprinted with permission from *Nano Energy* 2025, 135, 110652. Copyright 2025 The Author(s). 129

Figure A2 (a) AFM height image of CuS nanosheets on wafer. (b) The vertical distance of different sites in the AFM image.[144] Reprinted with permission from *Nano Energy* 2025, 135, 110652. Copyright 2025 The Author(s). 129

Figure A3 AFM height images of (a) pristine PTAA and (b) PTAA with CuS. (c) AFM image of bare ITO. (d) The vertical distance of ITO surface.[144] Reprinted with permission from *Nano Energy* 2025, 135, 110652. Copyright 2025 The Author(s). 130

Figure A4 Tauc plots of (a) pristine PTAA and (b) PTAA with CuS films.[144] Reprinted with permission from *Nano Energy* 2025, 135, 110652. Copyright 2025 The Author(s). 130

Figure A5 KPFM images of (a) ITO/PTAA and (b) ITO/PTAA-CuS.[144] Reprinted with permission from *Nano Energy* 2025, 135, 110652. Copyright 2025 The Author(s). 131

Figure A6 Grain size distribution of perovskite crystals formed on (a) PTAA and (b) PTAA-CuS.[144] Reprinted with permission from *Nano Energy* 2025, 135, 110652. Copyright 2025 The Author(s). 131

Figure A7 FTIR spectra of CuS and CuS + PbI_2.[144] Reprinted with permission from *Nano Energy* 2025, 135, 110652. Copyright 2025 The Author(s). 132

Figure A8 PCE evolution of Pero-SCs stored in N_2 and at room temperature. The data were analyzed from 5 samples for each group. All the samples were stored in the dark.[144] Reprinted with permission from *Nano Energy* 2025, 135, 110652. Copyright 2025 The Author(s). 133

Figure B1 (a) TEM and (b) SEM images of CuS nanoparticles. 134

Figure B2 DLS results of (a) CuS nanoparticles in DMF/DMSO (b) PbI_2 precursor solutions without and with CuS nanoparticles. 134

Figure B3 Grain size distribution of perovskite (a) without and (b) with CuS nanoparticles. 135

Figure B4 The absorbance plots of perovskite films without and with CuS nanoparticles. 135

Figure B5 *J-V* curves of Pero-SC with different concentrations of CuS nanoparticles. 136

Figure B6 Nyquist plots of Pero-SCs without or with CuS nanoparticles. 137

Figure C1 TGA analysis of SL measured in N_2.[165] Reprinted with permission from *ACS Appl. Mater. Interfaces* 2025, 17 (31), 44481–44489. Copyright 2025 American Chemical Society. 138

Figure C2 The chemical structure of SL.[165] Reprinted with permission from *ACS Appl. Mater. Interfaces* 2025, 17 (31), 44481–44489. Copyright 2025 American Chemical Society. 138

Figure C3 (a) Pb 4f and (b) I 3d XPS spectra of the perovskite films without and with SL.[165] Reprinted with permission from *ACS Appl. Mater. Interfaces* 2025, 17 (31), 44481–44489. Copyright 2025 American Chemical Society. 139

Figure C4 Grain size distributions of perovskite films (a) without and (b) with SL.[165] Reprinted with permission from *ACS Appl. Mater. Interfaces* 2025, 17 (31), 44481–44489. Copyright 2025 American Chemical Society. 139

Figure C5 Absorption coefficient–photon energy plots of the perovskite films.[165] Reprinted with permission from *ACS Appl. Mater. Interfaces* 2025, 17 (31), 44481–44489. Copyright 2025 American Chemical Society. 140

Figure C6 The UPS results of perovskite films without and with SL.[165] Reprinted with permission from *ACS Appl. Mater. Interfaces* 2025, 17 (31), 44481–44489. Copyright 2025 American Chemical Society. 141

Figure C7 *J–V* curves of the Pero-SCs with SL in different scan directions.[165] Reprinted with permission from *ACS Appl. Mater. Interfaces* 2025, 17 (31), 44481–44489. Copyright 2025 American Chemical Society. 142

Figure C8 ^{1}H NMR spectra of FAI and FAI+SL.[165] Reprinted with permission from *ACS Appl. Mater. Interfaces* 2025, 17 (31), 44481–44489. Copyright 2025 American Chemical Society. 143

Figure D1 (a) *J*−*V* curves of the Pero-SCs with different concentrations of GAI. The concentration of CsI is 16.0 mg mL^{-1}. (b) *J*−*V* curves of the Pero-SCs with different concentrations of CsI. The concentration of GAI is 1.0 mg mL^{-1}. 144

Figure D2 (a) J_{SC} and (b) FF distribution analyzed from 30 cells. 145

Figure D3 (a) XRD patterns of different perovskite films. (b) Locally enlarged XRD patterns at (110) peak. (c) UV–vis spectra and (d) Tauc plots of perovskite films without and with GAI and CsI..... 146

Figure D4 Grain size distribution of (a) the pristine perovskite film and (b) GCP film. 146

List of Tables

Table 3.1 Overview of existing ISOS protocols and suggested additional protocols that account for the properties of perovskite materials and devices. [110] Reprinted with permission from *Nat. Energy* 2020, 5, 35–49. Copyright 2020 The Author(s). 41

Table 3.2 Overview of suggested ISOS-I protocols for ageing experiments in an inert atmosphere.[110] Reprinted with permission from *Nat. Energy* 2020, 5, 35–49. Copyright 2020 The Author(s). 42

Table 3.3 Stability test conditions employed in this thesis. 43

Table 5.1 Detailed photovoltaic parameters of the control and Pero-SCs with CuS. The average values were obtained from 10 devices. 72

Table 6.1 Photovoltaic parameters of champion Pero-SCs without and with SL. [165] Reprinted with permission from *ACS Appl. Mater. Interfaces* 2025, 17, 44481–44489. Copyright 2025 American Chemical Society. 87

Table 7.1 Photovoltaic parameters of Pero-SCs. The concentrations of CsI and GAI were 16.0 and 1.0 mg mL^{-1}, respectively. The average values were calculated based on 30 cells. 94

Table A1 Lifetimes and fractions derived from TRPL.[144] Reprinted with permission from *Nano Energy* 2025, 135, 110652. Copyright 2025 The Author(s). 131

Table A2 Photovoltaic parameters of PSCs with different concentrations of CuS added to the PTAA. The average values were obtained from 15 devices.[144] Reprinted with permission from *Nano Energy* 2025, 135, 110652. Copyright 2025 The Author(s). 132

Table A3 Parameters of the equivalent circuit for Pero-SCs with or without CuS.[144] Reprinted with permission from *Nano Energy* 2025, 135, 110652. Copyright 2025 The Author(s). 133

Table B1 Lifetimes and fractions derived from TRPL. 135

Table B2 Photovoltaic parameters of Pero-SCs with different concentrations of CuS nanoparticles. The average values were obtained from 15 devices. 136

Table B3 Parameters of the equivalent circuit for Pero-SCs with or without CuS nanoparticles. 137

Table C1 Photovoltaic parameters of Pero-SCs with different concentrations of SL.[165] Reprinted with permission from *ACS Appl. Mater. Interfaces* 2025, 17 (31), 44481–44489. Copyright 2025 American Chemical Society. 140

Table C2 The values of the energy levels of perovskite films without and with SL.[165] Reprinted with permission from *ACS Appl. Mater. Interfaces* 2025, 17 (31), 44481–44489. Copyright 2025 American Chemical Society. 141

Table C3 Photovoltaic parameters of Pero-SCs with different concentrations of SL.[165] Reprinted with permission from *ACS Appl. Mater. Interfaces* 2025, 17 (31), 44481–44489. Copyright 2025 American Chemical Society. 141

Table C4 Photovoltaic parameters of Pero-SCs at different scan directions. The HI is calculated by (PCE_{FS} − PCE_{RS})/PCE_{FS}.[165] Reprinted with permission from *ACS Appl. Mater. Interfaces* 2025, 17 (31), 44481−44489. Copyright 2025 American Chemical Society. 142

Table D1 Photovoltaic parameters of Pero-SCs with different concentrations of GAI. The concentration of CsI is 16.0 mg mL^{-1}. 144

Table D2 Photovoltaic parameters of Pero-SCs with different concentrations of CsI. The concentration of GAI is 1.0 mg mL^{-1}. 145

Table D3 Lifetimes and fractions derived from TRPL. 147

List of Abbreviations

2PACz	[2-(9H-carbazol-9-yl)ethyl]phosphonic acid
AFM	atomic force microscopy
BCP	bathocuproine
CsI	cesium iodide
DLS	dynamic light scattering
DMF	*N,N*-dimethylformamide
DMSO	dimethyl sulfoxide
EDX	energy-dispersive X-ray spectroscopy
EIS	electrochemical impedance spectroscopy
EQE	external quantum efficiency
ETL	electron transport layer
FAI	formamidine iodide
FF	fill factor
FTIR	Fourier-transform infrared spectroscopy
GAI	guanidinium iodide
HTL	hole transport layer
IPA	isopropanol
ITO	indium tin oxide
J-V	current density-voltage
KPFM	Kelvin probe force microscopy
MABr	methylammonium bromide
MACl	methylammonium chloride
MAI	methylammonium iodide
PbI_2	lead iodide
$PC_{61}BM$	[6,6]-phenyl-C_{61}-butyric acid methyl ester
PCE	power conversion efficiency
Pero-SC	perovskite solar cell
PEAI	2-phenylethylammoniumiodide

PFN	poly[(9,9bis(3'-(N,N-dimethylamino)propyl)-2,7-fluorene)-alt-2,7(9,9-dioctylfluorene)]
PL	photoluminescence
PSBMA	poly(sulfobetaine methacrylate)
PTAA	poly[bis(4-phenyl) (2,4,6-trimethylphenyl) amine]
SCLC	space charge limited current
SEM	scanning electron microscopy
SL	soybean lecithin
Spiro-OMeTAD	2,2',7,7'-tetrakis[*N,N*-bis(4-methoxyphenyl) amino]-9,9'-spirobifluorene
SRH	Shockley–Read–Hall
TEM	transmission electron microscope
TGA	thermogravimetric analysis
TPC	transient photocurrent
TPV	transient photovoltage
TRPL	time-resolved photoluminescence
UPS	ultraviolet photoelectron spectroscopy
XPS	X-ray photoelectron spectroscopy
XRD	X-ray diffraction

List of Symbols

α	absorption coefficient
ε	relative dielectric constant
ε_0	vacuum permittivity
E_U	Urbach energy
h	Planck constant
k_B	Boltzmann's constant
n	ideality factor
N_t	trap density
τ_1	fast decay component in TRPL
τ_2	slow decay component in TRPL
τ_R	recombination time constant
τ_T	carrier transport lifetime constant
J_0	saturation current density
J_D	dark current density
J_{int}	integrated current density
J_{SC}	short circuit current density
P_{light}	light intensity
P_{max}	maximum power output
q	element charge
R_S	series resistance
R_{CT}	charge-transfer resistance
T	temperature
V_{bi}	built-in electric field
V_{TFL}	trap-filled voltage
V_{OC}	open circuit voltage

Chapter 1
Introduction

1.1 Perovskite solar cells

To achieve environmentally friendly and sustainable development, perovskite solar cells (Pero-SCs) have drawn much attention due to their rapidly increasing power conversion efficiency (PCE) from 3.8% to 27.3% (**Figure 1.1a**) [1-6] and simple and environmentally friendly preparation process that has great commercialization potential. Pero-SCs are usually composed of a transparent conductive electrode, hole transport layer (HTL), perovskite layer, electron transport layer (ETL) and metal electrode. For single-junction Pero-SCs, there are two common device structures (**Figure 1.1b**): *p–i–n* (inverted) and *n–i–p* (conventional) structures.

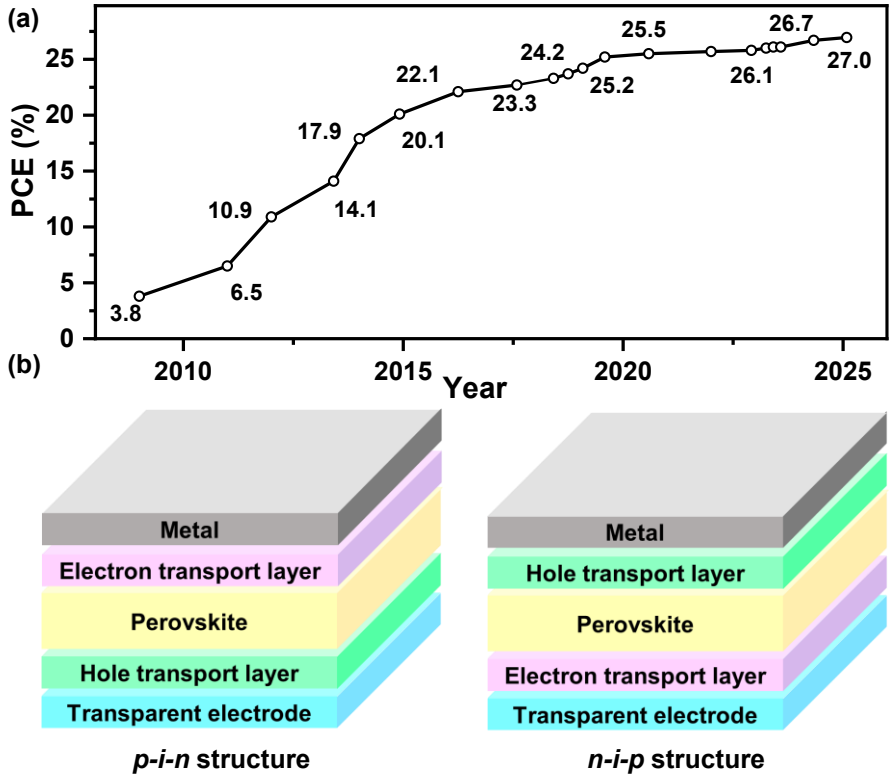


Figure 1.1 (a) Efficiencies certified by the National Renewable Energy Lab. (b) Schematic diagram of *p-i-n* and *n-i-p* device structures of Pero-SCs.

The general working processes of Pero-SCs involve four key steps: light absorption, charge transport, charge separation, and charge collection.[7, 8] As illustrated in **Figure 1.2**, when light is absorbed by the perovskite material, excitons immediately dissociate into electrons (e-) and holes (h+) due to their low binding energy. Facilitated by the perovskite material's long carrier diffusion length, these carriers then diffuse through the perovskite film toward the respective charge transport layers. The energy level alignment at the interface between the perovskite and the charge transport layers promotes efficient extraction of electrons by the ETL and holes by the HTL. Moreover, the ETL acts as a hole-blocking layer, preventing carrier recombination and thus enhancing charge collection efficiency. Finally, the separated carriers are collected by the corresponding electrodes and driven through the external circuit and load to generate electricity.

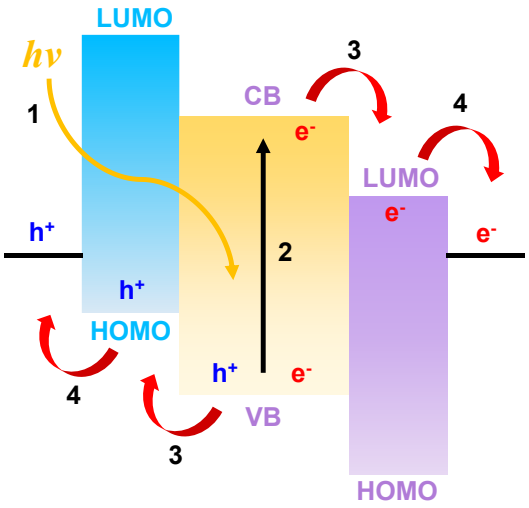


Figure 1.2 Schematic diagram of working principle of Pero-SCs.

1.2 Perovskite layers

Perovskites are a class of materials with an ABX_3-type crystal structure. In the cubic unit cell (as shown in **Figure 1.2**), the A cation is in the center of the unit cell and coordinates with 12 X anions to form AX_{12} cuboctahedron, mainly to stabilize the perovskite structure; the metal cation B is in the corner of the unit cell, forming a BX_6 symmetrical octahedral structure with 6 X anions. In Pero-SCs, A mainly refers to monovalent metal or non-metal cations such as methylammonium (MA^+), formamidine (FA^+), cesium (Cs^+) and rubidium (Rb^+), B is divalent metal cations, such as $Pb^{2+}$and Sn^{2+}, and X is mostly halogen anions, such as Cl^-, Br^-, and I^-.

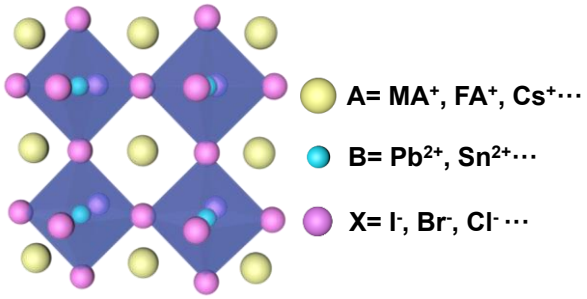


Figure 1.3 Perovskite structure in Pero-SCs.

Perovskites exhibit outstanding optoelectronic properties, including broad-spectrum absorption[9], a high absorption coefficient[10], low exciton binding energy[11] and excellent bipolar transport capability[12] making them highly efficient in light harvesting and photoelectric conversion. As such, the quality of perovskite layers—governed by crystallinity, defect density, and film coverage—critically determines the performance of Pero-SCs. However, organic-inorganic hybrid perovskites suffer from intrinsic instability due to weak van der Waals interactions, excessive ionic migration pathways, and loosely bound ionic lattices, all of which promote defect formation and degrade device efficiency.[13, 14] Moreover, perovskites are highly sensitive to environmental factors such as moisture, oxygen, light, and heat, further compromising the long-term stability of Pero-SCs. To address these challenges, optimizing perovskite film quality and stability is imperative. To date, various strategies have been developed, including composition engineering, additive engineering, interface engineering, and encapsulation techniques.

1.3 Thesis objective

Although the efficiency of Pero-SCs is now comparable to that of commercial silicon solar cells, to further promote the commercialization of Pero-SCs, many efforts are needed, such as further efficiency improvements and improved device stability. Enhancing perovskite quality is critical for advancing their applications, and various types of materials offer distinct advantages in perovskite optimization: (1) Inorganic materials provide exceptional stability and favorable semiconducting characteristics; (2) Zwitterionic materials enable dual passivation of oppositely charged defects while modulating surface energies; and (3) Perovskite A-site cation additives can structurally engineer the crystal lattice to enhance stability. Therefore, this thesis aims to investigate the

influences of inorganic CuS nanomaterials, the zwitterionic molecule soybean lecithin (SL) and the cooperation of guanidium cation (GA^+) and Cs^+ on the performance of Pero-SCs.

The detailed objectives are listed below:

1. To synthesize CuS nanosheets and apply them as additives in the HTL poly[bis(4-phenyl) (2,4,6-trimethylphenyl) amine] (PTAA), explore the properties of PTAA such as morphology, conductivity and work function through atomic force microscopy (AFM), ultraviolet photoelectron spectroscopy (UPS) and Kelvin probe force microscope (KPFM), investigate the interaction between perovskite and CuS nanosheets through Fourier-transform infrared spectroscopy (FTIR) and X-ray photoelectron spectroscopy (XPS) and explore the device performance through various characterizations such as current density-voltage (*J-V*), external quantum efficiency (EQE) and electrochemical impedance spectroscopy (EIS) measurements. To investigate the potential benefits of CuS nanosheets on the charge transport and the energy level alignment between PTAA and FA-based perovskite, *p-i-n* Pero-SCs with the structure of ITO/PTAA without or with CuS nanosheets/$FA_xMA_{1-x}PbI_3$/C_{60}/BCP/Ag are fabricated.

2. To synthesize CuS nanoparticles and apply them as additives in the perovskite, explore the changes to the PbI_2 layer and perovskite layers through film characterization such as scanning electron microscopy (SEM) and X-ray diffraction (XRD) and explore the device performance through various characterizations such as *J-V* curves, EIS, transient photovoltage (TPV) and transient photocurrent (TPC) measurements. Currently, Pero-SCs utilizing self-assembled monolayers as HTLs already demonstrate excellent PCE. Therefore, to explore whether the addition of CuS nanoparticles can further enhance the PCE and stability of such high-performance devices, the self-assembled monolayer [2-(9H-carbazol-9-yl)ethyl]phosphonic acid (2PACz) is chosen as the HTL and *p-i-n* Pero-SCs with the structure of ITO/2PACz/$FA_xMA_{1-x}PbI_3$ without or with CuS nanoparticles/C_{60}/BCP/Ag are fabricated.

3. To introduce SL molecules as additives into the perovskite, explore the contact angles of different perovskite precursor solutions upon hydrophobic HTLs and the coverage of different perovskite films, investigate the interaction between the perovskite and SL through FTIR, explore the carrier recombination through fluorescence characterization and explore the device performance through *J-V*, light-dependent, TPV and TPC measurements. SL is anticipated to address the challenge of inadequate perovskite film coverage on hydrophobic substrates; therefore, the conventional

hydrophobic polymer PTAA was selected as the HTL and *p-i-n* Pero-SCs with the configuration of ITO/PTAA/$FA_xMA_{1-x}PbI_xBr_{3-x}$ without or with SL/C_{60}/BCP/Ag are fabricated.

4. To introduce guanidinium iodide (GAI) and cesium iodide (CsI) into perovskite films, evaluate the device stability, explore the charge recombination in the perovskite through SEM, XRD, fluorescence and KPFM measurements and explore the device performance through *J-V*, light-dependent, TPV and Mott-Schottky measurements. For multi-cation perovskites, *n-i-p* structured devices can achieve high PCE due to the favorable properties of the SnO_2 ETL including its high conductivity, high mobility and good energy alignment with the perovskite. Thus, *n-i-p* structured Pero-SCs with the configuration of ITO/SnO_2/$FA_xMA_{1-x}PbI_xBr_{3-x}$ without or with GAI and CsI/Spiro-OMeTAD/MoO_3/Ag are fabricated.

1.4 Chapter Synopses

Chapter 2 is a literature review. The factors influencing perovskite quality including defects, excess PbI_2, mismatched surface energy and unstable perovskite framework are introduced. Additive engineering and interface engineering for high-quality perovskite films are introduced.

Chapter 3 introduces the methodology used to characterize photovoltaics performance, including *J-V*, EQE and stability measurements.

Chapter 4 reports the development of CuS nanosheets as additives in the HTL of *p-i-n* Pero-SCs. CuS nanosheets are synthesized and introduced into PTAA. The properties of PTAA without and with CuS nanosheets are investigated. The properties of perovskite films formed on different HTLs are explored. Finally, the device performance, including PCE and stability, is explored.

Chapter 5 reports how CuS nanoparticles are used to induce porous PbI_2 for the formation of high-performance *p-i-n* Pero-SCs. CuS nanoparticles are synthesized and introduced into PbI_2 precursor solution. The interaction between CuS and PbI_2 is confirmed and the morphology of the PbI_2 and perovskite films is investigated. The PCE and the stability are explored.

Chapter 6 reports the use of SL as a passivator and compatibilizer in *p-i-n* Pero-SCs. SL molecules are introduced into perovskite layers. The coverage of different perovskite films is compared. The interaction between the SL and perovskite is confirmed and the defects in the perovskite are analyzed. The performance of devices with different active areas is explored.

Chapter 7 investigates the synergistic effect of GAI and CsI for enhanced perovskite crystal quality and device performance in hybrid Pero-SCs. The device PCE and stability are studied. The properties of different perovskite films including the defect density, surface potential and stability are compared.

Chapter 8 summarizes several conclusions and proposed future work is presented.

Chapter 2
Literature Review

2.1 Factors influencing the perovskite quality

2.1.1 Numerous defects

Due to the solution-processing nature and rapid crystallization at elevated temperatures, perovskite films inherently develop a variety of defects (**Figure 2.1**). Taking $MAPbI_3$ as an example, there are 12 possible intrinsic point defects in $MAPbI_3$, among which undercoordinated halide ions (I^-), undercoordinated Pb^{2+}, lead clusters, iodine trimers, and Pb–I antisite defects are deep energy-level defects. These defects promote non-radiative recombination and significantly degrade the optoelectronic performance of perovskite devices. In contrast, certain point defects (e.g., iodide vacancies (V_I^+), Pb^{2+} vacancies, and MA^+ vacancies) primarily form shallow traps with lower formation energies. While these defects have minimal direct impact on photovoltaic efficiency, their migration under an electric field can lead to detrimental effects, such as ion accumulation, band bending, hysteresis, phase segregation and accelerated degradation of the perovskite layer or metal electrodes. For instance, V_i^+ disrupt the octahedral $[PbI_6]^{4-}$ framework, altering the chemical environment around Pb^{2+} and triggering iodide migration. This process breaks Pb–I bonds, generating undercoordinated Pb^{2+}—a defect that further propagates additional vacancies, establishing a detrimental feedback loop that severely compromises device stability. Beyond point defects, polycrystalline perovskite thin films exhibit extended defects, including dislocations, grain boundaries, surface defects and unsaturated bonds. These defects do not act in isolation; their interactions exacerbate charge recombination, ion migration, and material degradation, collectively undermining perovskite device performance. [15-17] In addition to bulk defects, the negative impact caused by defects at the perovskite interface cannot be ignored. Interface defects will lead to lattice mismatch and increase the probability of non-radiative recombination at the interface. It is particularly worth noting that the defect-state density at the interface of the perovskite film is 1-2 orders of magnitude higher than that of the bulk phase, which has a greater impact on the performance of the perovskite device. [18-20]

In addition to reducing the PCE, defects also have a negative impact on the device stability. For example, in terms of humidity stability, defects at the grain boundaries provide a pathway for water

molecules to invade, allowing water molecules to penetrate into the perovskite, resulting in the transformation of the optically active phase into an optically inactive phase.[21-23] In terms of thermal stability, under the action of heat, vacancies and interstitial defects can cause irregular local atomic arrangement, twisting or breaking chemical bonds, leading to the degradation of the perovskite film.[24-26] In addition, O_2 molecules in the air tend to interact with V_i^+ on the surface of the perovskite to form superoxide and peroxide, inducing the deprotonation of organic cations in the perovskite, thereby generating H_2O that accelerates the degradation of the perovskite film.[27, 28]

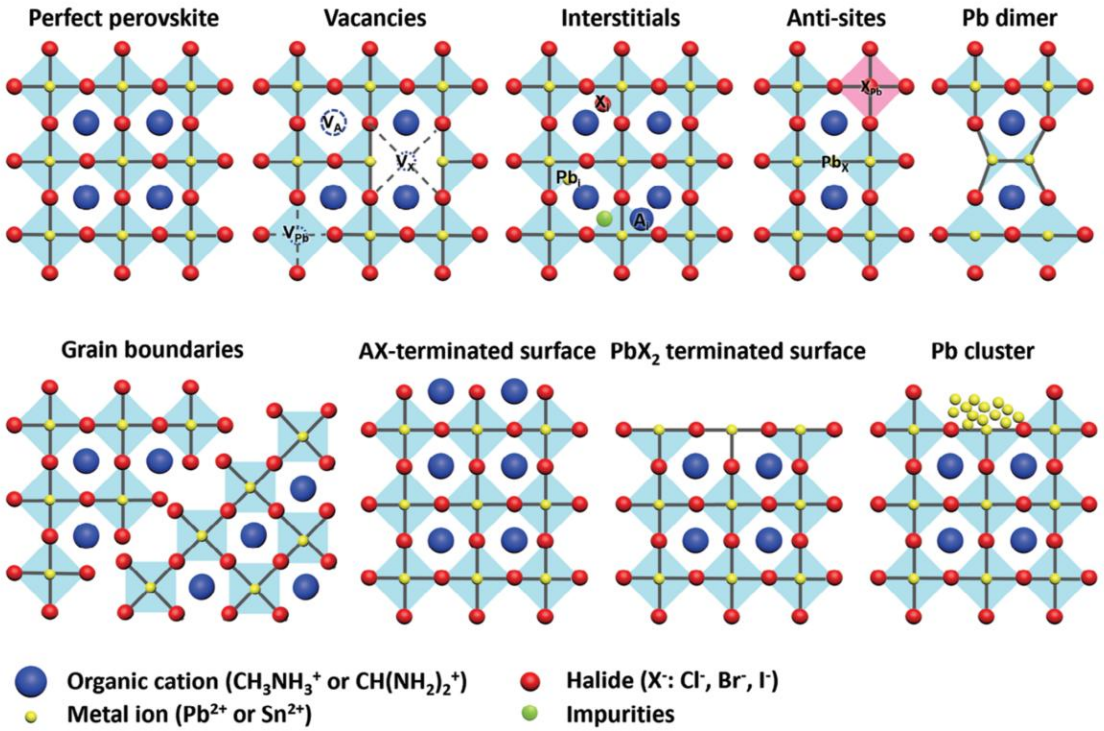


Figure 2.1 Various type of perovskite defects.[15] Reprinted with permission from *Adv. Energy Mater.* 2024, 14 (6), 2302659. Copyright 2023 Wiley-VCH GmbH.

2.1.2 Excess PbI_2

Deviations in the stoichiometry of the precursor solution, incomplete conversion of PbI_2 to perovskite, and degradation of perovskite are reasons for the formation of excess PbI_2.[29] Studies have shown that a small amount of residual PbI_2 can improve the PCE. Unreacted PbI_2 is usually present at grain boundaries, the surface of the perovskite, and at the interface between the perovskite layer and the charge transport layer. Therefore, it can prevent the formation of organic-rich surfaces,

thereby effectively limiting carrier recombination, enhancing carrier extraction and reducing hysteresis effects (**Figure 2.2a and 2.2b**).[30, 31] In addition, due to the *p*-type characteristic of PbI_2, in the *p-i-n* structure, PbI_2 accumulated at the bottom interface can promote hole transport. Additionally, PbI_2 serves as an effective passivation material between perovskite grains, further improving device performance.[32-34]

However, the intrinsic photo instability of Pero-SCs is mainly attributed to residual PbI_2. Under continuous illumination, PbI_2 decomposes into Pb^0 and I_2 (**Figure 2.2c**). Pb^0 acts as a carrier quencher, capturing electrons and holes, exacerbating the formation of non-radiative complexes, resulting in reduced device efficiency. Another product of photodegradation, I_2, spontaneously catalyzes further degradation of neighboring perovskite unit cells and induces the formation of more I_2 and PbI_2. In addition, the release of excess I_2 can lead to increased pressure inside the perovskite and eventually cause the top electrode of the device to break.[30, 31, 35, 36]

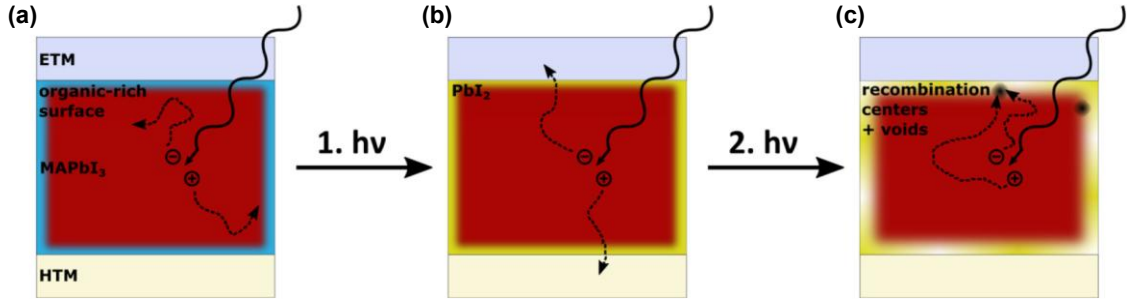


Figure 2.2 Schematic representation of the effect of PbI_2 on the device performance. (a) An organic-rich surface layer impedes the extraction of photoexcited charge carriers. (b) Under continuous illumination, PbI_2 is generated, which facilitates charge extraction. (c) Simultaneously, the photolysis of PbI_2 leaves voids that negate its beneficial effect on charge collection and creates recombination centers.[30] Reprinted with permission from *J. Phys. Chem. Lett.* 2020, 11 (16), 6505–6512. Copyright 2020 American Chemical Society.

2.1.3 Mismatched surface energy

The properties of the perovskite growth substrate, including lattice matching with the perovskite materials, surface energy, and thermal expansion coefficient differences, are critically linked to the crystalline quality and optoelectronic performance of the resulting perovskite film. Among them, the surface energy of the substrate plays a pivotal role in governing the wetting behavior of

perovskite precursor solutions and the resulting film uniformity, which is a critical factor determining the feasibility of large-scale Pero-SC manufacturing. For instance, in *p-i-n* Pero-SCs, the hydrophobicity of the HTL on which the perovskite is crystallized crucially impacts its performance as an HTL. In contrast to hydrophilic interfaces, a hydrophobic HTL surface suppresses perovskite nucleation, leading to fewer but larger grains and reduced grain boundaries, which enhance charge transport and device performance.[37] However, this hydrophobicity also introduces a critical challenge: the mismatch in surface energies between a hydrophobic HTL surface and the hydrophilic perovskite precursor solution hinders uniform wetting. This results in poor precursor spreading, incomplete perovskite coverage (**Figure 2.3**), perovskite films filled with pinholes and difficulties in scaling device fabrication.[38-41]

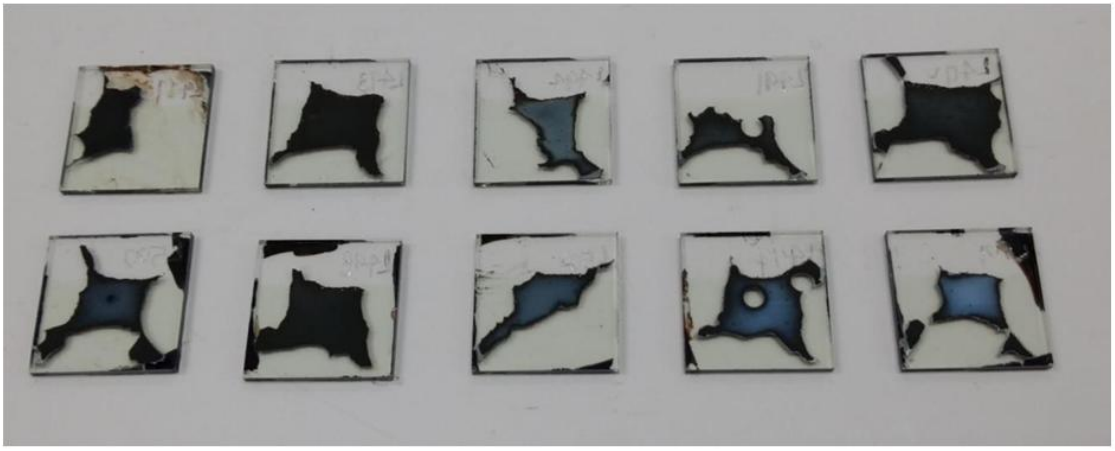


Figure 2.3 Photograph of perovskite films deposited on a hydrophobic HTL.[39] Reprinted with permission from *Adv. Mater.* 2017, 29 (22), 1606363. Copyright 2017 WILEY-VCH Verlag GmbH & Co. KGaA, Weinheim.

2.1.4 Thermodynamically unstable perovskite framework

The thermodynamically unstable perovskite framework represents a fundamental limitation in metal halide perovskite materials, where the crystal structure exists in a metastable state with respect to its compositional and environmental conditions. This instability mainly originates from three aspects. First, the significant ionic radius mismatch between Pb^{2+}, halide ions (X^-) and A-site cations, combined with their high polarizability, leads to inherently weak Pb-X bonds. This results in low lattice energy (~0.1-0.3 eV) within the $[PbX_6]^{4-}$ octahedra, making the structure susceptible

to bond dissociation under thermal/mechanical stress and facilitating ion migration and phase transitions.[42] Second, the dynamic behavior of organic A-site cations (e.g., MA^+, FA^+) introduces configurational entropy. At elevated temperatures, these cations rotate freely within the Pb-X cage, while their degradation (e.g., $MA^+ \rightarrow CH_3NH_2 \uparrow + HI \uparrow$, $\Delta G < 0$) further destabilizes the lattice, driving phase segregation.[43, 44] Third, the shallow formation energy of defects (e.g., V_i, Pb^0) lowers the activation barrier for ion migration under external stimuli (electric fields, temperature and humidity). This accelerates non-radiative recombination and perovskite degradation. [15-17]

2.1.5 External factors affecting the stability of perovskite films

The primary source of device instability lies in the degradation of perovskite materials. In addition to the intrinsic instability of perovskites themselves, various external factors, such as moisture, oxygen, temperature and light, can also accelerate their degradation.

Among these factors, moisture is particularly detrimental to perovskite materials. Owing to their highly hydrophilic nature, organic-inorganic hybrid perovskites readily absorb water from the ambient environment. This leads to the formation of hydrate phases, such as $(CH_3NH_3)_4PbI_6 \cdot 2H_2O$, which disrupt the crystalline perovskite structure. Consequently, the perovskite undergoes decomposition into hydroiodic acid (HI), PbI_2 and methylammonium (CH_3NH_2), resulting in irreversible degradation (**Figure 2.4a**).[45, 46] As displayed in **Figure 2.4b**, perovskites undergo degradation under the combined influence of oxygen and light. Oxygen molecules adsorb onto the perovskite surface and diffuse through iodide vacancies, both on the surface and within the bulk crystal, thereby penetrating the lattice. Upon adsorption at these vacancies, the oxygen molecules capture electrons from the photoexcited conduction band of the perovskite, forming charged and highly reactive superoxide species. This superoxide then initiates an acid-base reaction with the acidic A-site cations, ultimately leading to the decomposition of the perovskite material.[27, 47] In addition to its interplay with oxygen, light influences perovskite stability through multiple other mechanisms. For instance, light can provide the energy required for ion migration within the perovskite lattice, such as I^-, MA^+ and Cs^+, thereby accelerating their movement. The enhanced ion mobility can lead to phase separation, alterations in the bandgap, and overall performance decline (**Figure 2.4c and 2.4d**).[48] Moreover, ion accumulation at interfaces promotes degradation, impeding charge extraction and accelerating interfacial side reactions.[49, 50] Furthermore, continuous illumination will lead to a rise in the device temperature. Rising temperature accelerates ion

migration within the perovskite, which in turn promotes phase separation. Simultaneously, elevated temperatures induce the volatilization and thermal decomposition of organic constituents in the material, resulting in lattice vacancies and disruption of the crystalline framework. Ultimately, these processes lead to the irreversible degradation of the perovskite film, manifesting as the formation of yellow PbI_2 or other photoinactive perovskite phases.[51]

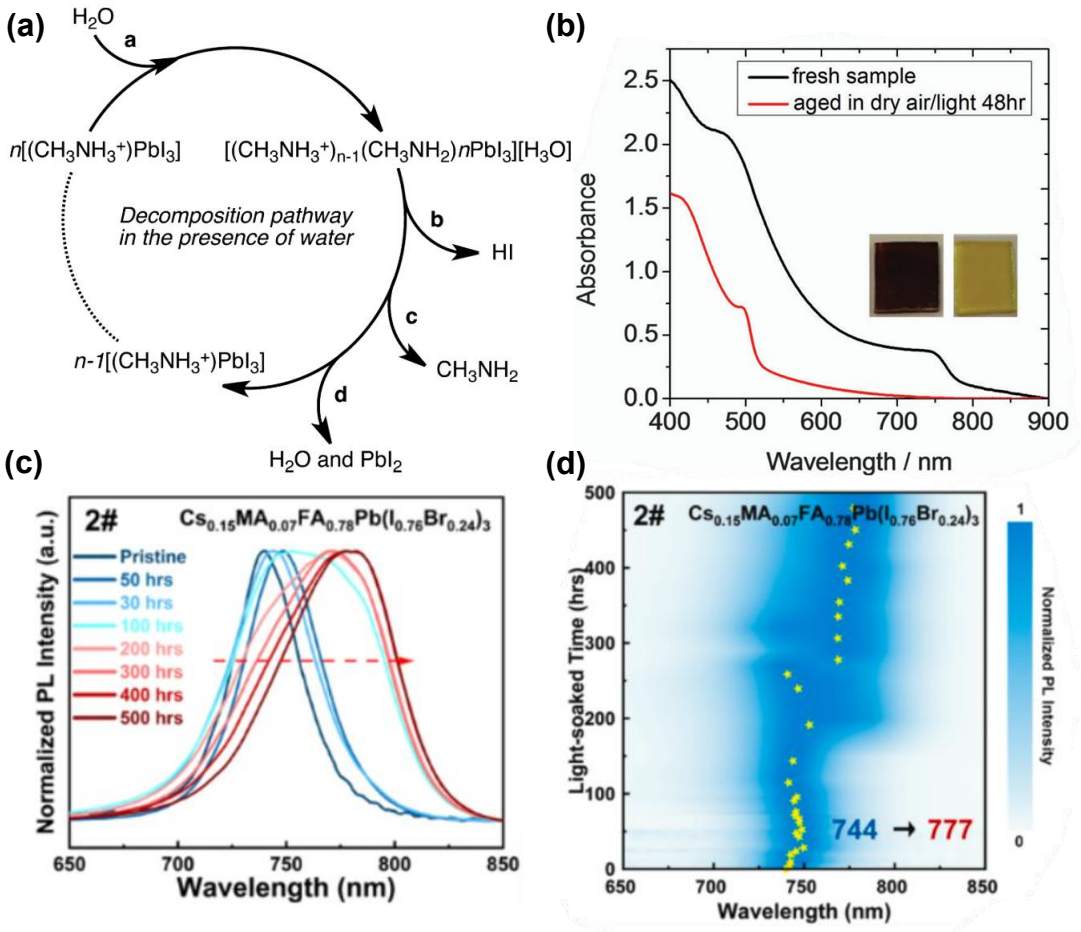


Figure 2.4 (a) Possible decomposition pathway of hybrid halide perovskites in the presence of water.[45] Reprinted with permission from *Nano Lett.* 2014, 14(5), 2584-2590. Copyright 2014 American Chemical Society. (b) Absorption spectra and photographs of $CH_3NH_3PbI_3$ films on glass before (black) and after (red) ageing in dry air under illumination.[27] Reprinted with permission from *Energy Environ. Sci.* 2016, 9, 1655–1660. Copyright 2016 The Royal Society of Chemistry. (c) PL spectra and (d) in-situ PL spectra of $Cs_{0.15}MA_{0.07}FA_{0.78}Pb(I_{0.76}Br_{0.24})_3$ under illumination.[48] Reprinted with permission from *Chem. Eng. J.* 2025, 520, 165704. Copyright 2025 Elsevier B.V.

2.2 Additive engineering for high-quality perovskite

Additive engineering plays a pivotal role in Pero-SCs by optimizing film quality, enhancing device performance, and improving long-term stability. The incorporation of functional additives serves multiple critical purposes: (1) modulating crystallization kinetics to achieve uniform and compact film morphology, (2) passivating bulk and interfacial defects to suppress non-radiative recombination, (3) fine-tuning energy level alignment for efficient charge extraction and transport, and (4) enhancing phase stability and environmental resilience against moisture, heat, and ion migration. So far, a large number of additives have been developed, such as Lewis acids, Lewis bases, zwitterionic molecules, inorganic nanomaterials, perovskite A-site cation halide, organic solvents, low-dimensional perovskites and ionic liquids, etc.

2.2.1 Inorganic nanomaterials

As perovskite additives, inorganic nanomaterials offer several advantages: (1) Inorganic nanomaterials typically exhibit superior charge carrier mobility and well-defined semiconductor characteristics, enabling effective energy-level modulation and enhanced charge transport/extraction when incorporated as additives. (2) Nanomaterials can serve as heterogeneous nucleation centers to promote the formation of large-grained perovskite films with reduced defect density. (3) Specific elements (e.g., Cl, S) in inorganic additives can chemically interact with the perovskite to passivate defects and suppress non-radiative recombination. (4) The crystal structure of nanomaterials can serve as a template for the oriented growth of perovskites. (5) The inherent hydrophobicity of many inorganic nanomaterials provides an additional protective barrier against moisture penetration, thereby improving operational stability.

Guo et al. introduced $Ti_3C_2T_x$, where T_x is a surface termination group, as an additive in a $MAPbI_3$-based perovskite layer. The van der Waals interaction O-H···I^- formed between the -OH groups of $Ti_3C_2T_x$ and MAI suppressed the number of the nucleus and retarded the nucleation process, which increased the perovskite grain size (**Figure 2.5a**), thereby increasing the light-absorption capacity of the perovskite layer. In addition, the high conductivity and mobility of $Ti_3C_2T_x$ are beneficial to facilitate charge carrier transfer. Therefore, a 12% enhancement in device performance was achieved.[52] To achieve high-crystallinity perovskite films and long-term stability against high humidity, Cl-terminated Ti_3C_2 quantum dots (QDs) were doped as additives in a perovskite precursor solution by Liu et al. Due to the strong interaction between the Cl terminations

and Pb^{2+} ions (**Figure 2.5b**), the perovskite crystallization rate was retarded and the perovskite grains grew in a preferred orientation during the film crystallization process, thereby achieving a high-quality perovskite film with high crystallinity, fewer defects, and supressed residual tensile strain. Meanwhile, $Ti_3C_2Cl_x$ QDs were distributed in an increasing manner from top to bottom in the perovskite layer, facilitating the charge extraction and benefiting band alignment between SnO_2 and the perovskite layer. As shown in **Figure 2.5c**, after the addition of $Ti_3C_2Cl_x$ QDs, the conduction band of the perovskite was closer to the conduction band of the SnO_2. As a result, an enhanced efficiency of 21.31% and negligible hysteresis was achieved with the $Ti_3C_2Cl_x$ QDs. In addition, by substituting the OH terminations, Cl-terminated $Ti_3C_2Cl_x$ QDs can avoid possible deprotonation of protonated organic amine in perovskite, improving the overall stabilities.[53] Zhang et al. fabricated Nb_2CT_x MXene nanosheets with $-NH_2$ groups and used them as a perovskite additive. The abundant surface-terminated $-NH_2$ groups can form hydrogen bonds with I^- in the perovskite precursor so N_2H_4 treated Nb_2CT_x MXene (T-Nb_2CT_x) can retard the crystallization process, which promotes the formation of high-quality and oriented perovskite films. Consequently, with further optimization of T-Nb_2CT_x as an ETL, the device with T-Nb_2CT_x exhibited the highest PCE of 21.79% along with good stability due to the suppressed I^- migration caused by the $-NH_2$ groups. [54] The quasi-monolayer two-dimensional WSe_2 was added into a $MAPbI_3$ perovskite layer by Zhao et al. The Pb-related defects were passivated through Pb−Se coordination bonding (**Figure 2.5d**), helping to form a perovskite film with higher quality and the photovoltaic performance was significantly improved with good photostability due to suppressed Pb^0 defects. In addition to passivated defects, $MAPbI_3/WSe_2$ shows a better energy alignment between the perovskite layer and HTL, accelerating hole extraction.[55]

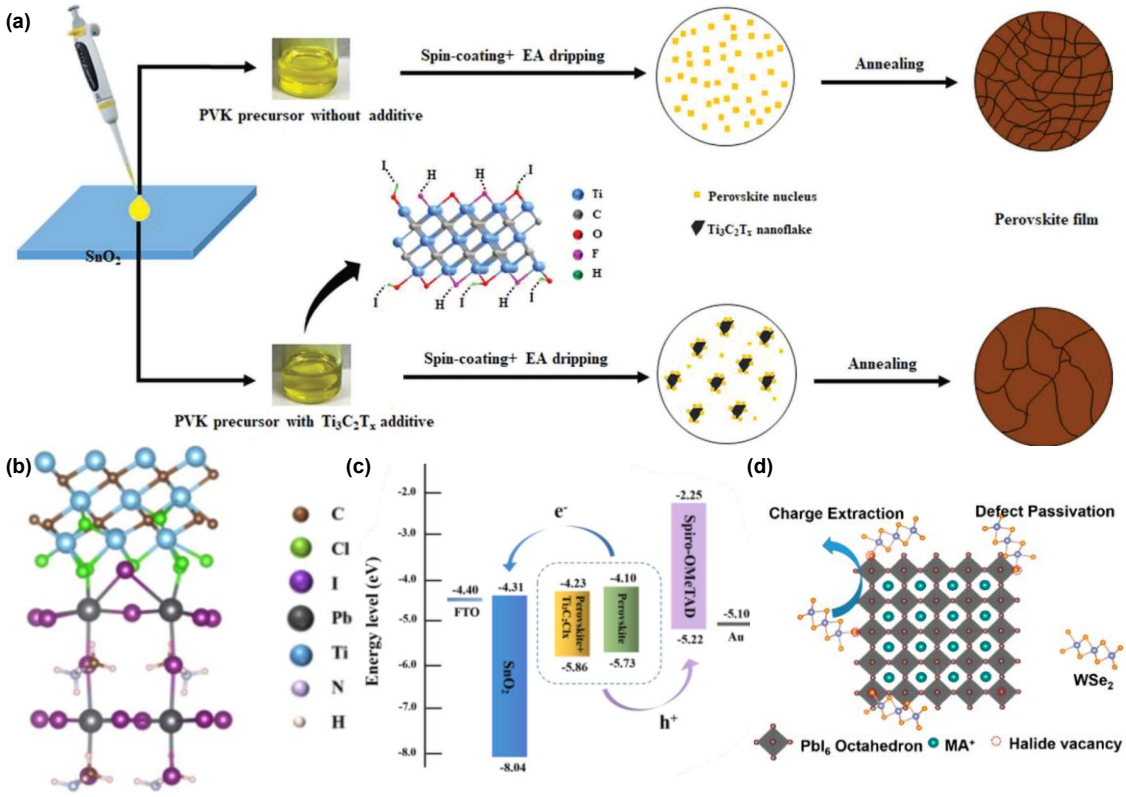


Figure 2.5 (a) Proposed nucleation and growth route of perovskite with and without $Ti_3C_2T_x$ additive.[52] Reprinted with permission from *Small* 2018, 14 (47) 1802738. Copyright 2018 WILEY-VCH Verlag GmbH & Co. KGaA, Weinheim. (b) Geometry-optimized structure of the $Ti_3C_2Cl_x$ QDs-$MAPbI_3$ heterojunction based on the DFT calculation.[53] (c) Schematic energy-level diagram of perovskite films without and with $Ti_3C_2Cl_x$.[53] Reprinted with permission from *Chem. Eng. J.* 2022, 432, 134382. Copyright 2021 Elsevier B.V. (d) Schematic of the defect passivation and better charge extraction in perovskite by the Pb−Se coordination bonds formed between WSe_2 and $MAPbI_3$.[55] Reprinted with permission from *J. Phys. Chem. Lett.* 2021, 12 (29), 6883–6888. Copyright 2021 American Chemical Society.

Zhao et al. incorporated black phosphorus (BP) into the perovskite layer. The BP inhibited the formation of Pb^0 defects and retarded hot carrier recombination, enhancing the photostability in addition to the PCE.[56] Liquid phase-exfoliated BPQDs were incorporated into the perovskite precursor solution by Chen et al. It was found that during the perovskite formation, the BPQDs serve as heterogeneous nucleation centers, which improved the perovskite crystallinity and decreased nonradiative defects, leading to longer carrier lifetime and higher carrier collection

efficiency. Consequently, the Pero-SCs with BPQDs achieved a higher PCE and better stability.[57] Lin et al. embedded non-toxic SnS QDs into $MAPbI_3$ by a facile and universal in situ crystallization method. The SnS QDs improved the crystallinity of the perovskite, enhanced the separation and transport of photo-induced carriers, and improved incident light utilization, resulting in a 25% enhancement in efficiency.[58] Yang et al. prepared SnS QDs of different sizes by varying the reaction temperature of the thermal injection method and applied them as additives in a perovskite. The SnS QDs provided more nucleation sites, which contributed to perovskite films with higher crystallinity, increased grain numbers and fewer surface defects, thus improving the light utilization, accelerating carrier transfer and reducing carrier recombination. [59]

Cubic PbS nanosheets with (200) preferred crystal planes were synthesized through anisotropy growth and regarded as additives in perovskite precursor solution by Lin et al. The lattice parameters of the cubic PbS (200) plane and $FAPbI_3$ (200) plane are similar, constructing PbS nanosheets-$FAPbI_3$ heterostructure. Thus, the epitaxial growth of $FAPbI_3$ along the (100) plane of PbS nanosheets was realized, which increased the ratio of the (100) plane with a low defect density of PbS nanosheets-perovskite hybrid films, improved the perovskite crystallinity and enlarged the perovskite grains. In addition, there was chemical interaction and compressive strain between PbS (100) plane and the α-$FAPbI_3$ (100) plane (**Figure 2.6a**). As a result, the device PCE improved with better light, humidity, thermal, and long-term storage stability.[60] Iván Mora-Seró et al. selected PbS nanoplatelets with (100) preferential crystal orientation as additives to improve the perovskite black-phase stability. With PbS, vertical growth of perovskite grains was achieved and a stable incident-photon-to-current efficiency in the infrared region of the spectrum was maintained for 4 months. Moreover, better reproducibility and better device stability were realized.[61] Zhang et al. synthesized MoS_2 nanosheets with different thicknesses and sizes by changing the centrifugation speed and used them as a perovskite additive. The MoS_2 nanosheets with a thickness of 1.2 nm and a width of 215.3 nm, which were centrifugated at 6000 rpm, served as a suitable nano-scaffold that intercalated into the PbI_2 skeleton layer to expand its physical volume and provide an efficient pathway for the organic iodide to penetrate the inner region of the PbI_2 layer (**Figure 2.6b**). Moreover, due to the interaction between MoS_2 and PbI_2, MoS_2 could also delay the quick crystallization reaction of the perovskite at the surface region, thus converting more inner PbI_2 components to the perovskite phase with oriented growth and high crystal-phase purity. This resulted in greatly reduced surface residual stress and trap densities. Therefore, the optimized

device showed an encouraging PCE of 22.50% along with excellent long-term, thermal, and ambient light-soaking stability.[62]

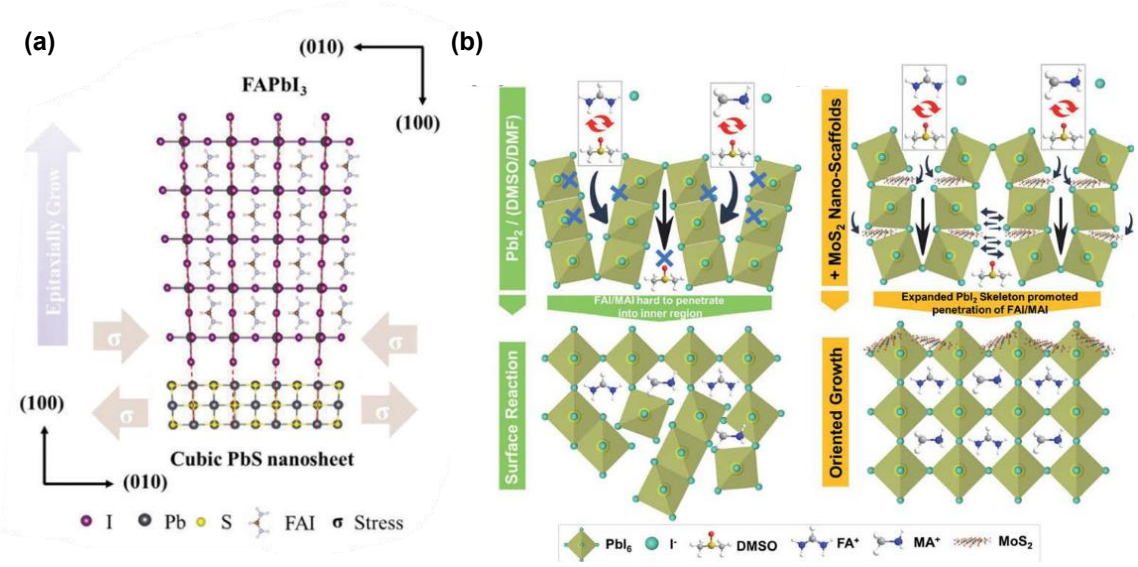


Figure 2.6 (a) Schematic diagram of the $FAPbI_3$-PbS nanosheet epitaxial heterostructure with the interfacial strain.[60] Reprinted with permission from *Adv. Funct. Mater.* 2023, 33 (38), 2304140. Copyright 2023 Wiley-VCH GmbH. (b) The schematic illustration of perovskite crystallization.[62] Reprinted with permission from *J. Mater. Chem. A*, 2022, 10 (7), 3605–3617. Copyright 2022 The Royal Society of Chemistry.

2.2.2 Zwitterionic molecules

Zwitterionic molecules are unique molecules that contain at least two functional groups with opposite charges—a positively charged cation and a negatively charged anion—resulting in an overall neutral charge. In these zwitterionic structures, the cationic and anionic groups are covalently bonded, forming stable molecular dipoles. The strong Coulombic interactions between the oppositely charged groups also confer exceptional hydrophilicity to zwitterionic materials. The introduction of zwitterionic molecules can yield the following benefits: (1) Unlike conventional organic molecules, which can only passivate either negatively charged (e.g., Pb−I antisite defects) or positively charged (e.g., undercoordinated Pb^{2+}) defects in perovskites, zwitterionic molecules offer a dual passivation mechanism. Their simultaneous interaction with both types of defects makes them highly effective in defect suppression and perovskite crystal growth modulation. (2) The dipoles can align the energy levels of the perovskite, facilitating charge transport. (3)

Zwitterionic molecules with long alkyl chains can change the surface energy of the perovskite precursor solution and increase the coverage of the perovskite films on the hydrophobic substrates. Consequently, various zwitterionic molecules have been explored as multifunctional additives in perovskite materials to enhance defect passivation, control crystallization and improve the charge transport.

Huang et al. applied a sulfonic zwitterion 3-(decyldimethylammonio)-propane-sulfonate inner salt (DPSI) **(Figure 2.7a)** as a dopant to tune the crystallization behavior and passivate the defects of perovskites through the reaction between the functional ligands and perovskite, which suppresses pinhole formation, reduces the charge trap density, and lengthens the carrier recombination lifetime.[63] Lee et al. employed an amino acid, L-alanine **(Figure 2.7b)**, as the additive in $MAPbI_3$. At a specific solvent pH, L-alanine has both positive (NH_3^+) and negative (COO^-) functional groups, which could passivate both the cation and anion defects. The perovskite films containing L-alanine had larger grains and prolonged carrier lifetime. Finally, the PCE was improved from 18.3% to 20.3% with enhanced shelf storage and photoirradiation stabilities.[64] Yang et al. added an imidazole sulfonate zwitterion, 4-(1H-imidazol-3-ium-3-yl) butane-1-sulfonate (IMS) **(Figure 2.7c)** into perovskite as a bifunctional additive. The sulfonate moiety of IMS can passivate undercoordinated Pb^{2+} via coordination interactions and the imidazole of IMS interacts electrostatically with the I^- ion of $MAPbI_3$. Additionally, IMS regulated crystalline grain orientation. As a result, the PCE was improved from 18.77% to 20.84%.[65] A betaine-based zwitterionic molecule, 3-[[2-(methacryloyloxy)ethyl]dimethylammonio]propane-1-sulfonate (SBMA) (**Figure 2.7d**), was employed as an additive in *p-i-n* Pero-SCs by Song et al. The ester groups and SO_3^- of SBMA passivated the positively charged defects and the quaternary ammonium ions passivated the negatively charged defects. The dipole moment induced by zwitterionic moieties also improved the built-in electric field, facilitating charge transportation. Consequently, for the SBMA-based *p-i-n* Pero-SCs with an active area of 0.0757 cm^2, a champion PCE as high as 21.39% was achieved with improved thermal and humidity stability. Moreover, the SBMA device with larger areas of 0.27 cm^2 and 1.1 cm^2 could achieve PCEs of 20.18% and 18.43%, respectively. In addition to the monomer, the elastomer of SBMA was synthesized via in situ cross-linking and introduced into a perovskite film by Ge et al. Apart from controlling the perovskite growth and passivating the defects, the zwitterionic cross-linked elastomers located at the grain boundaries enabled the flexible perovskite film to instantly self-solidify under mild processing conditions (40 °C, 15 minutes). The

resulting flexible device achieved record-breaking PCE of 24.51% (certified 24.04%) and demonstrated excellent mechanical sustainability and durability.[66] Han et al. investigated the influence of the alkyl chain on a zwitterionic sulfobetaine passivator. As the alkyl length increased, due to the inductive effect, the positive charge of the quaternary ammonium salt was dispersed, thereby weakening the internal interaction between the positive ammonium group and the negative sulfonic acid group while strengthening the interaction between the sulfonic acid group and the perovskite, resulting in a significantly enhanced defect passivation effect, which increases the carrier lifetime by more than 5 times. However, the longer alkyl chain easily induced aggregation between adjacent sulfonated betaine molecules, thereby reducing the fill factor of the device and limiting further performance improvement. Based on the optimal octyl group, the PCE of printable mesoscopic Pero-SCs was successfully improved from 19.92 % to 21.62 %.[67] An imidazolium-based zwitterionic ionic liquid, 1-(1-ethyl-3-imidazolium) propane3-sulfonate (EIMS) (**Figure 2.7e**), was established as an effective perovskite additive. Strong interactions between Pb^{2+} and EIMS were confirmed and the addition of EIMS resulted in a porous PbI_2 film, which promotes the reaction of PbI_2 with formamidinium iodide (FAI), improving the quality of the perovskite films. Finally, EIMS promoted the extraction of electrons, inhibited the formation of pinholes, and reduced the defect density, which led to an increased efficiency of 22.1% with negligible hysteresis behavior. Moreover, Pero-SCs with EIMS had a better stability after being stored in dry air for 45 days.[68] Another zwitterionic ionic liquid (ZIL) (**Figure 2.7f**) with 4-fluorophenylammonium ($4FB^+$) as cations and tetrafluoroborate (BF_4^-) as anions was applied by Song et al. First, the $4FB^+$ with a π-conjugated benzene ring can donate electrons for carrier extraction. In addition, the molecular packing of the C-F bond could enhance moisture blocking. Second, the high ionic conductivity of the pseudohalogen anion BF_4^- can significantly enhance the carrier lifetime and reduce energy loss. Third, $4FB^+$ and BF_4^- could passivate vacancy defects induced by ion migration. As a result, the ZIL-modified Pero-SCs can reach a PCE as high as 22.5% with excellent long-term stability.[69]

Wide-bandgap Pero-SCs are promising candidates for tandem solar cells when paired with narrow-bandgap sub-cells, offering significant potential for commercialization. However, the complex composition of wide-bandgap perovskites and their challenging crystallization kinetics often lead to the formation of bulk and interfacial defects in polycrystalline films. These defects induce severe non-radiative recombination of charge carriers, ultimately resulting in substantial energy losses in wide-bandgap Pero-SCs. Formamidine sulfinic acid (FSA) (**Figure 2.7g**) was

introduced into wide-bandgap Pero-SCs by Zhan et al. The robust interaction between the sulfinyl group (-S=O) and Pb^{2+} could retard the perovskite crystallization. Furthermore, Lewis acid-base interactions were generated between undercoordinated Pb^{2+} and negative $–SO_2^-$ groups and hydrogen bonds formed between halogen and positive $–C(NH_2)_2^+$ groups. With this strategy, the wide-bandgap Pero-SCs achieved a champion efficiency of 22.06% and the 2-terminal perovskite/silicon tandem solar cells were fabricated with an efficiency of 28.81%.[70] Similarly, to enhance the performance of the wide-bandgap Pero-SCs, a zwitterionic food sweetener, aspartame (ASP) (**Figure 2.7h**), was used as a multifunctional additive in a $Cs_{0.1}FA_{0.65}MA_{0.25}Pb(I_{0.8}Br_{0.2})_3$ perovskite. The proton transfer process occurred within the perovskite precursor solution, suggesting that ASP exists in the film in the form of a zwitterion. ASP contained carboxyl (-COOH), carbonyl (C=O), and amino ($=NH_2$) groups, which can establish strong and diverse interactions with PbI_2 and FAI, thereby passivating charged defects in the film, reducing defect density. Moreover, the addition of ASP created a band gradient at the interface, facilitating effective charge transfer. Consequently, single-junction wide-bandgap Pero-SCs achieved a PCE of 23.20%, and perovskite/Si tandem solar cells reached a PCE of 30.68% with enhanced photostability and operational durability.[71]

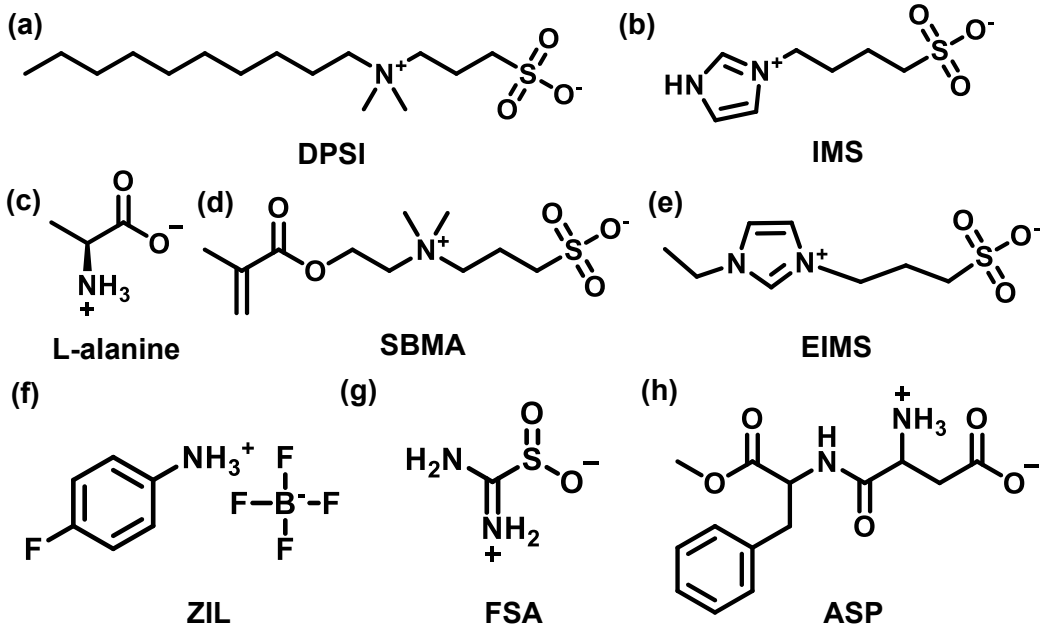


Figure 2.7 Chemical structures of (a) DPSI, (b) L-alanine, (c) IMS, (d) SBMA, (e) EIMS, (f) ZIL, (g) FSA, and (h) ASP.

An alcohol-soluble zwitterionic molecule named bethanechol chloride (BTCC) was adopted by Xu et al. as a dopant for the perovskite layer. With the addition of BTCC, the Pb-I framework could be stabilized through hydrogen bonding and the defects could be passivated owing to its zwitterionic functional groups. After being treated by BTCC, perovskite films with reduced nonradiative charge recombination and prolonged carrier lifetime were obtained. For the BTCC-treated device, a higher PCE was acquired with enhanced moisture-resistance.[72] Wang et al. introduced fluorinated D-pentafluoro-phenylalanine (D-PFPAA) zwitterions into a perovskite to consolidate the Pb–X framework to suppress ion migration. As shown in **Figure 2.8**, the amino, carboxyl, and fluorine groups in D-PFPAA can passivate both positive (undercoordinated Pb^{2+}) and negative (halogen anions) defects, thereby effectively suppressing trap-assisted recombination. Apart from suppressed nonradiative recombination, the fluorine groups in D-PFPAA can protect the perovskite film from moisture-related erosion by forming a hydrophobic barrier. As a consequence, a D-PFPAA-modified cell showed the highest PCE of 21.56% with better humidity stability.[73]

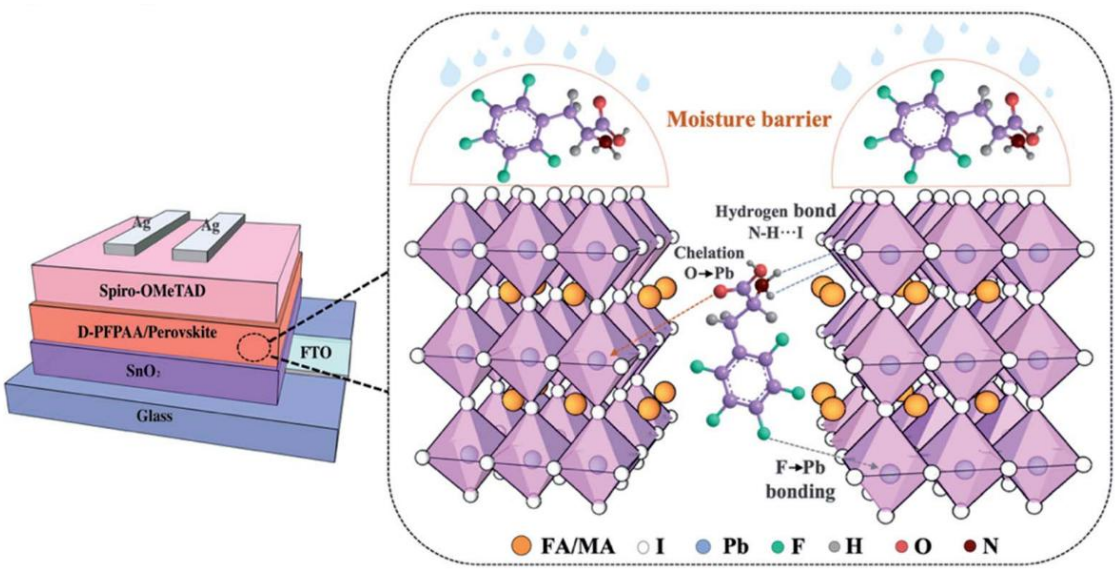


Figure 2.8 A schematic representation of the interactions involving D-PFPAA and the perovskite, including the coordination between carbonyl/fluorine and Pb^{2+}, the hydrogen bonding between amine and I^-, and the hydrophobic properties of fluorine. [73] Reprinted with permission from *J. Mater. Chem. A*, 2022,10 (19), 10750–10758. Copyright 2022 The Royal Society of Chemistry.

Beyond defect passivation, zwitterionic molecules can modulate the energy-level alignment through their intrinsic dipole moments. For instance, Hayase et al. designed and synthesized three squaraine molecules (**Figure 2.9a**) with different halogen atoms. The squaraine molecules with resonance-stabilized zwitterions could passivate the undercoordinated Pb^{2+} and Pb−I antisite defects simultaneously, resulting in a reduced trap density and controlled crystal growth. Furthermore, because of the good energy alignment between the squaraine molecules and perovskite (**Figure 2.9c**), squaraine molecules could enhance charge separation. Prepared in ambient atmosphere with more than 60% relative humidity (RH), the device based on squaraine achieved a PCE of 18.83%, while the control device only reached a PCE of 15.77%. Besides PCE, the humidity stability was also enhanced.[74] The zwitterionic molecule cocamidopropyl betaine (CAPB) (**Figure 2.9b**) was introduced into perovskite films to enable dual bulk and surface passivation. The introduction of CAPB plays multiple roles. Firstly, the quaternary ammonium group in CAPB formed electrostatic interactions with iodine ions from PbI_2, effectively passivating halide vacancies. Secondly, the electron-rich carboxylate ($-COO^-$) and amide (−CONH−) act as multidentate ligands, chelating undercoordinated Pb^{2+} ions. Thirdly, hydrogen bonding interactions between the $-COO^-$ and −CONH− moieties of CAPB and the amine N-H groups significantly suppressed amine volatilization at elevated temperatures. Fourthly, the formation of an interfacial dipole induced by CAPB on the perovskite surface adjusted the energy levels of the perovskite layers, effectively inhibiting carrier reverse recombination (**Figure 2.9d**). As a result, CAPB-based devices exhibited a PCE of 21.47 % along with excellent humidity stability and thermal stability.[75]

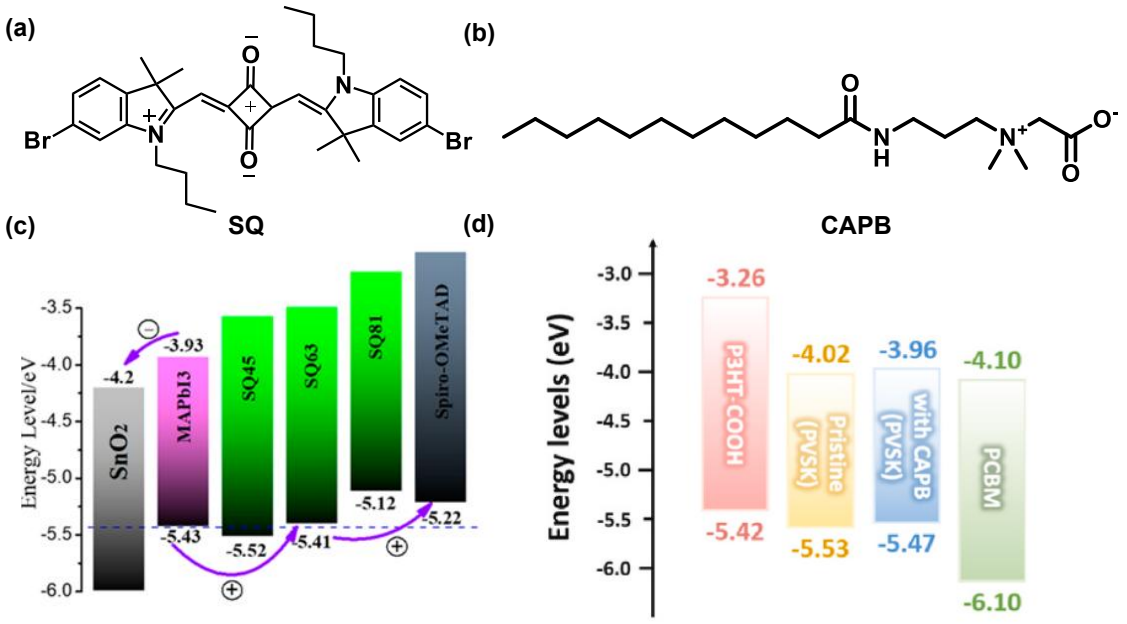


Figure 2.9 Chemical structures of (a) SQ and (b) CAPB. (c) Energy-level diagrams of the Pero-SCs based on SQ molecules.[74] Reprinted with permission from *ACS Appl. Mater. Interfaces* 2019, 11, 10012–10020. Copyright 2019 American Chemical Society. (d) Energy-level diagrams of the Pero-SCs CAPB.[75] Reprinted with permission from *Mater. Today Energy* 2025, 52, 101933. Copyright 2025 Elsevier Ltd.

Li et al. employed a multifunctional sulfobetaine-based zwitterionic surfactant, tetradecyldimethyl (3-sulfopropyl) ammonium hydroxide inner salt (TAH), featuring distinct hydrophilic zwitterionic groups and a hydrophobic long alkyl chain, as an additive in perovskite ink. As shown in **Figure 2.10a,** due to its amphipathic nature, TAH tuned the surface energy of the perovskite ink and enhanced its adhesion to the hydrophobic substrate, which decreased the formation energy of the heterogeneous nucleation, facilitating the fabrication of uniform and high-quality perovskite films with full coverage. Furthermore, the functional zwitterionic groups passivated the charge defects, suppressing the nonradiative recombination (**Figure 2. 10b**). Under the dual functions, the efficiencies of Pero-SCs fabricated by blade-coating increased up to 22% (0.04 cm^2 active area) and 21% (0.8 cm^2). Beyond efficiency enhancement, this strategy also substantially improved the moisture, thermal and light-illumination stability.[76]

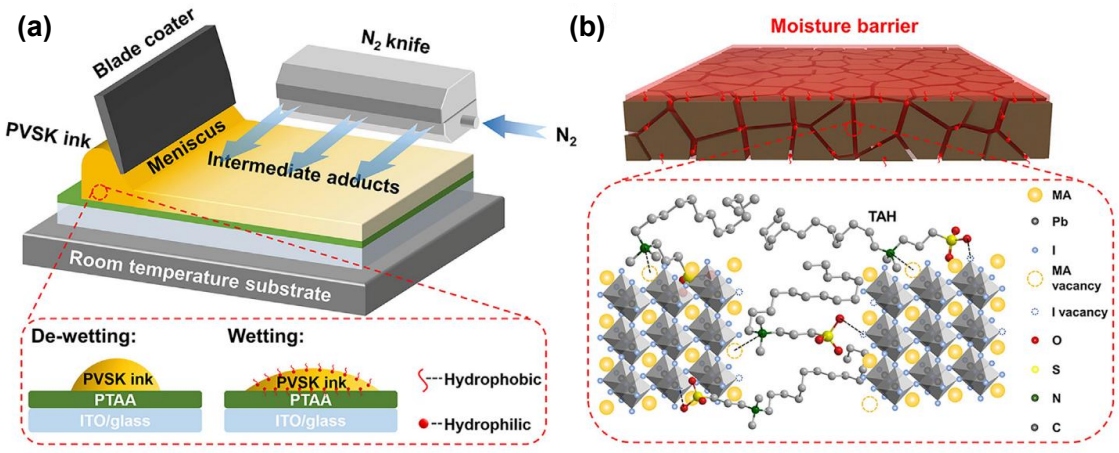


Figure 2.10 (a) Schematic illustration of the zwitterionic surfactant-assisted meniscus coating at room temperature. (b) Schematic illustration of the coordinate interaction between TAH and charged defects at the perovskite surface and GBs and spontaneous formation of a moisture barrier.[76] Reprinted with permission from *Joule*, 2020, 4 (11), 2404–2425. Copyright 2020 Elsevier Inc.

2.2.3 A-site cation halides

Doping of A-site cation halides serves as a critical strategy for optimizing the optoelectronic properties and stability of perovskite materials. The primary roles of A-site cation doping include: (1) By adjusting the tolerance factor (*t*) within the optimal range (0.8-1.0), A-site doping suppresses phase segregation and the formation of non-photoactive phases (e.g., *δ*-phase $FAPbI_3$), thereby enhancing phase stability. (2) Tailoring the electronic structure through cation substitution enables precise control over the bandgap and energy level alignment, improving light-harvesting efficiency and carrier transport. (3) Cations with hydrogen-bonding capabilities reinforce the inorganic $[PbX_6]^{4-}$ framework, mitigating halide migration and ion vacancy formation, which are critical for long-term operational stability. (4) Strategic incorporation of bulky cations facilitates the growth of low-dimensional/3D hybrid perovskites, combining the stability of low-dimensional phases with the superior charge transport of 3D networks. Among various cations, Cs^+ and GA^+ have emerged as the most strategically selected A-site cations, each offering distinct advantages for perovskite stability and device performance.

The ionic radius of Cs^+ (167 pm) is between MA^+ (217 pm) and FA^+ (253 pm). It can regulate the *t* in mixed cation perovskites and suppress the formation of non-photoactive phases. Compared

with volatile organic cations, the inorganic cation Cs^+ has excellent thermal stability.[77] Jeon et al. replaced some of the FA^+ in $FAPbI_3$ with Cs^+. Due to its smaller ionic radius, the addition of Cs^+ led to a volume contraction of the cuboctahedron, which enhanced the FA-I interaction and improved the stability of the perovskite. In addition, the trap density was reduced by an order of magnitude after the addition of Cs^+, which ultimately led to an increase in the average PCE from 14.9% to 16.5%. Moreover, the Pero-SC based on $FA_{0.9}Cs_{0.1}PbI_3$ showed higher stability under continuous illumination than the $FAPbI_3$-based devices.[78] Theoretical calculations were performed by Islam et al. to investigate the changes in atomic-scale structure and optoelectronic properties in the $FA_{1-x}Cs_xPbI_3$ ($x \leq 0.25$) system. The results suggest that the incorporation of Cs^+ cations into the $FAPbI_3$ structure resulted in a chemical stress or lattice strain effect due to the mismatched Cs/FA ionic radius, leading to structural deformation, while introducing stronger hydrogen bonding interactions, which enhances structural and thermal stability. The dynamic tilting of the PbI_6 octahedron and the rotational motion of the FA cations are also suppressed, resulting in a lattice symmetry break, which induces a Rashba-type effect that causes spin splitting of the frontier electron energy band, turning the direct band gap into an indirect band gap. The direct-to-indirect band gap transition may be a factor in the reduced charge-carrier recombination rate in these mixed-cation perovskites.[79] Although Cs^+ doping shows great potential for improving PCE and device stability, the phase separation problem of $CsPbI_3$ also emerges. Compared with MAX, CsX and PbX_2 have limited solubility in solvents, so perovskites with higher Cs atomic content are preferentially precipitated. **Figure 2.11a** shows the Cs/Pb atomic ratio from top to bottom perovsktie when CsX was doped into perovskite. After 800 s, a sudden rise of the ratio indicates the co-precipitation of Cs and Pb atoms in the bottom layer. The preferentially precipitated heavily Cs-doped perovskite can served as the heterogeneous nucleation sites and lowered the surface energy of (112)/(200) planes, faciliating perovskite growth along the <112>/<200> direction. Based on this, Wang et al. successfully prepared an ultra-smooth perovskite film oriented along the <112>/<200> direction with a homogeneous tetragonal phase of $(MAPbI_3)_{1-x}(CsPbBr_3)_x$. In addition, compared with $MAPbI_3$, the stability of $(MAPbI_3)_{0.9}(CsPbBr_3)_{0.1}$ to UV light and moisture was significantly improved, originating from the reduction of defects in the perovskite and the lattice shrinkage caused by the introduction of Cs and Br, respectively.[80] Saliba et al. demonstrated that the introduction of Cs^+ into FAMA-based hybrid perovskites suppressed the formation of non-optically active phases and facilitates uniform growth of perovskites, facilitating charge transport.

A stable efficiency of over 21% and an output of 18% were achieved after 250 hours of aging under operational conditions. The triple cation perovskite films had better thermal stability (**Figure 2.11b and 2.11c**) and were less affected by fluctuations in environmental variables such as temperature, solvent vapor, or heating regimens, improving device reproducibility.[81] Nazeeruddin et al. used Cs-doped $MAPbI_3$ as a model to investigate other effects of Cs^+ on the properties of organic-inorganic hybrid perovskites, in addition to the known phase stabilization effect. As shown in **Figure 2.11d**, the temperature-dependent electrical conductivity was measured to determine the defect activation energy for V_{MA} and V_I in the perovskite thin films and the activation energy was higher after the doping of Cs^+, indicating partial substitution of MA^+ with Cs^+ in $MAPbI_3$ could inhibit ion migration. The improved interfacial charge transport and suppressed ion migration resulted in a significant increase in PCE from 19.73% to 21.72% accompanied by excellent operational stability and negileble hysteresis. More importantly, Cs^+ doping significantly increased the carrier diffusion length of the samples, thereby improving the scalability of perovskite devices and facilitating their commercialization. Eventually, a 6.5 cm × 7 cm module was fabricated with a PCE as high as 21.08%.[82] In order to realize efficient tandem perovskite solar cells, Snaith et al. partially replaced FA^+ with Cs^+ and found that the phase instability region was completely eliminated, thus achieving full tunability of the band gap of about 1.75 eV. For all compositions of the $FA_{0.83}Cs_{0.17}Pb(I_{1-x}Br_x)_3$, a sharp optical band edge was obtained, while $FAPb(I_{1-x}Br_x)_3$ indicated weak absorption in the intermediate range. The final composition-stable, light-stable perovskite $FA_{0.83}Cs_{0.17}Pb(I_{0.6}Br_{0.4})_3$ was constructed, with an optical band gap of about 1.74 eV. The PCE of the small-area device exceeded 17%, and by combining it with a silicon cell with an efficiency of 19%, it demonstrated the feasibility of realizing a four-terminal tandem Pero-SC with an efficiency of more than 25%.[83] Sargent et al. incorporated Cs^+ into $FAPbI_3$-based perovskite films through a perovskite seeding growth method. In this method, submicron-sized Cs-containing perovskite seeds were added into the PbI_2 precursor solution in the two-step sequential deposition. As shown in the Region I in **Figure 2.11e**, a nucleus needs to grow beyond the critical radius r^* through overcoming the critical energy barrier G^*， then the crystallization of perovskites occurs. However， in the case of perovskite seeds introduced in PbI_2, the size of the seed crystals has exceeded r^*, so crystallization of perovskite starts spontaneously from the seed crystals, as displayed in **Figure 2.11f**. The perovskite seeding growth method achieves perovskite films with large grain size, low trap density,

and quasi-single-crystalline orientation. Finally, a stabilized efficiency of 21.5% was realized with better operation stability under one sun illumination.[84]

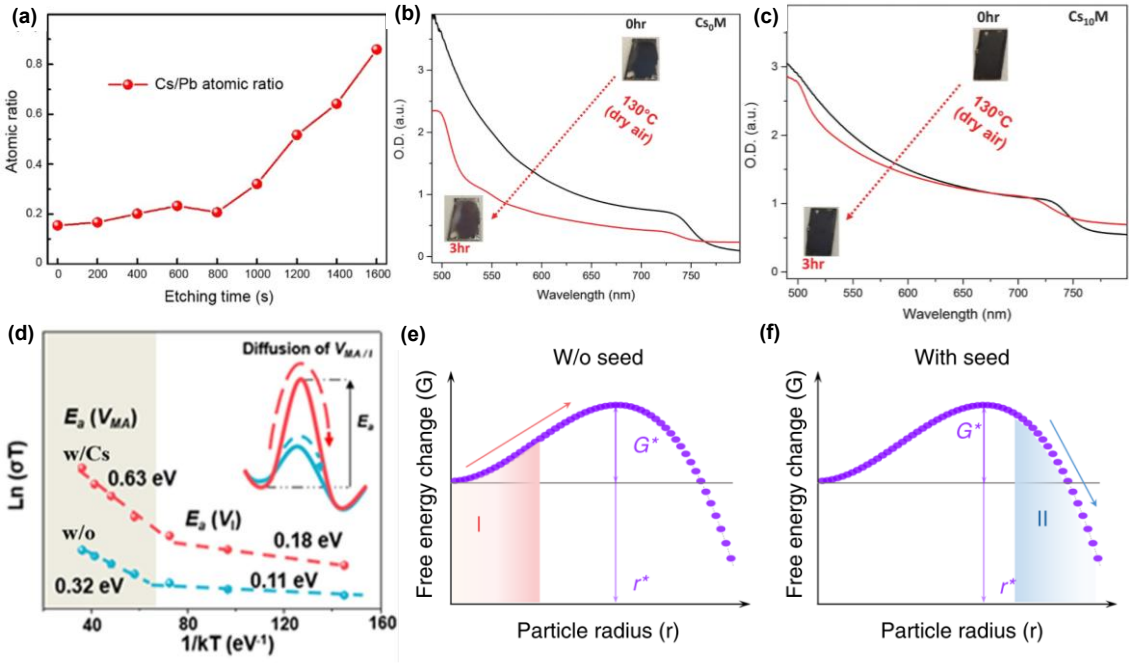


Figure 2.11 (a) The calculated Cs/Pb atomic ratio of the film.[80] Reprinted with permission from *Nano Energy* 2016, 27, 87-94. Copyright 2016 Elsevier Ltd. UV-visible absorption of (b) Cs_0M and (c) $Cs_{10}M$ films annealed at 130 ℃ for 3 hours in dry air with the corresponding images.[81] Reprinted with permission from *Energy Environ. Sci.*, 2016, 9 (6), 1989–1997. Copyright 2016 The Royal Society of Chemistry. (d) Results of temperature-dependent conductivity measurement of perovskite films without Cs (w/o) and with Cs (w/Cs).[82] Reprinted with permission from *Chem. Eng. J.* 2022, 431 (4), 133713. Copyright 2022 The Authors. Thermal stability and film formation dependence on processing conditions. Evolution of total Gibbs energy during the crystallization process (e) without and (f) with the seed crystal.[84] Reprinted with permission from *Nat. Commun.* 2018, 9, 1607. Copyright 2018 The Author(s).

Compared to the commonly used MA^+ and FA^+, GA^+ has a larger ionic radius (278 pm) and cannot form a 3D perovskite structure as the sole A-cation due to an inappropriate *t* value. However, when it is doped into a 3D perovskite in small amounts, it can play some positive roles. GA^+ has a dipole moment of nearly zero, which assists to suppress ionic mobility and hysteresis in Pero-SCs. Most importantly, owing to the plentiful ammonium groups, compared with other cations, GA^+ can

provide more hydrogen bonds to coordinate with the surrounding halides, thus stabilizing the perovskite structure. In addition, GA^+ can offer a lone pair of electrons to passivate defects at the surface and in the bulk perovskite films.[85] Yang et al. introduced GA^+ into $MAPbI_3$ through adding GAI or GACl to the ammonium salt solution in a two-step method. The hydrogen bonding provided by GA can increase the grain size and continuity of perovskite films. More importantly, GA^+ helps to effectively passivate the insufficiently coordinated iodine species between adjacent grains. Finally, compared with pristine $MAPbI_3$, the nonradiative recombination of perovskite containing GA^+ was mitigated significantly and the carrier lifetime was improved by an order of magnitude.[86] Nazeeruddin et al. proposed that although GA^+ has a large radius, slightly above the upper limit of the tolerance factor, and forms a low-dimensional perovskite when mixed with PbI_2, the introduction of GA^+ unexpectedly forms a highly stable 3D crystal structure. The theoretical calculations show that this stabilization arose from the increase in the number of hydrogen bonds within the inorganic framework (**Figure 2.12**). Remarkably, the GA-containing perovskite retained the good optoelectronic properties of organic lead halide materials with better stability.[87] Zhang et al. proposed a method for preparing annealing-free high-quality perovskite films by introducing GAI. The addition of GAI was conducive to the formation of a stable intermediate phase, while reducing the nucleation density in the intermediate phase film, thereby achieving a controllable perovskite crystallization rate and realizing a spontaneous crystallization process at room temperature, eliminating the need for traditional high-temperature annealing steps, and avoiding heterogeneous nucleation caused by thermal degradation. Finally, a perovskite film with larger grain size and lower defect density was obtained. The PCE of the Pero-SC prepared at room temperature was as high as 19.25%, much higher than the 16.78% of the control device.[88] Pang et al. investigated the effect of GA^+ on iodide ion migration in perovskite films. Through the measurement of temperature-dependent ionic conductivity, it was found that by increasing the GA ratio, the activation energy of iodide ion migration increased significantly, increasing the ion migration barrier and improving the lattice stability. The efficiency of a $MA_{0.8}FA_{0.1}GA_{0.1}PbI_3$-based device increased from 18.35% to 22.17%, and a Pero-SC module with an efficiency of more than 19% was prepared. Due to the effective suppression of ion migration, the unencapsulated device showed excellent operational stability under continuous illumination.[89] In addition to the improved device efficiency and stability, Minussi et al. further studied several important properties of polycrystalline $GA_xMA_{1-x}PbI_3$. The results showed that the introduction of GA^+ reduces the phase

transition temperature from the tetragonal to cubic phase. A change in the dielectric constant with temperature showed that an increased GA^+ content in $GA_xMA_{1-x}PbI_3$ affects the polarization behavior and low-temperature phase transition of the material. In addition, the ionic conductivity decreased sharply with an increased GA^+ content.[90]

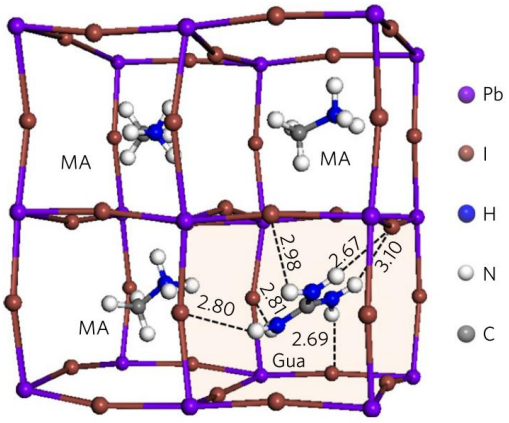


Figure 2.12 Optimized simulated structure of the unit cell of $MA_{0.75}GA_{0.25}PbI_3$ including the six H-bond distances with respect to I atoms. [87] Reprinted with permission from *Nat. Energy* 2017, 2, 972–979. Copyright 2017 Macmillan Publishers Limited, part of Springer Nature.

While both Cs^+ and GA^+ doping have demonstrated significant improvements in device performance, their individual incorporation presents inherent limitations due to ionic radius mismatch. When Cs^+ is used as the sole dopant, compressive strain in the perovskite lattice is induced, causing tetragonal-to-orthorhombic phase distortion. As for GA^+ as the sole dopant, tensile strain is generated and the possibility of 2D phase formation is promoted as the GA concentration increases. Therefore, co-doping of Cs^+ and GA^+ has been adopted to offset the respective disadvantages. Miguel et al. incorporated Cs^+ and GA^+ into the $MAPbI_3$ perovskite to generate a triple cation $Cs_xGA_yMA_{1-x-y}PbI_3$ perovskite and investigate the structural and optoelectronic impact. Specifically, while Cs^+ incorporation induces lattice shrinkage, subsequent GA^+ doping reverses this effect through lattice expansion. Consequently, photovoltaic devices fabricated with $Cs_xGA_yMA_{1-x-y}PbI_3$ perovskites exhibit enhanced performance and stability compared to $Cs_xMA_{1-x}PbI_3$ perovskite, highlighting the beneficial role of GA^+ in mitigating the detrimental effects observed with Cs^+ incorporation.[91] Daoud et al. found that the introduction of GA^+ into a CsFAMA-based perovskite resulted in a phase separation of 3D $CsFAMA_{1-x}GA_x$, 2D $FAGAPbI_4$, and 1D δ-$FAPbI_3$. As the GA^+ content was increased, the MA was replaced with GA^+ gradually and 3D

$CsFAMA_{1-x}GA_x$ was formed with an enhanced carrier lifetime. However, excess GA^+ resulted in the formation of 2D-phase $FAGAPbI_4$ and 1D δ-$FAPbI_3$ (**Figure 2.13a**), which could passivate the defects but reduce the absorbance. By tuning the content of GA^+, a δ-$FAPbI_3$/$CsFAMA_{1-x}GA_x$ (1D/3D) perovskite with superior optoelectronic properties was constructed. A champion device with an efficiency of 20.29% was obtained. Moreover, humidity, thermal and light stability were improved.[92] Sessolo et al. simultaneously sublimated CsI, MAI, FAI, and a pre-alloyed mixture of PbI_2 and $PbBr_2$, and prepared a triple-cation CsMAFA perovskite film by vacuum evaporation. Although this process can obtain homogeneous perovskite films and efficient wide-bandgap Pero-SCs, the perovskite films and devices have poor thermal stability at 85 °C. Therefore, in order to solve this problem, GA^+ was added into the perovskite lattice because GA^+ can introduce well-oriented hydrogen bonds in the inorganic skeleton. Taking advantage of the similar sublimation characteristics of GAI and FAI, GA^+ was introduced by sublimation from a single heat source together with FAI. Finally, the PCE of the Pero-SCs based on CsMAFAGA quadruple-cation perovskite was comparable to that based on the triple-cation CsMAFA perovskite but the thermal stability was enhanced.[93] To mitigate ion migration-induced hysteresis in $FA_{0.83}Cs_{0.17}PbI_3$ Pero-SCs, Wang et al. partially substituted FA with GA. Owing to GA's zero dipole moment, the incorporation of 2% GA significantly suppressed interfacial charge recombination and accumulation, enhancing device performance and nearly eliminating hysteresis (**Figure 2.13b**). However, further increasing the GAI content resulted in hysteresis reversal, though this phenomenon remained scan-rate dependent.[94] Lu et al. manipulated the nucleation and growth of perovskite crystals by sequentially doping Cs^+ and GA^+ in a two-step process. The doping of Cs^+ cations in the first step inhibited the crystallization of PbI_2 and induced the formation of δ-$CsPbI_3$ phase. The sparse nucleation sites of δ-$CsPbI_3$ contributed to the grain growth, but many pinholes were generated due to the uneven nucleation, as shown in **Figure 2.13c**. This problem was resolved by doping GA^+ in the second step. The doping of GA^+ significantly accelerated the crystal growth rate and produced large pinhole-free grains through Ostwald ripening and enhanced grain boundary migration. Consequently, a PCE of 23% was achieved due to the improved morphology, increased crystallinity and reduced defects.[95]

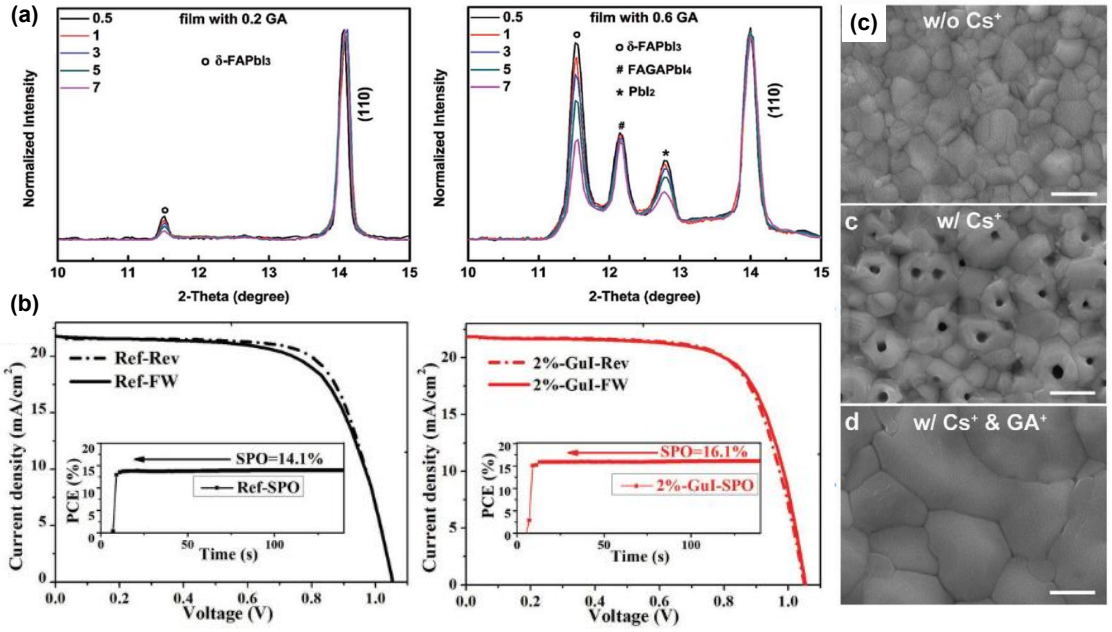


Figure 2.13 (a) Grazing-incident XRD patterns of 0.2 GA and 0.6 GA films with different incident angles varying from 0.5° to 7°.[92] Reprinted with permission from *J. Mater. Chem. A,* 2019, 7 (16), 9486-9496. Copyright 2019 The Royal Society of Chemistry. (b) *J–V* curves of the Pero-SCs without and with GAI measured in different scan directions.[94] Reprinted with permission from *Adv. Funct. Mater.* 2019, 29 (1), 1806479. Copyright 2018 WILEY-VCH Verlag GmbH & Co. KGaA, Weinheim. (c) Top-view SEM images of perovskite films without Cs^+ doping, with 5% Cs^+, and with Cs^+ and GA^+.[95] Reprinted with permission from *Adv. Mater.* 2020, 32 (42), 2004630. Copyright 2020 Wiley-VCH GmbH.

2.3 Buried interface engineering for high-quality perovskite

In Pero-SCs, the buried interface specifically refers to the critical interfacial region between the perovskite layers and the underlying charge transport layers. Beyond inheriting defect-related issues common to bulk perovskites, the buried interface introduces additional detrimental effects including lattice strain of perovskite, reduced perovskite crystallinity, and enhanced ion migration.[18, 19, 96] Consequently, the optimization of the buried interface is also crucial to improving device performance. In addition to energy-level alignment and defect passivation, buried interface engineering serves as a powerful strategy for controlling perovskite crystallization mainly through multiple synergistic mechanisms: (1) The interaction between the interface and perovskite delays

perovskite crystallization and passivates the defects in the perovskite, obtaining perovskite films with fewer defects and more perovskite phase. (2) The surface energy of the substrate is modulated to enhance its compatibility with that of the perovskite precursor solutions, promoting the formation of pinhole-free perovskite films with high coverage. (3) Lattice matching between the substrate and perovskite induces epitaxial growth of perovskite, facilitating the formation of preferentially orientated perovskite films.

2.3.1 Interactions at the perovskite-substrate interface

Feng et al. applied phenylhydrazinium chloride (PC) as a buried interface modification material for perovskite films. Various characterizations demonstrated that there was a strong interaction between PC and PbI_2, which could effectively passivate defects at the interface. The surface of the perovskite film without PC modification had a large amount of PbI_2, and the grain size distribution was uneven. On the contrary, the surface of the perovskite film modified by PC had almost no PbI_2 and the grain size was uniform. This is because the interaction could make the reaction between PbI_2 and organic ammonium salt more complete and delay perovskite crystallization, as proved by in-situ UV-visible spectroscopy (**Figure 2.14a**), thereby obtaining high-quality perovskite films with fewer defects. As a result, the average PCE increased from 24.37% to 25.62%. Additionally, the PCE of the flexible Pero-SC was improved to 24.54% and excellent humidity stability was achieved.[20] Tan et al. designed an amphoteric organic salt, 2-(4-fluorophenyl)ethylammonium-4-methyl benzenesulfonate (4FPEAPSA) as a buried interfacial layer between the HTL and perovskite. Through theoritical calculation, the S and O atoms in $-SO_3^-$ groups tended to combine with Pb^{2+} and cause distortion of the structure, resulting in changes in the S-C and S-O bond lengths. Simultaneously, the 4FPEA cation tends to insert into the $[PbX_6]^{4-}$octahedral lattice, which induces crystallization of the perovskite film. The interaction can also passivate iodine and formamidine vacancies. In addition, a *p*-type doped buried interface was formed, promoting interfacial charge extraction and transport. Therefore, 4FPEAPSA-treated Pero-SCs achieved a PCE as high as 25.03% with better storage, thermal, and humidity stability.[97] Li et al. proposed the modification of the bottom perovskite interface with hydroxylamine salts diethanolammonium iodide (DOAI) and ethanolammonium iodide (EOAI). As shown in **Figure 2.14b**, hydroxyl and ammonium groups formed hydrogen bonds with the PSS and with the A-site organic cations and the oxygen in hydroxyl groups coordinated with Sn^{2+} and Pb^{2+} metal ions, which could regulate the crystal growth of Sn−Pb perovskite and passivate different defects. Compared with EOAI, hydrogen bonds

between the two hydroxyl groups of DOAI and FAI were stronger, thereby enhancing the conjugation of FA cations and leading to the differentiation of cis and trans N-H protons with respect to C-H protons due to the diamagnetic anisotropy in conjugated systems like FA. The dynamic motion of FA ions could be restricted via non-covalent hydrogen bonds formed by the dihydroxyl groups of DOAI. As a result, multiple active nucleation sites were formed at the buried interface of perovskite, controlling the growth of perovskite. Through buried interface engineering, the PCE was improved to 23.8% and the stability improved.[98] Dou et al. served a molecule with an amidine head, ethyl 2-amidinoacetate hydrochloride (E-2AH), as a passivator at the buried perovskite interface. The strong interaction between perovskites and E-2AH significantly retards the crystallization process of perovskites, eliminating the intermediate phase of perovskites at the buried interface and passivating the undercoordinated Pb^{2+}. In addition, E-2AH molecules could adjust the surface contact potential and wettability of the substrates. Under multiple effects, high-quality perovskite films with less defects and vertically grown crystal grains were acquired. As a result, the suppressed nonradiative recombination and accelerated charge extraction at the buried perovskite interface realized an impressive PCE of 25.25 % at a small aperture area of 0.04 cm^2 and 21.25 % at a 15 cm^2 active area. Furthermore, the unencapsulated devices with E-2AH has good long-term aging and high operational stability.[99]

In addition to organic moieties, inorganic nanomaterials can also interact with perovskites to regulate the growth of perovskites. For instance, Rui et al. synthesized 2D SnS_2 nanosheets by a simple hydrothermal route and used them as an effective interfacial modifier for the traditional SnO_2 ETL, where they tuned the energy alignment between the SnO_2 and the perovskite layer. They also benefited from the interaction between Pb and S, which improved the perovskite crystallization and passivated defects at the interface. A PCE of 21.5% was obtained for the SnO_2-SnS_2-based Pero-SCs along with enhanced stability.[100]

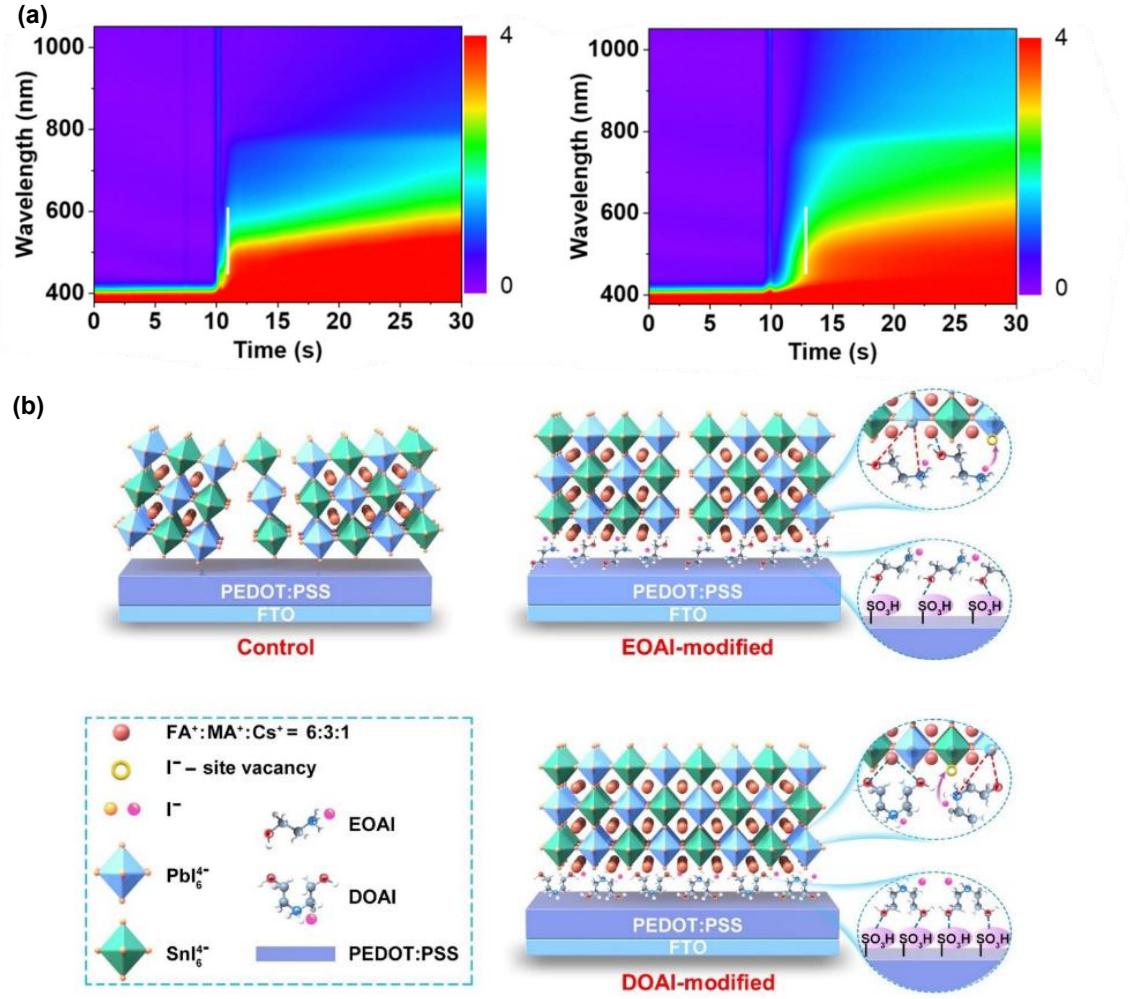


Figure 2.14 (a) 2D contour maps of UV-Vis spectra of the perovskite film prepared without and with PC buried interface modification during the spinning process.[20] Reprinted with permission from *Energy Environ. Sci.*, 2025, 18 (8), 3659–3667. Copyright 2025 The Royal Society of Chemistry. (b) Proposed evolution of the nucleation and crystallization during the film-forming process with and without interface-modifying materials. [98] Reprinted with permission from *Angew. Chem. Int. Ed.* 2024, 63 (48), e202409330. Copyright 2024 Wiley-VCH GmbH.

2.3.2 Modulation of surface energy

Rational engineering of substrate surface energy is able to address the incompatibility between hydrophobic interfaces and hydrophilic perovskite precursors, enabling uniform solution deposition and controlled crystallization. For instance, Burn et al. found that upon oxygen plasma

treatment, the hydrophobic HTLs became sufficiently hydrophilic. In addition, the oxygen plasma treatment could adjust the energy alignment between the HTL and perovskite and increase the conductivity, facilitating more efficient charge extraction.[38] Chen et al. synthesized a novel conjugated carbazole-based molecule, 9-(diphenylphosphanyl)-3-(1,2,2-triphenylvinyl)-9H-carbazole (TCzP), as a dopant for PTAA. TCzP doping reduced the energy barrier between the PTAA and perovskite and formed high-quality perovskite films owing to its hydrophilicity for better association with the polar perovskite precursor. Consequently, both the device PCE and stability were improved.[101] Lee et al. inserted an amphiphilic conjugated polyelectrolyte, poly[(9,9bis(3'-(N,N-dimethylamino)propyl)-2,7-fluorene)-alt-2,7(9,9-dioctylfluorene)] (PFN), as an interface compatibilizer to change the wettability of the perovskite precursor solution on the hydrophobic substrates, thus obtaining a perovskite film without holes (**Figure 2.15**). The device efficiency reached up to 19.14% with improved reproducibility and excellent stability. In addition, the efficiency of the device with an area of 1 cm^2 exceeded 17%.[39] PFN was also applied by another research group in Pero-SCs based on two-dimensional perovskites. After PTAA was modified by PFN, the surface wettability was improved, so that the two-dimensional perovskite film grown on the PFN layer had better surface coverage and repeatability. The study also found that the PFN layer reduced the formation of the n=1 phase in the two-dimensional perovskite film, thereby enhancing the light absorption of the active layer.[102] Song et al. found the zwitterionic polymer, poly(sulfobetaine methacrylate) (PSBMA), that has hydrophilic zwitterionic groups could improve the affinity of PTAA to perovskite and facilitate the crystallization of perovskite films. After introducing PSBMA, the perovskite precursor solution could spread more easily on PTAA due to the improved surface energy, and the perovskite films become smoother and have less pin holes.[40] Küffner et al. utilized silicon oxide (SiO_2) nanoparticles as a wetting agent upon PTAA. The nanoparticles enhanced the HTL surface energy, thus, wetting and homogeneous spreading of the precursor solution was achieved so that large-area modules with a maximum PCE of 9.3% for 49.60 cm^2 aperture area were fabricated successfully.[103] Wang et al. applied poly(methyl methacrylate) (PMMA) as the interfacial layer between dopant-free PTAA and $MAPbI_3$. PMMA can promote the hydrophilicity of the PTAA surface and facilitate the charge-carrier transfer.[104] A series of anionic conjugated polyelectrolytes (CPEs) based on poly(fluorene-co-phenylene) (MPS2-TMA, MPS4-TMA, and MPS6-TMA) were synthesized and applied on PTAA by Woo et al. Owing to the improved wettability of perovskites on hydrophobic PTAA, interfacial defect passivation, and

improved crystal growth of the perovskites, the Pero-SCs with CPE interlayers demonstrated a significantly enhanced device performance, and a large-area (1 cm^2) Pero-SC was successfully fabricated with MPS6-TMA.[41]

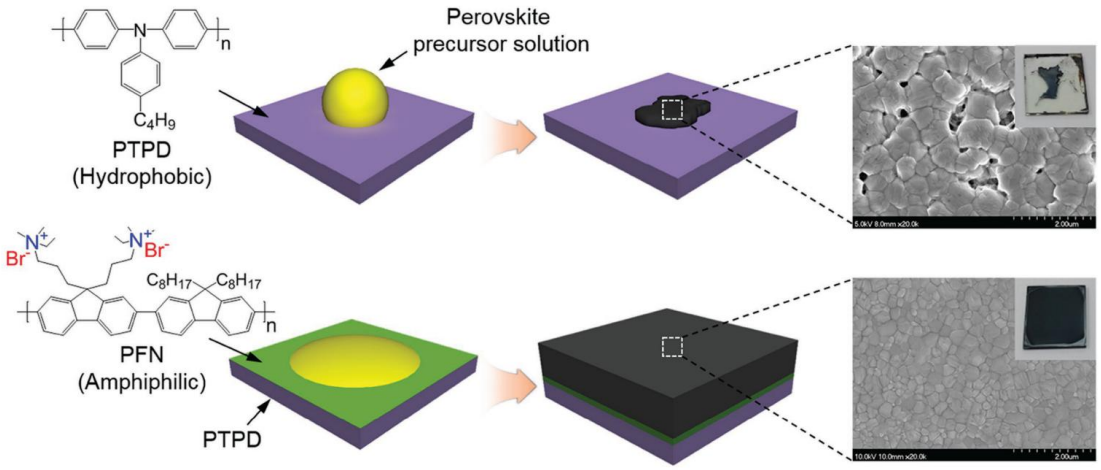


Figure 2.15 Schematic illustrations of perovskite film formation on organic HTLs with and without PFN as well as corresponding photographs and SEM images.[39] Reprinted with permission from *Adv. Mater.* 2017, 29 (22), 1606363. Copyright 2017 WILEY-VCH Verlag GmbH & Co. KGaA, Weinheim.

2.3.3 Epitaxial growth

Inorganic nanomaterials are widely considered as epitaxial growth templates. Tang et al. reported solution-phase van der Waals epitaxial growth of $MAPbI_3$ perovskite films on MoS_2 flakes. It was observed that the (008) plane of $MAPbI_3$ and the (110) plane of MoS_2 (**Figure 2.16a**) can match perfectly, which facilities the out-of-plane growth of perovskite films with preferential orientation along (110) plane of perovskite. This led to high-quality perovskite films with larger grain size, lower trap density, and a substantially enhanced PCE due to the increased crystallinity of the perovskite layer and the improved hole extraction and transfer rate at the interface.[105] Similarly, WS_2 was also applied as a van der Waals epitaxial growth substrate and benefited from the good match between the (020) plane of $MAPbI_3$ and the (110) plane of WS_2, as shown in **Figure 2.16b**, leading to perovskite grains with enlarged sizes. Moreover, the perfect perovskite/WS_2 interface and its interaction between S and I can facilitate efficient charge extraction and reduce interfacial carrier recombination. Therefore, with a WS_2 interlayer, the efficiency of the Pero-SCs increased

from 18.5% to 21.1% along with excellent device stability.[106] Li et al. introduced MXene into SnO_2 to tune the dispersion of SnO_2 nanocrystals. Perovskite with preferentially oriented growth was obtained on the MXene-SnO_2 due to lattice matching between the (110) plane of perovskite and the (100) plane of MXene (**Figure 2.16c**). Combined with better energy alignment, the PCE was improved by 15% with better stability.[107] The Cl-terminated $Ti_3C_2T_F$ ($Ti_3C_2T_{F,Cl}$) was synthesized through HCl etching by Song et al. and served as a buried interlayer between SnO_2 and the perovskite. The insertion of $Ti_3C_2T_{F,Cl}$ improved charge extraction and simultaneously modulates perovskite crystallization by providing lattice matching to minimize interfacial strain (**Figure 2.16d**), achieving an excellent PCE of 25.09%.[108] To solve the disordered crystallization of perovskite, a highly transparent and conductive oxide perovskite $SrSnO_3$ was synthesized by Zhao et al. and applied as the underlaying ETL. The lattice parameters of $SrSnO_3$ are highly matched with perovskite, promoting the preferred orientation growth of perovskite, eliminating residual lattice strain, and inhibiting ion migration. The enhanced crystallinity and improved energy level alignment resulted in a champion PCE of 25.17% along with remarkable operational stability.[109]

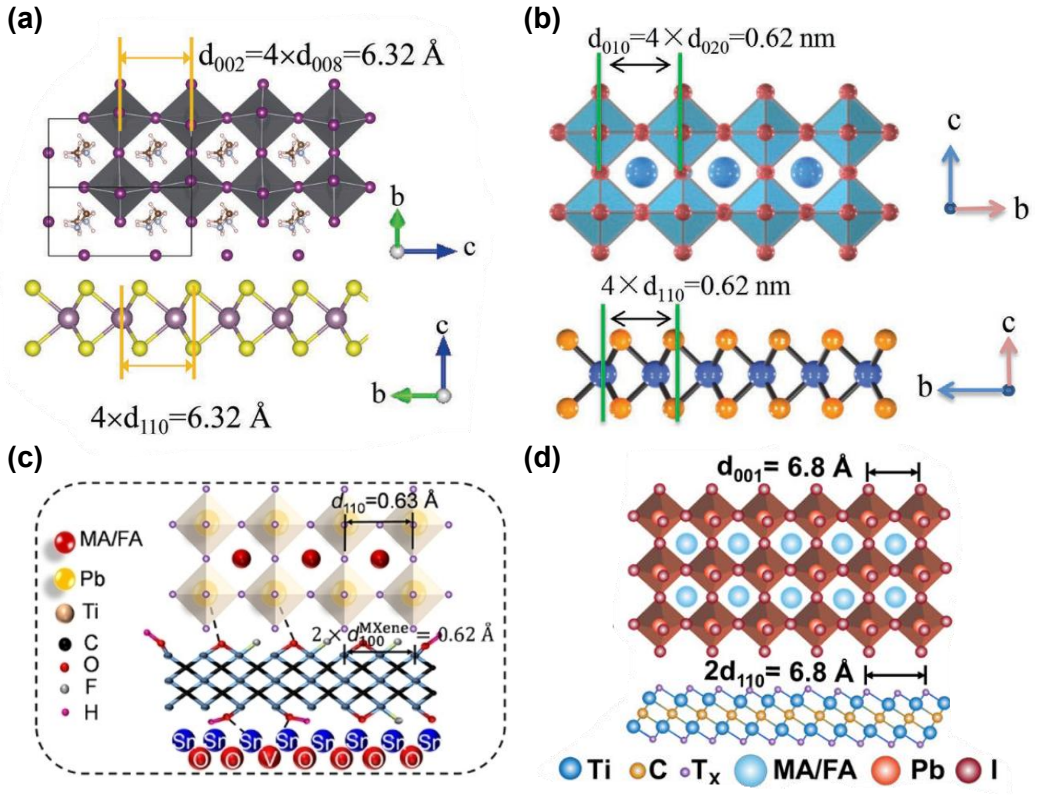


Figure 2.16 (a) Side view of atomic crystal heterojunction of $MAPbI_3$ and MoS_2.[105] Reprinted with permission from *Adv. Mater.* 2019, 31 (24), 1807689. Copyright 2019 WILEY-VCH Verlag GmbH & Co. KGaA, Weinheim. (b) Side view of crystal structure and lattice constant of perovskite and WS_2.[106] Reprinted with permission from *Adv. Funct. Mater.* 2020, 30 (38), 2002358. Copyright 2020 WILEY-VCH Verlag GmbH & Co. KGaA, Weinheim. (c) Detailed diagram of the mechanism of MXene bridging SnO_2 and perovskite.[107] Reprinted with permission from *Angew. Chem. Int. Ed.* 2022, 61 (43), e202210970. Copyright 2022 Wiley-VCH GmbH. (d) MXene-induced crystal epitaxial growth diagram of the perovskite.[108] Reprinted with permission from *Energy Environ. Sci.*, 2024, 17 (10), 3454–3469. Copyright 2024 The Royal Society of Chemistry.

Chapter 3
Methodology

3.1 Photovoltaic performance parameters

The performance of solar cells is usually characterized by *J*-*V* curves, from which some parameters include the open-circuit voltage (V_{OC}), the short-circuit current density (J_{SC}), the fill factor (FF), maximum power output (P_{max}), and the PCE are obtained, as shown in **Figure 3.1**. When V=0, the corresponding J is J_{SC} and analogously, when J=0, the corresponding V is V_{OC}. FF is equal to the ratio of the product of P_{max} to the product of J_{SC} and V_{OC}, as shown in **Equation 3.1**:

$$FF = \frac{P_{max}}{V_{OC} \times J_{SC}} \tag{3.1}$$

PCE is the ratio of P_{max} to the incident light intensity (P_{in}), as shown in **Equation 3.2**:

$$\text{PCE} = \frac{P_{max}}{P_{in}} = \frac{V_{OC} \times J_{SC} \times FF}{P_{in}} \tag{3.2}$$

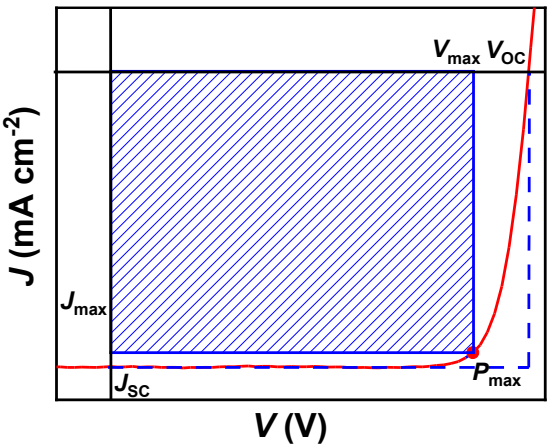


Figure 3.1 Typical *J*-*V* curve.

3.2 EQE measurement

As a photovoltaic device that directly converts incident photons to electrical energy, the EQE serves as a critical performance metric for evaluating the photon-to-electron conversion efficiency in Pero-SCs, as shown in **Equation 3.3**:

$$EQE(\lambda) = \frac{\text{Number of electrons output by the device}}{\text{Number of incident photons}} = \frac{I_{ph}/q}{P_{in}/(hc/\lambda)} \quad (3.3)$$

where I_{ph} is the photocurrent (A), q is the element charge (1.6×10^{-19} C), h is Planck constant (6.626×10^{-34} J·s), c is speed of light (3×10^{8} m s^{-1}) and λ is incident light wavelength (m).

Through the EQE spectrum (**Figure 3.2**) and the solar spectrum (AM1.5G), the integrated current density (J_{int}) can be calculated via **Equation 3.4**:

$$J_{int} = q \int EQE(\lambda) \cdot AM1.5G(\lambda) d\lambda \quad (3.4)$$

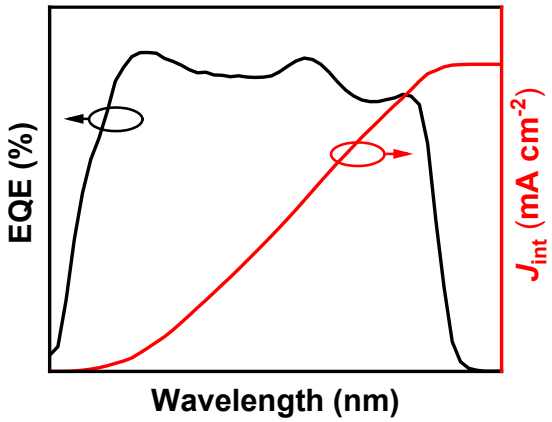


Figure 3.2 Typical EQE curve and J_{int}.

3.3 Stability measurement

Improving the long-term stability of Pero-SCs is critical for their commercialization. However, stability-testing variations in light intensity, temperature, humidity, and measurement methods across different laboratories has led to poor comparability among published results, making it difficult to reliably evaluate the performance of new materials and technologies. Therefore, in response to the need for reproducible and comparable data across studies, as well as a deeper understanding of degradation mechanisms, researchers in the Pero-SC field have reached a consensus on a set of standardized testing procedures for Pero-SC stability, adapted from the protocols established by the International Summit on Organic Photovoltaic Stability (ISOS).[110] As shown in **Table 3.1 and 3.2**, the ISOS protocols for Pero-SC stability are organized into eight main categories: shelf-life or dark storage testing (ISOS-D), bias testing (ISOS-V), light soaking testing (ISOS-L), outdoor testing (ISOS-O), thermal cycling testing (ISOS-T), light cycling testing (ISOS-

LC), light–humidity–thermal cycling (ISOS-LT) and intrinsic stability testing (ISOS-I). Each category is further subdivided into three levels of sophistication (basic, intermediate and advanced) to accommodate varying levels of laboratory capability and infrastructure.

Table 3.1 Overview of existing ISOS protocols and suggested additional protocols that account for the properties of perovskite materials and devices. [110] Reprinted with permission from *Nat. Energy* 2020, 5, 35–49. Copyright 2020 The Author(s).

Test ID	Light source	Temperature	Rel. humidity	Environment/Set-up	Characterization light source	Load
Dark storage (ISOS-D)						
ISOS-D-1	None	Ambient (23 ± 4 °C)	Ambient	Ambient air	Solar simulator or sunlight	OC
ISOS-D-2	None	65, 85 °C	Ambient	Oven, ambient air	Solar simulator	OC
ISOS-D-3	None	65, 85 °C	85%	Env. chamber	Solar simulator	OC
Bias stability (ISOS-V)						
ISOS-V-1	**None**	**Ambient (23 ± 4 °C)**	**Ambient**	**Ambient air**	**Solar simulator**	**Positive: V_{MPP}; V_{oc}; E_g/q; J_{SC} Negative: $-V_{oc}$, J_{MPP}[a]**
ISOS-V-2	**None**	**65, 85 °C**	**Ambient**	**Oven, ambient air**	**Solar simulator**	
ISOS-V-3	**None**	**65, 85 °C**	**85%**	**Env. chamber**	**Solar simulator**	
Light-soaking (ISOS-L)						
ISOS-L-1	Solar simulator	Ambient (23 ± 4 °C)	Ambient	Light only	Solar simulator	MPP or OC
ISOS-L-2	Solar simulator	65, 85 °C	Ambient	Light & temperature	Solar simulator	MPP or OC
ISOS-L-3	Solar simulator	65, 85 °C	~50%	Light, temperature & RH	Solar simulator	MPP
Outdoor stability (ISOS-O)						
ISOS-O-1	Sunlight	Ambient	Ambient	Outdoor	Solar simulator	MPP or OC
ISOS-O-2	Sunlight	Ambient	Ambient	Outdoor	Sunlight	MPP or OC
ISOS-O-3	Sunlight	Ambient	Ambient	Outdoor	Sunlight and Solar simulator	MPP
Thermal cycling (ISOS-T)						
ISOS-T-1	None	RT to 65, 85 °C	Ambient	Hot plate/ oven	Solar simulator	OC
ISOS-T-2	None	RT to 65, 85 °C	Ambient	Oven/env. chamber	Solar simulator	OC
ISOS-T-3	None	−40 to + 85 °C	**< 55%**[b]	Env. chamber	Solar simulator	OC
Light cycling (ISOS-LC)						
ISOS-LC-1	**Solar simulator/ Dark Cycle period: 2, 8, or 24 h Duty cycle: 1:1 or 1:2**	**Ambient (23 ± 4 °C)**	**Ambient**	**Light only**	**Solar simulator**	**MPP or OC**
ISOS-LC-2		**65, 85 °C**	**Ambient**	**Light & temperature**	**Solar simulator**	**MPP or OC**
ISOS-LC-3		**65, 85 °C**	**< 50%**	**Light, temperature & RH**	**Solar simulator**	**MPP**
Solar-thermal cycling (ISOS-LT)						
ISOS-LT-1	Solar simulator	Linear or step ramping between room temp. and 65 °C	Monitored, uncontrolled	Weathering chamber	Solar simulator	MPP or OC
ISOS-LT-2	Solar simulator	Linear ramping between 5 °C and 65 °C	Monitored, controlled at 50% beyond 40 °C	Env. chamber with sun simulator	Solar simulator	MPP or OC
ISOS-LT-3	Solar simulator	Linear ramping between −25 °C and 65 °C	Monitored, controlled at 50% beyond 40 °C	Env. chamber with sun simulator and freezing	Solar simulator	MPP or OC

Each test group is divided into three levels of sophistication that reflect the complexity of required equipment and the harshness of the applied stress. Reported ISOS protocols are taken from ref. [7]. Proposed additional ISOS protocols are printed in bold. [a]V_{OC}, V_{MPP}, and J_{MPP} are determined from light *J*–*V* curves measured under standard solar cell testing conditions on a fresh device. E_g and q are the band gap of the active layer and elementary charge, respectively. [b]Relative humidity is controlled at temperatures above 40 °C and is not controlled for the remainder of the cycle. Env., environmental; OC, open-circuit condition; MPP, maximum power point; RT, room temperature; RH, relative humidity.

Table 3.2 Overview of suggested ISOS-I protocols for ageing experiments in an inert atmosphere.[110] Reprinted with permission from *Nat. Energy* 2020, 5, 35–49. Copyright 2020 The Author(s).

Test ID	Elevated temperature	Electrical bias	Light
ISOS-D-1I	–	–	–
ISOS-D-2I	✓	–	–
ISOS-V-1I	–	✓	–
ISOS-V-2I	✓	✓	–
ISOS-L-1I	–	–	✓
ISOS-L-2I	✓	–	✓
ISOS-T-1I	Cycled	–	–
ISOS-T-2I	Cycled	–	–
ISOS-T-3I	Cycled	–	–
ISOS-LC-1I	–	–	Cycled
ISOS-LC-2I	✓	–	Cycled
ISOS-LC-3I	✓	–	Cycled

Ticks and dashes denote the presence and absence of the stress, respectively. In case of temperature, '–' refers to room temperature.

The ISOS-D protocol assesses the stability of Pero-SCs under ambient conditions and dark storage conditions, simulating periods without light exposure. ISOS-V examines the impact of applied bias voltage on device stability while in the dark to investigate the degradation mechanism of perovskite under bias voltage. ISOS-L evaluates performance degradation under continuous illumination. ISOS-O aims to replicate stability behavior in natural outdoor environments. ISOS-T investigates device performance changes during thermal cycling, simulating diurnal and seasonal temperature variations. ISOS-LT provides a comprehensive assessment of combined light, humidity, and temperature stresses. ISOS-LC studies the effects of light-dark cycling, mimicking day-night patterns to explore both reversible and irreversible degradation mechanisms. Finally, ISOS-I evaluates the intrinsic stability of devices in an inert atmosphere, helping to distinguish between internal and externally induced degradation factors.[110]

In this thesis, appropriate conditions for stability testing including N_2 stability, thermal stability, humidity stability and light stability were set in accordance with the ISOS protocols, taking into consideration both the standard guidelines and the specific constraints of the laboratory environment, as shown in **Table 3.3**.

Table 3.3 Stability test conditions employed in this thesis.

Test ID	Light source	Temperature	Atmosphere	Characterization light source	Encapsulated or not
ISOS-D-1I (N_2)	None	RT 25 ± 5 ℃	Glove box N_2	Solar simulator	No
ISOS-T-1I (thermal)	None	Hotplate 65 ± 5 ℃	Glove box N_2	Solar simulator	No
ISOS-D-1 (humidity)	None	RT 25 ± 5 ℃	Ambient air RH 30-50%	Solar simulator	No
ISOS-D-1 (humidity)	None	RT 25 ± 5 ℃	Ambient air RH 80 ± 5%	Solar simulator	Yes
ISOS-L-1I (light)	Continuous illumination, White LED 100 mW cm^{-2}	35 ± 5 ℃	Glove box N_2	White LED 100 mW cm^{-2}	No

Chapter 4
CuS Nanosheets as Additives in the Hole Transport Layers for Stable *p-i-n* Perovskite Solar Cells

4.1 Introduction

For effective carrier extraction and transportation, charge transport layers play an indispensable role.[111, 112] Among *p-i-n* Pero-SCs, PTAA is a widely used HTL because of its high thermal and mechanical stability. However, the energy barrier between the highest occupied molecular orbital (HOMO) of PTAA and the valance band maximum (VBM) of perovskites, especially FA-based perovskites, aggravates interfacial carrier recombination[113-115]. In addition, a low conductivity and intrinsic hole mobility of PTAA lead to an increase of the charge-transport resistance of Pero-SCs[116-118].

To address the above problems, additives, such as tetrafluoro-7,7,8,8-tetracyanoquinodimethane[119], tris-(pentafluorophenyl) borane bis(trifluoromethane) sulfonimide[120], lithium salt[113, 121] and 4-tert-butylpyridine[113, 121], have been employed in PTAA. However, these organic dopants are unstable and hygroscopic or can induce decomposition of the perovskite.[116, 117] Inorganic dopants, such as MoO_3[116], are often preferred because of their low chemical activity and excellent carrier transport properties. Among different inorganic materials, copper sulfide derivatives ($Cu_{2-x}S$, $0 < x < 1$) are a class of *p*-type semiconductors with tunable optical bandgaps, high hole mobility and conductivity and good chemical stability.[122, 123] Among the different stable phases of $Cu_{2-x}S$, CuS presents the highest concentration of valence-band-delocalized holes.[122, 123] Owing to these properties, CuS nanomaterials have been successfully employed in Pero-SCs. For example, CuS can be deposited upon ITO to tune the work function[124] or upon a perovskite as an HTL[125] and can be incorporated into carbon electrodes to improve hole mobility.[126] Moreover, CuS can behave as a barrier against environmental moisture, which increases the humidity stability of Pero-SCs.[127]

In this work, CuS nanosheets were synthesized and added to PTAA in *p-i-n* Pero-SCs for the first time. The addition of CuS not only increases the conductivity of the HTL twofold, decreasing the transport resistance but also improves the work function of PTAA, thus aligning the energy levels between the HTL and perovskite. In addition, there is interaction between the CuS and PbI_2,

which can control the perovskite growth, and consequently, perovskite films with better quality were obtained. Upon the addition of CuS into PTAA, the PCE increased from 21.99% to 22.92%. Moreover, the device can maintain approximately 73% of the initial PCE at 65°C~70°C for 960 h and maintain approximately 69% of the initial PCE after storage in air with a relative humidity of 40%-50% for 800 h.

4.2 Experimental methods

4.2.1 Materials

$CuCl_2$ was purchased from Sigma–Aldrich. $Na_2S_2O_3$ was purchased from Shang Aladdin Biochemical Technology Co., Ltd. ITO-coated glass (10 Ω/sq) was obtained from Advanced Election Technology Co., Ltd. PTAA, FAI, methylammonium chloride (MACl), methylammonium iodide (MAI), PbI_2 and bathocuproine (BCP) were purchased from Xi'an Yuri Solar Co., Ltd. C_{60} was purchased from Henan Fullerene Nano New Materials Technology Co., Ltd.

4.2.2 Synthesis of CuS nanosheets

In this work, a simple, template-free and mild solution-chemistry route was employed to synthesize CuS nanosheets according to the literature[128]. In a 100 mL round bottom flask, 40 mL of solvent (the ratio of water and ethylene glycol was 1:3) was added. Then, $CuCl_2$ (2 mmol) and $Na_2S_2O_3$ (2 mmol) were added to the solvent (the final concentrations of Cu^{2+} and $S_2O_3^{2-}$ were 0.05 M). The solution was stirred to mix the precursors until a yellowish green solution was obtained, then the round bottom flask containing the solution was placed in an oil bath at 70°C and heated for 6 h with constant stirring. After 6 h, the flask was removed from the oil bath and cooled to room temperature. The products were washed with ethanol and water three times, and a centrifuge was used to collect them. Finally, the products were dried at 60°C for 12 h in a vacuum oven.

4.2.3 Fabrication of devices

The ITO-coated glass was cleaned by sequential ultrasonication in detergent, DI water, acetone, ethanol, and isopropanol (IPA), twice each solvent for 15 min each time. For the pristine PTAA layers, PTAA (2 mg mL^{-1}) was dissolved in toluene. For the PTAA-CuS layers, CuS was dispersed in toluene through ultrasonication, the CuS solution was doped into PTAA, and the final concentration of CuS was varied from 0.01 mg mL^{-1} to 0.03 mg mL^{-1}. The prepared HTL solution

was spin-coated onto the cleaned ITO substrates at 5000 rpm for 30 s, and the substrates were annealed at 100°C for 10 min in a glove box. The perovskite films were fabricated via a two-step deposition method. First, 1.5 mol L^{-1} PbI_2 dissolved in *N,N*-dimethylformamide/dimethyl sulfoxide (DMF/DMSO) (9:1 by volume) was stirred at 70°C for 12 h. Warm PbI_2 was spin-coated at 2000 rpm for 20 s, and then a drop of the mixed solution containing FAI:MAI:MACl (90 mg:6.4 mg:9 mg) in 1 mL of IPA was added to the spinning substrate for 30 s. The as-prepared samples were annealed at 110°C for 20 min. C_{60} (~20 nm), BCP (~8 nm) and Ag electrodes (~100 nm) were deposited respectively by thermal evaporation under a pressure of 2×10^{-4} Pa.

4.2.4 Characterization

SEM images and EDX mapping were acquired on a Hitachi SU8010 scanning electron microscope. XRD data were collected on a D2 PHASER diffractometer with Cu Ka radiation from Bruker. The UV−vis spectra were recorded on a Cary 5000 spectrometer from Agilent Technologies. UPS was performed on an ESCALAB Xi+ instrument from Thermo Scientific. AFM images and KPFM results were acquired in air on a Multimode 8 microscope from Bruker. FTIR spectra were measured with a Bruker VERTEX 70 V. XPS was recorded on an ESCALAB 250Xi instrument from Thermo Fisher. An FLS980 instrument from Edinburgh Instrument (U.K.) was employed to record the steady-state PL spectra, and the excitation wavelength was set at 470 nm. The TRPL spectra were acquired with an excitation wavelength of 477 nm on a Lifespec II instrument from Edinburgh. The *J–V* curves of the Pero-SCs were recorded via a Keithley 2400 source meter. The measurements were conducted in a glove box filled with N_2 under simulated AM 1.5G solar illumination with an intensity of 100 mW cm^{-2}. The EQE curves were measured by a QE-R3011 solar cell spectral response measurement system from Enli Technology Co., Ltd., in air in the dark. EIS was performed on an IM6 electrochemical workstation from Zahner Zennium in the dark.

4.3 Results and discussion

4.3.1 Characterization of the CuS nanosheets

First, SEM was used to explore the nanomorphology of the synthesized powder. **Figure 4.1a** shows the morphology of the synthesized CuS before grinding. The nanosheets had average lateral dimensions of approximately 150 nm (**Figure A1** in the Appendix A) and appeared to form nanoflowers. To disperse the nanomaterials better in toluene, the powder was ground through a

mortar for 1 h, which resulted in the formation of multilayered nanosheets, as shown in **Figure 4.1b**. The elemental composition was then investigated via EDX. As shown in **Figure 4.1c**, the atomic ratio of Cu to S is close to 1. XRD was subsequently carried out to confirm the crystal structure of the nanosheets. As shown in **Figure 4.1d**, the (102), (103) and (110) peaks of covellite CuS are evident (JCPDS card No. 06-0464 is included for reference).[129, 130] These results prove that our product is stoichiometric CuS.

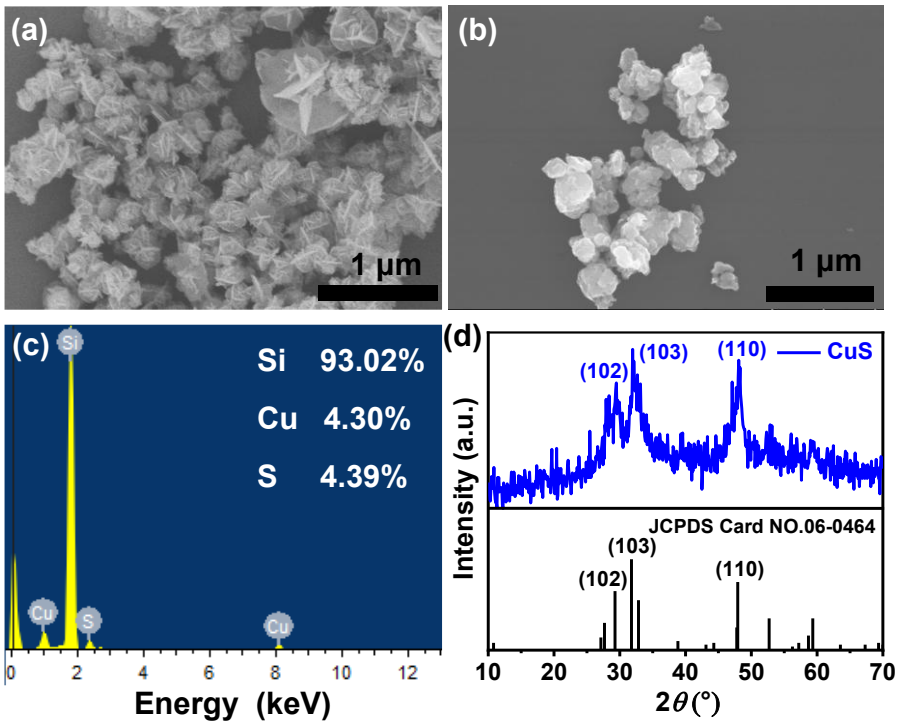


Figure 4.1 SEM images of the CuS nanosheets (a) before and (b) after grinding. (c) EDX spectrum of CuS nanosheets on a silicon substrate. (d) XRD pattern of the CuS nanosheets.[144] Reprinted with permission from *Nano Energy* 2025, 135, 110652. Copyright 2025 The Author(s).

4.3.2 Improving the conductivity, energy-level alignment, and charge transport

The CuS nanosheets were incorporated into the hole transport material PTAA at a concentration of 0.02 mg mL^{-1}. For *p-i-n* devices, the light passes through the ITO glass and HTL first and then is captured by the perovskite layer, so the transparency of the HTL is important. As shown in **Figure 4.2a**, there is no obvious change in the transmittance of the HTL after the addition of CuS, which suggests that the introduction of CuS does not influence the photon capture of the perovskite layer.

The AFM images in **Figure A2** indicate that there is no obvious change in the morphology of the HTL; hence, the introduction of CuS does not impact the roughness of the HTL and should not negatively influence the growth of the perovskite.

To explore the effect of CuS on the conductivity of the HTL, devices with a structure of ITO/HTL/Ag were fabricated. Owing to the good conductivity of the CuS nanosheets, the conductivity of the HTL increased from 2.72×10^{-6} S cm^{-1} to 6.75×10^{-6} S cm^{-1}, as shown in **Figure 4.2b**. The binding energy cutoff edge ($E_{\text{cut-off}}$) and binding energy onset value ($E_{\text{on-set}}$) of PTAA and PTAA-CuS were investigated via UPS (**Figure 4.2c**). The energy levels of the highest occupied molecular orbital (E_{HOMO}) and the Fermi level (E_{F}) were determined from the UPS measurements, and the energy level of the lowest unoccupied molecular orbital (E_{LUMO}) was calculated from E_{HOMO} and E_{g} measured on the basis of the results shown in Tauc plots (**Figure A3**). The energy level diagram is shown in **Figure 4.2d**. Combined with the results obtained by KPFM (**Figure A4**), it can be concluded that, compared with PTAA, PTAA-CuS had a higher work function and the E_{HOMO} was closer to the valance band of the perovskite (**Figure 4.2d**), which is expected to facilitate charge extraction and transportation.

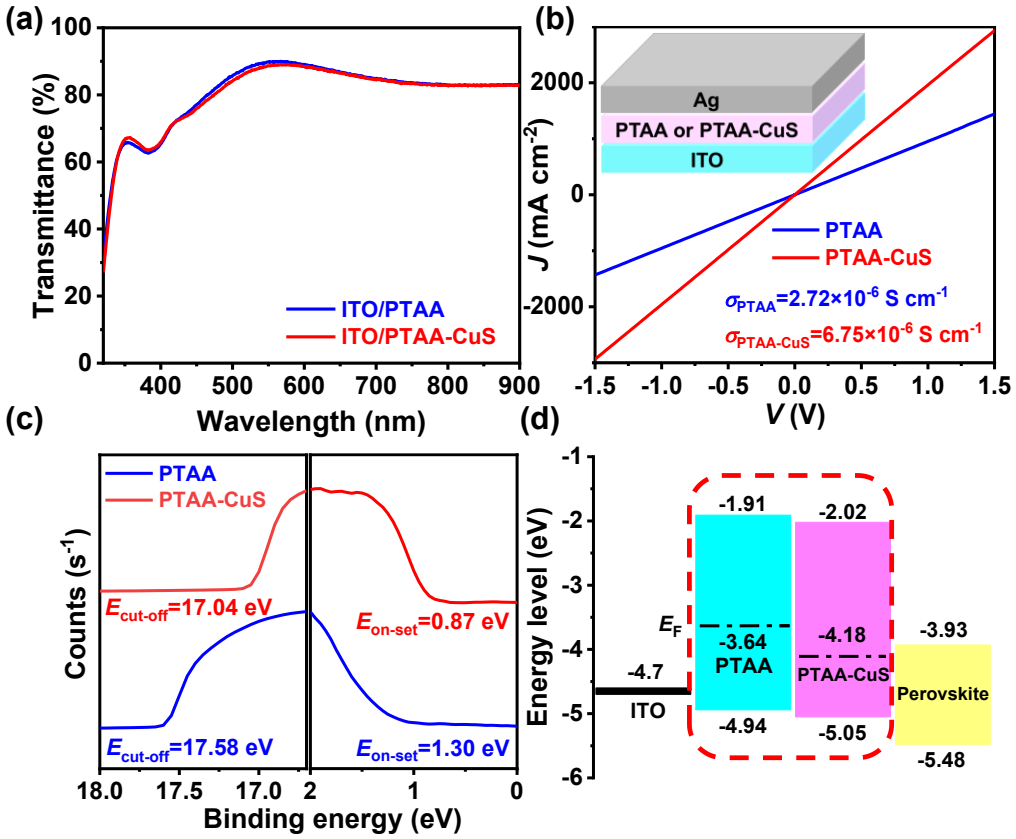


Figure 4.2 (a) Transmission spectra of HTLs. (b) *J*-*V* curves of devices based on ITO/HTL/Ag. (c) UPS spectra of HTLs. (d) Energy level diagrams of the HTLs and perovskite. [144] Reprinted with permission from *Nano Energy* 2025, 135, 110652. Copyright 2025 The Author(s).

Fluorescence emission is often used to evaluate interfacial charge extraction. **Figure 4.3a** displays the steady-state PL of the ITO/PTAA/perovskite and ITO/PTAA-CuS/perovskite films. Upon the addition of CuS, the PL intensity of the perovskite film decreased, suggesting improved charge transfer.[108] (Note that the results were normalized by the absorbance at 785 nm, and the measurement conditions were kept the same). The improved charge transfer can also be proven by TRPL (**Figure 4.3b**). To fit the curves, a two-component exponential decay function (**Equation 4.1**[131]) was employed (see the detailed parameters in **Table A1**):

$$I_t = A_1 \, exp\left(-\frac{t}{\tau_1}\right) + A_2 \, exp\left(-\frac{t}{\tau_2}\right) \tag{4.1}$$

where A_1 and A_2 represent the PL decay amplitudes. The fast decay component (τ_1) is assigned to the nonradiative recombination caused by trap states or PL quenching via interfacial charge transfer,

and the slow decay component (τ_2) is assigned to radiative recombination in the bulk perovskite.[76, 132] The pristine film had a τ_1 of 53.3 ns and a τ_2 of 716.2 ns. In contrast, the perovskite film based on PTAA-CuS has a shorter τ_1 of 46.4 ns and a decreased τ_2 of 435.6 ns. The decreased lifetime indicates that the addition of CuS can promote charge transfer from the perovskite to the HTL, which is attributed to the increased conductivity and better energy level alignment.

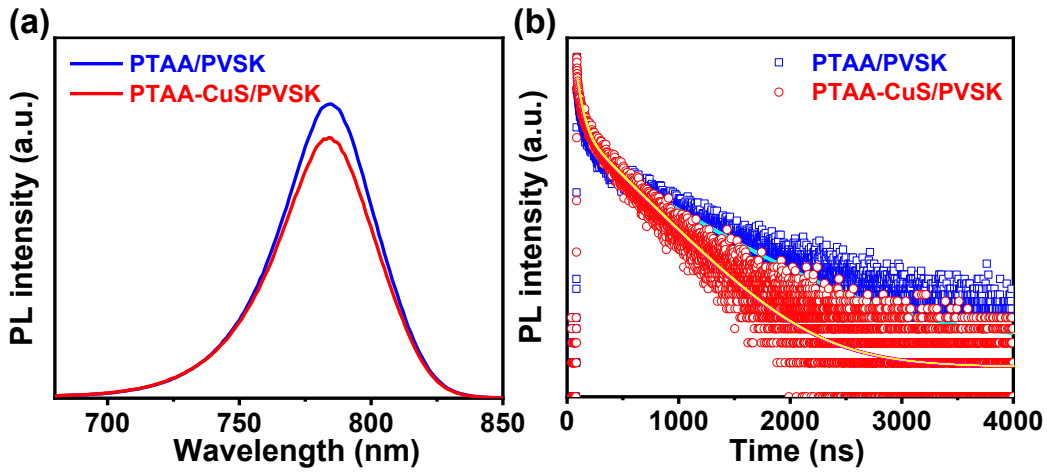


Figure 4.3 (a) Steady-state PL and (b) TRPL of perovskite films on PTAA and PTAA-CuS. [144] Reprinted with permission from *Nano Energy* 2025, 135, 110652. Copyright 2025 The Author(s).

4.3.3 Improving the perovskite quality

Since the perovskite layer was located on the top of the HTL, the nature of the HTL may influence the growth of the perovskite crystals. **Figure 4.4a** and **4.4b** show SEM top-view images of perovskite films formed on pristine PTAA and PTAA-CuS, respectively. After the addition of CuS (0.02 mg mL^{-1}) in PTAA, there was no obvious change in the average perovskite grain size; however, the size distribution was narrower, as shown in **Figure A5**, indicating that the perovskite growth was more uniform. In addition, combined with the cross-sectional SEM images in **Figure 4.4c** and **4.4d**, the perovskite film formed on PTAA-CuS had fewer pinholes and was closely packed. Moreover, the amount of PbI_2 (yellow circles) in the perovskite film formed on PTAA-CuS was less than that formed on PTAA. Consistent with the SEM results, the XRD patterns in **Figure 4.4e** indicate that after the addition of CuS, the intensity ratio of the dominant perovskite peak to the PbI_2 peak increased from 1.34 to 2.78, which suggests that more PbI_2 was transformed to perovskite through the reaction with FAI/MAI. Although excess PbI_2 can play a role in

improving device efficiency, the decomposition of PbI_2 under long-term operating conditions is harmful to device stability.[29] Thus, a decrease in PbI_2 will favor long-term stability.

An observed decrease in the trap density (N_t) of the perovskite films further proves the improvement in the perovskite quality. As shown in **Figure 4.4f**, N_t was determined via the space-charge-limited current (SCLC) method and was calculated via **Equation 4.2**[35, 133]:

$$N_t = \frac{2\varepsilon\varepsilon_0 V_{TFL}}{eL^2} \tag{4.2}$$

where ε is the relative dielectric constant, ε_0 is the vacuum permittivity, V_{TFL} represents the trap-filled voltage, e is the elementary charge, and L is the thickness of the perovskite film. With the addition of CuS, the V_{TFL} decreased from 0.75 V to 0.60 V, and the corresponding N_t of the perovskite layer decreased from 2.7×10^{15} cm^{-3} to 2.2×10^{15} cm^{-3}.

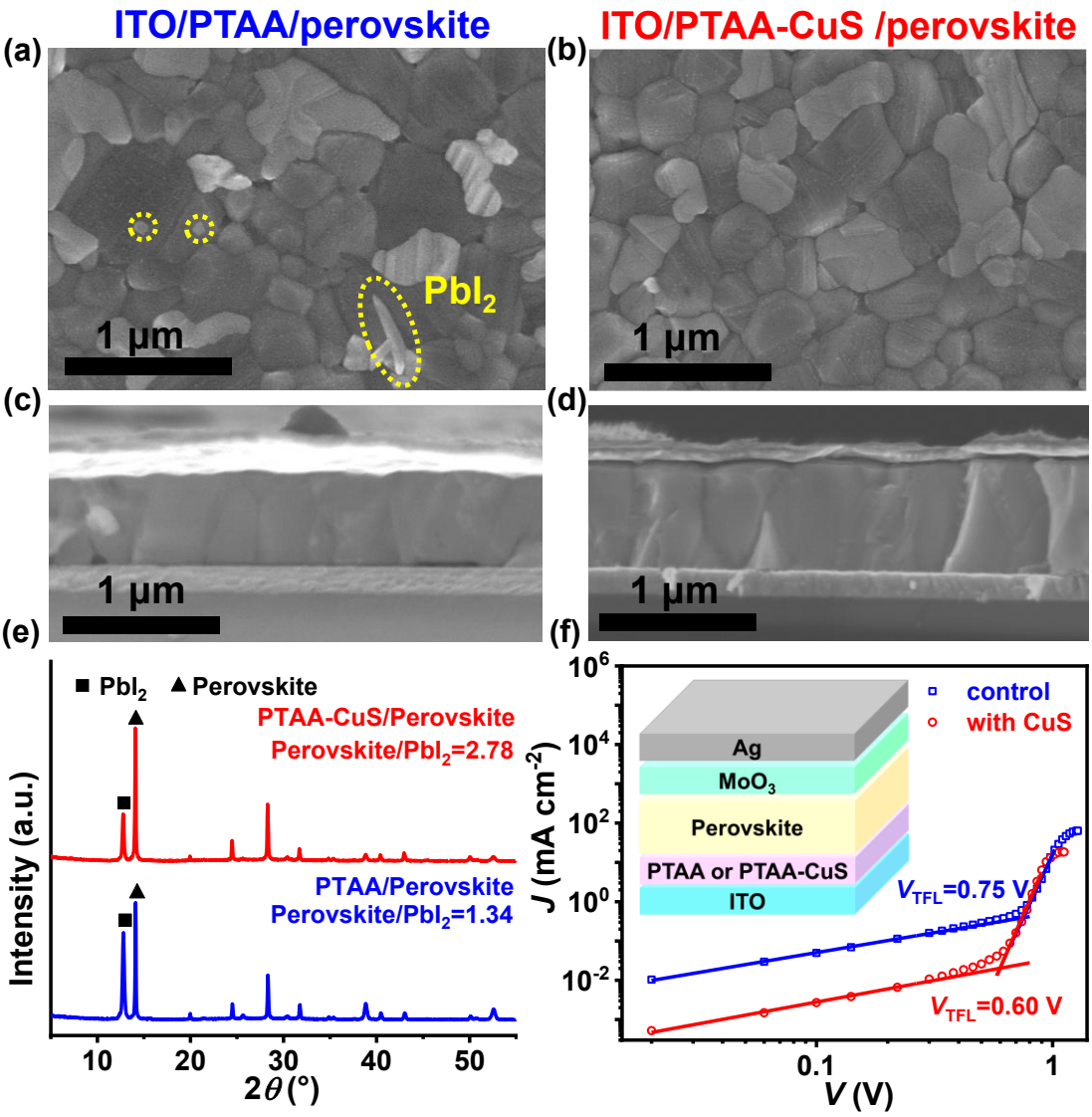


Figure 4.4 Top-view SEM images of perovskite films formed on (a) PTAA and (b) PTAA-CuS. Cross-sectional SEM images of perovskite films formed on (c) PTAA and (d) PTAA-CuS. (e) XRD patterns of perovskite films formed on PTAA and PTAA-CuS. (f) *J*-*V* curves in the dark of hole-only devices based on perovskite films formed on PTAA and PTAA-CuS for SCLC analysis.[144] Reprinted with permission from *Nano Energy* 2025, 135, 110652. Copyright 2025 The Author(s).

The change in the perovskite films may be caused by the interaction between CuS and the perovskite. To clarify this hypothesis, the interaction between CuS and PbI_2 was investigated through FTIR and XPS. To conduct FTIR, the CuS/PbI_2 films were fabricated via drop casting, and

the films were scraped off and ground into powder. **Figure A6** shows the FTIR spectra of the pristine CuS powder and the CuS/PbI_2 powder. The FTIR peak at 619 cm^{-1} is attributed to the stretching vibration of Cu-S[134]. After mixing the CuS with PbI_2, the peak shifted to 622 cm^{-1}. Notably, the FTIR measurement resolution was set to 0.5 cm^{-1}, so a shift of 3 cm^{-1} can indicate that there was interaction between CuS and PbI_2. To further explain the interaction between CuS and PbI_2, XPS was carried out. To investigate the changes in the signals of Pb and I, the XPS spectra of the pristine PbI_2 film and PbI_2/CuS film were compared. The peaks located at 143.0 and 138.1 eV in **Figure 4.5a** correspond to Pb $4f_{5/2}$ and Pb $4f_{7/2}$, respectively, and the peaks at 630.5 and 619.1 eV in **Figure 4.5b** are assigned to I $3d_{3/2}$ and I $3d_{5/2}$, respectively [135, 136]. After CuS was introduced, both of the Pb 4f peaks shifted from 0.1 eV to a higher binding energy, and both of the I 3d peaks shifted to a higher binding energy by 0.2 eV. For the changes in the Cu and S peaks (**Figure 4.5c** and **4.5d**), the XPS spectra of pristine CuS and CuS deposited upon PbI_2 were compared. The peaks at 952.4 and 932.8 eV correspond to Cu $2p_{1/2}$ and Cu $2p_{3/2}$, respectively, and the peaks at 163.6 and 161.6 eV correspond to S $2p_{1/2}$ and S $2p_{3/2}$, respectively[123, 137, 138]. After CuS was deposited upon PbI_2, the Cu 2p and S 2p peaks shifted to lower binding energies. Combined with the changes in the Pb 2p and I 3d spectra, it can be concluded that Pb-S and Cu-I bonds were generated between PbI_2 and CuS[139]. As illustrated in **Figure 4.5e**, the interaction can retard perovskite growth and facilitate the reaction between PbI_2 and FAI/MAI, which decreases the amount of PbI_2 and makes the perovskite grains more uniform[140-142].

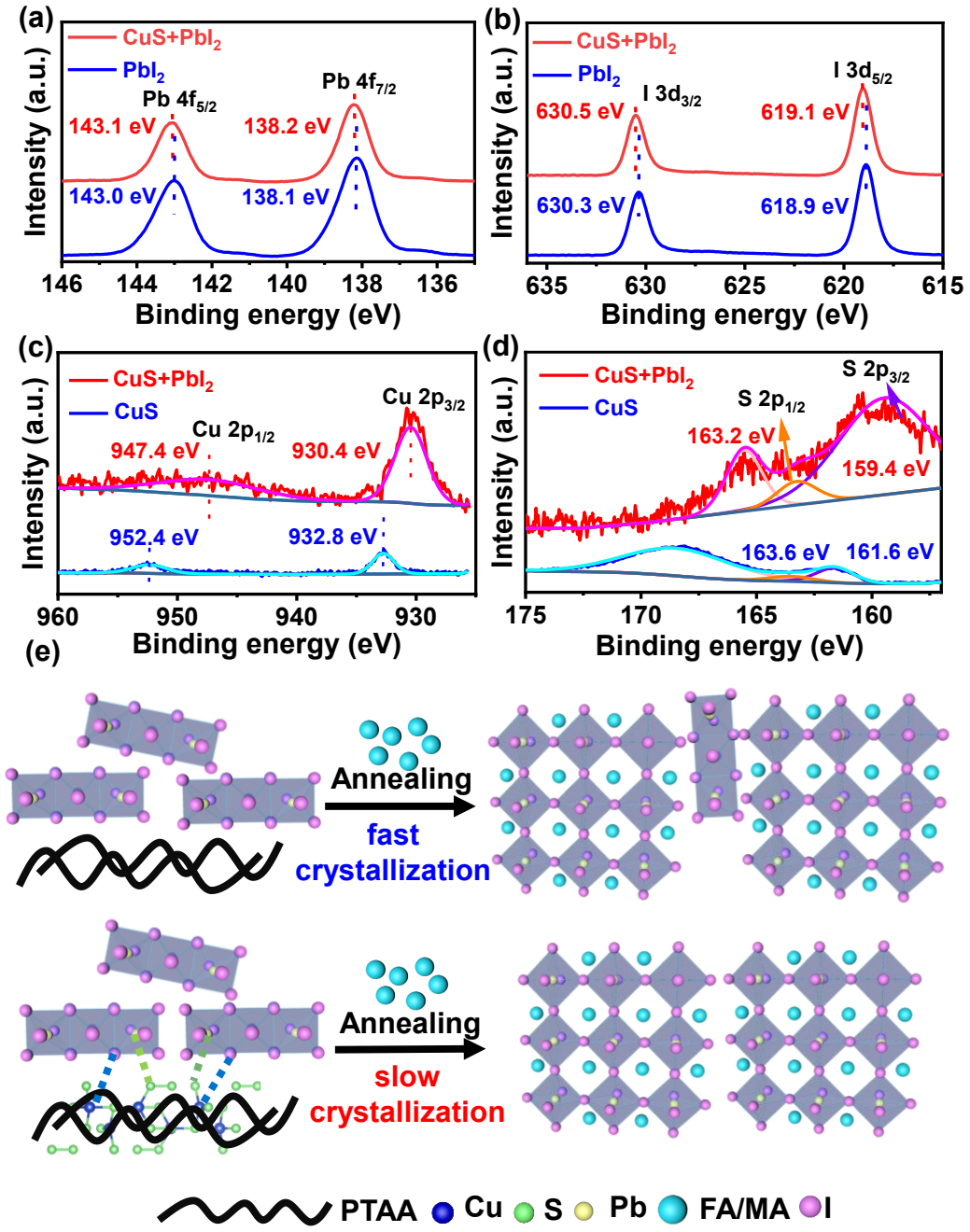


Figure 4.5 (a) Pb 4f and (b) I 3d XPS spectra of the PbI_2 samples. (c) Cu 2p and (d) S 2p XPS spectra of the CuS samples. (e) Schematic illustration of the interactions between PbI_2 and CuS.[144] Reprinted with permission from *Nano Energy* 2025, 135, 110652. Copyright 2025 The Author(s).

4.3.4 Device performance

To investigate the photovoltaic performance, devices with a structure of ITO/HTL/$FA_{0.92}MA_{0.08}PbI_3$/C_{60}/BCP/Ag were fabricated, as shown in the inset of **Figure 4.6a**. As listed in **Table A2**, the optimized concentration of CuS was determined to be 0.02 mg mL^{-1}, although all concentrations of CuS (0.01-0.03 mg mL^{-1}) resulted in improved PCEs compared with those of the control devices with pristine PTAA. The *J-V* curves for devices with pristine PTAA and PTAA with 0.02 mg mL^{-1} CuS are shown in **Figure 4.6a**. The control device achieved the highest PCE of 21.99%, with an open circuit voltage (V_{OC}) of 1.04 V, a short-circuit current density (J_{SC}) of 25.28 mA cm^{-2} and a fill factor (FF) of 83.38%. For the PTAA-CuS-based device, the best PCE of 22.92% was achieved, with an improved V_{OC} of 1.06 V, a slightly improved J_{SC} of 25.55 mA cm^{-2}, and an improved FF of 84.47%. The integrated current densities obtained from the EQE curves in **Figure 4.6b** were 24.43 and 24.41 mA cm^{-2} for the control and Pero-SC with PTAA-CuS, respectively, which deviated by only 4% from J_{SC} values obtained from the *J–V* curves. The steady output PCEs of the control and PTAA-CuS-based devices were measured under continuous illumination and a constant voltage of 0.92 V for 600 s. As shown in **Figure 4.6c**, the steady-state output PCEs of the devices without and with CuS were 21.50% and 22.46%, respectively, which is in good agreement with the results obtained from the *J–V* curves. From the PCE histograms based on 100 cells for each group in **Figure 4.6d**, the addition of CuS resulted in a higher PCE and a narrower distribution, which was due to the more uniform perovskite films.

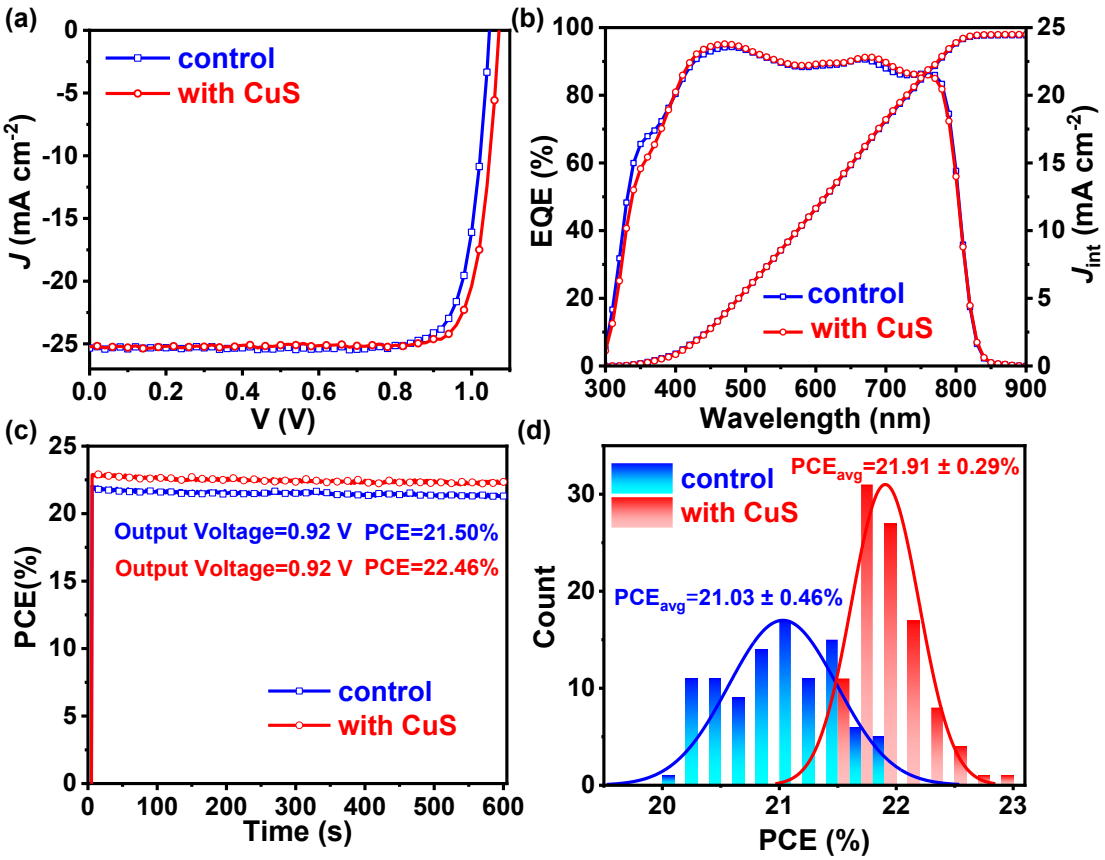


Figure 4.6 (a) *J-V* characteristic curves, (b) EQE spectra, (c) steady-state outputs, and (d) PCE histograms of the control and PTAA-CuS-based devices.[144] Reprinted with permission from *Nano Energy* 2025, 135, 110652. Copyright 2025 The Author(s).

The charge carrier recombination was investigated by measuring the V_{OC} as a function of light intensity (P_{light}), as shown in **Figure 4.7a**. The ideality factor (n) is commonly used to determine the type of recombination in Pero-SCs and was calculated via **Equation 4.3**[143, 144]:

$$V_{OC}=\frac{nk_BT\ln P_{light}}{q} \tag{4.3}$$

where k_B is Boltzmann's constant, T is the temperature, and q is the element charge. The value of n exceeds 1 if trap-assisted Shockley–Read–Hall (SRH) recombination occurs in addition to Langevin recombination (n=1) [143, 144]. When CuS was introduced into the PTAA, n decreased from 1.34 to 1.21, indicating that SRH recombination was effectively suppressed due to reduced trap densities, which is consistent with the SCLC results.

Characterization of the dark current is an effective way to explore charge carrier transport. **Figure 4.7b** illustrates the *J–V* curves in the dark, which show typical diode characteristics. The *J–V* curves in the dark can be divided into three regimes: a leakage contribution at low voltages (green), an exponential regime at medium voltages (blue) and a space-charge-limited regime (pink). In the first regime, the leakage current density of the Pero-SC with CuS was lower than that of the control, confirming improved charge transfer and less trap-assisted recombination.[145, 146] In the second regime, the *J–V* curve is exponential and can be fitted according to the Shockley diode equation (**Equation 4.4**) [147, 148]:

$$\ln(J_{\mathrm{D}}) = \ln(J_0) + \frac{q}{nk_{\mathrm{B}}T}V \tag{4.4}$$

where J_{D} is the dark current density and J_0 is the saturation current. According to the slopes and intercept values, when V equals to 0, the PTAA-CuS-based Pero-SC has a lower J_0 and lower n than the control device does, implying that the device has less charge recombination and a higher V_{OC}, which agrees with the results obtained from the illuminated *J-V* measurements[149].

EIS is another powerful tool for investigating charge transport. Nyquist plots for devices with and without CuS and the equivalent electro-circuit are shown in **Figure 4.7c** and **4.7d**, respectively, and the detailed fitting parameters are summarized in **Table A3**. R_{S} represents the internal series resistance, which is related to the sheet resistance of the electrodes, and R_{CT} represents the charge-transfer resistance between the charge transport layers and the perovskite layer and between the electrodes and the charge transport layers.[40, 150] Through fitting, the device based on pristine PTAA shows an R_{CT} of 56.50 Ω, whereas the R_{CT} of the PTAA-CuS device is reduced to 39.96 Ω, suggesting that CuS makes charge transport more efficient. These results are consistent with the analysis of the *J–V* curves in the dark.

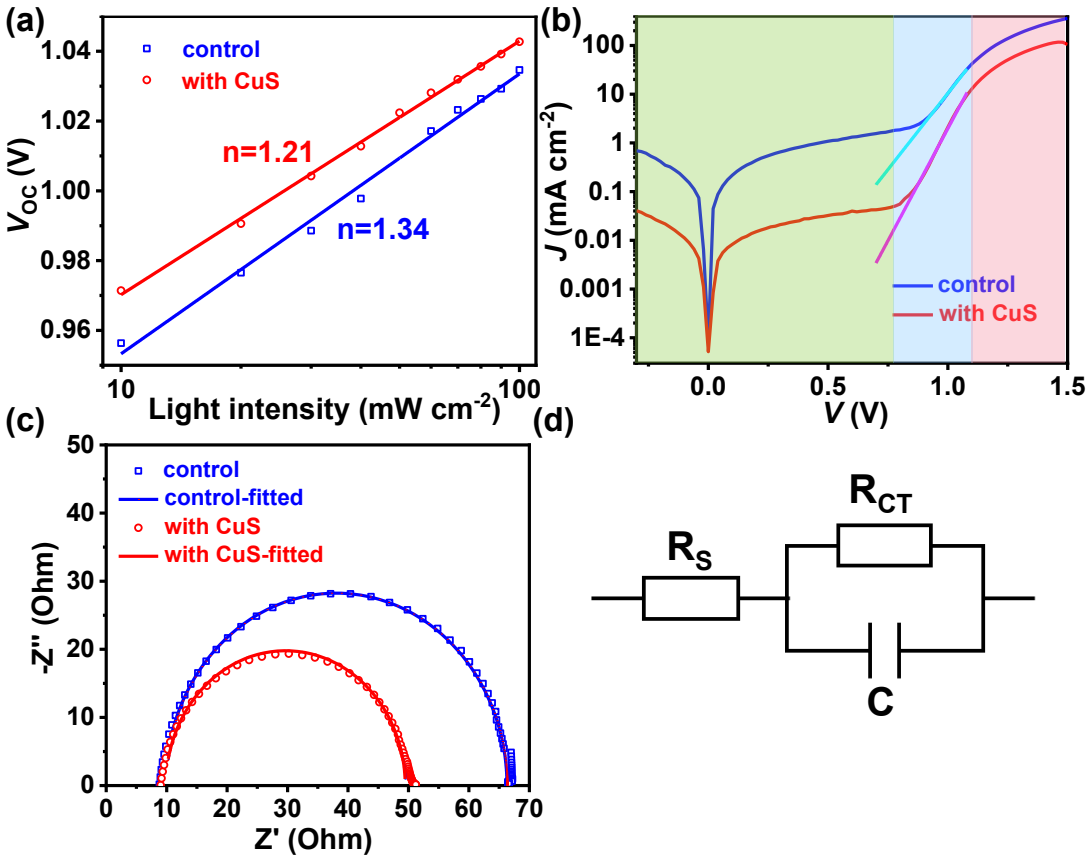


Figure 4.7 (a) Plots of V_{OC} versus light intensity, (b) *J–V* curves in the dark, and (c) Nyquist plots measured near the V_{OC} under dark conditions for Pero-SCs without and with CuS. (d) The equivalent circuit for EIS fitting.[144] Reprinted with permission from *Nano Energy* 2025, 135, 110652. Copyright 2025 The Author(s).

4.3.5 Stability of devices

In addition to the PCE, device stability is also an essential benchmark for evaluating the commercialization potential of Pero-SCs. In a N_2 atmosphere at room temperature, the devices without encapsulated CuS maintained 96% of the initial PCE over 2300 h, which was slightly higher than that of the control device, as shown in **Figure A7**. To test their thermal stability, the unencapsulated Pero-SCs were stored at 65~70 °C in N_2. As shown in **Figure 4.8a**, the Pero-SCs with CuS maintained approximately 73% of the initial PCE, whereas the control device retained 60% of the initial PCE after 960 h. To test the humidity stability, the unencapsulated Pero-SCs were stored in air with an RH ranging from 40%-50%, as shown in **Figure 4.8b**. After 800 h, the PCE

of the control device decreased to approximately 50% of the initial value, whereas that of the Pero-SCs with CuS remained at approximately 69%. Both the improved thermal and humidity stabilities are attributed to the improved quality of the perovskite films and the reduction in PbI_2 with the introduction of CuS.

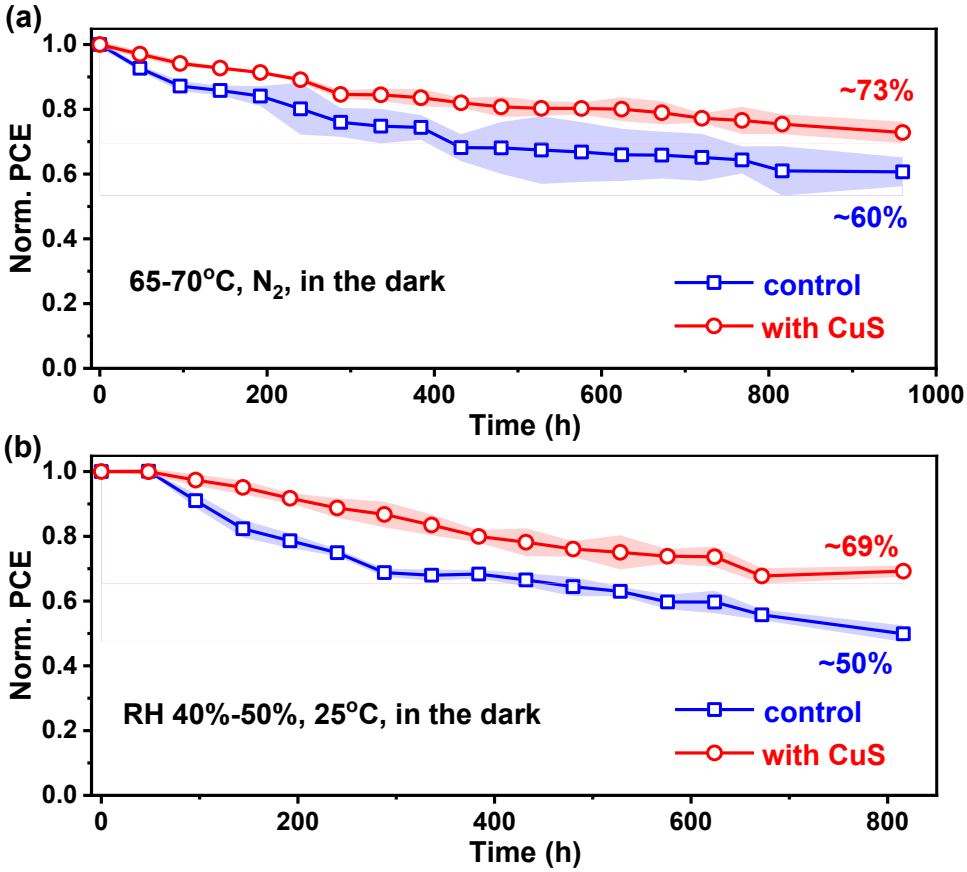


Figure 4.8 PCE evolution of Pero-SCs analyzed from 5 samples for each group. (a) Stored at 65–70 °C in N_2. (b) Stored in air with an RH of 40–50%. All the samples were stored in the dark.[144] Reprinted with permission from *Nano Energy* 2025, 135, 110652. Copyright 2025 The Author(s).

4.4 Conclusions

In summary, CuS nanosheets were introduced into PTAA, which was employed as HTL in *p-i-n* Pero-SCs. After the addition of CuS, the conductivity of the HTL increased twofold, and the work function increased, thus decreasing the transport resistance and promoting charge transfer and transport. In addition, through interactions between CuS and PbI_2, perovskite growth was controlled,

and perovskite films with better quality were obtained, which reduced nonradiative recombination. Finally, upon the addition of CuS, the PCE and device stability improved.

Chapter 5
CuS-Nanoparticle-Induced Porous PbI_2 for High-Performance *p-i-n* Perovskite Solar Cells

5.1 Introduction

Excess PbI_2 can improve the PCE, prevent the formation of organic-rich surfaces and passivate perovskite boundaries. However, under continuous illumination, PbI_2 will decompose into Pb^0 and I_2, introducing non-radiative recombination centers and decompose the perovskite, leading to poor operational stability.[30] One of the approaches for mitigating the side effects of lead iodide in perovskite materials involves surface passivation post-treatment of the perovskite film. For instance, Abate et al. developed functionalized oxo-graphene nanosheets to bind the excess PbI_2.[151] However, this approach only addresses surface-level lead iodide, leaving the bulk-phase and bottom-layer lead iodide unaffected. Consequently, comprehensive regulation of lead iodide distribution throughout the entire perovskite layer requires precise control over perovskite crystallization dynamics. In the two-step fabrication method, excess lead iodide formation primarily results from incomplete reactions between PbI_2 and ammonium salts. Thus, developing a porous lead iodide layer has emerged as a crucial strategy for effective lead iodide management. Wei et al. introduced some strong Lewis bases into the PbI_2/DMF solution to obtain a PbI_2 film with a mesoporous structure, improving the conversion rate of PbI_2 to $MAPbI_3$.[152] Zhou et al. mixed polyvinyl pyrrolidone with PbI_2 to suppresses PbI_2 crystallization, resulting in smaller PbI_2 grains and more porous PbI_2, which facilitates the formation of perovskite phases.[36] Pentafluoroanilinium trifluoromethanesulfonate was introduced into a PbI_2 precursor solution by Fang et al. to acquire porous PbI_2 films due to the pre-aggregation induced by an intermediate phase, promoting intercalation of the organic ammonium salts into the PbI_2.[35] Beyond organic materials, inorganic materials like MoS_2 nanosheets have been functionalized as nano-scaffolds to delay the quick nucleation process of PbI_2 and expand the physical volume of the PbI_2 film with a nanoporous skeleton morphology.[62]

In this work, to obtain porous PbI_2 films, CuS nanoparticles were synthesized and incorporated into the PbI_2 solution. The interaction between PbI_2 and CuS nanoparticles leads to a decrease in the PbI_2 crystallinity and a slight decrease in the PbI_2 particle size, resulting in a more porous PbI_2

film, which promotes the diffusion of ammonium salts and the formation of the perovskite phase. Furthermore, the interaction allows CuS nanoparticles to replace the role of PbI_2 as a passivating agent. In addition, the p-type properties of CuS nanoparticles improved the charge transport between the HTL and perovskite. Eventually, the PCE of Pero-SCs improved from 23.21% to 24.31% with improved J_{SC} and FF. Moreover, compared with the control groups, Pero-SCs with CuS showed better N_2, humidity and light stability. The unencapsulated devices with CuS nanoparticles maintained 90% of the initial PCE over 6800 h in N_2, maintained 67% after 288 h in air with a RH of 30 %-40 %, and retained 83% after 888 h under continuous illumination by a white-light LED.

5.2 Experiment methods

5.2.1 Materials

Sodium sulfide nonahydrate ($Na_2S{\cdot}9H_2O$) was acquired from Shang Aladdin Biochemical Technology Co., Ltd. 2PACz and 2-phenylethylammoniumiodide (PEAI) were purchased from Xi'an Yuri Solar Co., Ltd. The details for $CuCl_2$, ITO, PbI_2, MAI, MACl, C_{60}, BCP and Ag are detailed in Section 4.2.1.

5.2.2 Synthesis of CuS nanoparticles

In this work, the CuS NP solution was synthesized according to the literatures.[124, 153] In a 250 mL round bottom flask, $CuCl_2$ (0.0170 g, 1 mmol) was dissolved in 100 mL of deionized water. 1 mL of Na_2S aqueous solution (0.1 M) was slowly added into the $CuCl_2$ aqueous solution under constant stirring. After adding the Na_2S solution (about 3 min), the round bottom flask containing the solution was placed in an oil bath at 90 °C and heated for 20 min with constant stirring and a dark-green CuS NP solution was obtained. Then the flask was removed from the oil bath and cooled to room temperature. The products were washed twice with water, ethanol and IPA respectively, and a centrifuge was used to collect them. Finally, the products were dried at 60°C for 12 h in a vacuum oven. The synthesized powders were stored in a N_2-filled glovebox.

5.2.3 Fabrication of devices

Before the deposition of HTLs, the cleaned ITO was treated with UV-ozone for 30 min. Then a layer of 2PACz (0.5 mg mL^{-1} in IPA) was spin-coated onto the cleaned ITO substrates at 3000 rpm

for 50 s, and the substrates were annealed at 100 ℃ for 20 min in a glove box. For the PbI_2 solution with CuS nanoparticles, the CuS nanoparticles were dispersed in DMF (0.1 mg mL^{-1}) via ultrasonication for 1 hour and then the CuS-nanoparticle DMF solution was added into the PbI_2 solution, and the final concentration of CuS nanoparticles was varied from 0.002 mg mL^{-1} to 0.006 mg mL^{-1}. The PbI_2 solution was filtered with a 0.45 μm PTFE filter. After the deposition of perovskite films, a layer of PEAI (1 mg mL^{-1}) was spin-coated at 4000 rpm for 30 s. The deposition of perovskite films, C_{60} and BCP is detailed in Section 4.2.3.

5.2.4 Characterization

The dynamic light scattering (DLS) was measured at 25 °C with a Zetasizer Nano (Malvern, UK) equipped with a 633 nm laser. The transmission electron microscope (TEM) images were collected using a JEOL JEM 2100F operated at 200 kV. The TPV and TPC spectra were obtained from a TPVC-1G of SouthPort Co., Ltd. The TPV test was conducted with a halogen light bias, and the TPC test was conducted in the dark. The measurement of SEM, XPS XRD, UV−vis spectra, PL spectra, TRPL spectra, *J–V* curves, EQE curves, and EIS is detailed in Section 4.2.4.

5.3 Results and discussion

5.3.1 Making PbI_2 films more porous

The synthesized CuS nanoparticles were dispersed in DMF through ultrasound treatment first and then added into PbI_2 solution. It has been reported that there exists an interaction between CuS and PbI_2.[139, 154] To confirm this, XPS of PbI_2 films without and with 0.004 mg mL^{-1} of CuS nanoparticles was performed, as displayed in **Figure 5.1**. The appearance of Cu and S signals proved the existence of CuS nanoparticles in the PbI_2 films, even though the precursor solution was filtered. For pristine PbI_2, the peaks corresponding to Pb $4f_{5/2}$ and Pb $4f_{7/2}$ are located at 143.0 and 138.2 eV, respectively, and the peaks assigned to me $3d_{3/2}$ and I $3d_{5/2}$ are located at 630.6 and 619.1 eV, respectively. For pristine CuS nanoparticles, the peaks at 952.7 and 933.0 eV correspond to Cu $2p_{1/2}$ and Cu $2p_{3/2}$, respectively, and the peak at 167.5 eV corresponds to S $2p_{1/2}$. After the CuS nanoparticles were introduced in the PbI_2, the Pb 4f peaks and I 3d peaks shifted to higher binding energies, whereas the Cu 2p and S 2p peaks shifted to lower binding energies, which is attributed to the interaction between PbI_2 and CuS. The interaction will influence the morphology of the PbI_2 films, which will be discussed later.

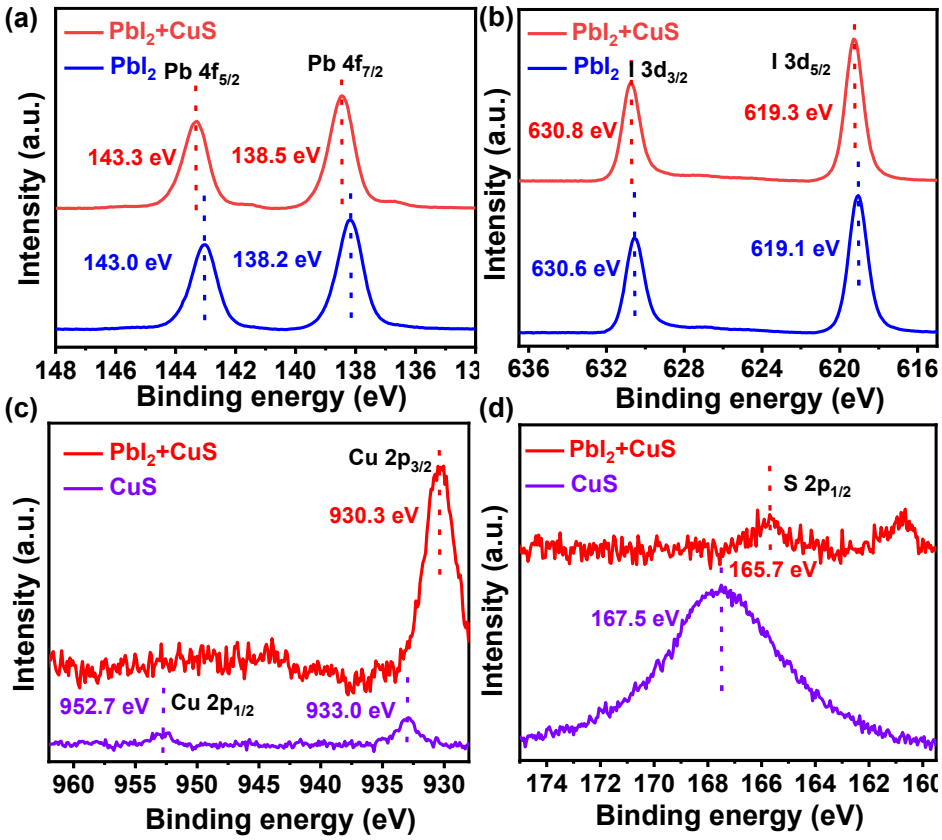


Figure 5.1 (a) Pb 4f and (b) I 3d XPS spectra of PbI_2. (c) Cu 2p and (d) S 2p XPS spectra of CuS nanoparticles.

The TEM and SEM images in **Figure B1** display the nanomorphology of the synthesized CuS nanoparticles and the inset in **Figure B1b** shows the grain-size-distribution histogram. The nanoparticles have an average size of approximately 16 nm. It is noted that to successfully obtain CuS powder samples by centrifugation, compared with the method reported in the literature, no sodium citrate was added in this work, which led to the aggregation of nanoparticles, as shown in the SEM image (**Figure B1b**). To check whether the aggregation of nanoparticles still occurred in the PbI_2 solution, DLS was carried out. As shown in **Figure B2**, in DMF/DMSO, the CuS nanoparticles shows a wide size distribution between 100 nm and 700 nm, indicating that aggregation occurred when only the CuS nanoparticles were present. However, **Figure B2b** shows that when 0.004 mg/ml CuS nanoparticles were added into PbI_2, there is no DLS signal in this range, indicating that the aggregation of CuS nanoparticles was inhibited in the precursor solution, which is likely caused by the interaction between the CuS and PbI_2.

The DLS results of both PbI_2 solution without and with CuS nanoparticles displays a bimodal distribution. It has been reported that colloidal species in perovskite precursor solutions comprise a series of iodoplumbate complexes, $[PbI_n]^{(n-2)-}$, which serve as fundamental building blocks for the self-assembly of extended lead polyiodide frameworks.[155] These frameworks exhibit long-range order and are interconnected via corner-sharing Pb–I–Pb coordination bonds. Thus, PbI_2 colloids of different sizes are formed, and most of them are concentrated in small size range. For the small-sized colloids in range of 1-5 nm, the colloid diameter size of the pristine PbI_2 solution was 2.5 nm. After the addition of CuS nanoparticles, a similar colloid diameter size of 2.3 nm was obtained. For the large-sized colloids in range of 2000–6000 nm, the relatively proportion (vs total DLS intensity) was decreased from 5.1% to 3.0% after the addition of CuS nanoparticles, which should be contributed to the promoted formation of separately dispersed small $[PbI_n]^{(n-2)-}$ colloids and inhibited formation of large $[PbI_n]^{(n-2)-}$ colloids due to the interaction between CuS and PbI_2.[155, 156]

Then the effects of the introduction of CuS nanoparticles on PbI_2 films were explored. **Figure 5.2a** presents XRD patterns and **Figure 5.2b** and **5.2c** display top-view SEM images of different PbI_2 films. Compared with the pristine PbI_2 film, the XRD peak intensity of the PbI_2 film with CuS decreased. From the SEM images, PbI_2 crystals with sharp edges can be observed in the pristine films, whereas for the PbI_2 with CuS, the edges of the crystals became smoother, indicating the crystallinity of PbI_2 was suppressed, which is consistent with the XRD. In addition to the crystallinity, compared with the pristine PbI_2, the PbI_2 with CuS has a wider full width at half maxima (FWHM) value (increased from 0.148° to 0.160°), that is, a smaller grain size (decreased from 54 nm to 50 nm), suggesting that the growth of PbI_2 was suppressed. The suppressed crystallinity and growth of PbI_2 with CuS can be attributed to the interaction between CuS and PbI_2 seen in the XPS analysis. Based on the controlled growth of PbI_2, a more porous PbI_2 film was obtained, as shown in **Figure 5.2c**, which will facilitate the diffusion of FAI and the formation of the perovskite phase. According to the above results, the possible perovskite growth process based on different PbI_2 films was proposed in **Figure 5.2d**. For the pristine PbI_2 films, smaller spaces between the PbI_2 grains hinder penetration of the ammonium salts, resulting in excessive PbI_2 residues extruded to the surface after the annealing process. On the contrary, for the PbI_2 films with CuS, the more porous morphology allows adequate interaction between PbI_2 and the ammonium salts, reducing the amount of PbI_2. Although the PbI_2 that can play a passivation role may be

reduced in the perovskite films with CuS, owing to the interaction between PbI_2 and CuS, it is expected that the CuS nanoparticles can replace PbI_2 as a passivating agent.

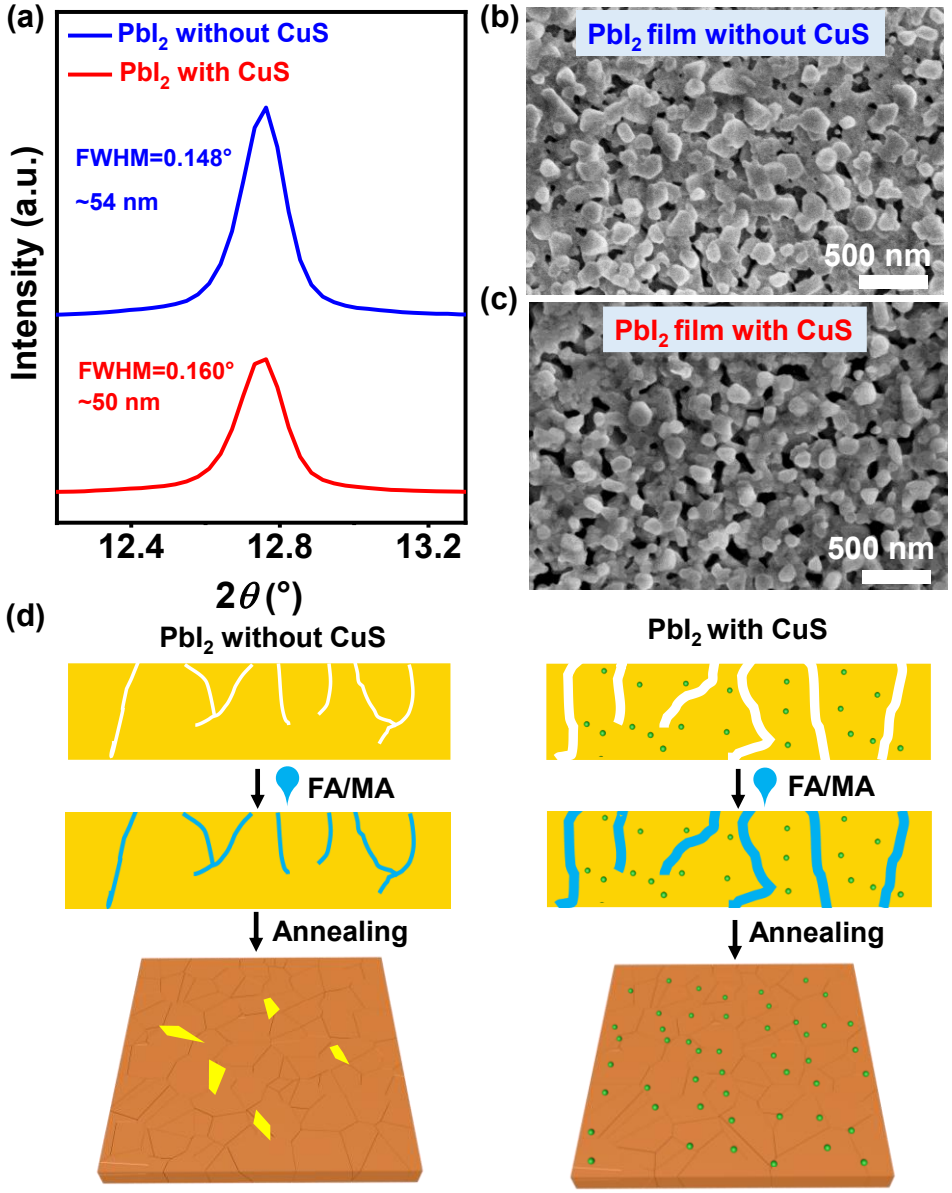


Figure 5.2 (a) XRD patterns of PbI_2 films without and with CuS nanoparticles. Top-view SEM images of PbI_2 films (b) without and (c) with CuS nanoparticles. (d) The schematic illustration of perovskite films based on different PbI_2 films.

5.3.2 Improving the quality of perovskite films and hole transport

In order to verify the perovskite-formation process proposed above, a series of characterizations on perovskite films were carried out. **Figure 5.3a** and **5.3c** show the top-view SEM images of perovskite films without and with CuS nanoparticles, respectively. As is depicted in **Figure 5.2d**, after the addition of CuS nanoparticles, the amount of residual PbI_2 (yellow circles) was less and the formation of the perovskite phase was facilitated. The average perovskite grain size was slightly increased from 369 ± 107 nm to 408 ± 142 nm (**Figure B3**). **Figure 5.3c** and **5.3d** show cross-sectional SEM images of the perovskite films. For the control film, the growth of the perovskite was irregular. In contrast, the perovskite film with CuS has a preferred vertical growth orientation, which is conducive to charge transport. In addition, the introduction of CuS nanoparticles increased the thickness of the perovskite film slightly from 680 nm to 730 nm, which could be attributed to the expanded PbI_2 skeleton. The increased thickness should improve the photon capture, as seen in the increased absorbance in **Figure B4**, and could result in a higher J_{SC}. **Figure 5.3e** displays the XRD patterns of the perovskite films. There is no obvious shift on the diffraction peaks. Combined with the unchanged absorption edge in **Figure B4**, this suggests the CuS nanoparticles did not enter into the perovskite lattice.

To investigate the change in the trap density resulting from the mitigation of PbI_2 with CuS nanoparticles, the SCLC method was conducted to quantify the N_t of perovskite films without and with CuS nanoparticles. The device structure of ITO/2PACz/Perovskite/MoO_3/Ag was used and the N_t can be calculated by **Equation 4.2**. As shown in **Figure 5.3f**, the V_{TFL}s of the control and Pero-SC with CuS were 0.42 V and 0.36 V, respectively, and the N_t decreased slightly from 1.3×10^{15} to 1.1×10^{15} cm^{-3}, indicating the introduction of CuS is sufficient to replace the passivation role of excess PbI_2 and the non-radiative recombination can still be suppressed.

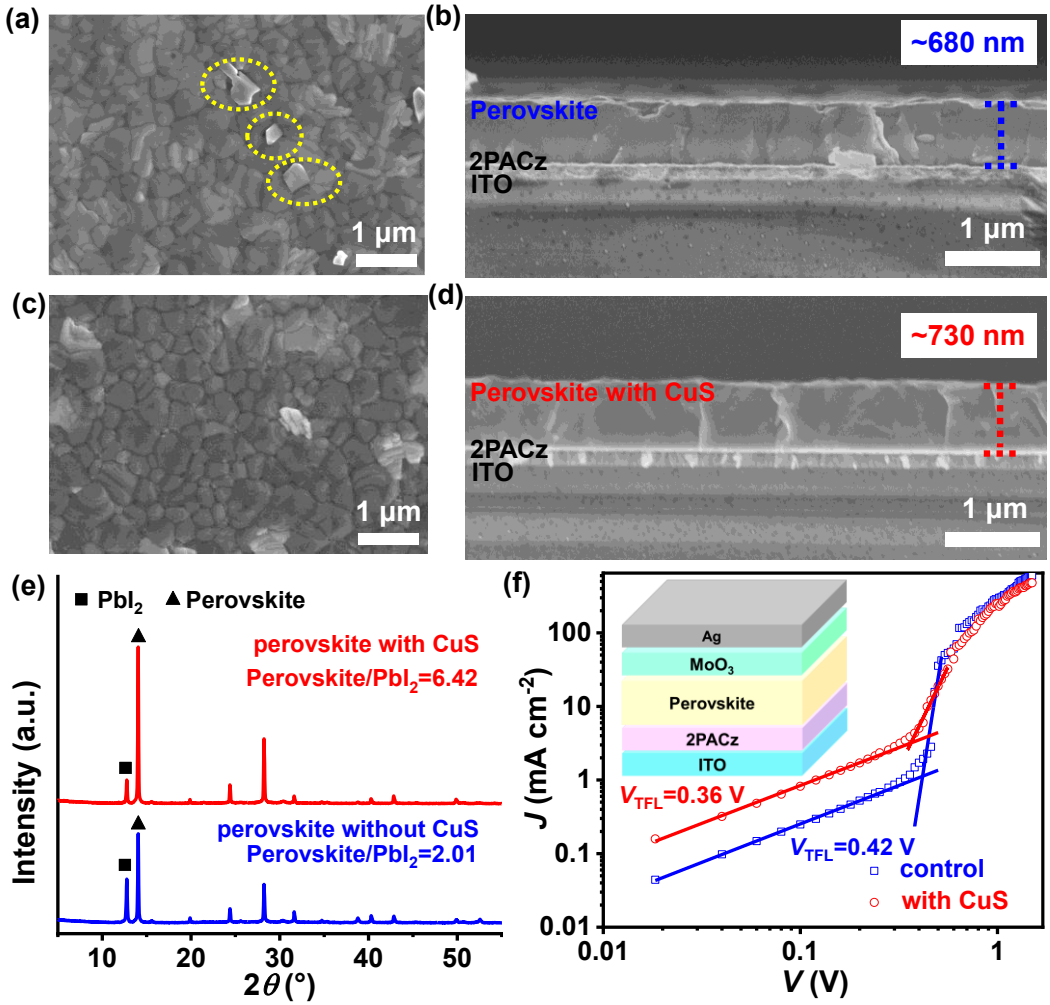


Figure 5.3 Top-view SEM images of perovskite film (a) without and (c) with CuS. Cross-sectional SEM images of perovskite film (b) without and (d) with CuS. (e) XRD patterns of the perovskite films. (f) *J*-*V* curves in the dark of hole-only devices based on the different perovskite films for SCLC analysis.

As a *p*-type semiconductor, CuS nanomaterials have been proven to enhance the charge transport between the hole transport layer and the perovskite layer.[124, 125, 138, 157] Consequently, in addition to regulating the perovskite growth, CuS nanoparticles may play a positive role in charge transportation. To evaluate the carrier recombination and interfacial charge extraction, the steady-state PL and TRPL of the different perovskite films on glass or ITO/2PACz were studied (**Figure 5.4**). On glass, compared with the pristine perovskite film, the PL intensity of the perovskite film

with CuS was significantly increased (**Figure 5.4a**), suggesting inhibited nonradiative recombination in the perovskite film. For TRPL, a two-component exponential decay function (**Equation 4.1**) was employed (see the detailed parameters in **Table B1**). On glass, the fast decay component (τ_1) is assigned to the nonradiative recombination of charge carriers caused by trap states at the interfaces and the slow decay component (τ_2) is assigned to radiative recombination of the free carriers in the bulk perovskite before extraction. After the introduction of CuS nanoparticles, the τ_1 increased from 438.9 ns (f_1 = 5.0%) to 503.4 ns (f_1 = 8.6%), indicating less non-radiative recombination and the τ_2 prolonged from 4076.9 ns (f_2 = 95.0%) to 5048.4 ns (f_2 = 91.4%), indicating more radiative recombination (**Figure 5.4b**). On ITO/2PACz, the PL intensity of the perovskite film with CuS was reduced (**Figure 5.4c**), suggesting improved charge transfer with the assistance of CuS nanoparticles. Different from the situation in **Figure 5.4b**, when the perovskite films are deposited on ITO/2PACz, the τ_1 represents the quenching of photogenerated carriers by charge extraction from the perovskite to the HTL. As shown in **Figure 5.4d**, upon the addition of CuS nanoparticles, the τ_1 was reduced from 355.1 ns with a f_1 of 6.3% to 209.1 ns with a f_1 of 8.7%, showing a faster and effective hole transfer from perovskite to HTL. The above results confirm that the addition of CuS nanoparticles in the perovskite layer not only improved the perovskite quality and inhibit the nonradiative recombination but also facilitated the charge transfer.

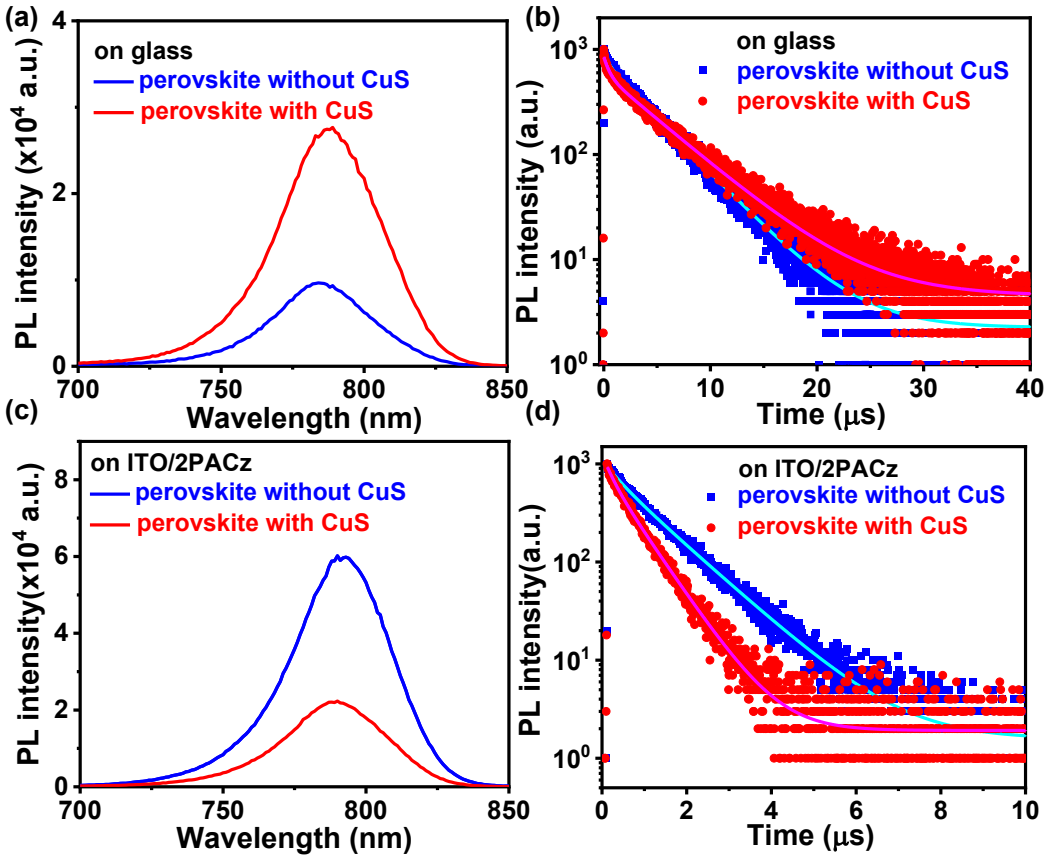


Figure 5.4 (a) Steady-state PL and (b) TRPL of different perovskite films on glass. (c) Steady-state PL and (d) TRPL of different perovskite films on ITO/2PACz.

5.3.3 Improving device performance

To investigate the photovoltaic performance, devices with a structure of ITO/2PACz/$FA_{0.92}MA_{0.08}PbI_3$/C_{60}/BCP/Ag were fabricated, as shown in the inset in **Figure 5.5a**. As listed in **Figure B5** and **Table B2**, the optimized concentration of CuS was determined to be 0.004 mg mL^{-1}. The *J-V* curves for the champion devices are shown in **Figure 5.5a** and the detailed parameters are listed in **Table 5.1**. The control device achieved a champion PCE of 23.21%, with an open circuit voltage (V_{OC}) of 1.14 V, a short-circuit current density (J_{SC}) of 25.02 mA cm^{-2} and a fill factor (FF) of 81.29%. The Pero-SC with CuS achieved a champion PCE of 24.31%, with a V_{OC} of 1.14 V, an improved J_{SC} of 25.48 mA cm^{-2}, and an improved FF of 83.49%. The improved J_{SC} is on account of the increased perovskite phase and thicker perovskite layer. From the PCE histograms based on 160 samples for each group in **Figure 5.5b**, the addition of CuS resulted in a

higher PCE and a narrower distribution, which was due to the high-quality perovskite films. Under continuous illumination and a constant voltage of 0.98 V for 600 s, the steady output efficiencies of the control and Pero-SC with CuS (**Figure 5.5c**) were 22.40% and 23.32%, respectively, which is in good agreement with the results obtained from the *J–V* curves. From the EQE curves in **Figure 5.5d**, the integrated current densities (J_{int}) were 23.81 and 24.19 mA cm^{-2} for the control and Pero-SC with CuS, respectively, which deviate by approximately 5% from the J_{SC} values obtained from the *J–V* curves, indicating the results were reliable. The higher EQE value and J_{int} of the Pero-SC with CuS further indicated the addition of CuS nanoparticles could increase the J_{SC}.

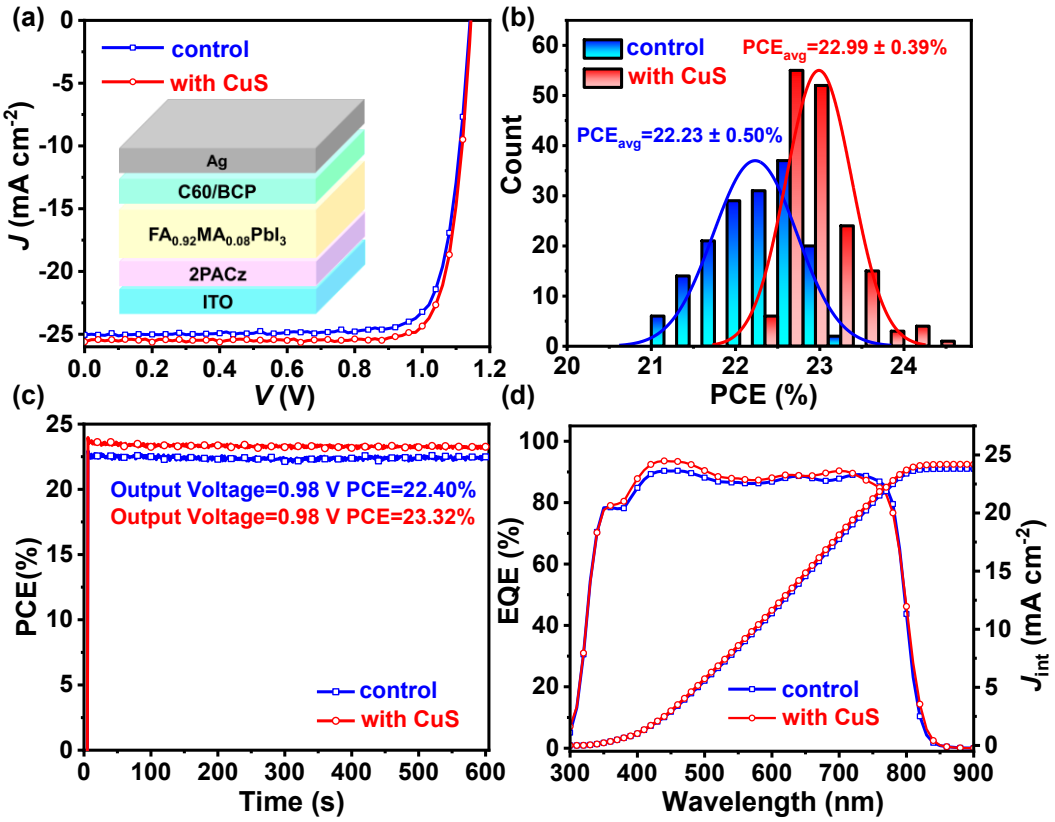


Figure 5.5 (a) *J-V* curves, (b) PCE histograms from 160 cells, (c) steady-state outputs, and (d) EQE spectra of the control and Pero-SC with CuS.

Table 5.1 Detailed photovoltaic parameters of the control and Pero-SCs with CuS. The average values were obtained from 10 devices.

	V_{OC} (V)	J_{SC} (mA cm^{-2})	FF(%)	PCE (%)
control	1.14	25.03	81.3	23.21
	1.14±0.01	24.57±0.32	81.0±0.6	22.77±0.33
with CuS	1.14	25.48	83.5	24.31
	1.14±0.01	25.23±0.17	82.9±1.0	23.83±0.38

The ideality factor (n) is commonly used to characterize the carrier recombination in Pero-SCs. As shown in **Figure 5.6a**, the n was calculated by measuring the V_{OC} as a function of P_{light} via **Equation 4.3**. A reduction of n from 1.44 to 1.26 indicates the trap-assisted non-radiative recombination was effectively suppressed when CuS nanoparticles were introduced, which is accordance with the PL and TRPL analysis.

The dark *J–V* curves of different devices were measured to explore charge carrier transport and recombination (**Figure 5.6b**). In the leakage contribution regime at low voltages (green), the leakage current density of the Pero-SC with CuS was lower than that of the control, confirming less trap-assisted recombination and improved charge transfer.[145, 146] In the exponential regime at medium voltages (blue), the *J–V* curve can be fitted according to the Shockley diode equation (**Equation 4.4**). Thus, the larger slope and decreased intercept of the Pero-SC with CuS indicates a lower n and lower J_0, implying that the device has less charge recombination, which agrees with the results obtained from the light-intensity-dependence characterization[149].

Then TPV and TPC measurements were performed to explore the charge carrier dynamics in the Pero-SCs. Under illumination, a faster voltage attenuation indicates more trap-assisted non-radiative recombination. As shown in **Figure 5.6c**, the carrier recombination lifetime (τ_R) of the control and Pero-SCs with CuS were 4.83 μs and 21.98 μs, respectively, indicating inhibited non-radiative recombination and effective defect passivation in Pero-SCs with CuS. [158, 159] The carrier transport lifetime (τ_T) in the Pero-SCs decreased from 0.45 to 0.24 μs with the addition of CuS nanoparticles, suggesting improved carrier transport (**Figure 5.6d**).[159]

EIS is also a powerful tool for investigating charge transport. As shown in **Figure B6**, under a bias of near V_{OC}, a semi-circle could be observed at high frequency. The Nyquist plots of different

Pero-SCs were fitted according to the equivalent electro-circuit (the inset) and the detailed fitting parameters are summarized in **Table B3**. R_S represents the internal series resistance and R_{CT} represents the charge-transfer resistance between the charge transport layers and the perovskite layer and between the electrodes and the charge transport layers.[40, 150] The control device shows an R_{CT} of 77.74 Ω, whereas the R_{CT} of the Pero-SC with CuS was decreased to 52.29 Ω, which suggests that CuS makes charge transport more efficient, further indicating that the *p*-type CuS can promote the hole transfer.

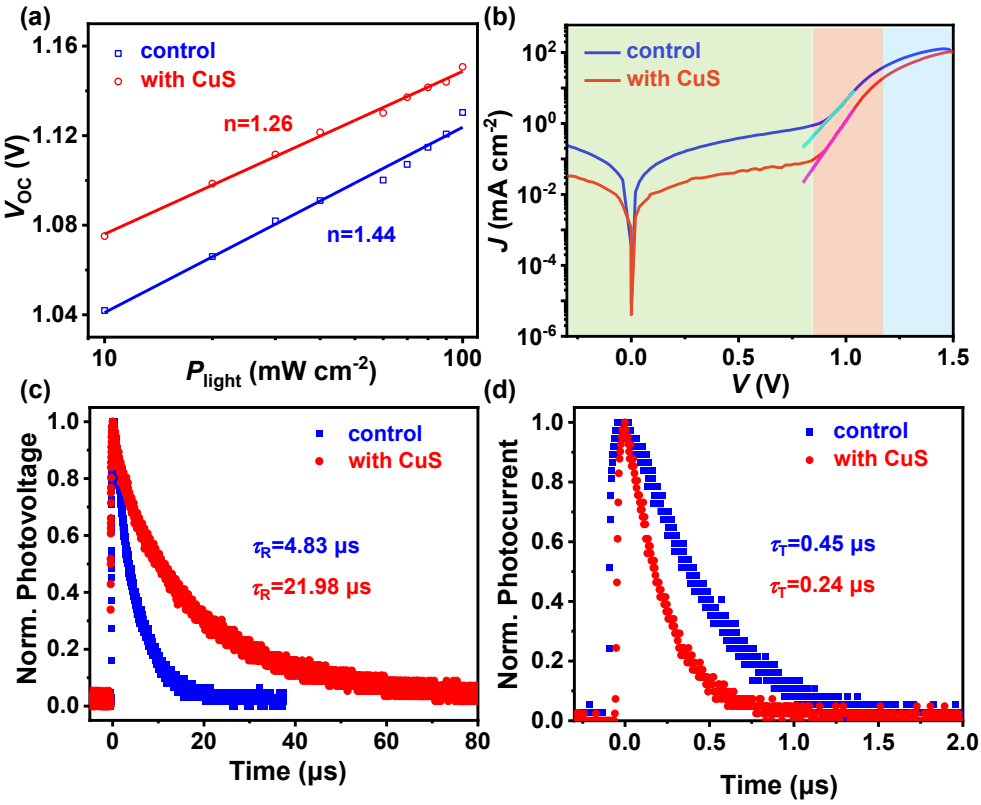


Figure 5.6 (a) Plots of V_{OC} versus P_{light}, (b) dark *J*-*V* curves, (c) normalized TPV and (d) normalized TPC curves of the control and Pero-SC with CuS.

5.3.4 Improved device stability

The regulation of excessive PbI_2 is expected to benefit the long-term stability of Pero-SCs. In a N_2 atmosphere at room temperature, the unencapsulated devices with CuS nanoparticles could maintain approximately 90% of the initial PCE over 6800 h, which was higher than that of the control device, as shown in **Figure 5.7a**. The unencapsulated Pero-SCs were stored in air with an

RH of 30%-40% to evaluate the humidity stability, as shown in **Figure 5.7b**. After 288 h, the PCE of the Pero-SCs with CuS remained at approximately 67% of the initial value, whereas that of the control device decreased to approximately 59%. The long-term continuous operational stability of the devices was tracked under a white LED with a simulated intensity of 100 mW cm^{-2} (**Figure 5.7c**). After 500 h, the PCE of the control device dropped to 22% of the initial value, whereas the Pero-SCs with CuS could retain 83% after 888 h. The slower degradation rate of devices can be attributed to the reduction in PbI_2 and the improved quality of the perovskite films with the introduction of CuS nanoparticles.

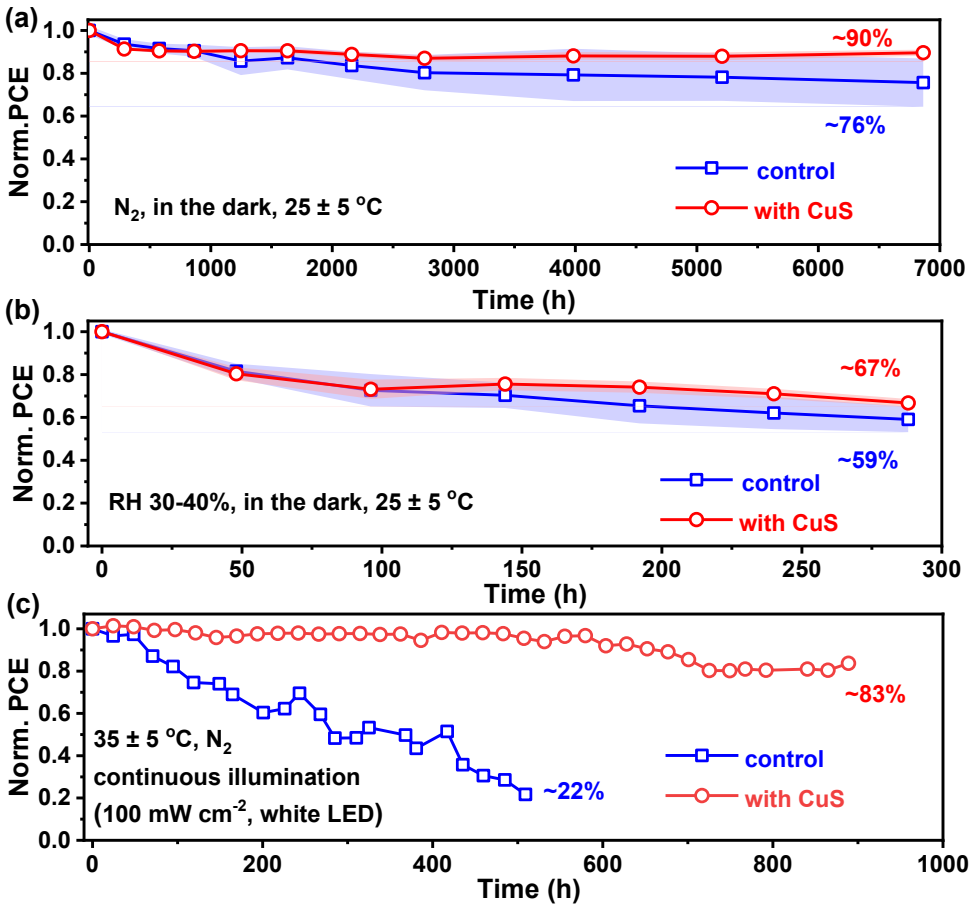


Figure 5.7 PCE evolution of Pero-SCs. (a) Stored in N_2 in the dark (analyzed from 10 samples for each group). (b) Stored in air with an RH of 30-40% in the dark (analyzed from 10 samples for each group). (c) Exposed to continuous illumination (white LED) at 35 ± 5 °C in an N_2-filled glovebox. All the samples were without encapsulation.

5.4 Conclusions

In summary, CuS nanoparticles were introduced into the PbI_2 precursor solution to control the morphology of PbI_2 films and the crystallinity of the perovskite. Due to the interaction between PbI_2 and CuS nanoparticles, the crystallinity of PbI_2 films and the PbI_2 particle size decreased, resulting in the formation of porous PbI_2 films. With the more-porous PbI_2 as a template, the reaction between PbI_2 and FAI was promoted and more perovskite phase was formed. Therefore, thicker perovskite films with less PbI_2 and larger grains were fabricated. With the addition of CuS nanoparticles, the champion PCE of the Pero-SCs improved from 23.21% to 24.31% along with better N_2, humidity and light stability.

Chapter 6
Soybean Lecithin as a Passivator and Compatibilizer in *p-i-n* Perovskite Solar Cells

6.1 Introduction

The surface energy is one of the crucial factors affecting the quality of perovskite films. In *p-i-n* Pero-SCs, widely used hydrophobic HTLs, such as PTPD and PTAA, have low surface energies, whereas the surface energy of the perovskite precursor solution, which often contains polar solvents such as DMF or DMSO, is greater.[160] Consequently, the difference in the surface energies between the HTLs and perovskite precursor solution leads to perovskite films with poor coverage and numerous pinholes.[37, 39, 40, 161] In addition to the mismatch of the surface energies, nonradiative recombination centers are also introduced by the numerous charged defects generated during the perovskite crystallization process, such as undercoordinated Pb^{2+} and Pb–I anti-site defects.[16, 17]

To reduce the difference in surface energy between the precursor solution and HTLs, there are two main approaches: adjusting the surface energy of the HTL or the perovskite precursor solution. On the one hand, to increase the surface energy of substrates, some polymers with hydrophobic and hydrophilic sides, such as PFN[39] and PSBMA[40], have been employed as interfacial layers, and their hydrophilic ends have been utilized to increase the surface energy. On the other hand, it has been reported that hydrophobic aliphatic chains can decrease the surface energy.[162, 163] Consequently, a decrease in the surface energy of the perovskite precursor solution can be realized through the introduction of molecules with hydrophobic aliphatic chains. For example, a zwitterion molecule with a long alkyl chain, TAH, was employed as an additive in a perovskite precursor solution, and its hydrophobic end increased the affinity between the perovskite precursor solution and PTAA.[76] Apart from adjusting the surface energy, zwitterionic molecules, such as DPSI[65], BTCC[164], IMS[63], squaraine[74] and D-PFPAA[73], are also promising passivating materials because their charged functional groups can passivate both positively charged and negatively charged defects.

In this work, SL, a zwitterionic amphiphile with long aliphatic chains, was incorporated into a perovskite precursor solution to simultaneously improve the perovskite coverage and decrease the defects. The long hydrophobic alkyl chain decreased the surface energy of the PbI_2 precursor solution and then improved the adhesion of the perovskite precursor to the underlying hydrophobic

PTAA, thus enabling the construction of perovskite films with full coverage. In addition to the improved coverage, there is coordination between the C=O and P=O groups and undercoordinated Pb^{2+} and electrostatic interactions between the quaternary ammonium groups and negatively charged defects, thus controlling perovskite growth and passivating defects. Through these dual effects, high-quality perovskite films were obtained. Notably, the PCE of Pero-SCs with an active area of 0.1 cm^2 increased from 20.12% to 22.93% with an improved V_{OC}, and SL-modified devices with a larger area of 1.1 cm^2 achieved a PCE of up to 18.32%. Moreover, compared with the Pero-SCs without SL, the unencapsulated Pero-SCs with SL showed better stability, maintaining 74% of the initial PCE after storage for 800 h under a relative humidity (RH) of 30–40%.

6.2 Experimental Methods

6.2.1 Materials

The SL was purchased from Energy Chemical. The methylammonium bromide (MABr) was purchased from Xi'an Yuri Solar Co., Ltd. The details for ITO, PTAA, PbI_2, FAI, MACl, C_{60} and BCP are provided in Section 4.2.1.

6.2.2 Fabrication of devices

Perovskite films were fabricated via a two-step deposition method. First, 1.3 mol L^{-1} PbI_2 dissolved in DMF/DMSO (9.5:0.5 by volume) was stirred at 70 °C for 12 h. For the PbI_2 with SL solution, SL was added to 1.3 mol L^{-1} PbI_2 at various mass ratios from 0.1 % to 0.5 %. Warm PbI_2 without or with SL was spin-coated at 4000 rpm for 20 s, and then a drop of the mixed solution containing FAI:MABr:MACl (60 mg:6 mg) in 1 mL of IPA was added to the spinning substrate for 30 s. The as-prepared samples were annealed at 140 °C for 10 min. The fabrication of PTAA, C_{60}, BCP and Ag electrodes were detailed in Section 4.2.3.

6.2.3 Characterization

Thermogravimetric analysis (TGA) was conducted on a Discovery TGA (Mettler Toledo Instruments, Switzerland) under N_2 flow at a 10 ℃/min heating rate. Contact angle tests were performed via a JC2000D6 (Powereach) instrument. For CLSM images, a JMAT-S confocal laser scanning microscope (SouthPort Co., Ltd.) was used. The excitation wavelength was 445 nm, and the confocal pinhole size was set to 50 μm with a 10× objective. The measurement of FTIR spectra,

SEM, UV−vis spectra, UPS, XRD, PL spectra, TRPL, *J–V* curves, and EQE curves was detailed in Section 4.2.4. TPV and TPC measurements were detailed in Section 5.2.3.

6.3 Results and discussion

6.3.1 Improving the coverage of perovskite films

First of all, the TGA was conducted to explore the decomposition of SL. As illustrated in **Figure C1** in the Appendix C, when the temperature achieved about 60 ℃, there was a slight weight loss of about 1.8%, which should be due to the evaporation of water adsorbed by the SL. As the temperature increases, the weight could maintain above 95% until obvious degradation occurred at 180 ℃, suggesting that SL is stable and can remain in the perovskite films after the thermal annealing process at 140 ℃.

As shown in **Figure 6.1a**, the contact angle of the PbI_2 precursor solution on PTAA was 66 ± 4°, which means that the droplet was not well spread on the substrate. Thus, as shown in **Figure 6.1b**, perovskite films with poor coverage are often obtained, which can cause short-circuit problems after silver is deposited. Therefore, the limited active area hinders large-scale device development. According to the molecular structure illustrated in **Figure C2**, SL possesses hydrophobic alkyl chains and charged functional groups. After the addition of SL, benefiting from the affinity between the alkyl chains and PTAA, the contact angle decreased to 44 ± 3°, and the coverage of the perovskite films improved (**Figure 6.1c&d**). These findings demonstrate the efficacy of this strategy in enhancing the affinity between the perovskite precursor solution and the underlying hydrophobic transport layer.

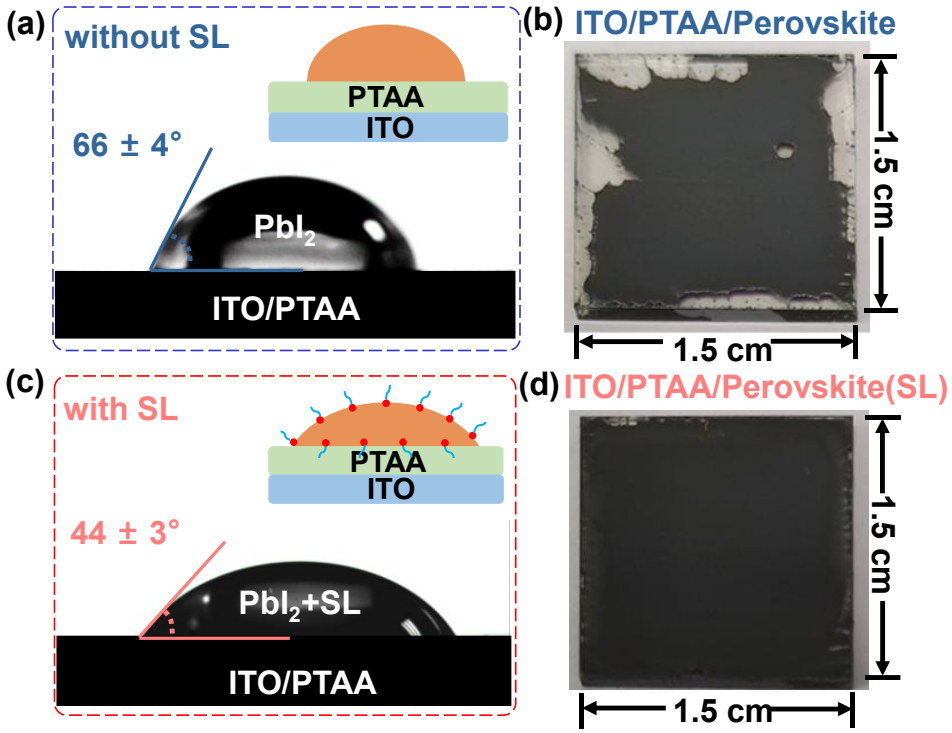


Figure 6.1 Contact angles of PbI_2 precursor solution (a) without SL and (c) with SL. Photographs of perovskite films (b) without SL and (d) with SL on PTAA.[165] Reprinted with permission from *ACS Appl. Mater. Interfaces* 2025, 17(31), 44481–44489. Copyright 2025 American Chemical Society.

6.3.2 Improving the quality of perovskite films

It is hypothesized that the C=O and P=O functional groups of SLS can serve as Lewis acids to coordinate with Pb^{2+}; therefore, FTIR spectroscopy was carried out to investigate the interactions between SL and PbI_2. As shown in **Figure 6.2a**, for SL, the peaks at 1739 cm^{-1} and 1232 cm^{-1} were assigned to the stretching vibrations of C=O and P=O, respectively.[166, 167] After mixing with PbI_2, the C=O peak shifted to a lower wavenumber of 1736 cm^{-1}, which is attributed to the coordination between the lone electron pair of C=O and the undercoordinated Pb.[25] The vibrational peak associated with the P=O bond shifted to a higher wavenumber of 1238 cm^{-1} because of the decreased spatial symmetry of PO_4^- after the coordination interaction with Pb^{2+}.[76] To further prove the interaction between SL and perovskite, the XPS of perovskite films without and with SL was carried out, as shown in **Figure C3**. In the control perovskite, the peaks at 143.4 and 138.5 eV are

assigned to Pb $4f_{5/2}$ and Pb $4f_{7/2}$, respectively; and the peaks at 631.0 and 619.5 eV are assigned to I $3d_{3/2}$ and I $3d_{5/2}$, respectively.[168] As the SL was added into perovskite, they both showed an approximately 0.1 eV shift, suggesting that the undercoordinated Pb^{2+} was passivated by C=O and P=O in SL.[154, 169] In addition to the passivation of the positively charged Pb^{2+}, the quaternary ammonium groups can passivate the negatively charged defects through electrostatic interactions, as illustrated in **Figure 6.2c**.[136, 170]

Owing to the dual effects of better coverage and passivation, perovskite films with better quality are expected. **Figure 6.2b** shows the SEM top-view and cross-sectional morphologies of the pristine perovskite film. Owing to the mismatched polarity and rapid crystallization, the growth of the perovskite grains was irregular, thereby leading to perovskite films with many pinholes. In contrast, the perovskite film with SL had preferentially oriented grains and fewer pinholes. With respect to the grain size, as shown in **Figure C4**, the pristine perovskite film had an average grain size of 258 ± 141 nm, whereas the average size of the perovskite film with SL increased to 349 ± 153 nm, which can be attributed to delayed perovskite growth controlled by the interaction between the SL and perovskite.[135]

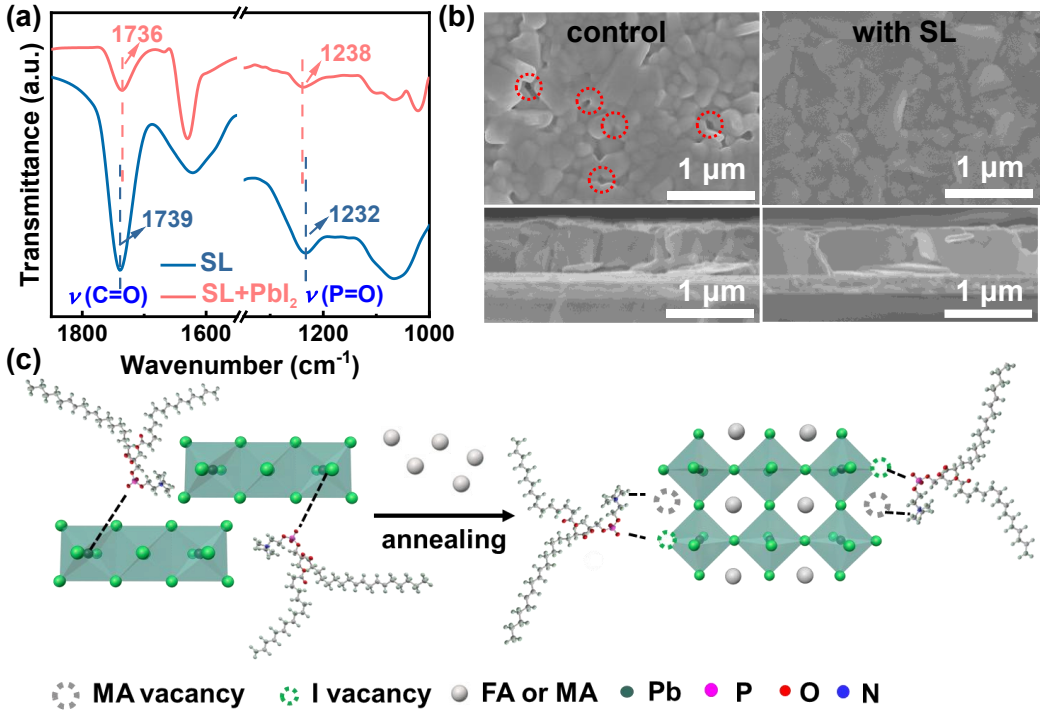


Figure 6.2 (a) FTIR spectra of SL and SL + PbI_2. (b) Top-view and cross-sectional SEM images of the perovskite films without and with SL. (c) Schematic illustration of the interactions between the perovskite and SL.[165] Reprinted with permission from *ACS Appl. Mater. Interfaces* 2025, 17 (31), 44481–44489. Copyright 2025 American Chemical Society.

The improved crystallinity was further confirmed by UV–vis spectra and XRD. **Figure 6.3a** shows that there was no obvious shift in the absorption edge; that is, the bandgap of the perovskite did not change, indicating that SL did not enter the perovskite lattice, which is consistent with the observation of the same diffraction peak positions in the XRD patterns in **Figure 6.3b**. The perovskite films with SL demonstrated a slight increase in the absorption intensity. The enhancement can be ascribed to more perovskite phases in the perovskite films with SL[171], which is consistent with the intensity changes in the XRD results. For the control perovskite film, the intensity of the PbI_2 XRD peak was stronger than that of the perovskite, whereas for the perovskite film with SL, the intensity of the perovskite peak was stronger with a narrower FWHM of (110) plane, which suggests that the perovskite with SL has better crystallinity and increased grain size than the control perovskite film. For control perovskite films, fast crystallization causes accumulation of perovskite on the surface of PbI_2, inhibiting further reaction between PbI_2 and

ammonium salts, which leads to residual PbI_2 in the perovskite. Nevertheless, the interaction between SL and PbI_2 can delay the perovskite crystalline, facilitating more reaction between PbI_2 and ammonium salts, which improves the transformation from PbI_2 to perovskite phase and decreases the amount of PbI_2. [140-142, 154]

The passivation effect of SL and improved perovskite film quality can decrease the N_t, which is determined by the SCLC method, as shown in **Figure 6.3c** and **3d**. The N_t was calculated according to **Equation 4.2**. The introduction of SL decreased the N_t of electron and hole from 1.14×10^{16} cm^{-3} to 8.54×10^{15} cm^{-3} and from 2.85×10^{16} cm^{-3} to 1.89×10^{16} cm^{-3}, respectively. This result confirms the passivation of defects with different charge states.[172]

In addition, given the small amount of SL (0.18 mg/mL, 0.3 wt‰ PbI_2), to evaluate whether SL indeed participates in charged defect passivation, the difference between the passivated trap and the number of molecules in a whole device was calculated. The results above revealed that the decrease in N_t of electron was 2.86×10^{15} cm^{-3}. Thus, for a whole perovskite layer with a volume of 1.20×10^{-4} cm^3, the number of passivated electron defects was 3.45×10^{11}. For the fabrication of perovskite films, 40 μL of precursor solution with 0.18 mg/mL SL was applied, so the number of SL molecules was 5.72×10^{15}, which was four orders of magnitude greater than the number of passivated defects. Similarly, the number of passivated hole defects was 1.16×10^{12} and the number of SL molecules was three orders of magnitude greater than it. Thus, even if, during spin-coating, not all the precursor solutions were applied, SL is sufficient and indeed participates in charged defect passivation.

Furthermore, the Urbach energies (E_Us, shown in **Figure C5**) of perovskite films without and with SL were evaluated via **Equation 6.1**[173, 174]:

$$\alpha=\alpha_0 exp(\frac{h\upsilon}{E_U}) \tag{6.1}$$

where α is the absorption coefficient and α_0 is a constant. The results indicate a decrease in the E_U value from 70 to 65 meV after the doping of SL, which suggests that the energetic disorder was suppressed due to decreased defects and improved crystallinity.

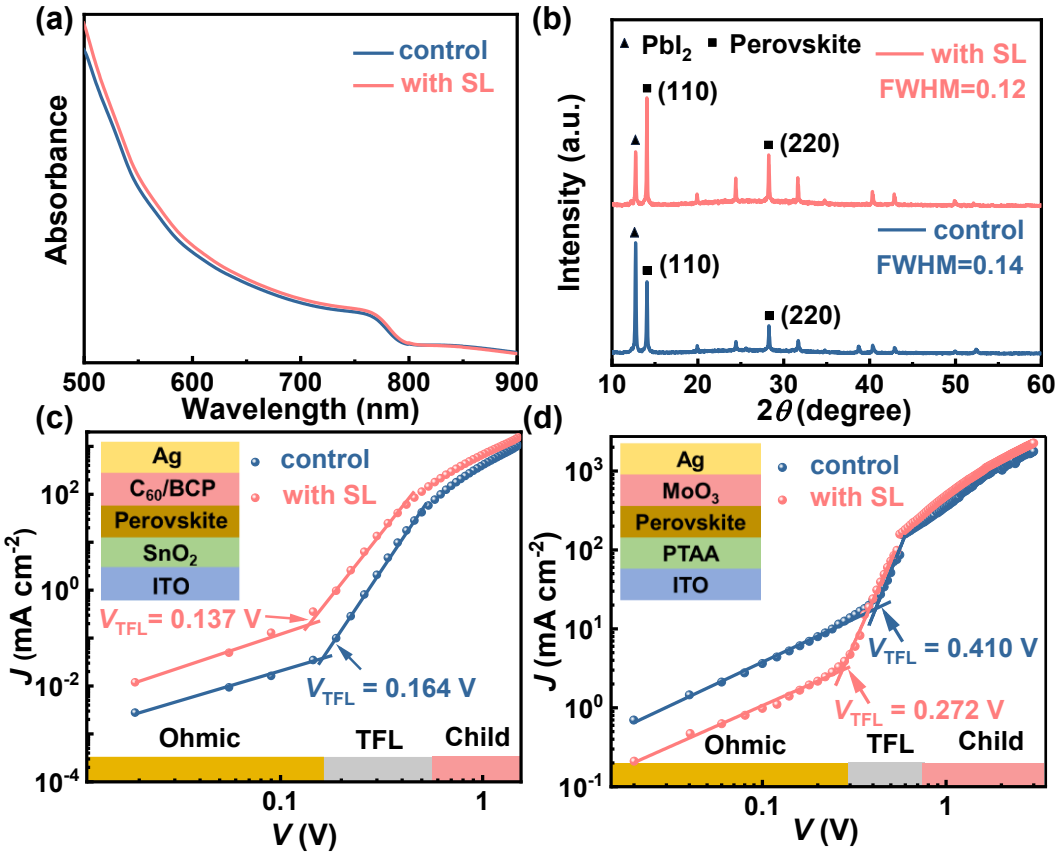


Figure 6.3 (a) UV–vis spectra of perovskite films without and with SL. (b) XRD patterns of perovskite films without and with SL. *J-V* curves measured in the dark for (c) electron-only and (d) hole-only devices based on perovskite films without and with a SL for SCLC analysis. [165] Reprinted with permission from *ACS Appl. Mater. Interfaces* 2025, 17 (31), 44481–44489. Copyright 2025 American Chemical Society.

To explore carrier recombination in the perovskite films, a series of fluorescence characterizations were performed on the perovskite films on glass substrates. As shown in **Figure 6.4a**, compared with that of the pristine perovskite film, the PL intensity of the perovskite films with SL significantly increased, suggesting that the nonradiative recombination was significantly suppressed due to decreased defects, which can also be proven by the TRPL measurements. A two-component exponential decay function was employed to fit the TRPL data shown in **Figure 6.4b**, and the detailed parameters are listed in **Table C1**. The fast decay component (τ_1) is assigned to the nonradiative recombination of charge carriers caused by trap states, and the slow decay component

(τ_2) is assigned to the radiative recombination of charge carriers in the bulk perovskite.[132, 175, 176] The pristine film had a τ_1 of 258.9 ns with an f_1 of 26.1% and a τ_2 of 688.0 ns with an f_2 of 73.9%. In contrast, the perovskite film with SL has a decreased f_1 of 12.4% and an increased τ_2 of 1259.5 ns with an increased f_2 of 87.6%.

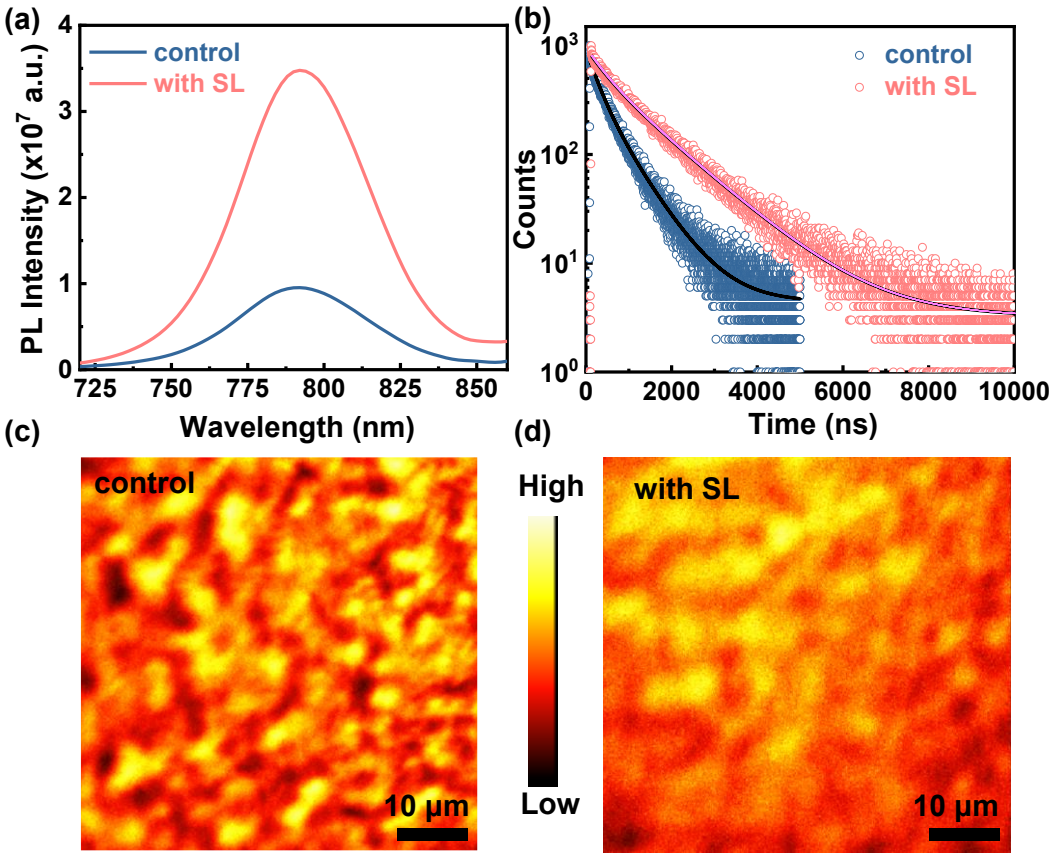


Figure 6.4 (a) Steady-state PL spectra of perovskite films without and with SL on glass substrates. (b) TRPL of perovskite films without and with SL on glass substrates. CLSM images of perovskite films (c) without and (d) with SL on glass substrates under ambient conditions.[165] Reprinted with permission from *ACS Appl. Mater. Interfaces* 2025, 17 (31), 44481–44489. Copyright 2025 American Chemical Society.

These results further indicate that SL can passivate defects and inhibit nonradiative recombination. **Figure 6.4c & 6.4d** shows CLSM images of perovskite films without and with SL. For the control perovskite film, there were many pinholes, and at these sites, the fluorescence was

quenched, whereas the average fluorescence intensities of the perovskite films with SL were greater due to fewer pinholes, which agreed well with the PL and TRPL results.

Beyond the decreased defects, the influence of SL on the energy levels of perovskite layers was explored. As the UPS results displayed in **Figure C6** and the corresponding energy levels listed in **Table C2**, after the addition of SL, there was no difference in the valence and conduction band energy levels, while the work function decreased slightly, which can facilitate the electron transport between perovskite and the electron transport layers. The decreased work function should be contributed to the generation of interfacial dipoles by the zwitterionic moieties of SL on the perovskite surface.

6.3.3 Improving the device performance

To investigate the photovoltaic performance, devices with a structure of ITO/PTAA/perovskite/C_{60}/BCP/Ag were fabricated. The *J–V* curves are shown in **Figure 6.5a**, and the detailed parameters are listed in **Table 6.1**. The concentration of SL was varied from 0 to 0.5 wt‰, and the optimum concentration was determined to be 0.3 wt‰ (**Table C3**). The control device achieved the highest PCE of 20.12%, with a V_{OC} of 1.08 V, a J_{SC} of 23.07 mA cm^{-2} and an FF of 80.94%. After the addition of 0.3 wt‰ SL, the V_{OC} improved to 1.13 V, the J_{SC} improved to 24.62 mA cm$^{-2,}$ and the FF improved to 82.78%, resulting in a maximum PCE of 22.93%. As shown in **Figure 6.5b**, the average PCE of 21.44% for the devices with SL was higher than that of 19.18% for the control devices. The improved performance can be attributed to decreased nonradiative recombination and better perovskite crystallinity. The steady-state photocurrent and power conversion efficiency of the devices at the maximum power point were tracked under continuous light illumination for 600 s, as shown in **Figure 6.5c**. Steady-state output efficiencies of 19.31% and 22.57% can be achieved for the control device and the devices with SL, with photocurrents of 22.86 and 23.14 mA cm^{-2}, respectively. These results are consistent with the results extracted from the *J–V* curves, confirming the reliability of the measured results. The device charge collection efficiency was investigated via EQE measurements, as shown in **Figure 6.5d**. The integrated circuit current density (J_{int}) values showed a deviation of merely 5% from the measured J_{SC} values, which suggests that the results obtained from the *J–V* curves are reliable. In addition, the hysteresis effect of the Pero-SCs was analyzed through the characterization of forward and reverse *J-V* curves (**Figure C7**) and the detailed photovoltaic parameters are displayed in **Table C3**. Furthermore, the

hysteresis effect was investigated and the hysteresis index (HI) is calculated by (PCE_{FS} – PCE_{RS})/PCE_{FS}. Compared with the control device, the HI decreased dramatically from 0.15 to 0.03. As reported, the hysteresis in Pero-SCs are usually on account of the non-radiative recombination centers and ion migration in perovskite.[177-179] Consequently, the reduced hysteresis should be contributed to the inhibited non-radiative recombination due to the interaction between the functional groups of SL and the perovskite.

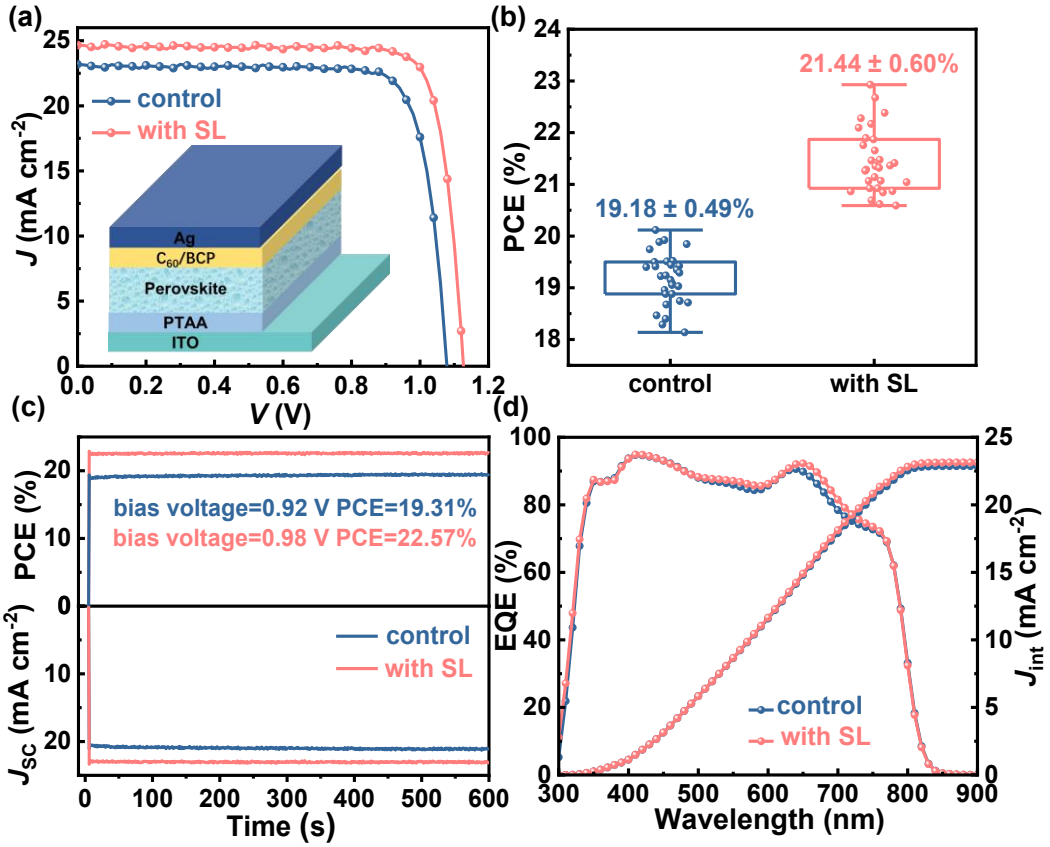


Figure 6.5 (a) *J–V* curves, (b) statistical PCEs analyzed from 30 individual cells in each group, (c) steady-state outputs, (d) EQE curves of the control and SL-modified devices.[165] Reprinted with permission from *ACS Appl. Mater. Interfaces* 2025, 17 (31), 44481–44489. Copyright 2025 American Chemical Society.

Table 6.1 Photovoltaic parameters of champion Pero-SCs without and with SL. [165] Reprinted with permission from *ACS Appl. Mater. Interfaces* 2025, 17 (31), 44481–44489. Copyright 2025 American Chemical Society.

	V_{OC}(V)	J_{SC} (mA cm^{-2})	FF (%)	PCE (%)
control	1.08	23.07	80.9	20.12
	1.05 ± 0.02	23.31 ± 0.65	78.1 ± 2.3	19.18 ± 0.49
with SL	1.13	24.62	82.8	22.93
	1.10 ± 0.02	24.21 ± 0.49	80.8 ± 1.2	21.44 ± 0.60

The dark current can be utilized to explore charge carrier transport. As shown in **Figure 6.6a**, the dark *J–V* curves show typical diode characteristics. The leakage current density of the Pero-SC with SL was lower than that of the control, confirming improved charge transfer and less trap-assisted recombination.[146]

As shown in **Figure 6.6b**, the V_{OC} as a function of P_{light} was measured to investigate the charge carrier recombination. The type of recombination in Pero-SCs can be determined by the ideality factor *n,* which is calculated via Equation 4.3. *n* will exceed 1 if trap-assisted recombination occurs in addition to Langevin recombination (n=1). [143, 144] After the addition of SL, *n* decreased from 1.96 to 1.17, indicating that trap-assisted recombination was effectively suppressed due to reduced trap densities, which is consistent with the SCLC results.

TPV and TPC tests were performed to investigate the charge carrier dynamics, as illustrated in **Figure 6.6c & 6.6d**. The τ_R increases from 10.32 μs for the control device to 20.53 μs for the device with SL, indicating suppressed carrier recombination and effective passivation of defects in the perovskite.[158, 159] The τ_T in the Pero-SCs decreased from 0.32 to 0.15 μs with the addition of SL, suggesting a decrease in the number of defects in the perovskite film and an improvement in the carrier transport ability[159].

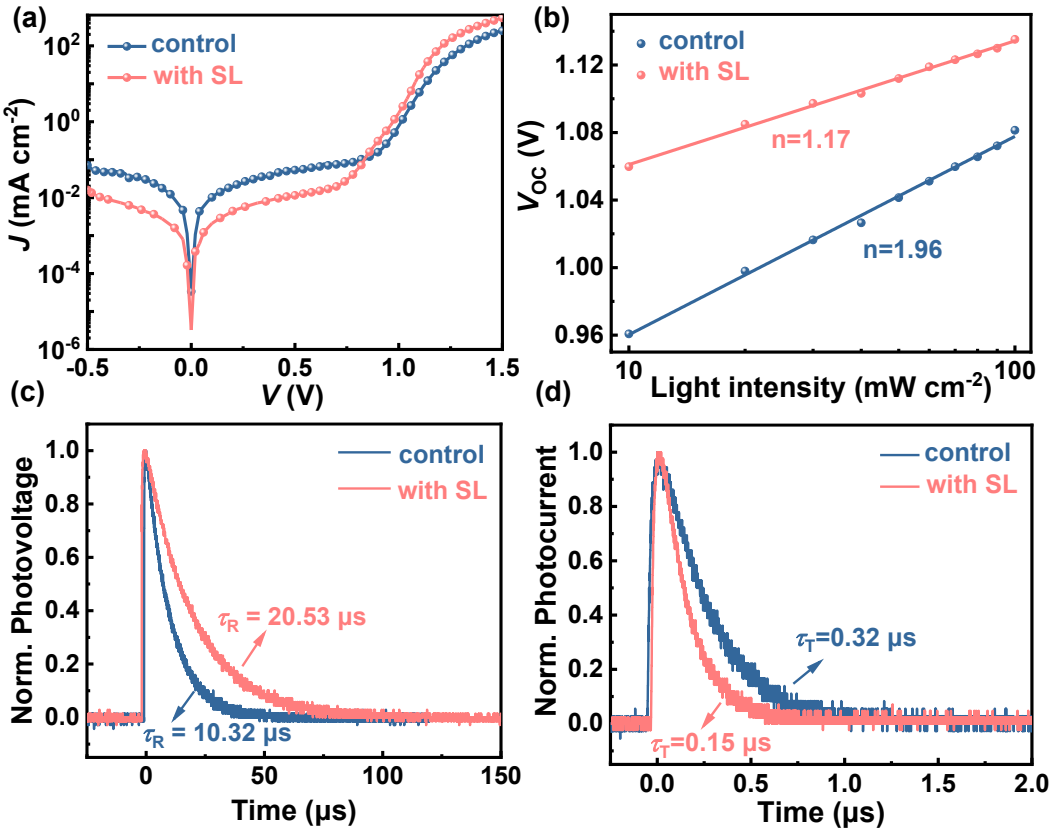


Figure 6.6 (a) Dark *J-V* curves, (b) plots of V_{OC} versus light intensity, (c) normalized TPV and (d) normalized TPC curves of the control and SL-modified devices.[165] Reprinted with permission from *ACS Appl. Mater. Interfaces* 2025, 17 (31), 44481–44489. Copyright 2025 American Chemical Society.

6.3.4 Potential of SL in practical applications

To explore the potential of SL for practical applications, devices with an active area of 1.1 cm^2 (**Figure 6.7a**) were fabricated, and a *J-V* curve is shown in **Figure 6.7b**. The optimal device exhibited the best PCE of 18.32% with a V_{OC} of 1.10 V, a J_{SC} of 21.82 mA cm^{-2}, and an FF of 77.4%. Remarkably, scaling up the device area by nearly 10 times did not result in a significant decrease in the efficiency of the Pero-SCs with SL, emphasizing the promising potential of SL for large-area device applications.

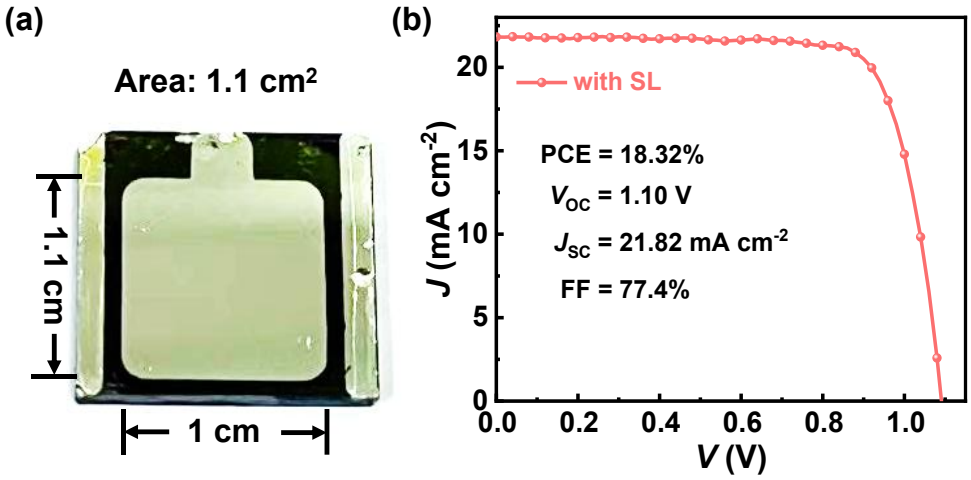


Figure 6.7 (a) Photo of a device with an effective area of 1.1 cm^2. (b) *J-V* curve of a 1.1 cm^2 Pero-SC doped with SL.[165] Reprinted with permission from *ACS Appl. Mater. Interfaces* 2025, 17 (31), 44481–44489. Copyright 2025 American Chemical Society.

In conjunction with the PCE, the stability of Pero-SCs plays a crucial role in their practical implementation. The unencapsulated Pero-SCs were stored in air at an RH ranging from 40%~50%, and the evolution of the PCE over time was monitored, as illustrated in **Figure 6.8a**. The PCE of the control device decreased to 38% of its initial value after 800 hours. In contrast, the device with SL maintained 74% of its initial PCE after the same duration, demonstrating notably enhanced stability. **Figure 6.8b** shows the deterioration of perovskite films in air with an RH of 40%~50%. After 5 days, the color of the undoped perovskite film changed from black to yellow due to degradation. However, perovskite films doped with SL displayed negligible changes. In addition, from the ^{1}H-NMR spectrum in **Figure C8**, the shift in the characteristic signal of FAI from 8.65 ppm to 8.70 ppm indicates that hydrogen bonding formed between FAI and SL, which favors an improvement in perovskite stability. [180] These results demonstrate a clear improvement in stability, which is attributed to the improved quality of the perovskite films with the addition of SL.

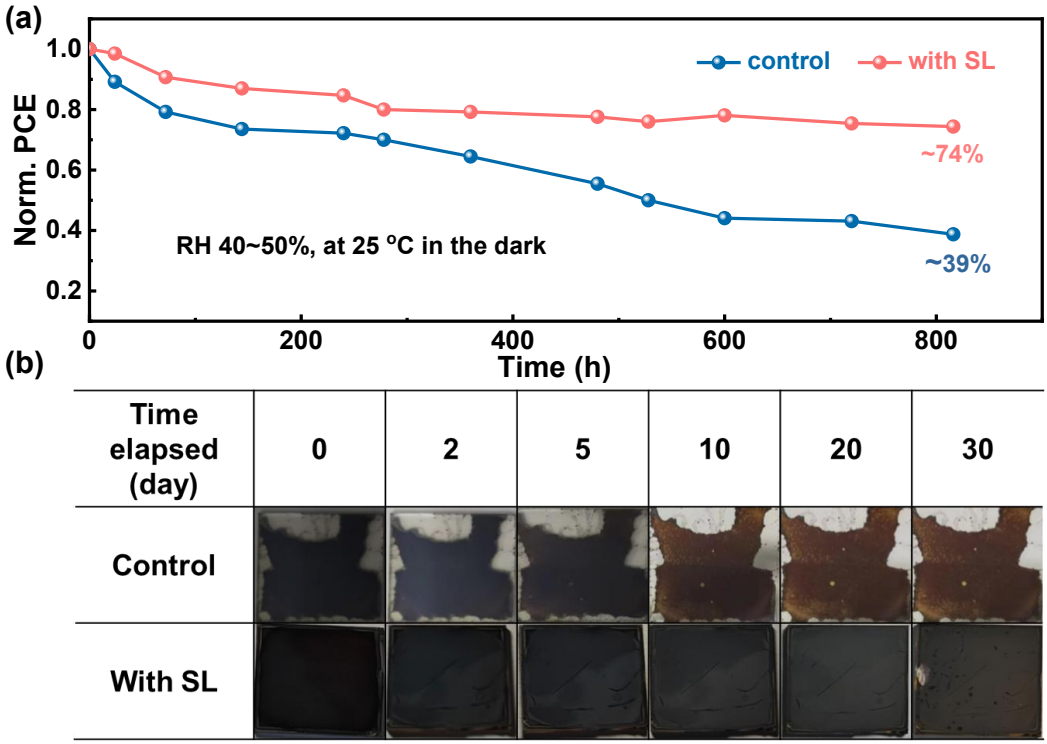


Figure 6.8 (a) PCE evolution of unencapsulated Pero-SCs stored in air with RHs ranging from 40%~50%. (b) Photographs of perovskite films over time stored in air with RHs ranging from 40%~50%.[165] Reprinted with permission from *ACS Appl. Mater. Interfaces* 2025, 17 (31), 44481–44489. Copyright 2025 American Chemical Society.

6.4 Conclusions

In summary, we presented the incorporation of SL into a perovskite precursor solution to fabricate high-quality perovskite films. SL improved the device performance in two ways: (1) SL promoted the affinity between the hydrophobic PTAA and the hydrophilic precursor solution to improve the coverage of perovskite films, which is promising for the fabrication of large-area devices. (2) Different functional groups passivate different defects in the perovskite, which controls the growth of the perovskite and decreases nonradiative recombination. The highest PCE of the *p-i-n* Pero-SCs increased from 20.12% to 22.93% with the addition of SL, and a large-area optimized device achieved a PCE of up to 18.32%. Furthermore, the humidity stability of Pero-SCs was improved through the addition of SL.

Chapter 7
Synergistic Effect of Guanidinium Iodide and Cesium Iodide for Enhanced Perovskite Crystal Quality and Device Performance in Hybrid Perovskite Solar Cells

7.1 Introduction

The long-term device stability in harsh environments such as high humidity is one of the indicators to judge the potential of Pero-SCs' commercialization. Many studies have implied that hydrogen bonds can be considered as a powerful tool for improving the PCE and stability of Pero-SCs[181-183] along with affecting charge transport properties[182, 184] and influencing the orientation of the organic cations and phase transitions[182, 183, 185]. In the perovskite, the hydrogen bond, N-H···I, exists between the organic cations and the surrounding inorganic $[PbI_6]^{4-}$ lattice. Compared to the MA^+ and FA^+, the GA^+ can provide an increased number of hydrogen bonds owing to the abundant ammonium groups in its molecular structure[186], thus increasing the formation energy of halide vacancies and improving the perovskite structural stability.[85] However, the slightly larger radius (278 pm) of GA^+ will expand the perovskite lattice, causing a deviation from the desirable tolerance factor for a stable 3D perovskite phase and a decrease in the device performance.[187] To solve this conflict, smaller cations, such as Cs^+ can be employed to alleviate the expansion stress.[85, 94] For Cs-based perovskites, the low PCE and instability are commonly attributed to the phase separation and transition into a undesired δ-phase, which is mainly induced by ion migration. Fortunately, the hydrogen bonds between the GA^+ and the $[PbI_6]^{4-}$ octahedron can stabilize the lattice and GA^+ has a dipole moment of nearly zero, which inhibits the I^- migration and alleviates the hysteresis effect.[87, 188-190] Consequently, the cooperation of GA^+ and Cs^+ can not only bring out their respective strengths but also make up for each other's shortcomings, thus improving the device PCE and stability.

So far, the co-doping of GA^+ and Cs^+ in mixed-cation perovskites has been realized through different approaches.[91, 93-95] For instance, in the anti-solvent deposition method, GA^+-containing precursor solutions for obtaining mixed-cation perovskites with tailored crystal structure were prepared by mixing a $FA_{0.83}Cs_{0.17}PbI_3$ precursor solution and GAI/DMSO precursor solution in a desired volume ratio.[94] In comparison to the one-step method, in the two-step sequential method, the optimization of each precursor can be realized individually, which allows a better control of the perovskite crystallization.[95, 191] Lu et.al incorporated Cs^+ in the PbI_2 precursor solution in the first step to induce the transition from

δ-$CsPbI_3$ to α-phase perovskite and then incorporated GA^+ in the FAI/MABr/MACl precursor solution in the second step to eliminate pinholes and enhance grain boundary migration.[95]

In this work, through the two-step sequential deposition method, GAI and CsI were introduced into the PbI_2 precursor solution simultaneously to reach higher-quality perovskite films with better stability. On the premise of not destroying the stable 3D perovskite, the GA^+ and Cs^+ were introduced into the A-sites in the perovskite lattice successfully. The hydrogen bonds generated between GAI and $[PbI_6]^{4-}$ octahedral framework can stabilize the perovskite structure and with the assistance of Cs^+, the negative expansion stress caused by the large size of GA^+ was relieved. Finally, perovskite films with larger grain sizes, less pinholes and preferred-orientation were obtained, reducing the nonradiative recombination. Based on the optimized perovskite films, a champion PCE of 24.29% can be achieved with a significantly improved V_{OC} of 1.17 V. Most importantly, the unencapsulated optimized device can maintain 95% of the initial efficiency after about 5200 h in N_2 atmosphere and when placed in air with a high RH of 80 ± 5%, the encapsulated device can still maintain 86% of the initial PCE after 1000 h, suggesting better stability compared to the control device.

7.2 Experimental methods

7.2.1 Materials

GAI was purchased from Advanced Election Technology Co., Ltd. SnO_2 colloid precursor (12% in H_2O colloidal dispersion), CsI, bis(trifluoromethane) sulfonimide lithium salt (Li-TFSI) and 2,2',7,7'-tetrakis[*N,N*-di(4-methoxyphenyl)amino]-9,9'-spirobifluorene (Spiro-OMeTAD) were purchased from Xi'an Yuri Solar Co., Ltd. [6, 6]-phenyl-C_{61}-butyric acid methyl ester ($PC_{61}BM$) was purchased from 1-Material Co. Ltd. The details for ITO, PbI_2, FAI, MACl, C_{60} and BCP are provided in Section 4.2.1 and the details for MABr are detailed in Section 6.2.1.

7.2.2 Fabrication of devices

A thin film of SnO_2 nanoparticles was spin-coated on the substrate at 3000 rpm for 30 s and annealed in ambient air at 150 ℃ for 30 min. The perovskite films were fabricated by a two-step deposition method. For the pristine PbI_2 precursor solution, 599.3 mg mL^{-1} PbI_2 was dissolved in DMF/DMSO (9.5: 0.5 by volume). For the precursor solution with CsI and GAI, 599.3 mg mL^{-1} PbI_2, 16 mg mL^{-1} CsI and GAI were dissolved in DMF/DMSO (9.5: 0.5 by volume). The concentration of GAI was varied from 0.5-2 mg mL^{-1}. The two precursor solutions were stirred at 70 ℃ for 12 h. The warm PbI_2 was

spin-coated at 4000 rpm for 20 s, and then a drop of the mixed solution containing FAI: MABr: MACl (60 mg: 6 mg: 6 mg) in 1 mL of IPA was added to the spinning substrate for 30 s. A layer of PEAI (0.5 mg ml^{-1}) was spin-coated on the perovskite at a spin rate of 3000 rpm for 30 s. Then, the spiro-OMeTAD was deposited at a spin rate of 3000 rpm for 30 s. The spiro-OMeTAD solution was prepared by dissolving 72.3 mg of spiro-OMeTAD, 17.5 μL of Li-TFSI solution (520 mg Li-TFSI in 1 mL acetonitrile), and 28.8 μL of 4-tertbutylpyridine in 1 mL of chlorobenzene. Finally, 8 nm of MoO_3 and 100 nm of Ag were deposited by thermal evaporation. For the electron-only devices, $PC_{61}BM$ solution (7 mg mL^{-1} in chloroform) was spin-coated on the perovskite films at a speed of 3000 rpm for 30 s.

7.2.3 Characterization

The SEM, FTIR, XRD, AFM, KPFM, UV−vis absorbance, PL, TRPL, *J–V*, EQE, and EIS measurements are detailed in Section 4.2.4. The TPV measurement is detailed in Section 5.2.4. The CLSM imaging is detailed in Section 6.2.3.

7.3 Results and discussion

7.3.1 Improved device performance and stability

The performance of Pero-SCs with a structure of ITO/SnO_2/Perovskite/Spiro-OMeTAD/MoO_3/Ag was investigated. The devices without and with GAI and CsI were denoted as the control and the GCP-SC, respectively. Although GAI can increase the perovskite lattice energy and stabilize the perovskite lattice, excessive GAI will cause heavy lattice expansion and distortion, which will hinder the carrier transport, causing a sharp drop in the FF. The *J-V* curves shown in **Figure D1** and the detailed photovoltaic parameters listed in **Table D1 and D2** indicate that the optimal concentrations of GAI and CsI were 1.0 mg/mL and 16.0 mg/mL, respectively. **Figure 7.1a** shows the *J-V* curves of the best results of the control and the GCP-SC and the detailed parameters are listed in **Table 7.1**. The control achieved a PCE of 22.66% with a V_{OC} of 1.11 V, a J_{SC} of 25.10 mA/cm^2 and an FF of 81.11%, whereas the PCE of the GCP-SC was as high as 24.29% with a significantly improved V_{OC} of 1.17 V, a J_{SC} of 25.08 mA/cm^2 and an FF of 82.43%. **Figure 7.1b** shows the EQE curves and the integrated current densities (J_{int}) obtained from the curves were 24.15 and 24.42 mA/cm^2 for the control and the GCP-SC, respectively, indicating a deviation of less than 5% from the measured J_{SC} values obtained from the *J-V* curves, suggesting that the results should be reliable. From the distributions illustrated in **Figure D2**, **Figure 7.1c** and **7.1d**, all the average parameters of the GCP-SC were improved.

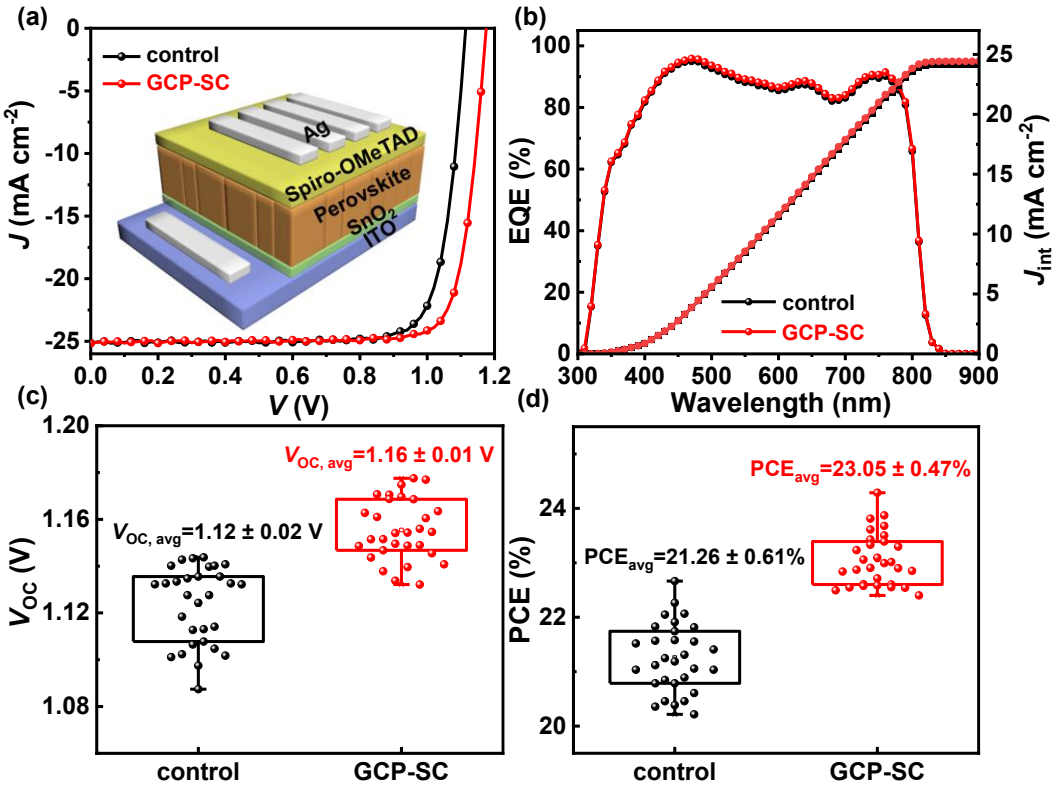


Figure 7.1 (a) $J-V$ curves of the champion Pero-SCs. (b) EQE curves and J_{int} of the Pero-SCs. (c) V_{OC} and (d) PCE distribution analyzed from 30 cells.

Table 7.1 Photovoltaic parameters of Pero-SCs. The concentrations of CsI and GAI were 16.0 and 1.0 mg mL^{-1}, respectively. The average values were calculated based on 30 cells.

	V_{OC} (V)	J_{SC} (mA cm^{-2})	FF (%)	PCE (%)
control	1.11	25.10	81.1	22.66
	1.12 ± 0.02	23.91 ± 0.72	79.1 ± 2.9	21.26 ± 0.61
GCP-SC	1.17	25.08	82.4	24.29
	1.16 ± 0.01	24.47 ± 0.40	81.5±1.0	23.05 ± 0.47

Then the effect of GAI and CsI on the stability of perovskite films and devices was comprehensively evaluated. **Figure 7.2a** shows the stability of the devices under N_2 atmosphere. After 3300 hours, the PCE of the unencapsulated control device dropped to 71% of its original value, whereas the GCP-SC maintained more than approximately 95% of the initial efficiency after about 5200 h, which

demonstrates its superior stability. To evaluate the humidity stability, considering the high hygroscopicity of Li^+ in Spiro-OMeTAD, the devices were encapsulated with UV curing adhesive and placed in air with a high RH of 80 ± 5%. From **Figure 7.2b**, the GCP-SC can still maintain approximately 86% of the initial PCE after 1000 h, while the control only kept 68%. In addition, the decomposition of the perovskite films without and with GAI in air with a RH of 30~40% was tracked. As shown in **Figure 7.2c**, the perovskite film with GAI and CsI has negligible change after 40 days, while the control perovskite film turned white after 10 days and the yellow phase appeared after 30 days, indicating the perovskite degraded into PbI_2 under the invasion of water and oxygen.

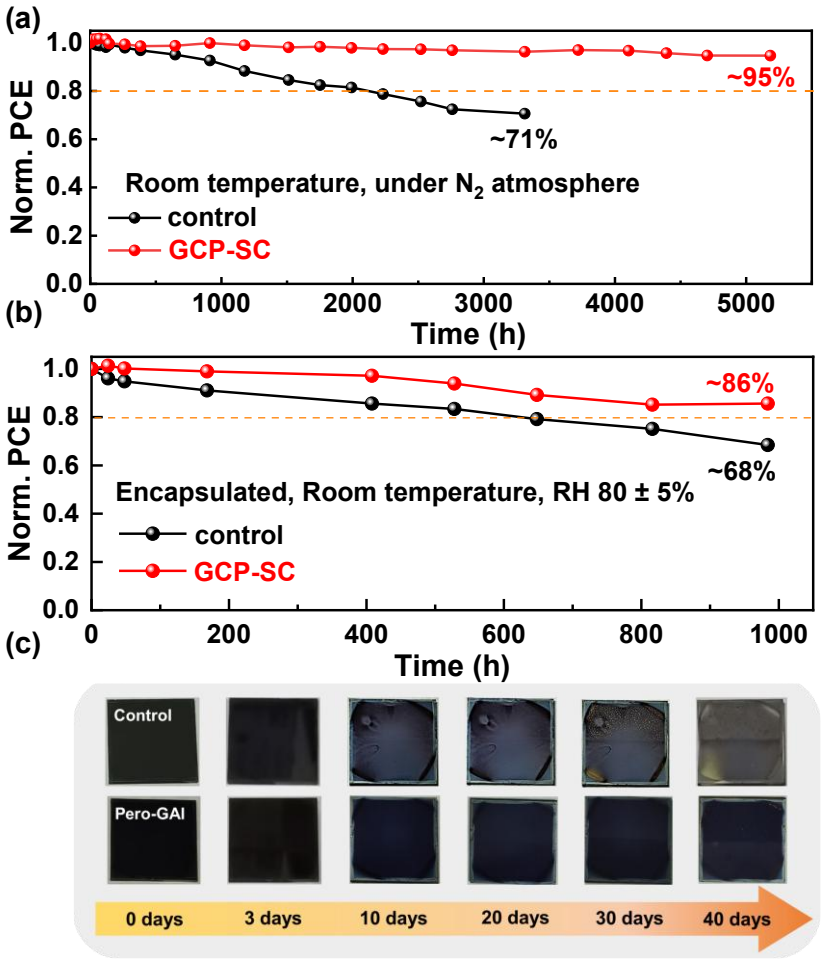


Figure 7.2 PCE evolution of (a) unencapsulated devices in N_2 (b) encapsulated devices stored in air with an RH of 80–85%. (c) Photographs of different perovskite films over time. All the samples were stored in the dark.

7.3.2 High-quality perovskite films

FTIR was applied to investigate whether hydrogen bonds form between GAI and PbI_2, as shown in **Figure 7.3a.** The peaks at 3151, 3235, 3317 and 3402 cm^{-1} are assigned to the stretching vibration absorption of the N-H.[192] After GAI was doped into PbI_2, these peaks were shifted significantly to 3184, 3256, 3328 and 3426 cm^{-1}, respectively, indicating the existence of the hydrogen bonds between PbI_2 and GAI.[193] Following from the FTIR results, the perovskite crystallization process is depicted in **Figure 7.3b**. GAI was introduced into the PbI_2 precursor solution and the hydrogen bonds between the H atoms of GAI and I atoms of PbI_2 could assist to stabilize the $[PbI_6]^{4-}$ octahedral frame, which favors the diffusion of organic cations such as FA^+ and MA^+ during the perovskite formation. In addition, to relieve the lattice expansion caused by the entrance of large cations into the perovskite lattice, Cs^+, a smaller cation, was introduced to regulate the growth of high-quality perovskite films.

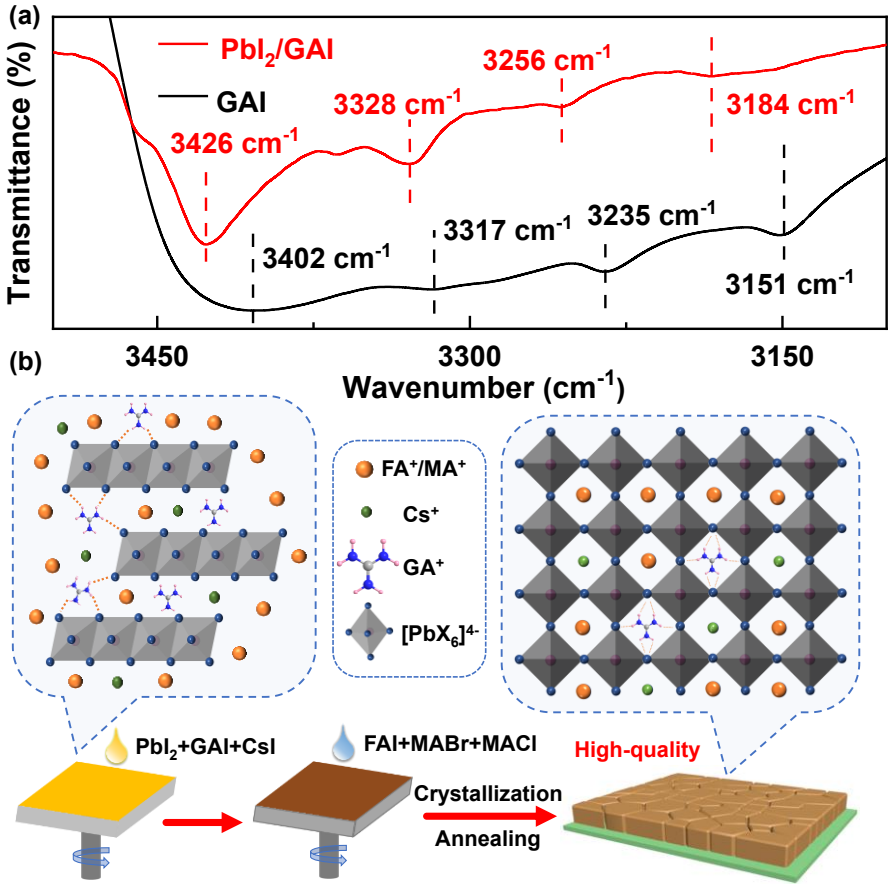


Figure 7.3 (a) FTIR spectra of GAI and GAI+PbI_2. (b) Schematic diagram of perovskite film fabrication.

To identify the reasons for the significant improvement in the device performance after the addition of GAI and CsI, the perovskite films were characterized. **Figure D3a and D3b** display the XRD patterns of perovskite films with different concentrations of GAI. After the addition of CsI, the diffraction peak at 14.08° assigned to the main (110) crystal plane of the perovskite shifted to a larger angle, which indicates shrinkage of the perovskite crystal structure caused by the replacement of FA^+ with the smaller Cs^+. Then the introduction of large GA^+ expands the perovskite crystal structure and the (110) peak shifted back. The peak shift confirms that both Cs^+ and GA^+ were incorporated into the A-sites of the perovskite lattice, which is consistent with the UV-vis spectra in **Figure D3c** and the corresponding Tauc plots in **Figure D3d**. Compared with the bandgap of pristine perovskite (1.53 eV), the perovskite with GAI and CsI (denoted as GCP) has a slightly wider bandgap (1.55 eV). In terms of the conversion from PbI_2 to perovskite, after the addition of GAI and CsI, the ratio of perovskite to PbI_2 increased, further indicating that GAI can stabilize the $[PbI_6]^{4-}$ octahedral frame and promote the perovskite formation, as illustrated in **Figure 7.3b**. The decreased PbI_2 will be beneficial to the long-term device stability. Moreover, from **Figure D3c**, for GCP, an enhanced absorption can be observed, indicating a stronger photon collection capability, which results in a higher average J_{SC} as shown in **Table 7.1** and **Figure D2a**.

SEM was carried out to investigate the influence on perovskite morphology. As shown in the SEM image in **Figure 7.4a**, the pristine perovskite film had obvious pinholes between grains with an average size of 433 ± 141 nm (**Figure D4a**). By contrast, for the perovskite treated with CsI and GAI (**Figure 7.4b**), the pinholes disappeared, and the average grain size was increased to 586 ± 234 nm (**Figure D4b**). The enlarged grain size can be attributed to the formation of perovskite crystal seeds containing GA^+ and Cs^+, which may decrease nucleation free energy and facilitate the perovskite crystallization.[194-196] From the cross-sectional images in **Figure 7.4c and 7.4d**, after the introduction of GAI and CsI, the perovskite grains illustrated a more uniform packing. Larger grains, less grain boundaries and preferentially oriented grain packing are conducive to improving the device stability and the carrier transfer and to decreasing the defect density of the perovskite films.

To quantify the influence of CsI and GAI on the trap density (N_t) of the perovskite films, the SCLC method was employed with the device structure of ITO/SnO_2/Perovskite/$PC_{61}BM$/Ag. As shown in **Figure 7.4e**, the *J-V* curves can be divided into three regimes, the linear ohmic response region under low bias voltage, the trap filling limited region under middle bias, where the current density increases rapidly as the traps are filled by electrons and the space charge-limited region with no traps at high bias

described by the Mott-Gurney law. The voltage at the point where the current density rises rapidly because the traps are filled with charges is the trap filling limit voltage (V_{TFL}), and the N_t can be calculated by **Equation 4.2**. Through fitting, V_{TFL} of the control and GCP-SC were 0.79 V and 0.61 V, respectively, and the N_t decreased from 3.0×10^{16} to 2.3×10^{16} cm^{-3}. As shown in **Figure 7.4f**, the E_Us of different films were calculated, which can be used to judge the degree of electronic disorder in the perovskite. The E_Us of the pristine perovskite film and GCP are 67.3 and 57.1 meV, respectively, calculated by **Equation 6.1.** The decrease in the E_U represented a reduction in the degree of electronic disorder due to less defects in the perovskite films formed with GAI and CsI.

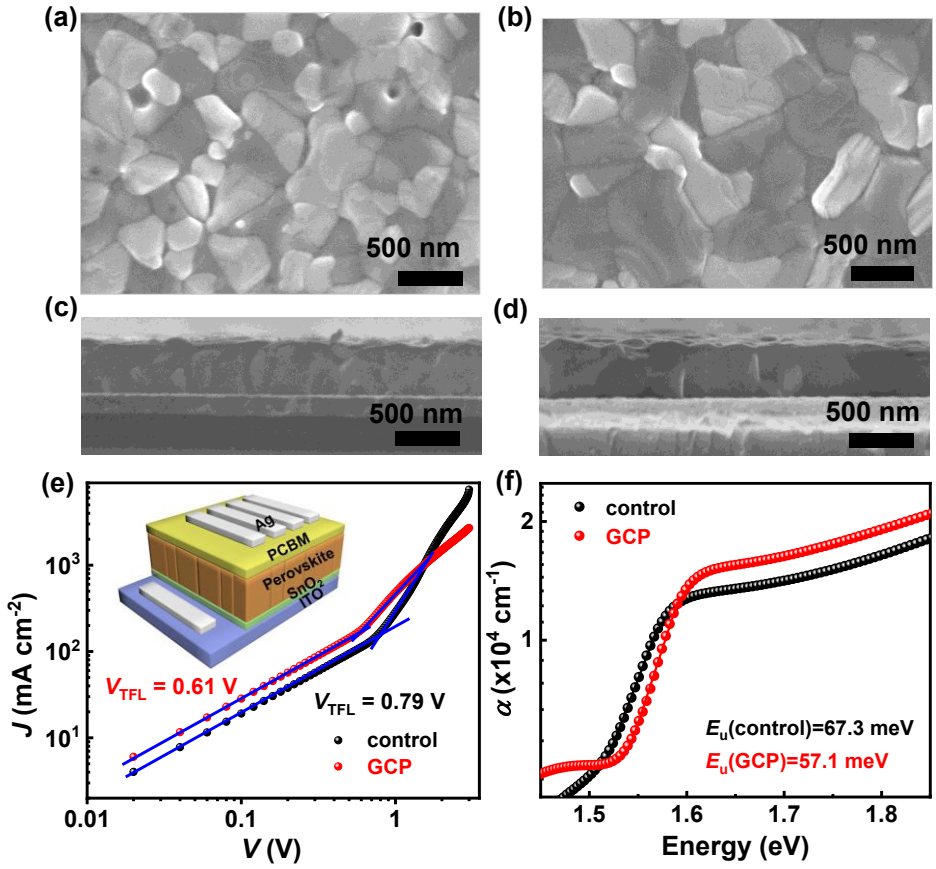


Figure 7.4 Top-view SEM images of (a) the pristine perovskite film and (b) GCP film. Cross-sectional SEM images of (c) the pristine perovskite film and (d) GCP film. (e) $J-V$ curves of electron-only devices based on different perovskite films. (f) Absorption coefficient-photon energy plots of different perovskite films.

From the *J-V* results, significant improvement in the V_{OC} was observed. The V_{OC} mainly depends on the splitting of the quasi-fermi level, and non-radiative recombination induced by defects will reduce the splitting of the quasi-Fermi level, resulting in voltage loss. To explore the nonradiative recombination in different perovskite films, a series of characterizations were employed. **Figure 7.5a** shows the steady-state PL spectra of different perovskite films deposited on glass. Compared with the pristine perovskite film, the PL intensity of the GCP film had a significant enhancement, indicating less nonradiative recombination. Then, TRPL (**Figure 7.5b**) was carried out to explore the recombination of the photogenerated carriers. A two-component exponential decay function (**Equation 4.1**) was employed to fit the TRPL spectra. The fast (τ_1) and slow (τ_2) decay components are assigned to the nonradiative recombination of carriers caused by trap states at the interfaces and the radiative recombination of charge carriers in the bulk perovskite, respectively. [76, 132] The detailed fitting parameters are listed in **Table D3**. In comparison to the pristine perovskite film, the fast decay ratio f_1 of the Pero-GACs film was decreased from 4.0% to 0.4% and the slow decay lifetime τ_2 was increased from 84.8 ns to 151.1 ns. The decreased f_1 and increased τ_2 further indicate that CsI and GAI can improve the film quality and suppress the trap-assisted nonradiative recombination. The average fluorescence intensities of different perovskite films were confirmed by CLSM images, as shown in **Figure 7.5c** and **7.5d.** For the pristine perovskite film, there were many pinholes, where the fluorescence was quenched. Thus, it is apparent that the average fluorescence intensity of the pristine perovskite films is lower than that of the Pero-GACs film, which agreed well with the PL and TRPL results.

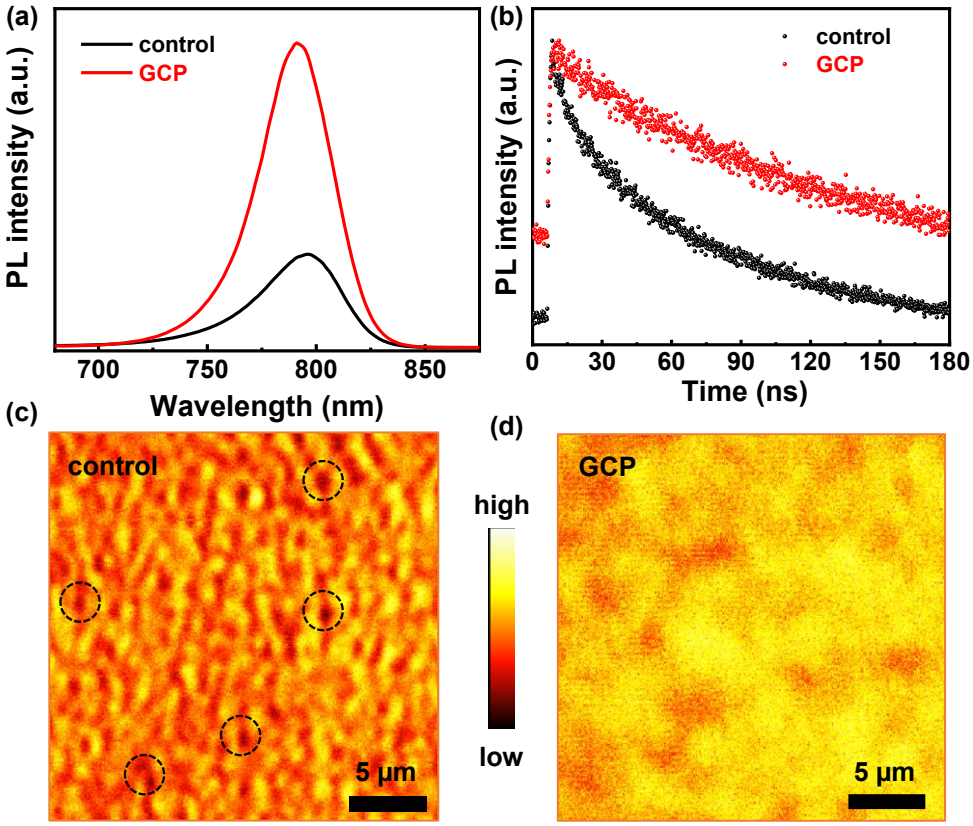


Figure 7.5 (a) Steady-state PL and (b) TRPL of perovskite films without and with GAI and CsI. CLSM images of perovskite films (c) without and (d) with GAI and CsI. All the perovskite films were deposited on glass substrates.

Carrier recombination may affect the accumulation of excess carriers inside the device and thus affect the performance of the device. The contact potential difference (V_{CPD}) recorded by detecting the electrostatic force between a scanning tip and film surface via KPFM can provide more evidence regarding the accumulation of excess carriers.[135] **Figure 7.6a** and **7.6d** show the surface morphologies of pristine perovskite films and GCP films, respectively. Similar to the SEM result, compared to the pristine perovskite film, the GCP film has larger grains and less pinholes. **Figure 7.6b** and 7.**6e** show the surface potential of pristine perovskite films and GCP films, respectively. There is relatively low contact potential inside the grain boundaries, indicating that charge carriers may be trapped at the grain boundaries, increasing the formation of leakage current. The potential difference between the grain boundary and the grain interior reflects the potential carrier behavior between the grain boundary and the grain. For the pristine perovskite film, the surface potential was disordered, and the potential

difference between the grain and grain boundary was as high as 27.3 mV. In contrast, due to larger grains and fewer grain boundaries, the potential distribution of the GCP films was more uniform and the potential difference between the grain and grain boundary was less than 21.0 mV, indicating decreased nonradiative recombination at the grain boundaries.

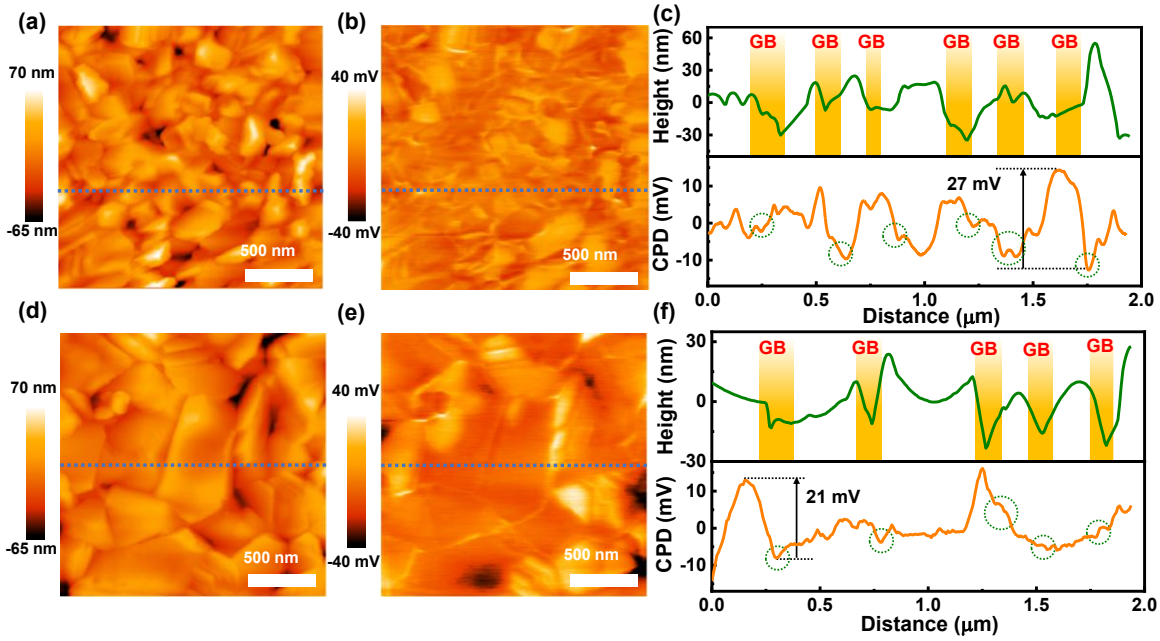


Figure 7.6 (a) Height AFM image (b) KPFM potential image and (c) the corresponding section analysis of height and V_{CPD} along the blue lines of the pristine perovskite films. (d) Height AFM image (e) KPFM potential image and (f) the corresponding section analysis of height and V_{CPD} along the blue lines of the perovskite films with GAI and CsI.

7.3.3 Better charge transport

To further verify the improvement of charge transfer and the reduction of trap defect states, the dark *J-V* curves were recorded. The existence of leakage current is caused by the accumulated charges at the interface. As shown in **Figure 7.7a**, compared with the control, the GCP-SC showed a relatively lower leakage current in the negative voltage region, indicating that the accumulation of charges at the interface was suppressed, which is consistent with the KPFM results. After the forward voltage is added, the current rises rapidly, indicating that the internal defects of the device were decreased. The relationship between P_{light} and V_{OC} was evaluated and the ideality factor n was calculated according to **Equation 4.3.** As shown in **Figure 7.7b**, n values of the control and GCP-SC were determined to be

1.78 and 1.43, respectively. Obviously, the introduction of Cs^+ and GA^+ can effectively reduce defects in the perovskite and inhibit the energy loss caused by non-radiative recombination.

Then, the charge recombination and extraction processes in Pero-SCs were investigated by TPV measurement (**Figure 7.7c**) under equivalent illumination conditions. Compared to the control device, the recombination time constant (τ_R) of the Pero-SCs increased from 7.50 to 14.58 μs, further confirming the suppressed nonradiative recombination.[158, 159] The effect of CsI and GAI on the built-in electric field (V_{bi}) of the Pero-SCs was then examined by analyzing the relationship between capacitance and applied bias through Mott-Schottky curves. As shown in **Figure 7.7d**, the V_{bi} of the control and GCP-SC were 1.05 and 1.10 V, respectively, which is consistent with the V_{OC} trend in the *J-V* results. The enhanced V_{bi} facilitates the separation, transport and collection of photogenerated carriers, reduces the accumulation of charge at the interface, and improves the device performance.

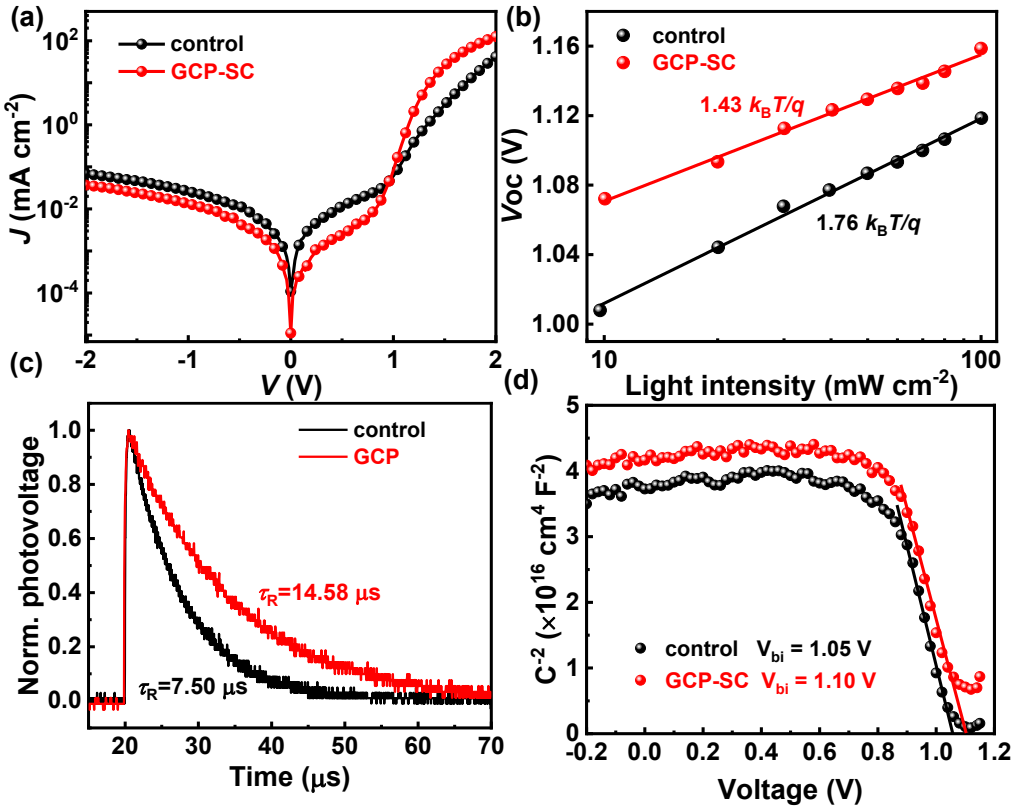


Figure 7.7 (a) Dark *J-V* curves. (b) Plots of V_{OC} versus P_{light}. (c) Normalized TPV. (d) Mott-Schottky plots of the control and GCP-SC.

7.4 Conclusions

To acquire stable and high-quality perovskite films, GAI and CsI were added into the PbI_2 precursor solution and introduced into the perovskite lattice. The incorporation of GA^+ and Cs^+ produced perovskite films with larger grains and less pinholes, which reduces the nonradiative recombination and improves the charge of transport. Furthermore, the degradation of perovskite films in a humid environment was inhibited, which is attributed to the hydrogen bonds between GAI and the $[PbI_6]^{4-}$ octahedron. Using the Pero-GACs films, a PCE as high as 24.29% was achieved. Moreover, the unencapsulated optimized device can maintain ~ 95% of the initial efficiency after about 5200 h in N_2 atmosphere and the encapsulated device can maintain more than 85% of the initial PCE after 1000 h in air with a high humidity (RH) of 80-85%, suggesting better device stability.

Chapter 8
Conclusions and Outlook

8.1 Conclusions

In this thesis, the optimization of perovskite films by additive engineering and interface engineering was studied. The application of inorganic nanomaterials, zwtterionic molecules and perovskite A-site cations as additives and their effects on the perovskite films were summarized. To fabricate Pero-SCs with high PCE and good stability, CuS nanosheets, CuS nanoparticles, SL, GAI and CsI were selected as additives in the hole transport layer or perovskite layers to control the perovskite growth. The key conclusions are as follows:

1. In Chapter 4, inorganic CuS nanosheets were synthesized and applied as additives in the PTAA HTL. Through interaction with the CuS nanosheets, perovskite growth was delayed and more PbI_2 transformed into perovskite. High-quality perovskite films with decreased defects and less PbI_2 were obtained, reducing nonradiative recombination and improving the stability. In addition, the introduction of CuS nanosheets improved the conductivity of PTAA and aligned the energy levels between PTAA and the FA-based perovskite, increasing the charge transport. Finally, the PCE was improved from 21.99 % to 22.92 %. Moreover, both thermal and humidity stability improved.

2. In Chapter 5, CuS nanoparticles were synthesized and incorporated into PbI_2 solution. High-quality perovskite films with more perovskite phases were successfully acquired by preparing porous PbI_2 films via the interaction between PbI_2 and CuS nanoparticles. Moreover, the CuS nanoparticles passivated the defects in the perovskite and improved the charge transport. Upon the addition of CuS nanoparticles, the PCE of Pero-SCs increased from 23.21% to 24.31% with improved N_2, humidity and light stability.

3. In Chapter 6, amphiphilic SL was applied as an additive in the perovskite to address the difference in surface energy between the hydrophobic PTAA and hydrophilic PbI_2 solution. The long alkyl chains of SL decreased the surface energy of the PbI_2 solution, assisting its spread on PTAA and improving the coverage of the perovskite films, which is conducive to the fabrication of large-scale devices. In addition, the C=O, P=O, and quaternary ammonium groups can passivate different defects. Under these dual effects, high-quality perovskite films with full coverage and inhibited nonradiative recombination were achieved, thus increasing the PCE from 20.11% to 22.93%. Notably, the SL-modified devices

with an active area of 1.1 cm^2 achieved a PCE of 18.32%. Moreover, the SL-modified Pero-SCs showed better humidity stability.

4. In Chapter 7, GAI and CsI were employed simultaneously as additives in PbI_2 to stabilize the $[PbI_6]^{4-}$ octahedra. The collaboration between GAI and CsI leverages the strengths of both additives while also addressing their shortcomings. The synergistic effects of GAI and CsI achieved high-quality perovskite films with larger grains, less pinholes and reduced defects. A *n-i-p* structured device achieved a champion efficiency of 24.29% and exhibited excellent operational stability under ambient conditions with 80 ± 5% relative humidity at room temperature.

8.2 Contributions

All four strategies successfully enhanced both the efficiency and stability of the Pero-SCs. Notably, CuS was employed for the first time as a dopant in both PTAA and the perovskite layer, expanding the application scope of CuS nanomaterials in photovoltaics. Whether incorporated into the hole transport layer or the perovskite absorber, CuS effectively modulates perovskite crystallization. Unlike organic additives, its intrinsic semiconductor properties facilitate charge transport, demonstrating the potential of inorganic materials in optimizing performance of Pero-SCs. Additionally, the zwitterionic additive SL not only passivates defects but also modifies surface energy, improving perovskite film coverage. This advancement enhances the commercial viability of Pero-SCs and provides valuable insights for the selection and molecular design of zwitterionic passivators. Furthermore, in contrast to previous reports on two-step perovskite deposition—where GAI is typically doped into the ammonium salt solution— GAI and CsI were introduced into the PbI_2 precursor to stabilize the PbI_2 framework. This approach yielded large-grained perovskite films with improved optoelectronic properties and excellent stability. Our findings offer a novel strategy for the fabrication of multi-cation perovskite films, contributing to the ongoing development of efficient and scalable perovskite solar cells.

8.3 Outlook

To further improve the performance of perovskite solar cells, more research can be conducted in the following aspects:

1. The CuS nanosheets synthesized in this thesis have a broad size distribution and a certain thickness. The synthesis conditions such as temperature, time and post-treatment can be optimized to obtain more uniform and thinner nanosheets, further improving the device efficiency and repeatability.

2. CuS nanomaterials have tunable nanomorphology and band gaps. Therefore, exploring the effects of different CuS nanomaterials on devices can expand their application in Pero-SCs. For example, CuS nanoparticles and nanosheets have been shown to be used to passivate perovskite surfaces and enhance hole transport, but their size effect has not been explored. Therefore, the effect of size on surface passivation can be further explored. In addition, the semiconductor properties of CuS can also be adjusted by changing the ratio of Cu and S, thereby broadening its application to different layers of perovskite solar cells.

3. CuS has been used to solve problems at the interface and in the perovskite bulk phase independently. Therefore, it is possible to try to combine the two strategies to solve the problems of the interface and bulk perovskite at the same time, and regulate the perovskite growth from bottom to top, which may result in higher device performance.

4. At present, in addition to PTAA, there are other commonly used HTLs such as nickel oxide and the currently popular self-assembled materials. However, these hole transport layers still have some problems, such as reaction with perovskite and poor stability. Therefore, CuS nanomaterials can be applied in other HTLs to explore whether they have positive effects.

5. While zwitterionic materials containing long alkyl chains can effectively lower the surface energy of perovskite precursors, their limited solubility in precursor solutions due to excessive alkyl chain length significantly restricts their practical applications. Furthermore, the extent of surface energy reduction varies considerably with different alkyl chain lengths. Consequently, investigating the influence of alkyl chain length on device performance represents an important research direction.

References

1. Chen H., Liu C., Xu J., Maxwell A., Zhou W., Yang Y., Zhou Q., Bati A. S. R., Wan H., Wang Z., Zeng L., Wang J., Serles P., Liu Y., Teale S., Liu Y., Saidaminov M. I., Li M., Rolston N., Hoogland S., Filleter T., Kanatzidis M. G., Chen B., Ning Z., Sargent E. H., Improved Charge Extraction in Inverted Perovskite Solar Cells With Dual-Site-Binding Ligands. *Science* **2024,** *384* (6692), 189–193.

2. Kojima A., Teshima K., Shirai Y., Miyasaka T., Organometal Halide Perovskites as Visible-Light Sensitizers for Photovoltaic Cells. *J. Am. Chem. Soc.* **2009,** *131* (17), 6050–6051.

3. Jung E. H., Jeon N. J., Park E. Y., Moon C. S., Shin T. J., Yang T. Y., Noh J. H., Seo J., Efficient, Stable and Scalable Perovskite Solar Cells Using Poly(3-Hexylthiophene). *Nature* **2019,** *567* (7749), 511–515.

4. Hou Y., Du X., Scheiner S., McMeekin D. P., Wang Z., Li N., Killian M. S., Chen H., Richter M., Levchuk I., Schrenker N., Spiecker E., Stubhan T., Luechinger N. A., Hirsch A., Schmuki P., Steinruck H. P., Fink R. H., Halik M., Snaith H. J., Brabec C. J., A Generic Interface to Reduce the Efficiency-Stability-Cost Gap of Perovskite Solar Cells. *Science* **2017,** *358* (6367), 1192–1197.

5. Park J., Kim J., Yun H. S., Paik M. J., Noh E., Mun H. J., Kim M. G., Shin T. J., Seok S. I., Controlled Growth of Perovskite Layers With Volatile Alkylammonium Chlorides. *Nature* **2023,** *616* (7958), 724–730.

6. Lu H., Liu Y., Ahlawat P., Mishra A., Tress W. R., Eickemeyer F. T., Yang Y., Fu F., Wang Z., Avalos C. E., Carlsen B. I., Agarwalla A., Zhang X., Li X., Zhan Y., Zakeeruddin S. M., Emsley L., Rothlisberger U., Zheng L., Hagfeldt A., Gratzel M., Vapor-Assisted Deposition of Highly Efficient, Stable Black-Phase $FAPbI_3$ Perovskite Solar Cells. *Science* **2020,** *370* (6512), eabb8985.

7. Marinova N., Valero S., Delgado J. L., Organic and perovskite solar cells: Working principles, materials and interfaces. *J Colloid Interface Sci* **2017,** *488*, 373–389.

8. Gonzalez-Pedro V., Juarez-Perez E. J., Arsyad W. S., Barea E. M., Fabregat-Santiago F., Mora-Sero I., Bisquert J., General working principles of $CH_3NH_3PbX_3$ perovskite solar cells. *Nano Lett* **2014,** *14* (2), 888–893.

9. Zheng L., Ma Y., Chu S., Wang S., Qu B., Xiao L., Chen Z., Gong Q., Wu Z., Hou X., Improved Light Absorption and Charge Transport for Perovskite Solar Cells With Rough Interfaces by Sequential Deposition. *Nanoscale* **2014,** *6* (14), 8171–8176.

10. Hu M., Bi C., Yuan Y., Xiao Z., Dong Q., Shao Y., Huang J., Distinct Exciton Dissociation Behavior of Organolead Trihalide Perovskite and Excitonic Semiconductors Studied in the Same System. *Small* **2015,** *11* (18), 2164–2169.

11. Kim H.-S., Im S. H., Park N.-G., Organolead Halide Perovskite: New Horizons in Solar Cell Research. *The Journal of Physical Chemistry C* **2014,** *118* (11), 5615–5625.

12. Stoumpos C. C., Malliakas C. D., Kanatzidis M. G., Semiconducting Tin and Lead Iodide Perovskites with Organic Cations: Phase Transitions, High Mobilities, and Near-Infrared Photoluminescent Properties. *Inorg. Chem.* **2013,** *52* (15), 9019–9038.

13. Mei A., Sheng Y., Ming Y., Hu Y., Rong Y., Zhang W., Luo S., Na G., Tian C., Hou X., Xiong Y., Zhang Z., Liu S., Uchida S., Kim T.-W., Yuan Y., Zhang L., Zhou Y., Han H., Stabilizing Perovskite Solar Cells to IEC61215:2016 Standards with over 9,000-h Operational Tracking. *Joule* **2020,** *4* (12), 2646–2660.

14. Chen Y., Lei Y., Li Y., Yu Y., Cai J., Chiu M. H., Rao R., Gu Y., Wang C., Choi W., Hu H., Wang C., Li Y., Song J., Zhang J., Qi B., Lin M., Zhang Z., Islam A. E., Maruyama B., Dayeh S., Li L. J., Yang K., Lo Y. H., Xu S., Strain Engineering and Epitaxial Stabilization of Halide Perovskites. *Nature* **2020,** *577* (7789), 209–215.

15. Min J., Choi Y., Kim D., Park T., Beyond Imperfections: Exploring Defects for Breakthroughs in Perovskite Solar Cell Research. *Adv. Energy Mater.* **2023,** *14* (6), 2302659.

16. Zhang F., Zhu K., Additive Engineering for Efficient and Stable Perovskite Solar Cells. *Adv. Energy Mater.* **2019,** *10* (13), 1902579.

17. Chen B., Rudd P. N., Yang S., Yuan Y., Huang J., Imperfections and Their Passivation in Halide Perovskite Solar Cells. *Chem. Soc. Rev.* **2019,** *48* (14), 3842–3867.

18. Gao Z. W., Wang Y., Choy W. C. H., Buried Interface Modification in Perovskite Solar Cells: A Materials Perspective. *Adv. Energy Mater.* **2022,** *12* (20), 2104030.

19. Yang X., Luo D., Xiang Y., Zhao L., Anaya M., Shen Y., Wu J., Yang W., Chiang Y. H., Tu Y., Su R., Hu Q., Yu H., Shao G., Huang W., Russell T. P., Gong Q., Stranks S. D., Zhang W., Zhu R., Buried Interfaces in Halide Perovskite Photovoltaics. *Adv. Mater.* **2021,** *33* (7), e2006435.

20. Cao Y., Yang L., Yan N., Meng L., Chen X., Zhang J., Qi D., Pi J., Li N., Feng X., Ma C., Xiao F., Zhao G., Tan S., Liu X., Liu Y., Zhao K., Liu S., Feng J., Buried Interface Modification for High-Performance and Stable Perovskite Solar Cells. *Energy Environ. Sci.* **2025,** *18* (8), 3659–3667.

21. Wang Q., Chen B., Liu Y., Deng Y., Bai Y., Dong Q., Huang J., Scaling Behavior of Moisture-Induced Grain Degradation in Polycrystalline Hybrid Perovskite Thin Films. *Energy Environ. Sci.* **2017,** *10* (2), 516–522.

22. Liu P., Liu X., Lyu L., Xie H., Zhang H., Niu D., Huang H., Bi C., Xiao Z., Huang J., Gao Y., Interfacial Electronic Structure at the $CH_3NH_3PbI_3/MoO_x$ Interface. *Appl. Phys. Lett.* **2015,** *106* (19), 193903

23. Schlipf J., Biessmann L., Oesinghaus L., Berger E., Metwalli E., Lercher J. A., Porcar L., Muller-Buschbaum P., In Situ Monitoring the Uptake of Moisture into Hybrid Perovskite Thin Films. *J. Phys. Chem. Lett.* **2018,** *9* (8), 2015–2021.

24. Ava T. T., Al Mamun A., Marsillac S., Namkoong G., A Review: Thermal Stability of Methylammonium Lead Halide Based Perovskite Solar Cells. *Applied Sciences* **2019,** *9* (1), 188.

25. Wang R., Xue J., Meng L., Lee J.-W., Zhao Z., Sun P., Cai L., Huang T., Wang Z., Wang Z.-K., Duan Y., Yang J. L., Tan S., Yuan Y., Huang Y., Yang Y., Caffeine Improves the Performance and Thermal Stability of Perovskite Solar Cells. *Joule* **2019,** *3* (6), 1464–1477.

26. Zhu C., Gao J., Chen T., Guo X., Yang Y., Intrinsic Thermal Stability of Inverted Perovskite Solar Cells Based on Electrochemically Deposited PEDOT. *J. Energy Chem.* **2023,** *83*, 445–453.

27. Bryant D., Aristidou N., Pont S., Sanchez-Molina I., Chotchunangatchaval T., Wheeler S., Durrant J. R., Haque S. A., Light and Oxygen Induced Degradation Limits the Operational Stability of Methylammonium Lead Triiodide Perovskite Solar Cells. *Energy Environ. Sci.* **2016,** *9* (5), 1655–1660.

28. Aristidou N., Eames C., Sanchez-Molina I., Bu X., Kosco J., Islam M. S., Haque S. A., Fast Oxygen Diffusion and Iodide Defects Mediate Oxygen-Induced Degradation of Perovskite Solar Cells. *Nat. Commun.* **2017,** *8*, 15218.

29. Chen C., Xu Y., Wu S., Zhang S., Yang Z., Zhang W., Zhu H., Xiong Z., Chen W., Chen W., CaI_2: A More Effective Passivator of Perovskite Films Than PbI_2 for High Efficiency and Long-Term Stability of Perovskite Solar Cells. *J. Mater. Chem. A* **2018,** *6* (17), 7903–7912.

30. Roose B., Dey K., Chiang Y.-H., Friend R. H., Stranks S. D., Critical Assessment of the Use of Excess Lead Iodide in Lead Halide Perovskite Solar Cells. *J. Phys. Chem. Lett.* **2020,** *11* (16), 6505–6512.

31. Jacobsson T. J., Correa-Baena J. P., Halvani Anaraki E., Philippe B., Stranks S. D., Bouduban M. E., Tress W., Schenk K., Teuscher J., Moser J. E., Rensmo H., Hagfeldt A., Unreacted PbI_2 as a Double-Edged Sword for Enhancing the Performance of Perovskite Solar Cells. *J. Am. Chem. Soc.* **2016,** *138* (32), 10331–10343.

32. Merdasa A., Kiligaridis A., Rehermann C., Abdi-Jalebi M., Stöber J., Louis B., Gerhard M., Stranks S. D., Unger E. L., Scheblykin I. G., Impact of Excess Lead Iodide on the Recombination Kinetics in Metal Halide Perovskites. *ACS Energy Lett.* **2019,** *4* (6), 1370–1378.

33. Jiang M., Wu Y., Zhou Y., Wang Z., Observation of Lower Defect Density Brought by Excess PbI_2 in $CH_3NH_3PbI_3$ Solar Cells. *AIP Advances* **2019,** *9* (8), 085301.

34. Shi B., Yao X., Hou F., Guo S., Li Y., Wei C., Ding Y., Li Y., Zhao Y., Zhang X., Unraveling the Passivation Process of PbI_2 to Enhance the Efficiency of Planar Perovskite Solar Cells. *The Journal of Physical Chemistry C* **2018,** *122* (37), 21269–21276.

35. Shao W., Wang H., Ye F., Wang C., Wang C., Cui H., Dong K., Ge Y., Wang T., Ke W., Fang G., Modulation of Nucleation and Crystallization in PbI_2 Films Promoting Preferential Perovskite Orientation Growth for Efficient Solar Cells. *Energy Environ. Sci.* **2023,** *16* (1), 252–264.

36. Yu X., Fang Z., Lin S., Wu S., Fang M., Xie H., Kong D., Zhou C., Polyvinyl Pyrrolidone Induced "Confinement Effect" on PbI_2 and the Improvement on Crystallization and Thermal Stability of Perovskite. *Small* **2024,** *20* (5), e2306101.

37. Bi C., Wang Q., Shao Y., Yuan Y., Xiao Z., Huang J., Non-Wetting Surface-Driven High-Aspect-Ratio Crystalline Grain Growth for Efficient Hybrid Perovskite Solar Cells. *Nat. Commun.* **2015,** *6*, 7747.

38. Zhang S., Stolterfoht M., Armin A., Lin Q., Zu F., Sobus J., Jin H., Koch N., Meredith P., Burn P. L., Neher D., Interface Engineering of Solution-Processed Hybrid Organohalide Perovskite Solar Cells. *ACS Appl. Mater. Interfaces* **2018,** *10* (25), 21681–21687.

39. Lee J., Kang H., Kim G., Back H., Kim J., Hong S., Park B., Lee E., Lee K., Achieving Large-Area Planar Perovskite Solar Cells by Introducing an Interfacial Compatibilizer. *Adv. Mater.* **2017,** *29* (22), 1606363.

40. Chen Q., Yuan L., Duan R., Huang P., Fu J., Ma H., Wang X., Zhou Y., Song B., Zwitterionic Polymer: A Facile Interfacial Material Works at Both Anode and Cathode in *p-i-n* Perovskite Solar Cells. *Sol. RRL* **2019,** *3* (9), 1900118.

41. Jung E. D., Harit A. K., Kim D. H., Jang C. H., Park J. H., Cho S., Song M. H., Woo H. Y., Multiply Charged Conjugated Polyelectrolytes as a Multifunctional Interlayer for Efficient and Scalable Perovskite Solar Cells. *Adv. Mater.* **2020,** *32* (30), 2002333.

42. Miyata K., Meggiolaro D., Trinh M. T., Joshi P. P., Mosconi E., Jones S. C., De Angelis F., Zhu X. Y., Large Polarons in Lead Halide Perovskites. *Sci. Adv.* **2017,** *3* (8), e1701217.

43. Ciccioli A., Latini A., Thermodynamics and the Intrinsic Stability of Lead Halide Perovskites $CH_3NH_3PbX_3$. *J. Phys. Chem. Lett.* **2018,** *9* (13), 3756–3765.

44. Saliba M., Matsui T., Domanski K., Seo J. Y., Ummadisingu A., Zakeeruddin S. M., Correa-Baena J. P., Tress W. R., Abate A., Hagfeldt A., Grätzel M., Incorporation of Rubidium Cations into Perovskite Solar Cells Improves Photovoltaic Performance. *Science* **2016,** *354* (6309), 206–209.

45. Frost J. M., Butler K. T., Brivio F., Hendon C. H., van Schilfgaarde M., Walsh A., Atomistic Origins of High-Performance in Hybrid Halide Perovskite Solar Cells. *Nano Lett.* **2014,** *14* (5), 2584–2590.

46. Wang D., Wright M., Elumalai N. K., Uddin A., Stability of Perovskite Solar Cells. *Sol. Energy Mater. Sol. Cells* **2016,** *147*, 255–275.

47. Aristidou N., Sanchez-Molina I., Chotchuangchutchaval T., Brown M., Martinez L., Rath T., Haque S. A., The Role of Oxygen in the Degradation of Methylammonium Lead Trihalide Perovskite Photoactive Layers. *Angew. Chem., Int. Ed.* **2015,** *54* (28), 8208–8212.

48. Jiang Y., Zheng Y., Li J., Pu Y., Du L., Guo Y., Jia N., Zhang X., Mukhametkarimov Y., Chen R., Liu Z., Wang H., Data-Driven Insights to Tackle Photo-Induced Phase Segregation for Mixed-Halide Perovskite Solar Cells. *Chem. Eng. J.* **2025,** *520*, 165704.

49. Cappel U. B., Svanström S., Lanzilotto V., Johansson F. O. L., Aitola K., Philippe B., Giangrisostomi E., Ovsyannikov R., Leitner T., Föhlisch A., Svensson S., Mårtensson N., Boschloo G., Lindblad A., Rensmo H., Partially Reversible Photoinduced Chemical Changes in a Mixed-Ion Perovskite Material for Solar Cells. *ACS Appl. Mater. Interfaces* **2017,** *9* (40), 34970–34978.

50. Boyd C. C., Cheacharoen R., Leijtens T., McGehee M. D., Understanding Degradation Mechanisms and Improving Stability of Perovskite Photovoltaics. *Chem. Rev.* **2019,** *119* (5), 3418–3451.

51. Zhou Y., Yin Y., Zuo X., Wang L., Li T.-D., Xue Y., Subramanian A., Fang Y., Guo Y., Yang Z., Cotlet M., Nam C.-Y., Rafailovich M. H., Improving Thermal Stability of Perovskite Solar Cells by Suppressing Ion Migration Using Copolymer Grain Encapsulation. *Chem. Mater.* **2021,** *33* (15), 6120–6135.

52. Guo Z., Gao L., Xu Z., Teo S., Zhang C., Kamata Y., Hayase S., Ma T., High Electrical Conductivity 2D MXene Serves as Additive of Perovskite for Efficient Solar Cells. *Small* **2018,** *14* (47), e1802738.

53. Liu X., Zhang Z., Jiang J., Tian C., Wang X., Wang L., Zhang Z., Wu X., Zheng Y., Liang J., Chen C.-C., Chlorine-Terminated MXene Quantum Dots for Improving Crystallinity and Moisture Stability in High-Performance Perovskite Solar Cells. *Chem. Eng. J.* **2022,** *432*, 134382.

54. Zhang J., Huang C., Sun Y., Yu H., Amino‐Functionalized Niobium‐Carbide MXene Serving as Electron Transport Layer and Perovskite Additive for the Preparation of High‐Performance and Stable Methylammonium‐Free Perovskite Solar Cells. *Adv. Funct. Mater.* **2022,** *32* (24), 2113367.

55. Qin Z., Chen Y., Wang X., Liu X., Miao Y., Zhao Y., Incorporation of Two-Dimensional WSe_2 into $MAPbI_3$ Perovskite for Efficient and Stable Photovoltaics. *J. Phys. Chem. Lett.* **2021,** *12* (29), 6883–6888.

56. Wang Y., Zhang H., Zhang T., Shi W., Kan M., Chen J., Zhao Y., Photostability of $MAPbI_3$ Perovskite Solar Cells by Incorporating Black Phosphorus. *Sol. RRL* **2019,** *3* (9), 1900197.

57. Yang W., Chen J., Lian X., Li J., Yao F., Wu G., Qiu W., Jin C., Heremans P., Chen H., Black Phosphorus Quantum Dots Induced High‐Quality Perovskite Film for Efficient and Thermally Stable Planar Perovskite Solar Cells. *Sol. RRL* **2019,** *3* (8), 1900132.

58. Han J., Yin X., Nan H., Zhou Y., Yao Z., Li J., Oron D., Lin H., Enhancing the Performance of Perovskite Solar Cells by Hybridizing SnS Quantum Dots with CH(3) NH(3) PbI(3). *Small* **2017,** *13* (32), 201902152.

59. Luo X., He Z., Meng R., Zhang C., Chen M., Lu H., Yang Y., SnS Quantum Sots with Sifferent Sizes in Active Layer for Enhancing the Performance of Perovskite Solar Cells. *Appl. Phys. A:Mater. Sci. Process.* **2021,** *127* (5), 317.

60. Liu X., Wu Z., Zhong H., Wang X., Yang J., Zhang Z., Han J., Oron D., Lin H., Epitaxial 2D PbS Nanosheet‐Formamidinium Lead Triiodide Heterostructure Enabling High‐Performance Perovskite Solar Cells. *Adv. Funct. Mater.* **2023,** *33* (38), 2304140.

61. Sánchez‐Godoy H. E., Erazo E. A., Gualdrón‐Reyes A. F., Khan A. H., Agouram S., Barea E. M., Rodriguez R. A., Zarazúa I., Ortiz P., Cortés M. T., Muñoz‐Sanjosé V., Moreels I., Masi S., Mora‐Seró I., Preferred Growth Direction by PbS Nanoplatelets Preserves Perovskite Infrared Light Harvesting for Stable, Reproducible, and Efficient Solar Cells. *Adv. Energy Mater.* **2020,** *10* (46), 2002422.

62. Zhang Z., Wang J., Lang L., Dong Y., Liang J., Zheng Y., Wu X., Tian C., Huang Y., Zhou Z., Yang Y., Wang L., Kong L., Chen C.-C., Size-Tunable MoS_2 Nanosheets for Controlling the Crystal Morphology and Residual Stress in Sequentially Deposited Perovskite Solar Cells with Over 22.5% Efficiency. *J. Mater. Chem. A* **2022,** *10* (7), 3605–3617.

63. Zheng X., Deng Y., Chen B., Wei H., Xiao X., Fang Y., Lin Y., Yu Z., Liu Y., Wang Q., Huang J., Dual Functions of Crystallization Control and Defect Passivation Enabled by Sulfonic Zwitterions for Stable and Efficient Perovskite Solar Cells. *Adv. Mater.* **2018,** *30* (52), e1803428.

64. Kim J. H., Kim Y. R., Park B., Hong S., Hwang I. W., Kim J., Kwon S., Kim G., Kim H., Lee K., Simultaneously Passivating Cation and Anion Defects in Metal Halide Perovskite Solar Cells Using a Zwitterionic Amino Acid Additive. *Small* **2021,** *17* (3), e2005608.

65. Zhou W., Li D., Xiao Z., Wen Z., Zhang M., Hu W., Wu X., Wang M., Zhang W. H., Lu Y., Yang S., Yang S., Zwitterion Coordination Induced Highly Orientational Order of $CH_3NH_3PbI_3$ Perovskite Film Delivers a High Open Circuit Voltage Exceeding 1.2 V. *Adv. Funct. Mater.* **2019,** *29* (23), 1901026.

66. Wang Y., Meng Y., Liu C., Cao R., Han B., Xie L., Tian R., Lu X., Song Z., Li J., Yang S., Lu C., Ge Z., Utilizing Electrostatic Dynamic Bonds in Zwitterion Elastomer for Self-Curing of Flexible Perovskite Solar Cells. *Joule* **2024,** *8* (4), 1120–1141.

67. Xiao X., Chen K., Qin M., Li X., Meng R., Wang X., Zhou Y., Mei A., Han H., Alkyl Chain Length Engineering of Zwitterionic Sulfobetaine Passivators for Efficient Printable Mesoscopic Perovskite Solar Cells. *Chem. Eng. J.* **2025,** *515*, 163528.

68. Li X., Zou Y., Yu S., Zhao X., Yu W., Yang S., Guo H., Xiao L., Chen Z., Qu B., Zwitterionic Ionic Liquid as Additive for High‐Performance $FAPbI_3$ Perovskite Solar Cells with Negligible Hysteresis. *Sol. RRL* **2023,** *7* (10), 2300091.

69. Yang L., Ma X., Shang X., Gao D., Wang C., Li M., Chen C., Zhang B., Xu S., Zheng S., Song H., Zwitterionic Ionic Liquid Confer Defect Tolerance, High Conductivity, and Hydrophobicity toward Efficient Perovskite Solar Cells Exceeding 22% Efficiency. *Sol. RRL* **2021,** *5* (9), 2100352.

70. Han X., Wang J., Jin L., Wang P., Shi B., Zhao Y., Zhang X., Zwitterion Reduces Open‐Circuit Voltage Loss in Wide‐Bandgap Perovskite Solar Cells with 22% Efficiency and Its Application in Tandem Devices. *Sol. RRL* **2023,** *8* (21), 2300648.

71. Wang S., Shao Y., Dai W., Wang K., Dong X., Luo T., He Y., Liu S., Wan L., Li D., Liu S., Sweet Zwitterionic Aspartame for High‐Performance Wide‐Bandgap Perovskite Solar Cells and Tandem Devices. *Adv. Funct. Mater.* **2025**, 2503592.

72. Xue J., Wang R., Yang Y., The Surface of Halide Perovskites From Nano to Bulk. *Nat. Rev. Mater.* **2020,** *5* (11), 809–827.

73. Wang H., Zou W., Ouyang Y., Deng X., Luo H., Xu J., Liu X., Li H., Gong X., Lei Y., Ni Y., Peng Y., Consolidating a Pb-X Framework via Multifunctional Passivation with Fluorinated Zwitterions for Efficient and Stable Perovskite Solar Cells. *J. Mater. Chem. A* **2022,** *10* (19), 10750–10758.

74. Wang Z., Pradhan A., Kamarudin M. A., Pandey M., Pandey S. S., Zhang P., Ng C. H., Tripathi A. S. M., Ma T., Hayase S., Passivation of Grain Boundary by Squaraine Zwitterions for Defect Passivation and Efficient Perovskite Solar Cells. *ACS Appl. Mater. Interfaces* **2019,** *11* (10), 10012–10020.

75. Tseng K.-W., Chen G.-L., Chen P.-Y., Hsieh H.-C., Wang L., Dual Bulk and Surface Passivation of 3D Perovskite Solar Cells Using Zwitterionic Molecules. *Mater. Today Energy* **2025,** *52*, 101933.

76. Liu K., Liang Q., Qin M., Shen D., Yin H., Ren Z., Zhang Y., Zhang H., Fong P. W. K., Wu Z., Huang J., Hao J., Zheng Z., So S. K., Lee C.-S., Lu X., Li G., Zwitterionic-Surfactant-Assisted RoomTemperature Coating of Efficient Perovskite Solar Cells. *Joule* **2020,** *4* (11), 2404–2425.

77. Ye F., Yang W., Luo D., Zhu R., Gong Q., Applications of Cesium in the Perovskite Solar Cells. *J. Semicond.* **2017,** *38* (1), 011003.

78. Lee J. W., Kim D. H., Kim H. S., Seo S. W., Cho S. M., Park N. G., Formamidinium and Cesium Hybridization for Photo‐ and Moisture‐Stable Perovskite Solar Cell. *Adv. Energy Mater.* **2015,** *5* (20), 1501310.

79. Ghosh D., Smith A. R., Walker A. B., Islam M. S., Mixed A-Cation Perovskites for Solar Cells: Atomic-Scale Insights Into Structural Distortion, Hydrogen Bonding, and Electronic Properties. *Chem. Mater.* **2018,** *30* (15), 5194–5204.

80. Niu G., Yu H., Li J., Wang D., Wang L., Controlled Orientation of Perovskite Films Through Mixed Cations Toward High-Performance Perovskite Solar Cells. *Nano Energy* **2016,** *27*, 87–94.

81. Saliba M., Matsui T., Seo J. Y., Domanski K., Correa-Baena J. P., Nazeeruddin M. K., Zakeeruddin S. M., Tress W., Abate A., Hagfeldt A., Gratzel M., Cesium-Containing Triple Cation Perovskite Solar Cells: Improved Stability, Reproducibility and High Efficiency. *Energy Environ. Sci.* **2016,** *9* (6), 1989–1997.

82. Liu X., Chen M., Zhang Y., Xia J., Yin J., Li M., Brooks K. G., Hu R., Gao X., Kim Y.-H., Züttel A., Luther J. M., Kinge S., Feng Y., Nazeeruddin M. K., High-Efficiency Perovskite Photovoltaic Modules Achieved via Cesium Doping. *Chem. Eng. J.* **2022,** *431*, 133713.

83. McMeekin D. P., Sadoughi G., Rehman W., Eperon G. E., Saliba M., Horantner M. T., Haghighirad A., Sakai N., Korte L., Rech B., Johnston M. B., Herz L. M., Snaith H. J., A Mixed-Cation Lead Mixed-Halide Perovskite Absorber for Tandem Solar Cells. *Science* **2016,** *351* (6269), 151–155.

84. Zhao Y., Tan H., Yuan H., Yang Z., Fan J. Z., Kim J., Voznyy O., Gong X., Quan L. N., Tan C. S., Hofkens J., Yu D., Zhao Q., Sargent E. H., Perovskite-Seeded Growth of Formamidinium-Lead-Iodide-Based Perovskites for Efficient and Stable Solar Cells. *Nat. Commun.* **2018,** *9* (1), 1607.

85. Wu P., Li D., Wang S., Zhang F., Magic Guanidinium Cations in Perovskite Solar Cells: from Bulk to Interface. *Mater. Chem. Front.* **2023,** *7* (13), 2507–2527.

86. De Marco N., Zhou H., Chen Q., Sun P., Liu Z., Meng L., Yao E. P., Liu Y., Schiffer A., Yang Y., Guanidinium: A Route to Enhanced Carrier Lifetime and Open-Circuit Voltage in Hybrid Perovskite Solar Cells. *Nano Lett.* **2016,** *16* (2), 1009–1016.

87. Jodlowski A. D., Roldán-Carmona C., Grancini G., Salado M., Ralaiarisoa M., Ahmad S., Koch N., Camacho L., de Miguel G., Nazeeruddin M. K., Large Guanidinium Cation Mixed with Methylammonium in Lead Iodide Perovskites for 19% Efficient Solar Cells. *Nat. Energy* **2017,** *2* (12), 972-979.

88. Dong H., Pang S., He F., Yang H., Zhu W., Chen D., Xi H., Zhang J., Hao Y., Zhang C., Annealing‐Free, High‐Performance Perovskite Solar Cells by Controlling Crystallization via Guanidinium Cation Doping. *Sol. RRL* **2021,** *5* (7), 2100097.

89. Li Z., Hao L., Liu D., Sun X., Zhao Q., Shao Z., Chen C., Wang X., Wang L., Cui G., Pang S., Inhibiting Ion Migration by Guanidinium Cation Doping for Efficient Perovskite Solar Cells with Enhanced Operational Stability. *Sol. RRL* **2022,** *6* (6), 2200003.

90. Minussi F. B., Bertoletti E. M., Reis S. P., Carvalho J. F., Araujo E. B., Guanidinium Substitution-dependent Phase Transitions, Ionic conductivity, and Dielectric Properties of $MAPbI_3$. *Chem. Commun.* **2022,** *58* (13), 2212–2215.

91. Ramos-Terrón S., Illanes J. F., Bohoyo-Gil D., Camacho L., de Miguel G., Insight into the Role of Guanidinium and Cesium in Triple Cation Lead Halide Perovskites. *Sol. RRL* **2021,** *5* (12), 2100586.

92. Zhang W., Xiong J., Li J., Daoud W. A., Guanidinium Induced Phase Separated Perovskite Layer for Efficient and Highly Stable Solar Cells. *J. Mater. Chem. A* **2019,** *7* (16), 9486–9496.

93. Susic I., Gil-Escrig L., Palazon F., Sessolo M., Bolink H. J., Quadruple-Cation Wide-Bandgap Perovskite Solar Cells with Enhanced Thermal Stability Enabled by Vacuum Deposition. *ACS Energy Lett.* **2022,** *7* (4), 1355–1363.

94. Pham N. D., Zhang C., Tiong V. T., Zhang S., Will G., Bou A., Bisquert J., Shaw P. E., Du A., Wilson G. J., Wang H., Tailoring Crystal Structure of $FA_{0.83}Cs_{0.17}PbI_3$ Perovskite Through Guanidinium Doping for Enhanced Performance and Tunable Hysteresis of Planar Perovskite Solar Cells. *Adv. Funct. Mater.* **2018,** *29* (1), 1806479.

95. Qin M., Xue H., Zhang H., Hu H., Liu K., Li Y., Qin Z., Ma J., Zhu H., Yan K., Fang G., Li G., Jeng U. S., Brocks G., Tao S., Lu X., Precise Control of Perovskite Crystallization Kinetics via Sequential A-Site Doping. *Adv. Mater.* **2020,** *32* (42), e2004630.

96. Singh S., Siliavka E., Löffler M., Vaynzof Y., Impact of Buried Interface Texture on Compositional Stratification and Ion Migration in Perovskite Solar Cells. *Adv. Funct. Mater.* **2024,** *34* (42), 2402655.

97. Zhang Y., Yu R., Li M., He Z., Dong Y., Xu Z., Wang R., Ma Z., Tan Z., Amphoteric Ion Bridged Buried Interface for Efficient and Stable Inverted Perovskite Solar Cells. *Adv. Mater.* **2024,** *36* (1), e2310203.

98. Sun X., Wu H., Li Z., Zhu R., Li G., Su Z., Zhang J., Gao X., Pascual J., Abate A., Li M., Multifunctional Modification of the Buried Interface in Mixed Tin-Lead Perovskite Solar Cells. *Angew. Chem., Int. Ed.* **2024,** *63* (48), e202409330.

99. Lv B.-H., Ye Y.-C., Wang J.-G., Zhang L.-J., Zhang Y.-H., Zheng M.-L., Chen X.-M., Du H.-W., Yang J., Zhang X.-Y., Xu M.-L., Ye Q.-F., Gao X., Tang J.-X., Tang Y., Dou W.-D., Vertically Oriented Micron-Thick Perovskite Film Enables Efficient and Stable Inverted Perovskite Solar Cells. *Chem. Eng. J.* **2025,** *511*, 161966.

100. Rui Y., Li T., Li B., Wang Y., Müller-Buschbaum P., Two-Dimensional SnS_2 Nanosheets as Electron Transport and Interfacial Layers Enable Efficient Perovskite Solar Cells. *J. Mater. Chem. C* **2022,** *10* (34), 12392–12401.

101. Xu L., Liu Y., Qiu W., Li Y., Wang H., Li M., Xian L., Zheng C., Chen Y., Chen R., Conjugated Molecule Doping of Triphenylamine-Based Hole-Transport Layer for High-Performance Perovskite Solar Cells. *J. Power Sources* **2021,** *506*, 230120.

102. Tian S., Chen J., Lian X., Wang Y., Zhang Y., Yang W., Wu G., Qiu W., Chen H., Engineering the Underlying Surface to Manipulate the Growth of 2D Perovskites for Highly Efficient Solar Cells. *J. Mater. Chem. A* **2019,** *7* (23), 14027–14032.

103. Kuffner J., Wahl T., Schultes M., Hanisch J., Zillner J., Ahlswede E., Powalla M., Nanoparticle Wetting Agent for Gas Stream-Assisted Blade-Coated Inverted Perovskite Solar Cells and Modules. *ACS Appl. Mater. Interfaces* **2020,** *12* (47), 52678–52690.

104. Wang J., Xu J., Li Z., Lin X., Yu C., Wu H., Wang H.-l., Front-Contact Passivation of PIN $MAPbI_3$ Solar Cells with Superior Device Performances. *ACS Appl. Energy Mater.* **2020,** *3* (7), 6344–6351.

105. Tang G., You P., Tai Q., Yang A., Cao J., Zheng F., Zhou Z., Zhao J., Chan P. K. L., Yan F., Solution-Phase Epitaxial Growth of Perovskite Films on 2D Material Flakes for High-Performance Solar Cells. *Adv. Mater.* **2019,** *31* (24), e1807689.

106. Cao J., Tang G., You P., Wang T., Zheng F., Zhao J., Yan F., Enhanced Performance of Planar Perovskite Solar Cells Induced by Van Der Waals Epitaxial Growth of Mixed Perovskite Films on WS_2 Flakes. *Adv. Funct. Mater.* **2020,** *30* (38), 2002358.

107. Wu C., Fang W., Cheng Q., Wan J., Wen R., Wang Y., Song Y., Li M., MXene-Regulated Perovskite Vertical Growth for High-Performance Solar Cells. *Angew. Chem., Int. Ed.* **2022,** *61* (43), e202210970.

108. Cao J., Chen Q., Wu W., Fu J., Zhang Z., Chen L., Wang R., Yu W., Wang L., Nie X., Zhang J., Zhou Y., Song B., Li Y., Chlorinated-$Ti_3C_2T_F$ as a Dual-Functional Buried Interface on SnO_2 Electron-Transporting Layers for 25.09% High-Performance *n–i–p* Perovskite Solar Cells. *Energy Environ. Sci.* **2024,** *17* (10), 3454–3469.

109. Luo C., Zheng G., Gao F., Wang X., Zhan C., Gao X., Zhao Q., Engineering the buried interface in perovskite solar cells via lattice-matched electron transport layer. *Nat. Photonics* **2023,** *17* (10), 856–864.

110. Khenkin M. V., Katz E. A., Abate A., Bardizza G., Berry J. J., Brabec C., Brunetti F., Bulović V., Burlingame Q., Di Carlo A., Cheacharoen R., Cheng Y.-B., Colsmann A., Cros S., Domanski K., Dusza M., Fell C. J., Forrest S. R., Galagan Y., Di Girolamo D., Grätzel M., Hagfeldt A., von Hauff E., Hoppe H., Kettle J., Köbler H., Leite M. S., Liu S., Loo Y.-L., Luther J. M., Ma C.-Q., Madsen M., Manceau M., Matheron M., McGehee M., Meitzner R., Nazeeruddin M. K., Nogueira A. F., Odabaşı Ç., Osherov

A., Park N.-G., Reese M. O., De Rossi F., Saliba M., Schubert U. S., Snaith H. J., Stranks S. D., Tress W., Troshin P. A., Turkovic V., Veenstra S., Visoly-Fisher I., Walsh A., Watson T., Xie H., Yıldırım R., Zakeeruddin S. M., Zhu K., Lira-Cantu M., Consensus Statement for Stability Assessment and Reporting for Perovskite Photovoltaics Based on ISOS Procedures. *Nat. Energy* **2020,** *5* (1), 35–49.

111. Zhang W. X., Guo X. M., Cui Z. B., Yuan H. B., Li Y. F., Li W., Li X. D., Fang J. F., Strategies for Improving Efficiency and Stability of Inverted Perovskite Solar Cells. *Adv. Mater.* **2024,** *36* (37), 2311025.

112. Lan Z.-R., Shao J.-Y., Zhong Y.-W., Self-Assembled Monolayers as Hole-Transporting Materials for Inverted Perovskite Solar Cells. *Mol. Syst. Des. Eng.* **2023,** *8* (12), 1440–1455.

113. Kim Y., Jung E. H., Kim G., Kim D., Kim B. J., Seo J., Sequentially Fluorinated PTAA Polymers for Enhancing V_{OC} of High-Performance Perovskite Solar Cells. *Adv. Energy Mater.* **2018,** *8* (29), 1801668.

114. Hu W., Jin X., Li A., Liu C. L., Wang X. F., Efficiency Improvement of Inverted Perovskite Solar Cells Enabled by PTAA/MoS_2 Double Hole Transporters. *Nanotechnology* **2022,** *33* (33), 335202.

115. Li Y., Wang B., Liu T., Zeng Q., Cao D., Pan H., Xing G., Interfacial Engineering of PTAA/Perovskites for Improved Crystallinity and Hole Extraction in Inverted Perovskite Solar Cells. *ACS Appl. Mater. Interfaces* **2022,** *14* (2), 3284–3292.

116. Wang C., Su Z., Chen L., Zhang H., Hui W., Liang D., Zheng G., Zhang L., Tang Z., Wen W., Tang J., Huang Q., Song F., Chen Q., Gao X., MoO_3 Doped PTAA for High-Performance Inverted Perovskite Solar Cells. *Appl. Surf. Sci.* **2022,** *571*, 151301.

117. Rombach F. M., Haque S. A., Macdonald T. J., Lessons Learned from Spiro-OMeTAD and PTAA in Perovskite Solar Cells. *Energy Environ. Sci.* **2021,** *14* (10), 5161–5190.

118. Liu Y., Liu Z., Lee E.-C., High-Performance Inverted Perovskite Solar Cells Using Doped Poly(triarylamine) as the Hole Transport Layer. *ACS Appl. Energy Mater.* **2019,** *2* (3), 1932–1942.

119. Wang Q., Bi C., Huang J., Doped Hole Transport Layer for Efficiency Enhancement in Planar Heterojunction Organolead Trihalide Perovskite Solar Cells. *Nano Energy* **2015,** *15*, 275–280.

120. Luo J., Xia J., Yang H., Chen L., Wan Z., Han F., Malik H. A., Zhu X., Jia C., Toward High-Efficiency, Hysteresis-Less, Stable Perovskite Solar Cells: Unusual Doping of a Hole-Transporting

Material Using a Fluorine-Containing Hydrophobic Lewis Acid. *Energy Environ. Sci.* **2018,** *11* (8), 2035–2045.

121. Jiang Q., Zhao Y., Zhang X., Yang X., Chen Y., Chu Z., Ye Q., Li X., Yin Z., You J., Surface Passivation of Perovskite Film for Efficient Solar Cells. *Nat. Photonics* **2019,** *13* (7), 460–466.

122. Sun S., Li P., Liang S., Yang Z., Diversified Copper Sulfide ($Cu_{2-X}S$) Micro-/Nanostructures: A Comprehensive Review on Synthesis, Modifications and Applications. *Nanoscale* **2017,** *9* (32), 11357–11404.

123. Xie Y., Riedinger A., Prato M., Casu A., Genovese A., Guardia P., Sottini S., Sangregorio C., Miszta K., Ghosh S., Pellegrino T., Manna L., Copper Sulfide Nanocrystals with Tunable Composition by Reduction of Covellite Nanocrystals with Cu^+ Ions. *J. Am. Chem. Soc.* **2013,** *135* (46), 17630–17637.

124. Rao H., Sun W., Ye S., Yan W., Li Y., Peng H., Liu Z., Bian Z., Huang C., Solution-Processed CuS NPs as an Inorganic Hole-Selective Contact Material for Inverted Planar Perovskite Solar Cells. *ACS Appl. Mater. Interfaces* **2016,** *8* (12), 7800–7805.

125. Tirado J., Roldán-Carmona C., Muñoz-Guerrero F. A., Bonilla-Arboleda G., Ralaiarisoa M., Grancini G., Queloz V. I. E., Koch N., Nazeeruddin M. K., Jaramillo F., Copper Sulfide Nanoparticles as Hole-Transporting-Material in a Fully-Inorganic Blocking Layers *n-i-p* Perovskite Solar Cells: Application and Working Insights. *Appl. Surf. Sci.* **2019,** *478*, 607–614.

126. Hu R., Zhang R., Ma Y., Liu W., Chu L., Mao W., Zhang J., Yang J., Pu Y., Li X. a., Enhanced Hole Transfer in Hole-Conductor-Free Perovskite Solar Cells via Incorporating CuS Into Carbon Electrodes. *Appl. Surf. Sci.* **2018,** *462*, 840–846.

127. Sun Q., Sadhu A., Lie S., Wong L. H., Critical Review ofCu-Based Hole Transport Materials for Perovskite Solar Cells: From Theoretical Insights to Experimental Validation. *Adv. Mater.* **2024,** *36* (31), 2402412.

128. Kundu J., Pradhan D., Controlled Synthesis and Catalytic Activity of Copper Sulfide Nanostructured Assemblies with Different Morphologies. *ACS Appl. Mater. Interfaces* **2014,** *6* (3), 1823–1834.

129. Lei Y., Jia H., Zheng Z., Gao Y., Chen X., Hou H., A Very Facile, Low-Temperature, One-Step Route to In Situ Fabricate Copper Sulfide Nanosheet Thin Films. *CrystEngComm* **2011,** *13* (20), 6212–6217.

130. Muhsen M. M., Al-Jawad S. M. H., Taha A. A., Gum Arabic-modified Mn-doped CuS Nanoprisms for Cancer Photothermal Treatment. *Chem. Pap.* **2022,** *76* (11), 6821–6838.

131. Zhang H., Chen Z., Qin M., Ren Z., Liu K., Huang J., Shen D., Wu Z., Zhang Y., Hao J., Lee C. S., Lu X., Zheng Z., Yu W., Li G., Multifunctional Crosslinking-Enabled Strain-Regulating Crystallization for Stable, Efficient α-$FAPbI_3$-Based Perovskite Solar Cells. *Adv. Mater.* **2021,** *33* (29), 2008487.

132. Lee J. W., Dai Z., Han T. H., Choi C., Chang S. Y., Lee S. J., De Marco N., Zhao H., Sun P., Huang Y., Yang Y., 2D Perovskite Stabilized Phase-Pure Formamidinium Perovskite Solar Cells. *Nat. Commun.* **2018,** *9* (1), 3021.

133. Meng W., Zhang K., Osvet A., Zhang J., Gruber W., Forberich K., Meyer B., Heiss W., Unruh T., Li N., Brabec C. J., Revealing the Strain-Associated Physical Mechanisms Impacting the Performance and Stability of Perovskite Solar Cells. *Joule* **2022,** *6* (2), 458–475.

134. Sreelekha N., Subramanyam K., Amaranatha Reddy D., Murali G., Ramu S., Rahul Varma K., Vijayalakshmi R. P., Structural, Optical, Magnetic and Photocatalytic Properties of Co Doped CuS Diluted Magnetic Semiconductor Nanoparticles. *Appl. Surf. Sci.* **2016,** *378*, 330–340.

135. Jiang Z., Fu J., Zhang J., Chen Q., Zhang Z., Ji W., Wang A., Zhang T., Zhou Y., Song B., Reducing Trap Densities of Perovskite Films by the Addition of Hypoxanthine for High-Performance and Stable Perovskite Solar Cells. *Chem. Eng. J.* **2022,** *436*, 135269.

136. Chen Q., Yang X., Zhang J., Fu J., Jiang Z., Song B., Xu P., Zhou Y., Defect Passivation by a Betaine-Based Zwitterionic Molecule for High-Performance *p-i-n* Methylammonium-Based Perovskite Solar Cells. *Sol. Energy Mater. Sol. Cells* **2024,** *264*, 112615.

137. Lei H., Yang G., Zheng X., Zhang Z.-G., Chen C., Ma J., Guo Y., Chen Z., Qin P., Li Y., Fang G., Incorporation of High-Mobility and Room-Temperature-Deposited Cu_xS as a Hole Transport Layer for Efficient and Stable Organo-Lead Halide Perovskite Solar Cells. *Sol. RRL* **2017,** *1* (6), 1700038.

138. Lei H., Fang G., Cheng F., Ke W., Qin P., Song Z., Zheng Q., Fan X., Huang H., Zhao X., Enhanced Efficiency in Organic Solar Cells via In Situ Fabricated p-Type Copper Sulfide as the Hole Transporting Layer. *Sol. Energy Mater. Sol. Cells* **2014,** *128*, 77–84.

139. Yao X., Fang Z., Ren H., Mu X., Xiao G. B., Zou X., Cao J., A Heteronuclear W/Cu/S Clusters-Based Donor–Acceptor Polymer for Perovskite Solar Cells. *Adv. Funct. Mater.* **2024,** *34* (42), 2404671.

140. You W., Ma Z., Du Z., Chen Y., Yang J., Yang Q., Huang Z., Hou S., Li Y., Zhang Q., Du H., Li Y., Gou F., Lv Z., Yu H., Xiang Y., Huang C., Yu J., Mai Y., Jiang F., Slow-Release Effect Assisted Crystallization for Sequential Deposition Realizes Efficient Inverted Perovskite Solar Cells. *ACS Appl. Mater. Interfaces* **2024,** *16* (22), 28905–28916.

141. Wu Y., Islam A., Yang X., Qin C., Liu J., Zhang K., Peng W., Han L., Retarding the Crystallization of PbI_2 for Highly Reproducible Planar-Structured Perovskite Solar Cells via Sequential Deposition. *Energy Environ. Sci.* **2014,** *7* (9), 2934–2938.

142. Yang W. S., Noh J. H., Jeon N. J., Kim Y. C., Ryu S., Seo J., Seok S. I., High-Performance Photovoltaic Perovskite Layers Fabricated Through Intramolecular Exchange. *Science* **2015,** *348* (6240), 1234–1237.

143. Zhang H., Ren X., Chen X., Mao J., Cheng J., Zhao Y., Liu Y., Milic J., Yin W.-J., Grätzel M., Choy W. C. H., Improving the Stability and Performance of Perovskite Solar Cells via Off-the-Shelf Post-Device Ligand Treatment. *Energy Environ. Sci.* **2018,** *11* (8), 2253–2262.

144. Choi K., Lee J., Kim H. I., Park C. W., Kim G.-W., Choi H., Park S., Park S. A., Park T., Thermally Stable, Planar Hybrid Perovskite Solar Cells with High Efficiency. *Energy Environ. Sci.* **2018,** *11* (11), 3238–3247.

145. Zheng H., Liu G., Wang Y., Chen F., Dong X., Wang C., Wu C., Yang L., Ren X., Yang L., Pan X., Huang Z., Directional Management Self-Additive Spacer Cations for Stable 2D Ruddlesden–Popper Perovskite Solar Cells with Efficiency over 21%. *Adv. Funct. Mater.* **2024,** *34* (32), 2401546.

146. Wang F., Zhou K., Zhou C., Liang X., Wang T., Sun Y., Li Y., Li Q., Zhou X., Yang G., Duan D., Zhu J., Zhu Q., Lin H., Shi Y., Yang C., Xing G., Hu H., Ionic Liquid-Induced 1D Perovskite: Exploring 1D Perovskite Structure to 1D/3D Heterojunction-Based Photovoltaics. *Adv. Energy Mater.* **2024,** *14* (23), 2400021.

147. Chen K., Wu J., Wang Y., Guo Q., Chen Q., Cao T., Guo X., Zhou Y., Chen N., Zhang M., Li Y., Defect Passivation by Alcohol-Soluble Small Molecules for Efficient *p–i–n* Planar Perovskite Solar Cells with High Open-Circuit Voltage. *J. Mater. Chem. A* **2019,** *7* (37), 21140–21148.

148. Li Y., Duan Y., Liu Z., Yang L., Li H., Fan Q., Zhou H., Sun Y., Wu M., Ren X., Yuan N., Ding J., Yang S., Liu S., In Situ Synthesized Low-Dimensional Perovskite for >25% Efficiency Stable MA-Free Perovskite Solar Cells. *Adv. Mater.* **2024,** *36* (21), 2310711.

149. Li Y., Nie T., Ren X., Wu Y., Zhang J., Zhao P., Yao Y., Liu Y., Feng J., Zhao K., Zhang W., Liu S., In Situ Formation of 2D Perovskite Seeding for Record-Efficiency Indoor Perovskite Photovoltaic Devices. *Adv. Mater.* **2023,** *36* (1), 2306870.

150. Bu T., Wu L., Liu X., Yang X., Zhou P., Yu X., Qin T., Shi J., Wang S., Li S., Ku Z., Peng Y., Huang F., Meng Q., Cheng Y.-B., Zhong J., Synergic Interface Optimization with Green Solvent Engineering in Mixed Perovskite Solar Cells. *Adv. Energy Mater.* **2017,** *7* (20), 1700576.

151. Li G., Hu Y., Li M., Tang Y., Zhang Z., Musiienko A., Cao Q., Akhundova F., Li J., Prashanthan K., Yang F., Janasik P., Appiah A. N. S., Trofimov S., Livakas N., Zuo S., Wu L., Wang L., Yang Y., Agyei-Tuffour B., MacQueen R. W., Naydenov B., Unold T., Unger E., Aktas E., Eigler S., Abate A., Managing Excess Lead Iodide with Functionalized Oxo-Graphene Nanosheets for Stable Perovskite Solar Cells. *Angew. Chem., Int. Ed.* **2023,** *62* (39), e202307395.

152. Cao X., Zhi L., Li Y., Fang F., Cui X., Yao Y., Ci L., Ding K., Wei J., Control of the Morphology of PbI_2 Films for Efficient Perovskite Solar Cells by Strong Lewis Base Additives. *J. Mater. Chem. C* **2017,** *5* (30), 7458–7464.

153. Zhou M., Zhang R., Huang M., Lu W., Song S., Melancon M. P., Tian M., Liang D., Li C., A Chelator-Free Multifunctional [^{64}Cu]CuS Nanoparticle Platform for Simultaneous Micro-PET/CT Imaging and Photothermal Ablation Therapy. *J. Am. Chem. Soc.* **2010,** *132* (43), 15351–15358.

154. Chen Q., Asgarimoghaddam H., Ji W., Wu W., Cao J., Wang R., Yu W., Nie X., Zhou Y., Song B., Musselman K. P., CuS Nanosheets as Additives in the Hole Transport Layers for Stable *p-i-n* Perovskite Solar Cells. *Nano Energy* **2025,** *135*, 110652.

155. Yan K., Long M., Zhang T., Wei Z., Chen H., Yang S., Xu J., Hybrid Halide Perovskite Solar Cell Precursors: Colloidal Chemistry and Coordination Engineering behind Device Processing for High Efficiency. *J. Am. Chem. Soc.* **2015,** *137* (13), 4460–4468.

156. Zhang Y., Wang Y., Yang X., Zhao L., Su R., Wu J., Luo D., Li S., Chen P., Yu M., Gong Q., Zhu R., Mechanochemistry Advances High-Performance Perovskite Solar Cells. *Adv. Mater.* **2022,** *34* (6), e2107420.

157. Chen X., Xu W., Ding N., Ji Y., Pan G., Zhu J., Zhou D., Wu Y., Chen C., Song H., Dual Interfacial Modification Engineering with 2D MXene Quantum Dots and Copper Sulphide Nanocrystals Enabled High‐Performance Perovskite Solar Cells. *Adv. Funct. Mater.* **2020,** *30* (30), 2003295.

158. Kiermasch D., Gil-Escrig L., Baumann A., Bolink H. J., Dyakonov V., Tvingstedt K., Unravelling Steady-State Bulk Recombination Dynamics in Thick Efficient Vacuum-Deposited Perovskite Solar Cells by Transient Methods. *J. Mater. Chem. A* **2019,** *7* (24), 14712–14722.

159. Fu J., Zhang J., Zhang T., Yuan L., Zhang Z., Jiang Z., Huang Z., Wu T., Yan K., Zhang L., Wang A., Ji W., Zhou Y., Song B., Synergistic Effects of Interfacial Energy Level Regulation and Stress Relaxation via a Buried Interface for Highly Efficient Perovskite Solar Cells. *ACS Nano* **2023,** *17* (3), 2802–2812.

160. Sangale S. S., Kwon S. N., Patil P., Lee H. J., Na S. I., Locally Supersaturated Inks for a Slot-Die Process to Enable Highly Efficient and Robust Perovskite Solar Cells. *Adv. Energy Mater.* **2023,** *13* (33), 2300537.

161. Zhang H., Hui W., Wang Z., Li M., Xi H., Zheng Y., Liu X., Ultraviolet-Light Induced H^+ Doping in Polymer Hole Transport Material for Highly Efficient Perovskite Solar Cells. *Mater. Today Energy* **2022,** *30*, 101159.

162. Shi P., Ding Y., Ding B., Xing Q., Kodalle T., Sutter-Fella C. M., Yavuz I., Yao C., Fan W., Xu J., Tian Y., Gu D., Zhao K., Tan S., Zhang X., Yao L., Dyson P. J., Slack J. L., Yang D., Xue J., Nazeeruddin M. K., Yang Y., Wang R., Oriented Nucleation in Formamidinium Perovskite for Photovoltaics. *Nature* **2023,** *620* (7973), 323–327.

163. Zhu N. X., Wei Z. W., Chen C. X., Wang D., Cao C. C., Qiu Q. F., Jiang J. J., Wang H. P., Su C. Y., Self-Generation of SurfaceRoughness by Low-Surface-Energy Alkyl Chains for Highly Stable Superhydrophobic/Superoleophilic MOFs with Multiple Functionalities. *Angew. Chem., Int. Ed.* **2019,** *58* (47), 17033–17040.

164. Wang D., Huang L., Chen Q., Hu L., Zeng F., Zhou X., Zhang L., Liu C., Wang X., Yan L., Xu B., A Dual Function-Enabled Novel Zwitterion to Stabilize a Pb-I Framework and Passivate Defects for Highly Efficient Inverted Planar Perovskite Solar Cells. *Chem. Commun.* **2020,** *56* (51), 6929–6932.

165. Chen Q., Nie X., Ji W., Su R., Yang X., Wu W., Wang R., Zhang Z., Musselman K. P., Zhou Y., Song B., Soybean Lecithin as a Passivator and Compatibilizer in *p-i-n* Perovskite Solar Cells. *ACS Appl. Mater. Interfaces* **2025,** *17* (31), 44481–44489.

166. Zhao Y., Li M., Qin X., Yang P., Zhang W.-H., Wei Z., Efficient Perovskite Light-Emitting Diodes by Buried Interface Modification with Triphenylphosphine Oxide. *ACS Appl. Mater. Interfaces* **2023,** *15* (2), 3644–3650.

167. Yukta, Chini M. K., Ranjan R., Satapathi S., Lewis Base Passivation of Quasi-2D Ruddlesden−Popper Perovskite for Order of Magnitude Photoluminescence Enhancement and Improved Stability. *ACS Appl. Electron. Mater.* **2021,** *3* (4), 1572–1582.

168. Zhang X., Luo Y., Wang X., Zhao K., Shi P., Tian Y., Xu J., Yao L., Sun J., Liu Q., Fan W., Wang R., Xue J., Locking Surface Dimensionality for Endurable Interface in Perovskite Photovoltaics. *Carbon Energy* **2025,** *7* (4), e718.

169. Shao N., Chen Q., Tao R., Yu W., Nie X., Ji W., Su Y., Zhou Y., Song B., Pb Defect Passivation and FA Immobilization: Towards Efficient and Stable Perovskite Solar Cells. *J. Mater. Chem. A* **2025,** *13* (22), 16870–16878.

170. Chen Q., Yang X., Zhou Y., Song B., Zwitterions: Promising Interfacial/Doping Materials for Organic/Perovskite Solar Cells. *New J. Chem.* **2021,** *45* (34), 15118–15130.

171. Xie F., Chen C.-C., Wu Y., Li X., Cai M., Liu X., Yang X., Han L., Vertical Recrystallization for Highly Efficient and Stable Formamidinium-Based Inverted-Structure Perovskite Solar Cells. *Energy Environ. Sci.* **2017,** *10* (9), 1942–1949.

172. Xu G., Muhammad I., Zhang Y., Zheng X., Xin M., Gao H., Li J., Liu C., Chen W., Tang J., Yang F., Su Y., Han P., Sheng Y., Khan D., Wang X., Tang Z., Amidinopyridine Ion Docking in Crown Ether Cavity to Modulate the Top Interface in Inverted Perovskite Solar Cells. *Adv. Energy Mater.* **2024,** *15* (18), 2405088.

173. Xi J., Wang H., Yuan J., Yan X., Siffalovic P., Tian J., High-Quality α-$FAPbI_3$ Film Assisted by Lead Acetate for Efficient Solar Cells. *Sol. RRL* **2021,** *5* (12), 2100747.

174. Zhang K., Forberich K., Lüer L., Cerrillo J. G., Meng W., Du X., Le Corre V. M., Zhao Y., Niu T., Xue Q., Koster L. J. A., Li N., Brabec C. J., Understanding the Limitations of Charge Transporting Layers in Mixed Lead-Tin Halide Perovskite Solar Cells. *Adv. Energy Sustainability Res.* **2021,** *3* (3), 2100156.

175. Wu W., Chen Q., Cao J., Fu J., Zhang Z., Chen L., Rui D., Zhang J., Zhou Y., Song B., Chirality-Induced Crystallization and Defect Passivation of Perovskites: Toward High-Performance Solar Cells. *ACS Appl. Mater. Interfaces* **2024,** *16* (13), 16340–16350.

176. Gan Y., Hao X., Li W., Zhang J., Wu L., Additive Combining Passivator for Inverted Wide-Bandgap Perovskite Solar Cells with 22% Efficiency and Reduced Voltage Loss. *Sol. RRL* **2023,** *7* (24), 2300519.

177. Azam M., Ke Z., Luo J., Wan Z., Hassan A., Jia C., Additive Engineering Enabled Non-Radiative Defect Passivation with Improved Moisture-Resistance in Efficient and Stable Perovskite Solar Cells. *Chem. Eng. J.* **2024,** *483*, 149424.

178. Wang Y., Yang T., Cai W., Mao P., Yang Y., Wu N., Liu C., Wang S., Du Y., Huang W., Zhao G., Ding Z., Yuan N., Ding J., Zhong Y., Liu S. F., Zhao K., Defect Passivation Refinement in Perovskite Photovoltaics: Achieving Efficiency over 45% under Low-Light and Low-Temperature Dual Extreme Conditions. *Adv. Mater.* **2024,** *36* (23), e2312014.

179. Wang J., Bi L., Fu Q., Jen A. K. Y., Methods for Passivating Defects of Perovskite for Inverted Perovskite Solar Cells and Modules. *Adv. Energy Mater.* **2024,** *14* (35), 2401414.

180. Zhang C., Li H. Y., Gong C., Zhuang Q. X., Chen J. Z., Zang Z. G., Crystallization Manipulation and Holistic Defect Passivation Toward Stable and Efficient Inverted Perovskite Solar Cells. *Energy Environ. Sci.* **2023,** *16* (9), 3825-3836.

181. El‐Mellouhi F., Marzouk A., Bentria E. T., Rashkeev S. N., Kais S., Alharbi F. H., Hydrogen Bonding and Stability of Hybrid Organic–Inorganic Perovskites. *ChemSusChem* **2016,** *9* (18), 2648–2655.

182. Lin L., Jones T. W., Yang T. C.-J., Li X., Wu C., Xiao Z., Li H., Li J., Qian J., Lin L., Shi J. Q., Stranks S. D., Wilson G. J., Wang X., Hydrogen Bonding in Perovskite Solar Cells. *Matter* **2024,** *7* (1), 38–58.

183. Cheng L., Liu Z., Li S., Zhai Y., Wang X., Qiao Z., Xu Q., Meng K., Zhu Z., Chen G., Highly Thermostable and Efficient Formamidinium‐Based Low‐Dimensional Perovskite Solar Cells. *Angew. Chem., Int. Ed.* **2020,** *60* (2), 856–864.

184. Amat A., Mosconi E., Ronca E., Quarti C., Umari P., Nazeeruddin M. K., Gratzel M., De Angelis F., Cation-Induced Band-Gap Tuning in Organohalide Perovskites: Interplay of Spin-Orbit Coupling and Octahedra Tilting. *Nano Lett.* **2014,** *14* (6), 3608–3016.

185. Weller M. T., Weber O. J., Henry P. F., Di Pumpo A. M., Hansen T. C., Complete Structure and Cation Orientation in the Perovskite Photovoltaic Methylammonium Lead Iodide Between 100 and 352 K. *Chem. Commun.* **2015,** *51* (20), 4180–4183.

186. Kanno S., Imamura Y., Hada M., First-Principles Calculations of the Rotational Motion and Hydrogen Bond Capability of Large Organic Cations in Hybrid Perovskites. *J. Phys. Chem. C* **2018,** *122* (28), 15966–15972.

187. Li H., Wines D., Chen B., Yumigeta K., Sayyad Y. M., Kopaszek J., Yang S., Ataca C., Sargent E. H., Tongay S., Abnormal Phase Transition and Band Renormalization of Guanidinium-Based Organic-Inorganic Hybrid Perovskite. *ACS Appl. Mater. Interfaces* **2021,** *13* (37), 44964–44971.

188. Kim Y.-H., Kim S., Kakekhani A., Park J., Park J., Lee Y.-H., Xu H., Nagane S., Wexler R. B., Kim D.-H., Jo S. H., Martínez-Sarti L., Tan P., Sadhanala A., Park G.-S., Kim Y.-W., Hu B., Bolink H. J., Yoo S., Friend R. H., Rappe A. M., Lee T.-W., Comprehensive Defect Suppression in Perovskite Nanocrystals for High-Efficiency Light-Emitting Diodes. *Nat. Photonics* **2021,** *15* (2), 148–155.

189. Giorgi G., Fujisawa J.-I., Segawa H., Yamashita K., Organic–Inorganic Hybrid Lead Iodide Perovskite Featuring Zero Dipole Moment Guanidinium Cations: A Theoretical Analysis. *J. Phys. Chem. C* **2015,** *119* (9), 4694–4701.

190. Wang K., Ma S., Xue X., Li T., Sha S., Ren X., Zhang J., Lu H., Ma J., Guo S., Liu Y., Feng J., Najar A., Liu S., Highly Efficient and Stable $CsPbTh_3$ (Th = I, Br, Cl) Perovskite Solar Cells by Combinational Passivation Strategy. *Adv. Sci.* **2022,** *9* (9), 202105103.

191. Bing J., Huang S., Ho-Baillie A. W. Y., A Review on Halide Perovskite Film Formation by Sequential Solution Processing for Solar Cell Applications. *Energy Technol.* **2019,** *8* (4), 1901114.

192. Antony C. J., Bushiri M. J., Varghese H. T., Panicker C. Y., Fleck M., Spectroscopic Properties of Guanidinium Zinc Sulphate $[C(NH_2)_3]_2Zn(SO_4)_2$ and Ab Initio Calculations of $[C(NH_2)_3]_2$ and $HC(NH_2)_3$. *Spectrochim. Acta, Part A* **2009,** *73* (5), 942–945.

193. Li F., Deng X., Shi Z., Wu S., Zeng Z., Wang D., Li Y., Qi F., Zhang Z., Yang Z., Jang S.-H., Lin F. R., Tsang S. W., Chen X.-K., Jen A. K. Y., Hydrogen-Bond-Bridged Intermediate for Perovskite Solar Cells With Enhanced Efficiency and Stability. *Nat. Photonics* **2023,** *17* (6), 478–484.

194. Yu G., Huang Y., Khan D., Sui Y., Wang S., Yang X., Zhou W., Chang K., Tang J., Chen W., Han P., Tang Z., $RbPbI_3$ Seed Embedding in PbI_2 Substrate Tailors the Facet Orientation and Crystallization Kinetics of Perovskites. *Small* **2024,** *20* (11), e2307219.

195. Wu T., Ji W., Zhang L., Chen Q., Fu J., Zhang J., Zhang Z., Zhou Y., Dong B., Song B., High-quality perovskite films prepared by nucleus epitaxial growth for efficient and stable perovskite solar cells. *J. Mater. Chem. A* **2023,** *11* (7), 3599–3607.

196. Yan N., Cao Y., Dai Z. H., Jiang L., Yang Y. B., Li T. T., Li L. W., Liu S. Z., Fang Z. M., Feng J. S., Heterogeneous Seed-Assisted $FAPbI_3$ Crystallization for Efficient Inverted Perovskite Solar Cells. *Energy Environ. Sci.* **2024,** *17* (14), 5070–5079.

Appendix A

Supporting Information of Chapter 4

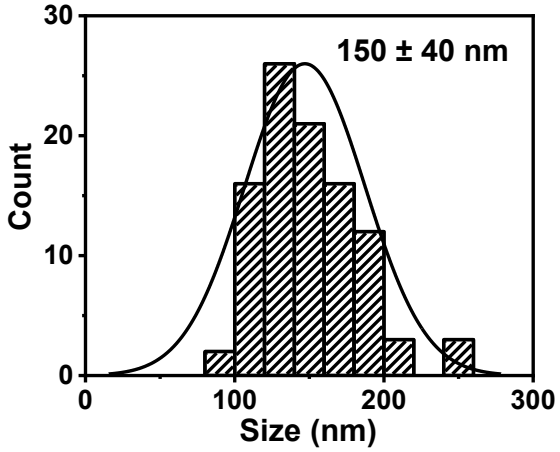


Figure A1 Size distribution of the CuS nanosheets.[144] Reprinted with permission from *Nano Energy* 2025, 135, 110652. Copyright 2025 The Author(s).

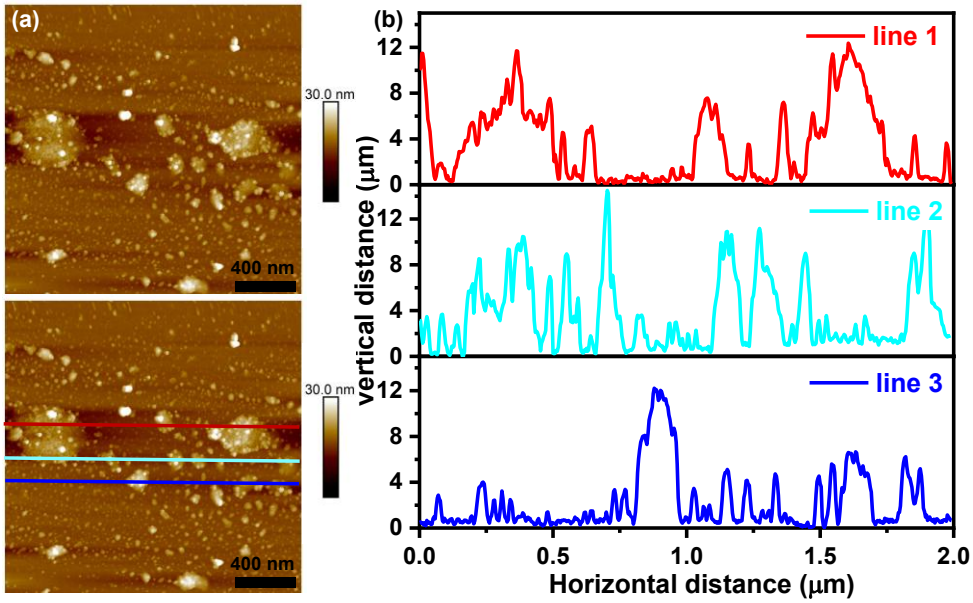


Figure A2 (a) AFM height image of CuS nanosheets on wafer. (b) The vertical distance of different sites in the AFM image.[144] Reprinted with permission from *Nano Energy* 2025, 135, 110652. Copyright 2025 The Author(s).

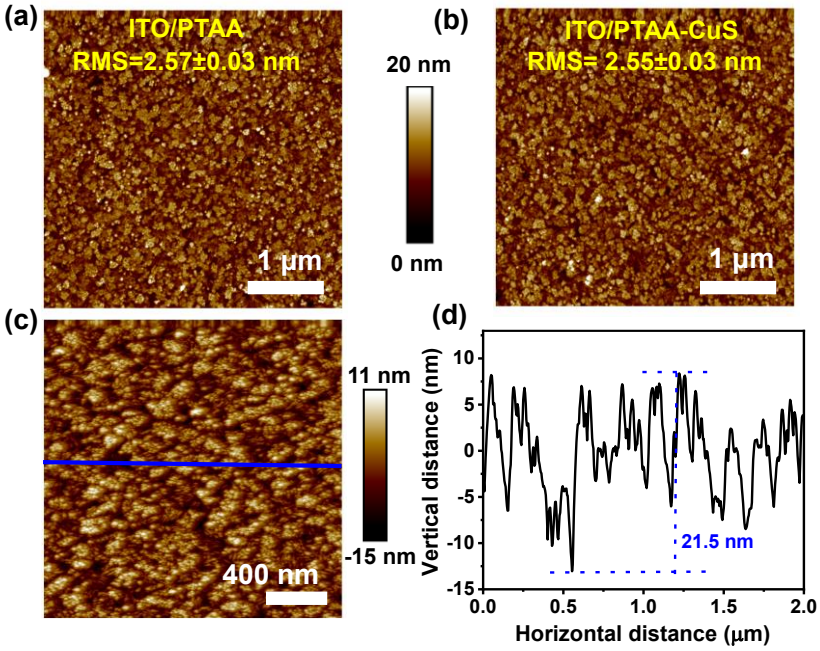


Figure A3 AFM height images of (a) pristine PTAA and (b) PTAA with CuS. (c) AFM image of bare ITO. (d) The vertical distance of ITO surface.[144] Reprinted with permission from *Nano Energy* 2025, 135, 110652. Copyright 2025 The Author(s).

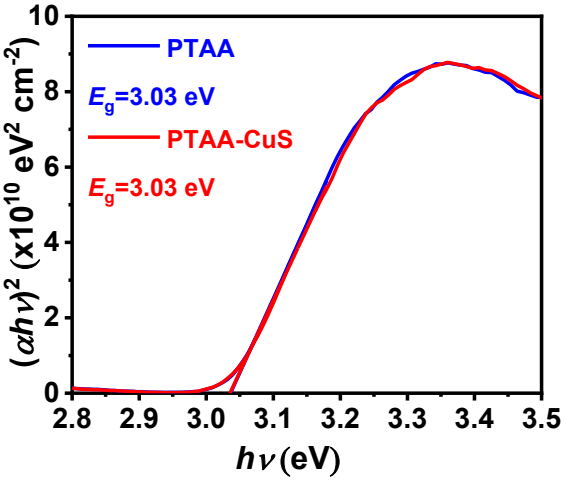


Figure A4 Tauc plots of (a) pristine PTAA and (b) PTAA with CuS films.[144] Reprinted with permission from *Nano Energy* 2025, 135, 110652. Copyright 2025 The Author(s).

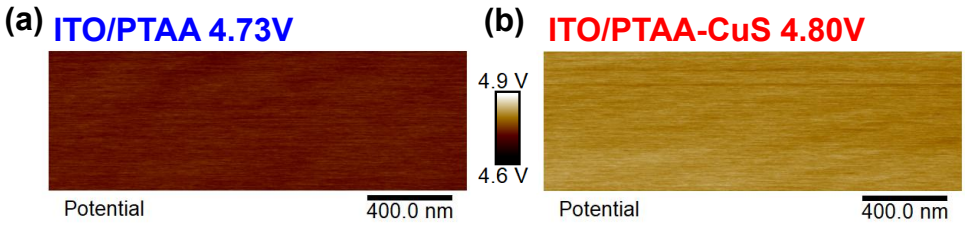


Figure A5 KPFM images of (a) ITO/PTAA and (b) ITO/PTAA-CuS.[144] Reprinted with permission from *Nano Energy* 2025, 135, 110652. Copyright 2025 The Author(s).

Table A1 Lifetimes and fractions derived from TRPL.[144] Reprinted with permission from *Nano Energy* 2025, 135, 110652. Copyright 2025 The Author(s).

	τ_1 (ns)	f_1 (%)	τ_2 (ns)	f_2 (%)	τ_{avg} (ns)
PTAA	53.3	15.7	716.2	84.3	612.1
PTAA-CuS	46.4	16.8	435.6	83.2	370.2

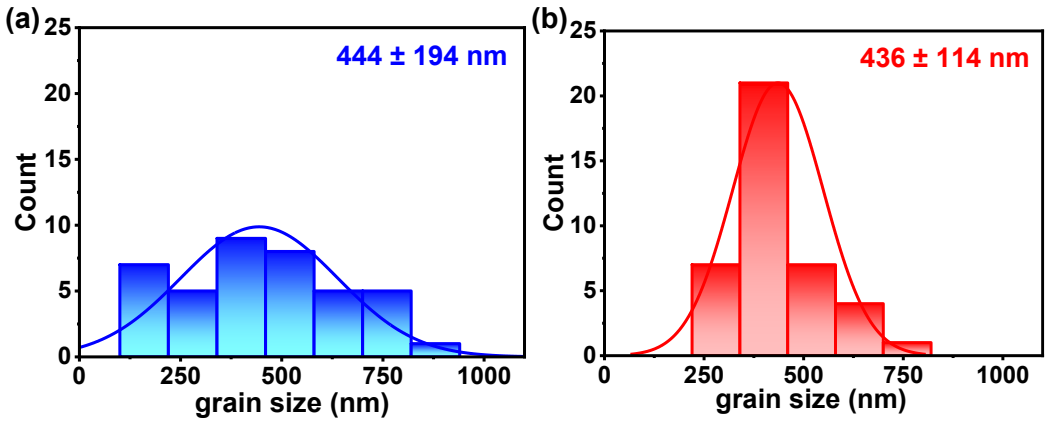


Figure A6 Grain size distribution of perovskite crystals formed on (a) PTAA and (b) PTAA-CuS.[144] Reprinted with permission from *Nano Energy* 2025, 135, 110652. Copyright 2025 The Author(s).

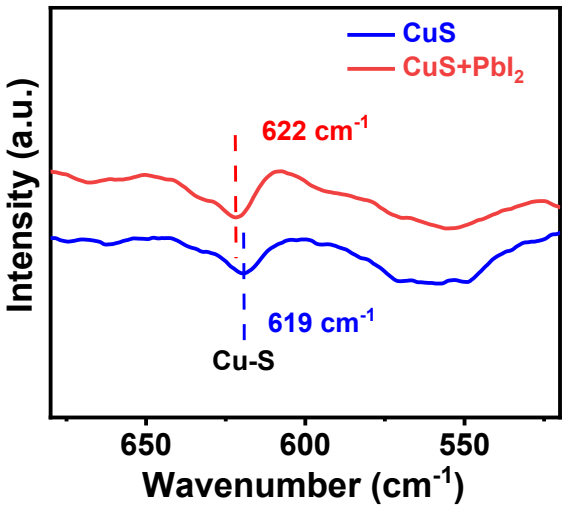


Figure A7 FTIR spectra of CuS and CuS + PbI_2.[144] Reprinted with permission from *Nano Energy* 2025, 135, 110652. Copyright 2025 The Author(s).

Table A2 Photovoltaic parameters of PSCs with different concentrations of CuS added to the PTAA. The average values were obtained from 15 devices.[144] Reprinted with permission from *Nano Energy* 2025, 135, 110652. Copyright 2025 The Author(s).

CuS		V_{OC} (V)	J_{SC} (mA cm^{-2})	FF(%)	PCE (%)
control	Best	1.04	25.28	83.4	21.99
	Average	1.03 ± 0.01	25.39 ± 0.19	82.7 ± 0.6	21.72 ± 0.15
0.01 mg/ml	Best	1.07	25.37	83.3	22.69
	Average	1.06 ± 0.01	25.40 ± 0.16	82.9 ± 1.1	22.37 ± 0.17
0.02 mg/ml	Best	1.06	25.55	84.5	22.92
	Average	1.05 ± 0.01	25.51 ± 0.14	82.5 ± 1.4	22.41 ± 0.21
0.03 mg/ml	Best	1.07	25.65	83.66	22.88
	Average	1.05 ± 0.01	25.33 ± 0.27	82.7 ± 1.2	22.36 ± 0.24

Table A3 Parameters of the equivalent circuit for Pero-SCs with or without CuS.[144] Reprinted with permission from *Nano Energy* 2025, 135, 110652. Copyright 2025 The Author(s).

	R_S(Ω)	R_{CT} (Ω)	C (nF)
control	9.80	56.50	4.02
PTAA-CuS	9.92	39.96	5.32

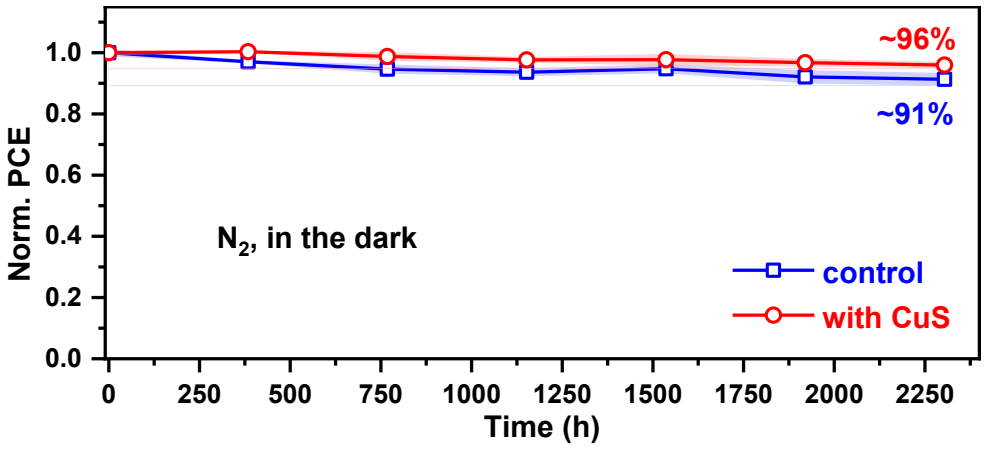


Figure A8 PCE evolution of Pero-SCs stored in N_2 and at room temperature. The data were analyzed from 5 samples for each group. All the samples were stored in the dark.[144] Reprinted with permission from *Nano Energy* 2025, 135, 110652. Copyright 2025 The Author(s).

Appendix B

Supporting Information of Chapter 5

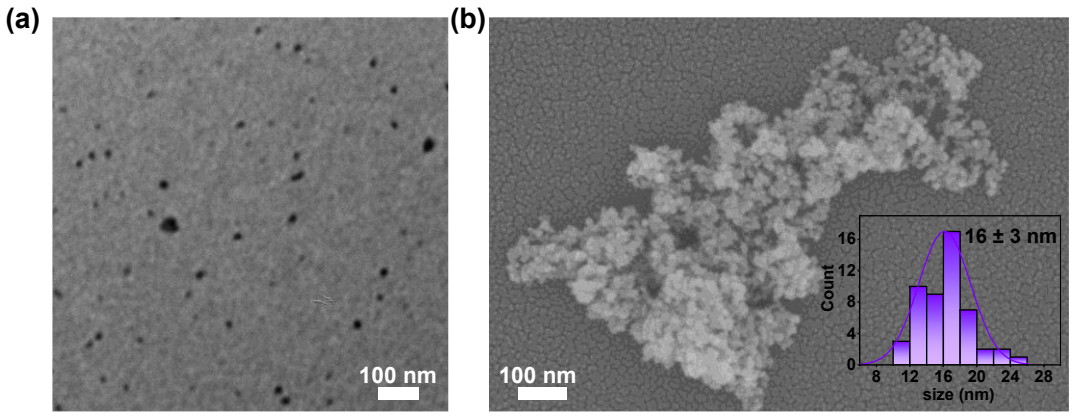


Figure B1 (a) TEM and (b) SEM images of CuS nanoparticles.

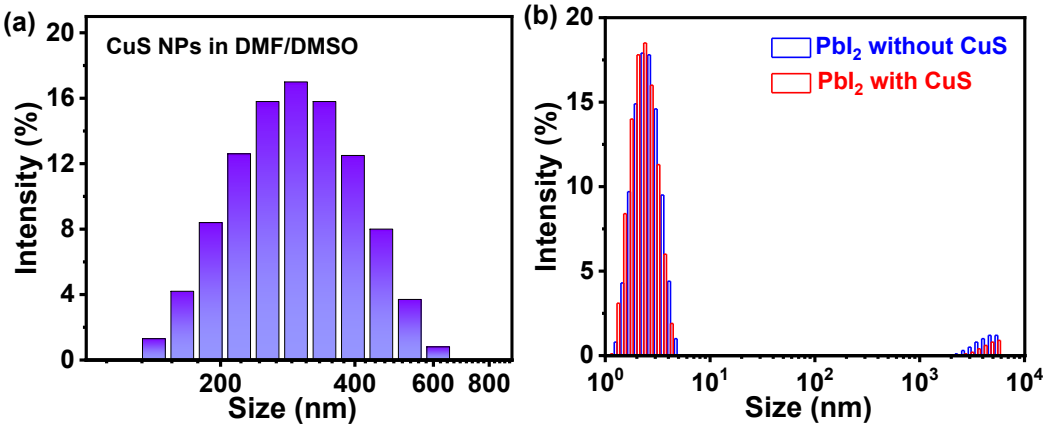


Figure B2 DLS results of (a) CuS nanoparticles in DMF/DMSO (b) PbI_2 precursor solutions without and with CuS nanoparticles.

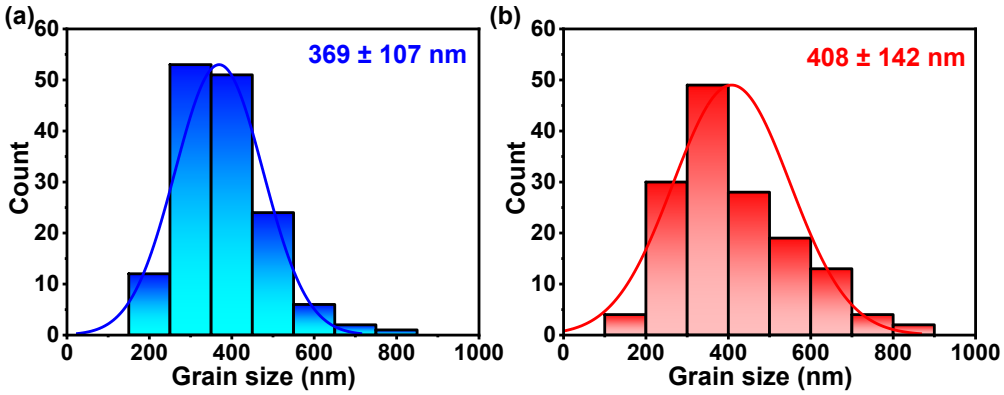


Figure B3 Grain size distribution of perovskite (a) without and (b) with CuS nanoparticles.

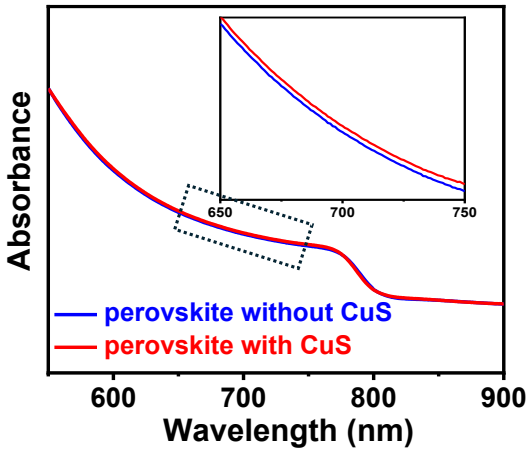


Figure B4 The absorbance plots of perovskite films without and with CuS nanoparticles.

Table B1 Lifetimes and fractions derived from TRPL.

	τ_1 (ns)	f_1 (%)	τ_2 (ns)	f_2 (%)
perovskite without CuS on glass	944.3	5.4	4274.6	94.6
perovskite with CuS on glass	1219.7	11.3	5712.8	88.7
perovskite without CuS on ITO/2PACz	355.1	6.3	1125.4	93.7
perovskite with CuS on ITO/2PACz	209.1	8.7	681.8	91.3

Table B2 Photovoltaic parameters of Pero-SCs with different concentrations of CuS nanoparticles. The average values were obtained from 15 devices.

CuS		V_{OC} (V)	J_{SC} (mA cm^{-2})	FF(%)	PCE (%)
control	Best	1.10	25.00	83.3	22.93
	Average	1.10±0.01	25.55±0.43	80.6±1.5	22.69±0.24
0.002 mg/ml	Best	1.13	24.99	83.5	23.48
	Average	1.11±0.01	25.71±0.41	81.9±1.2	23.29±0.08
0.004 mg/ml	Best	1.13	25.11	84.2	23.83
	Average	1.11±0.01	25.74±0.46	82.2±1.4	23.56±0.15
0.006 mg/ml	Best	1.12	25.15	84.3	23.72
	Average	1.11±0.01	25.44±0.26	82.7±1.1	23.40±0.17

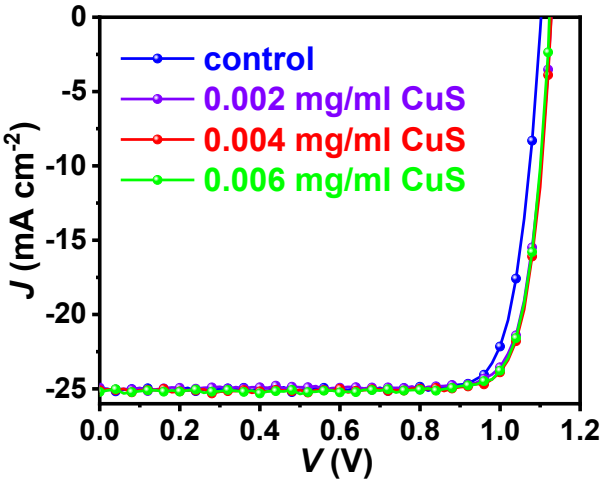


Figure B5 *J-V* curves of Pero-SC with different concentrations of CuS nanoparticles.

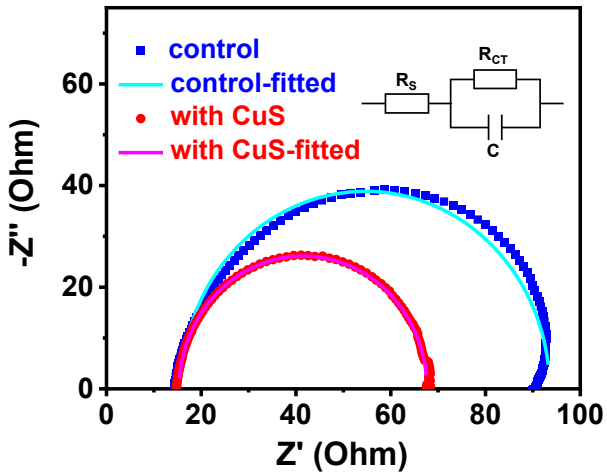


Figure B6 Nyquist plots of Pero-SCs without or with CuS nanoparticles.

Table B3 Parameters of the equivalent circuit for Pero-SCs with or without CuS nanoparticles.

	R_s (Ω)	R_{ct} (Ω)	C (nF)
control	15.77	77.74	18.3
with CuS	15.34	52.29	43.3

Appendix C

Supporting Information of Chapter 6

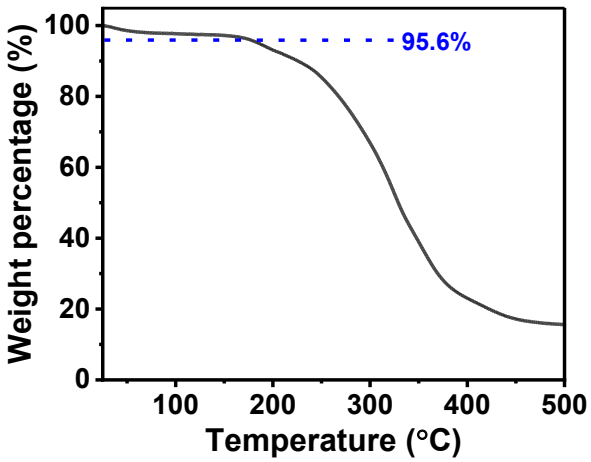


Figure C1 TGA analysis of SL measured in N_2.[165] Reprinted with permission from *ACS Appl. Mater. Interfaces* 2025, 17 (31), 44481–44489. Copyright 2025 American Chemical Society.

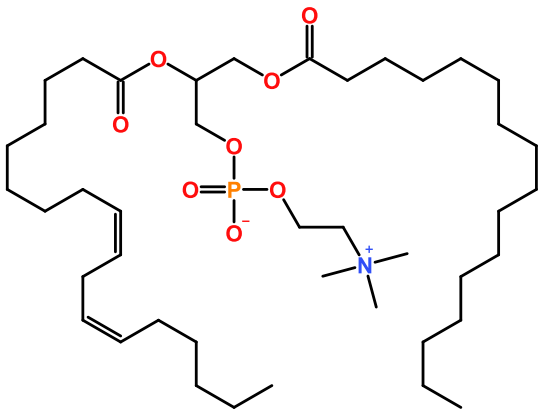


Figure C2 The chemical structure of SL.[165] Reprinted with permission from *ACS Appl. Mater. Interfaces* 2025, 17 (31), 44481–44489. Copyright 2025 American Chemical Society.

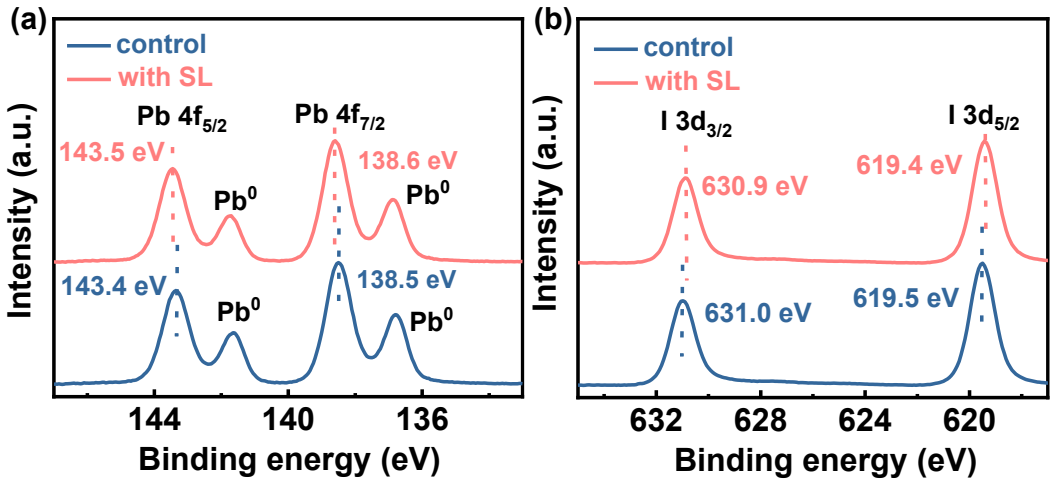


Figure C3 (a) Pb 4f and (b) I 3d XPS spectra of the perovskite films without and with SL.[165] Reprinted with permission from *ACS Appl. Mater. Interfaces* 2025, 17 (31), 44481–44489. Copyright 2025 American Chemical Society.

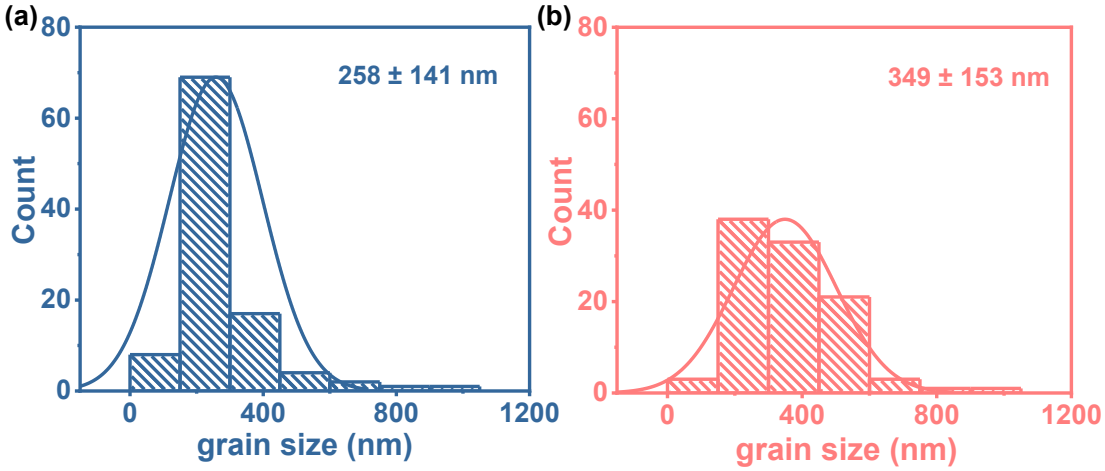


Figure C4 Grain size distributions of perovskite films (a) without and (b) with SL.[165] Reprinted with permission from *ACS Appl. Mater. Interfaces* 2025, 17 (31), 44481–44489. Copyright 2025 American Chemical Society.

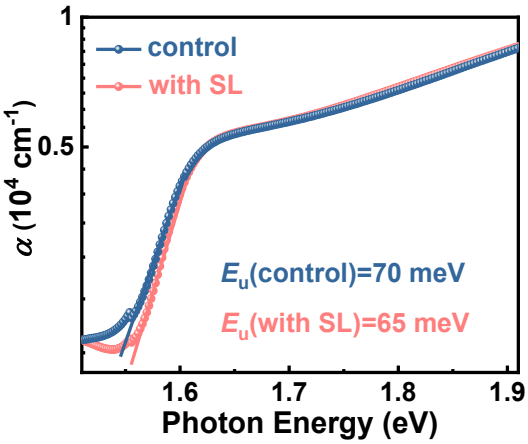


Figure C5 Absorption coefficient–photon energy plots of the perovskite films.[165] Reprinted with permission from *ACS Appl. Mater. Interfaces* 2025, 17 (31), 44481–44489. Copyright 2025 American Chemical Society.

Table C1 Photovoltaic parameters of Pero-SCs with different concentrations of SL.[165] Reprinted with permission from *ACS Appl. Mater. Interfaces* 2025, 17 (31), 44481–44489. Copyright 2025 American Chemical Society.

	τ_1 (ns)	f_1 (%)	τ_2 (ns)	f_2 (%)
control	258.9	26.1	688.0	73.9
with SL	417.6	12.4	1259.5	87.6

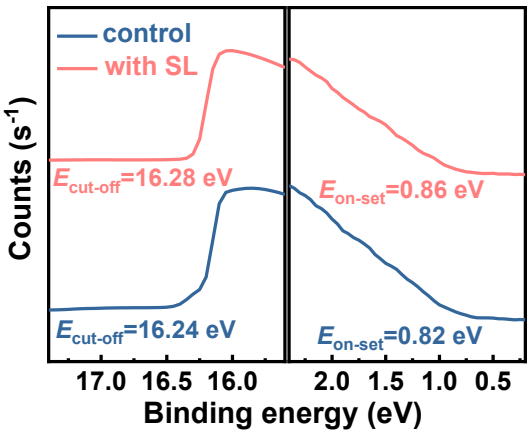


Figure C6 The UPS results of perovskite films without and with SL.[165] Reprinted with permission from *ACS Appl. Mater. Interfaces* 2025, 17 (31), 44481–44489. Copyright 2025 American Chemical Society.

Table C2 The values of the energy levels of perovskite films without and with SL.[165] Reprinted with permission from *ACS Appl. Mater. Interfaces* 2025, 17 (31), 44481–44489. Copyright 2025 American Chemical Society.

	WF (eV)	E_g (eV)	CB (eV)	VB (eV)
control	4.98	1.56	-5.80	-4.24
with SL	4.94	1.56	-5.80	-4.24

Table C3 Photovoltaic parameters of Pero-SCs with different concentrations of SL.[165] Reprinted with permission from *ACS Appl. Mater. Interfaces* 2025, 17 (31), 44481–44489. Copyright 2025 American Chemical Society.

SL (wt‰)	V_{OC}(V)	J_{SC} (mA cm^{-2})	FF (%)	PCE (%)
0	1.09	23.30	78.6	19.92
0.1	1.10	24.78	80.1	21.74
0.3	1.10	24.91	81.0	22.17
0.5	1.09	24.71	79.3	21.45

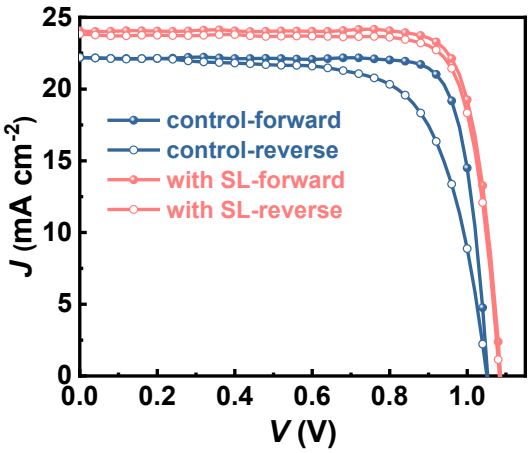


Figure C7 *J–V* curves of the Pero-SCs with SL in different scan directions.[165] Reprinted with permission from *ACS Appl. Mater. Interfaces* 2025, 17 (31), 44481–44489. Copyright 2025 American Chemical Society.

Table C4 Photovoltaic parameters of Pero-SCs at different scan directions. The HI is calculated by $(PCE_{FS} - PCE_{RS})/PCE_{FS}$.[165] Reprinted with permission from *ACS Appl. Mater. Interfaces* 2025, 17 (31), 44481−44489. Copyright 2025 American Chemical Society.

	V_{OC}(V)	J_{SC} (mA cm^{-2})	FF (%)	PCE (%)	HI
control-forward	1.05	22.20	83.0	19.34	0.15
control-reverse	1.05	22.21	70.5	16.44	
with SL-forward	1.08	24.06	82.6	21.47	0.03
with SL-reverse	1.08	23.84	81.2	20.91	

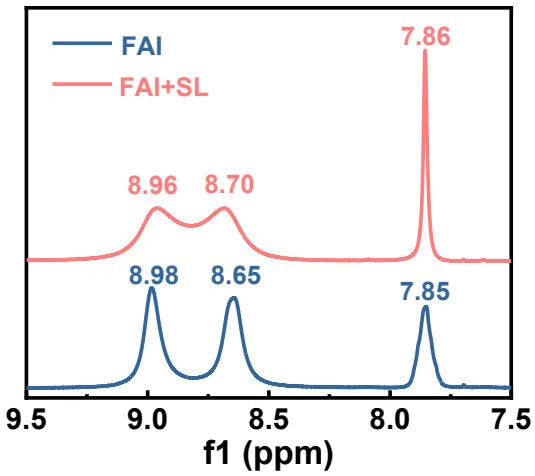


Figure C8 ^{1}H NMR spectra of FAI and FAI+SL.[165] Reprinted with permission from *ACS Appl. Mater. Interfaces* 2025, 17 (31), 44481–44489. Copyright 2025 American Chemical Society.

Appendix D

Supporting Information of Chapter 7

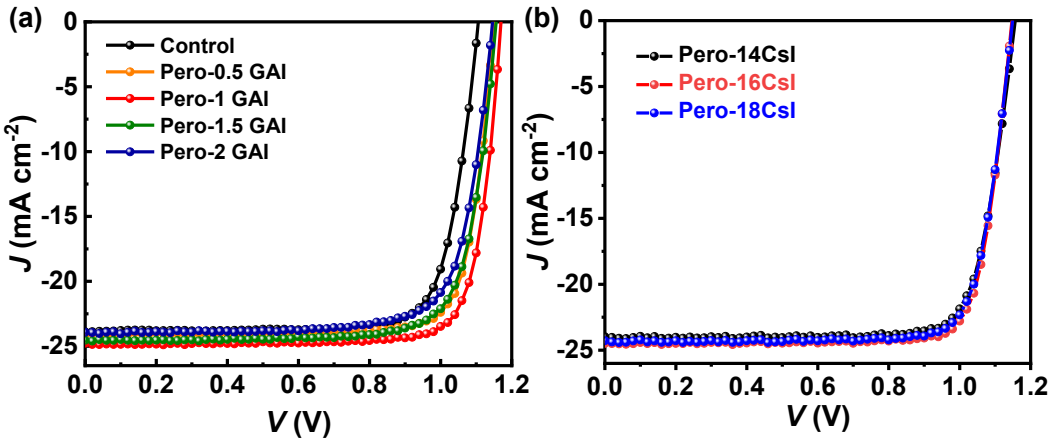


Figure D1 (a) *J*−*V* curves of the Pero-SCs with different concentrations of GAI. The concentration of CsI is 16.0 mg mL^{-1}. (b) *J*−*V* curves of the Pero-SCs with different concentrations of CsI. The concentration of GAI is 1.0 mg mL^{-1}.

Table D1 Photovoltaic parameters of Pero-SCs with different concentrations of GAI. The concentration of CsI is 16.0 mg mL^{-1}.

GAI	V_{OC} (V)	J_{SC} (mA cm^{-2})	FF (%)	PCE (%)
Control	1.11	23.89	78.2	20.65
0.5 mg mL^{-1}	1.15	24.09	80.7	22.34
1.0 mg mL^{-1}	1.17	24.83	81.1	23.55
1.5 mg mL^{-1}	1.16	24.57	77.8	22.09
2.0 mg mL^{-1}	1.15	23.95	76.7	21.03

Table D2 Photovoltaic parameters of Pero-SCs with different concentrations of CsI. The concentration of GAI is 1.0 mg mL^{-1}.

CsI	V_{OC} (V)	J_{SC} (mA cm^{-2})	FF (%)	PCE (%)
14 mg/ml	1.16	24.03	79.4	22.05
16 mg/ml	1.15	24.51	81.3	22.84
18 mg/ml	1.15	24.51	79.6	22.39

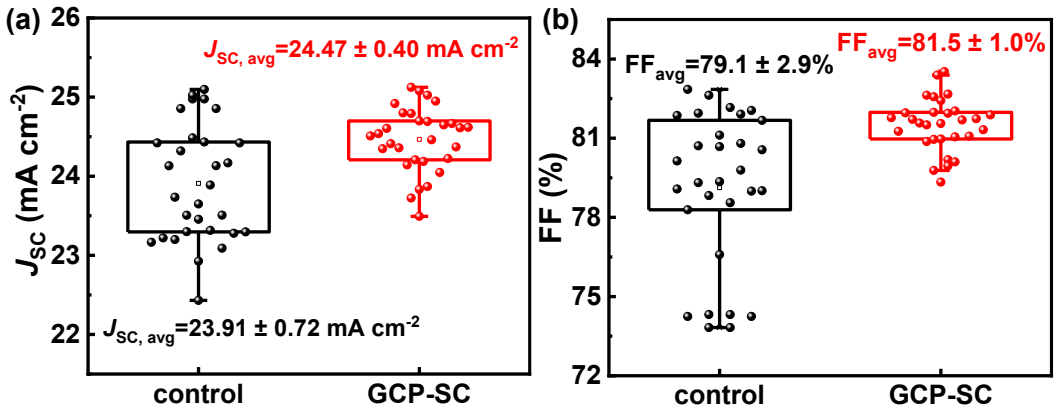


Figure D2 (a) J_{SC} and (b) FF distribution analyzed from 30 cells.

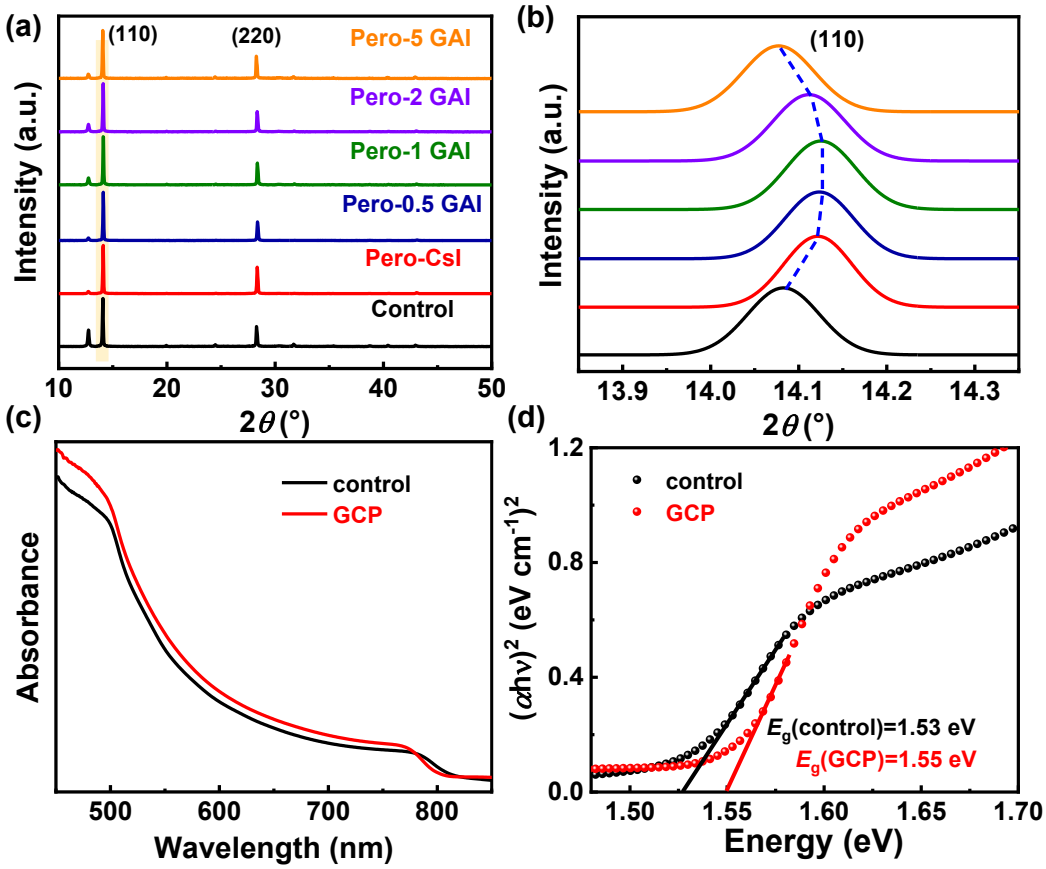


Figure D3 (a) XRD patterns of different perovskite films. (b) Locally enlarged XRD patterns at (110) peak. (c) UV–vis spectra and (d) Tauc plots of perovskite films without and with GAI and CsI.

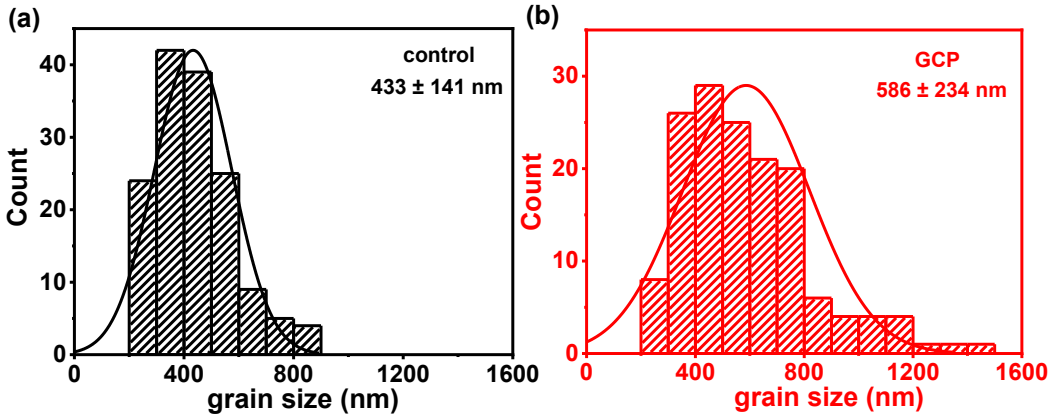


Figure D4 Grain size distribution of (a) the pristine perovskite film and (b) GCP film.

Table D3 Lifetimes and fractions derived from TRPL.

Sample	τ_1 (ns)	f_1 (%)	τ_2 (ns)	f_2 (%)
control	11.0	4.0	84.8	96.0
GCP	10.4	0.4	151.1	99.6